UNIVERSITY OF CALIFORNIA, SAN DIEGO

First-Principles Study of Two-Dimensional Electron Gas in Perovskite Oxide Heterostructures

A dissertation submitted in partial satisfaction of the
requirements for the degree
Doctor of Philosophy

in

Chemical Engineering

by

Jianli Cheng

Committee in charge:

Professor Kesong Yang, Chair
Professor Prabhakar R. Bandaru
Professor Eric E. Fullerton
Professor Jian Luo
Professor Shyue Ping Ong

2018

The dissertation of Jianli Cheng is approved, and it is acceptable in quality and form for publication on microfilm and electronically:

_____

_____

_____

_____

_____

Chair

University of California, San Diego

2018

DEDICATION

To my parents, sister and girlfriend.

EPIGRAPH

The principal applications of any sufficiently new and innovative technology always have been—and will continue to be—applications created by that technology.

—Herbert Kroemer

TABLE OF CONTENTS

LIST OF FIGURES

LIST OF TABLES

ACKNOWLEDGEMENTS

First and foremost, I would like to express my gratitude to my thesis advisor, Dr. Kesong Yang, for his guidance and support during my graduate studies. Beyond your always perceptive insights, your diligence and high-level scientific vision have set an excellent example for me to follow. My acknowledgments also go to my thesis committee Dr. Prabhakar R. Bandaru, Dr. Eric E. Fullerton, Dr. Jian Luo and Dr. Shyue Ping Ong for their ideas and support in the completion of this thesis. I also would like to thank the Sustainable Power and Energy Center for the Graduate Summer Fellowship.

I am grateful to Dr. Safdar Nazir, Maziar Behtash, Paul H. Joo, Yuheng Li, Dr. Yaqin Wang, Dr. Leigang Li, Dr. Haiyang Wang, Dr. Ying Li, Dr Tom Wu, and Dr. Junfeng Ding, who were great collaborators from start to finish. Much of the work in this thesis would not have been completed without your contributions. I would like to thank other members of the Yang research group for making my graduate life enjoyable and memorable. I also would like to thank Dr. Shyue Ping Ong's group members, especially Dr. Zhenbin Wang, for the enlightening discussions and help.

I cannot be more grateful to anyone than my parents. They have always provided me the best education and given me the full support for whatever path I decided to take. I also thank my sister for her constant love and support.

Finally, to my amazing girlfriend, Yuan Zhang, I thank you for your faith and commitment in our long-distance relationship. I know you will always be there for me in my dark days, even though we are thousands of miles apart. Your unconditional love and encouragement made sure we completed this journey together.

Chapter 2, in full, is a reprint of the material "δ-Doping Effects on Electronic and Energetic Properties of $LaAlO_3/SrTiO_3$ Heterostructure: First-Principles Analysis of 23 Transition-Metal Dopants" as it appears in Advanced Materials Interfaces. Jianli Cheng, Yaqin Wang, Jian Luo, Kesong Yang, 4, 1700579, 2017. The dissertation author was the primary investigator and author

of this paper.

Chapter 3, in full, is a reprint of the material "Comparison Studies of Interfacial Electronic and Energetic Properties of $LaAlO_3/TiO_2$ and $TiO_2/LaAlO_3$ Heterostructures from First-Principles Calculations" as it appears in ACS Applied Materials and Interfaces. Jianli Cheng, Jian Luo, Kesong Yang, 9, 76827690, 2017. The dissertation author was the primary investigator and author of this paper.

Chapter 4, in full, is currently being submitted for publication of the material "Two-Dimensional Electron Gas at Spinel/Perovskite Interface: Interplay between Polar Catastrophe and Structural Defects", Junfeng Ding, Jianli Cheng, Fatih Dogan, Yang Li, Weinan Lin, Yingbang Yao, Aurelien Manchon, Kesong Yang, and Tom Wu. The dissertation author was the co-author of this paper.

Chapter 5, in full, is a reprint of the material "First-Principles Prediction of Two-Dimensional Electron Gas Driven by Polarization Discontinuity in Nonpolar/Nonpolar $AHfO_3/SrTiO_3$ (A=Ca, Sr, and Ba) Heterostructures" as it appears in ACS Applied Materials and Interfaces. Jianli Cheng, Safdar Nazir, Kesong Yang, 8, 31959-31967, 2016. The dissertation author was the primary investigator and author of this paper.

Chapter 6, in full, is a reprint of the material "Design of Two-Dimensional Electron Gas Systems via Polarization Discontinuity from Large-Scale First-Principles Calculations". as it appears in Journal of Materials Chemistry C. Jianli Cheng, Kesong Yang, 6, 6680-6690, 2018. The dissertation author was the primary investigator and author of this paper.

Chapter 7, in full, is currently being submitted for publication of the material "Aimsgb: An Algorithm and Open-Source Python Library to Generate Periodic Grain Boundary Structures". Jianli Cheng, Jian Luo, Kesong Yang. The dissertation author was the primary investigator and author of this paper.

VITA

2012	B. E., Pharmaceutical Engineering, Beijing University of Chinese Medicine
2014	M. S., Chemical Engineering, Rutgers University
2014-2015	Teaching Assistant, University of California San Diego
2015-2018	Research Assistant, University of California San Diego
2018	Ph. D., Chemical Engineering, University of California San Diego

PUBLICATIONS

Jianli Cheng, Kesong Yang, "Design of Two-Dimensional Electron Gas Systems via Polarization Discontinuity from Large-Scale First-Principles Calculations", *J. Mater. Chem. C*, 6, 6680-6690, 2018

Jianli Cheng, Yaqin Wang, Jian Luo, Kesong Yang, "δ-Doping Effects on Electronic and Energetic Properties of $LaAlO_3/SrTiO_3$ Heterostructure: First-Principles Analysis of 23 Transition-Metal Dopants", *Advanced Materials Interfaces*, 4, 1700579, 2017

Jianli Cheng, Jian Luo, Kesong Yang, "Comparison Studies of Interfacial Electronic and Energetic Properties of $LaAlO_3/TiO_2$ and $TiO_2/LaAlO_3$ Heterostructures from First-Principles Calculations", *ACS Appl. Mater. Interfaces*, 9, 76827690, 2017

Jianli Cheng, Safdar Nazir, Kesong Yang, "First-Principles Prediction of Two-Dimensional Electron Gas Driven by Polarization Discontinuity in Nonpolar/Nonpolar $AHfO_3/SrTiO_3$ (A=Ca, Sr, and Ba) Heterostructures", *ACS Appl. Mater. Interfaces*, 8, 3195931967, 2016

Jianli Cheng, Jian Luo, Kesong Yang, "Aimsgb: An Algorithm and Open-Source Python Library to Generate Periodic Grain Boundary Structures", *submitted*, 2018.

Junfeng Ding, Jianli Cheng, Fatih Dogan, Yang Li, Weinan Lin, Yingbang Yao, Aurelien Manchon, Kesong Yang, Tom Wu, "Two-Dimensional Electron Gas at Spinel/Perovskite Interface: Interplay between Polar Catastrophe and Structural Defects", *submitted*, 2018

ABSTRACT OF THE DISSERTATION

First-Principles Study of Two-Dimensional Electron Gas in Perovskite Oxide Heterostructures

by

Jianli Cheng

Doctor of Philosophy in Chemical Engineering

University of California, San Diego, 2018

Professor Kesong Yang, Chair

Two-dimensional electron gas (2DEG) formed at the interface between two insulating perovskite oxides has provided a versatile playground to explore emergent interfacial electronic and magnetic properties. In this thesis, our efforts centered on studying the electronic and structural properties of different 2DEG heterostructures (HS), with the goal of designing novel 2DEG HS using first-principles methods.

In the first project, we studied the δ-doping effects on the electronic and energetic properties of $LaAlO_3/SrTiO_3$ HS with 23 transition-metal (TM) dopants. It has been found that there is a trade-off between achieving small electron effective mass and obtaining an energetically

favorable TM-doped $LaAlO_3/SrTiO_3$ system. More importantly, in addition to the experimentally confirmed Mn dopant, we proposed that Fe, Co, Ni, Ru, Rh, Pd, Os and Ir elements can also be promising dopants to yield light effective mass bands and good energetic stability.

In the second project, we compared the electronic and energetic properties of $TiO_2/LaAlO_3$ and $LaAlO_3/TiO_2$ HS. We found that $TiO_2/LaAlO_3$ is intrinsically metallic and has a larger interfacial charge carrier density, smaller electron effective mass and a stronger interface cohesion than $LaAlO_3/TiO_2$, which shows an insulator-to-metal transition at 4 unit cells of $LaAlO_3$.

In the third project, we introduced a hitherto unknown 2DEG formed at the interface between spinel $MgAl_2O_4$ and $SrTiO_3$. Our integrated approach combining experimental measurements and first-principles calculations reveals that an atomic-thin interfacial Ti-Al-O layer is key to the observed metallic transport. The 2DEG observed at spinel/perovskite interface implies the existence of emergent phenomena at the interfaces between spinel group minerals and perovskite oxides.

In the fourth and fifth project, we explored the possibility of creating 2DEG in nonpolar/nonpolar perovskite oxide HS. We found that the lattice-mismatch-induced compression strain from the substrate leads to a large polarization in the film, which then drives the charge transfer from the film to the substrate and results in a 2DEG at the interface. Then, by using high-throughput first-principles calculations and a group of combinatory descriptors, we rapidly designed more than 300 novel nonpolar/nonpolar 2DEG HS.

In the final project, we introduced an efficient and open-source Python library, aimsgb, for generating atomic coordinates in periodic grain boundary models. It is designed to construct various grain boundary structures from cubic and non-cubic initial configurations. Aimsgb is expected to greatly accelerate the theoretical and experimental investigation of grain boundary properties.

Chapter 1

Introduction

Interfaces are ubiquitous in nanocrystalline materials and represent a crystallographic and/or chemical discontinuity with a width ranging from two atomic diameters to a few number of interplanar spacings. [145] Physics phenomena at interface are correlated with the structural configurations and have stimulated a tremendous amount of research activities to tailor the interface at atomic length scale, yielding novel properties and functionalities. In particular, the recent advances in thin-film growth techniques and modeling have enabled the abrupt oxide heterointerfaces as an exciting platform for creation, characterization and engineering the new physics emerging at the interfaces. [38, 141, 219] A microscopic exploration of these interfacial phenomena has provided new insights not only for understanding the fundamental physics but also for designing novel nanoelectronic devices. [166]

Among the materials that form the oxide heterointerfaces, transition metal oxides (TMOs) are one of the most important classes as they expose a wealth of functional properties that are absent in conventional semiconductors. From the simple binary oxides to the complex ternary oxides, TMOs possess a rich spectrum of physics phenomena, including multiferroicity, [91] high-temperature superconductivity, [123] colossal magnetoresistance, [114] and metal-insulator transition. [108] These intriguing behaviors arise from the bonding geometries in the TMO

structures and the hybridization between the transition metals and oxygen, [165] and so naturally the interfaces formed by TMOs should display even more exotic phenomena.

One family of TMOs that has drawn a staggering amount of attention is the ABO_3 perovskite oxide and in this thesis, we focus on ABO_3 perovskite-oxide-based heterostructures, with an emphasis on the two-dimensional electron gas (2DEG) formed at the interface of two insulating perovskite oxides. In this chapter, we will first provide a brief introduction to the electronic and structural properties of perovskite oxides. Then, we discuss the physical phenomena occuring at the heterointerface, focusing on the charge transfer mechanisms of 2DEG. At the end, we summarize the organization of this thesis.

1.1 Perovskites oxides

Perovskite oxides represent the compounds with the chemical formula ABO_3 that crystallize into a cubic structure (Figure 1.1a). The interstitial A-site ion is usually an alkaline earth or rare earth element and the B-site ion is usually a transition metal element and coordinated with six O^{2-} anions in corner-connected octahedral. The A and B sites can span a broad range of elements in the periodic table with various valences and ionic radii, and in general, their oxidation states can be $A^{1+}B^{5+}$, $A^{2+}B^{4+}$ and $A^{3+}B^{4+}$, giving rise to an incredible diversity of materials properties. Due to the size mismatch between A and B sites, most perovskite oxides are not perfect cubic and undergo many symmetry-breaking structural distortions. The deviation from the centrosymmetric structure can be described by the Goldschmidt tolerance factor $t = r_{A-O}/(r_{B-O}\sqrt{2})$. For the ideal cubic structure (Figure 1.1a), the A-O and B-O bond lengths are such that $t = 1$. For $t > 1$ structure (Figure 1.1b), such as $BaTiO_3$, the B-site tends to move off-center, which distorts the structure into a tetragonal lattice. For $t < 1$ structure (Figure 1.1c), such as $CaTiO_3$, oxygen octahedral rotations are preferred, which yield an orthorhombic or rhombohedral lattice.

In the ABO_3 structure with B-site as a transition metal, the outermost electrons on

the B-site ion partially occupy d orbitals. In a cubic structure, the electrostatic interaction and hybridization between d orbital electrons and surrounding charges from oxygens create a crystal field which is able to lift the five-fold degenerated d orbitals into two high energy $e_g(d_{x^2-y^2}, d_{z^2})$ orbitals and three low energy $t_{2g}(d_{xy}, d_{xz}, d_{yz})$ orbitals with the crystal field splitting $\Delta_{CF} \sim 1 - 2eV$ (Figure 1.1d). The degeneracy in e_g and t_{2g} orbitals can be further lifted upon the elongation/compression of oxygen octahedral, as shown in Figure 1.1d.

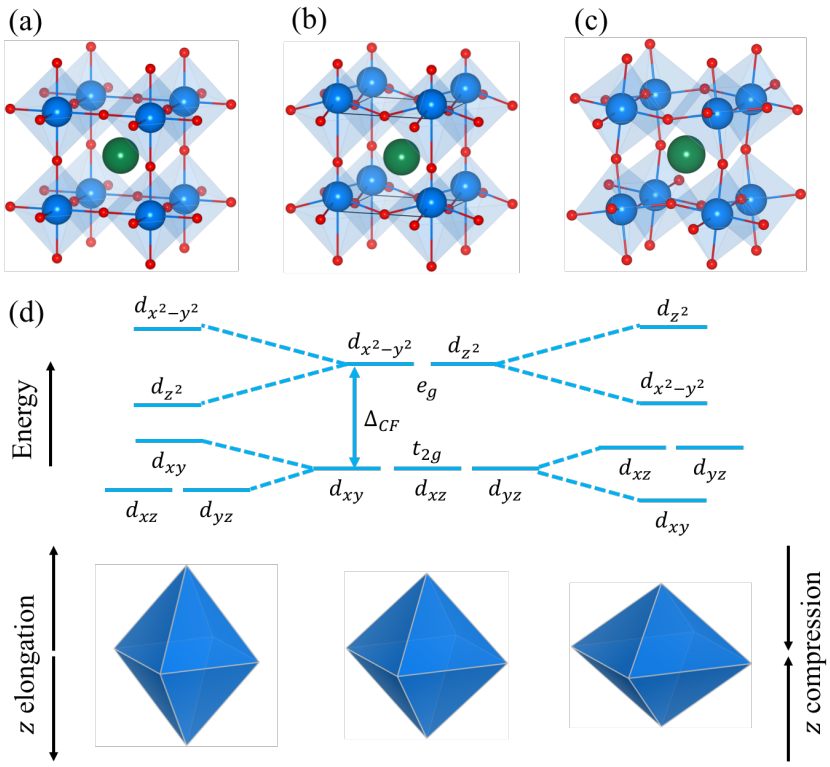

Figure 1.1: Structure of an ABO_3 perovskite for (a) ideal cubic , (b) B site distorted tetragonal and (c) octahedral rotated orthorhombic structure. (d) The effects of z elongation and compression on the degeneracies of e_g and t_{2g} orbitals.

With the co-exist and couplings among spin, charge, orbital and lattice degrees of freedom, perovskite oxides host a broad spectrum of physical phenomena, such as multiferroicity, [91] high-temperature superconductivity, [123] colossal magnetoresistance, [114] and metal-insulator transition. [108] Thus, with the affluence of materials properties, perovskite oxides provide an exciting playground for understanding the fundamental physics and developing novel materials

for applications. That being said, perhaps even more interesting is to combine the functional perovskite oxides into heterstructures, thereby engineering multifunctional materials. In the next section, we will discuss the physical phenomena occurring at the heterointerface, with an emphasis on the formation of interfacial 2DEG.

1.2 Formation of 2DEG at perovskite oxide interfaces

Enabled by the recent advances in epitaxial synthesis techniques, abrupt heterointerfaces and superlattices have risen as a powerful platform to explore the emergent material properties by manipulating the coupled charge, spin, orbital, and lattice degrees of freedom. Two-dimensional electron gas (2DEG), quantum hall effect, [252] superconductivity, [213] magnetism, [118] nanoscale-controlled metal-insulator transition, [47] and spin-to-charge conversion [147] are but a few examples of phenomena that arise from the heterointerfaces and in principle, they are induced by charge transfer, epitaxial strain, symmetry breaking, electrostatic coupling between the layers and frustration between different interactions. [282] Among these emerging physical properties, the 2DEG formed at the interface of two wide-band-gap perovskite insulators has received a disproportionate amount of attention, because it gives rise to not only a wide variety of new and unexpected behaviors, but also the potential applications in the nanoelectronics. [113, 236] So naturally this particular phenomenon occupies much of the focus in this thesis.

In terms of interfacial configurations of perovskite oxide heterostructures (HS), there are essentially three types of interfaces that can form the 2DEG, [255] as shown in Figure 1.2. The first one is polar/nonpolar interface, such as $(LaO)^{+}/(TiO_2)^{0}$ in $LaAlO_3/SrTiO_3$ HS. The 2DEG formation mechanism in $LaAlO_3/SrTiO_3$ is primarily attributed to the intrinsic electronic reconstruction, *i.e.*, polar catastrophe. [190,257] Other mechanisms, such as the oxygen vacancies, [158, 273] interface cation mixing, [179] and internal structural deformation, [196, 220] have also been proposed to explain the origins of the interfacial 2DEG conductivity. Despite the

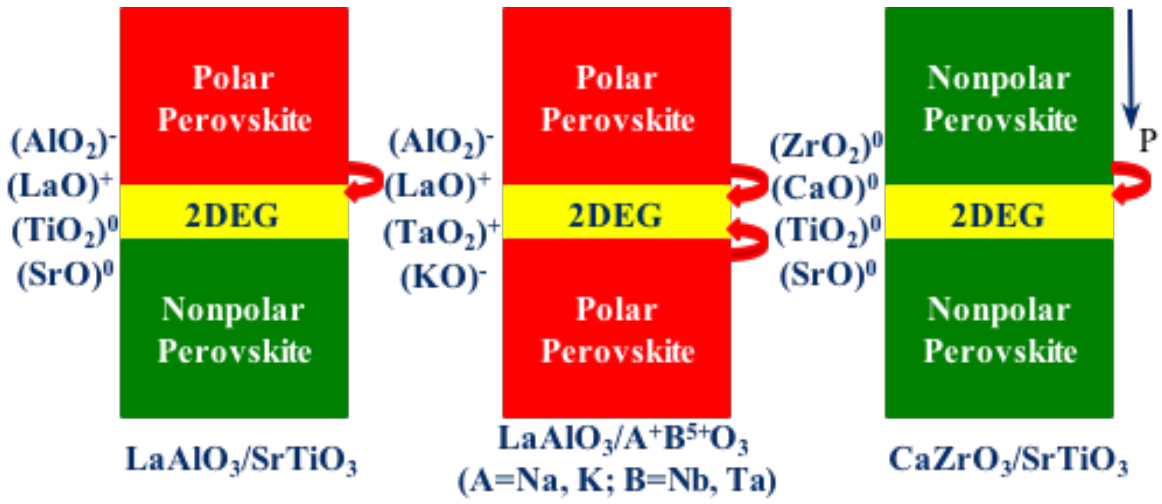

Figure 1.2: A schematic figure showing that the formation of 2DEG can be realized in three different interfacial configurations: polar/nonpolar, nonpolar/nonpolar and polar/polar heterointerfaces.

controversy, the polar/nonpolar interfacial configuration plays a critical role in forming the interfacial conductivity. For example, in addition to the intensively studied $LaAlO_3/SrTiO_3$ HS, other polar/nonpolar HS have also been synthesized and found to host the 2DEG as well, such as $LaTiO_3/SrTiO_3$, [16] $GdTiO_3/SrTiO_3$ [176] and $NdGaO_3/SrTiO_3$. [83]

The second interfacial configuration to produce 2DEG in perovskite oxide HS is polar/polar interface such as $(LaO)^{+1}/(TaO_2)^{+1}$ in $LaAlO_3/KTaO_3$. [255, 275, 281] In the computational side, by using first-principles electronic structures calculations, we have proposed to create 2DEG in the polar/polar perovskite oxide HS based on the $LaAlO_3/A^{+}B^{5+}O_3$ (A = Na and K, B = Nb and Ta). [255] Its interfacial conductivity is attributed to two donor layers, *i.e.*, $(LaO)^{+1}$ and $(BO_2)^{+1}$, in this polar/polar system, which has larger interfacial charge carrier density than the polar/nonpolar $LaAlO_3/SrTiO_3$ HS. In the experimental side, very recently, $LaAlO_3/KTaO_3$ interface has been successfully fabricated, and a highly mobile 2DEG has been observed at the interface; [275] Zou *et al.* has prepared a $LaTiO_3/KTaO_3$ HS and reported an interfacial 2DEG with a higher carrier mobility than the doped bulk $SrTiO_3$. [281]

The third interfacial configuration is based on nonpolar/nonpolar interface. Besides the HS

relying on the polar oxide layers to create the interfacial 2DEG, very recently, nonpolar/nonpolar oxide HS have also been found to produce 2DEG via the piezoelectric polarization, such as the $CaZrO_3/SrTiO_3$, both from the experiment and first-principles electronic structure calculations. [46, 187] In the $CaZrO_3/SrTiO_3$ HS, there exists an insulator-to-metal transition when the $CaZrO_3$ film thickness goes beyond 6 unit cells, and the 2DEG is attributed to the lattice-mismatch-induced polarization in the $CaZrO_3$ film. [46] Our first-principles computational study has confirmed the formation of the interfacial metallic states and shows that the compressive strain in the $CaZrO_3$ film leads to a polarization discontinuity at the interface that drives the charges from the $CaZrO_3$ film to the $SrTiO_3$ substrate, forming the 2DEG at interface. [187] Moreover, unlike polar/nonpolar and polar/polar HS, which rely on a specific interfacial termination to form the 2DEG, the creation of 2DEG in $CaZrO_3/SrTiO_3$ HS is less sensitive to the interfacial terminations and can be formed at both terminations. Soon later, we further proposed several other nonpolar/nonpolar perovskite oxide HS based on the $AHfO_3/SrTiO_3$ (A = Ca, Sr, and Ba). [49]

1.3 Summary

Perovskite oxide HS with emerging interfacial 2DEG are a promising new class of materials for nanoelectronics. In the rest of this thesis we will study the electronic and structural properties of different 2DEG HS, with the goal of designing novel 2DEG HS using first-principles methods. In Chapter 2 we will discuss the δ-doping effects on electronic and energetic properties of prototypical $LaAlO_3/SrTiO_3$ HS, highlighting the trade-off between electron effective mass and thermostability. In Chapter 3 we will present a different heterointerface between anatase TiO_2 and $LaAlO_3$, which has a higher conductivity than that in $LaAlO_3/SrTiO_3$ HS. In Chapter 4 we will introduce a hitherto unknown 2DEG formed at the interface between spinel $MgAl_2O_4$ and $SrTiO_3$. In Chapter 5 we will explore the possibility of producing 2DEG in nonpolar/nonpolar $AHfO_3/SrTiO_3$ (A=Ca, Sr, and Ba) HS, with 2DEG induced by polarization discontinuity. In

Chapter 6 we will show that by using high-throughput first-principles calculations and a group of effective materials descriptors, we are able to rapidly design more than 300 novel 2DEG HS based on nonpolar/nonpolar perovskite HS. From Chapter 2 to 6, the interfaces formed by different TMOs are called heterophase boundaries, as the adjoining two TMOs differ in chemical composition and lattice parameters. In Chapter 7 we will introduce a homophase boundary, called grain boundary, which is a region in a single-phase polycrystalline material, that separates two grains with atomic mismatch. We then present our newly developed software tool, aimsgb, which is an efficient and open-source Python library for generating atomic coordinates in periodic grain boundary models. Finally, in Chapter 8 we will summarize the results and conclusions in this thesis, present some on-going research projects and suggest future research directions.

Chapter 2

δ-Doping Effects on Electronic and Energetic Properties of $LaAlO_3/SrTiO_3$ Heterostructure

As outlined in Chapter 1, the two-dimensional electron gas (2DEG) formed at the interface between two insulating perovskite oxides, such as $LaAlO_3$ and $SrTiO_3$, provides an exciting playground for developing all-oxide electronic devices. However, improving the 2DEG mobility of $LaAlO_3/SrTiO_3$ heterostructure is still a formidable challenge. In particular, its room-temperature-mobility is as low as 6 $cm^2V^{-1}s^{-1}$. [111] One possible way of improving the 2DEG mobility is via δ-doping at the heterointerface. As a proof of concept, one recent experiment achieves an ultra-high low temperature 2DEG mobility of 73,000 $cm^2V^{-1}s^{-1}$ via Mn δ-doping at the $LaAlO_3/SrTiO_3$ heterointerface. [44] Inspired by this study, one may speculate whether δ-doping with other transition-metal dopants can have similar or further improve the carrier mobility of $LaAlO_3/SrTiO_3$. In this Chapter, we will present the electronic and energetic properties of δ-doped $LaAlO_3/SrTiO_3$ with 23 transition-metal dopants from group 3 to group 10 using first-principles calculations. We found a clear trend for the electron effective mass and

interfacial energy change in the δ-doped $LaAlO_3/SrTiO_3$, and there exists a trade-off between achieving light effective mass bands and forming energetically favorable structures. It is found that besides Mn, Fe, Co, Ni, Ru, Rh, Pd, Os and Ir could also serve as promising candidate dopants to produce light effective mass bands and relatively large energetic stability. Our findings provide a wide avenue to increase the 2DEG mobility in the $LaAlO_3/SrTiO_3$ heterostructure via δ-doping with transition metals.

2.1 Introduction

The interface at complex oxide heterostructures (HS) has been a subject of intense research interests in recent years due to a vast amount of fascinating properties. [34, 149, 190, 213, 247] One example is the polar/nonpolar $(LaO)^+/(TiO_2)^0$ interface between two insulating perovskites $LaAlO_3$ and $SrTiO_3$ along [001] direction. At this interface, there exists many intriguing phenomena such as the two-dimensional electron gas (2DEG), [190] superconductivity, [213] magnetism, [149], electric field tunable insulator-metal transition, [247] and a large Rashba spin-orbit coupling. [34] Such multifunctional properties have provided new insights not only from the fundamental physical perspective but also from practical applications in nanoelectronic devices. [14, 37, 166] For instance, considerable amount of efforts have been invested to develop the $LaAlO_3/SrTiO_3$-based devices such as rectifying junctions, [20] photodector, [110] single-electron transistor, [47] and field-effect transistors. [104, 155] Despite the versatile functionality of the $LaAlO_3/SrTiO_3$ HS, its practical application is still largely impeded because of its low room-temperature electron mobility (6-10 $cm^2V^{-1}s^{-1}$). [68, 111] Hence, it is essential to improve the room-temperature 2DEG mobility of the $LaAlO_3/SrTiO_3$ HS for the further practical applications. Meanwhile, other $SrTiO_3$-based HS have also been explored to find high electron mobility oxide materials. Notable systems are γ-$Al_2O_3/SrTiO_3$ and $CaZrO_3/SrTiO_3$, [43,46] the electron mobility of which is much higher than that in the $LaAlO_3/SrTiO_3$ HS.

In principle, the electron mobility can be improved either by increasing scattering time (also called relaxation time) or by reducing electron effective mass. Accordingly, there are several main-stream approaches proposed to improve the electron mobility in the $LaAlO_3/SrTiO_3$ HS system. One strategy is to tune the epitaxial strain at the interface including several top layers in the substrate or in the films, which can affect the structural distortion and strain at the interfacial region and thus manipulate electronic properties. It has been experimentally and theoretically proven that controlling the epitaxial strain is one effective way to tune the interfacial charge carrier density. [8, 10, 117, 182, 183, 188] Actually, a small lattice mismatch between the film and the substrate is expected to improve the crystalline quality of the heterointerface, thus increase the scattering time and accordingly electron mobility. For example, very recently, Ariando's team has reported that by replacing $LaAlO_3$ with cubic $(La_{0.3}Sr_{0.7})(Al_{0.65}Ta_{0.35})O_3$ (LSAT), the lattice mismatch between the film and the $SrTiO_3$ substrate is reduced from 3.0% to 1.0% and interfacial electron mobility can be significantly improved (about 35000 $cm^2V^{-1}s^{-1}$ at 2 K), which is almost 30 times larger than the prototypical $LaAlO_3/SrTiO_3$. [100] One the other hand, Gunkel *et al.* [84] proposed that the reduced epitaxial strain in $LSAT/SrTiO_3$ has only minor effects on the improved mobility. They attributed the increased electron mobility to the suppression of the defects at the interface, which corresponds to the second strategy to improve the mobility, as discussed below.

The second strategy is to improve the crystalline quality of thin films by varying growth parameters like temperature [63] or by reducing the growth-induced extrinsic defects. [84] For instance, Fête *et al.* reported that a lower growth temperature (650 °C) leads to a higher electron mobility and lower sheet carrier density while a higher growth temperature (800-900 °C) leads to a lower electron mobility and higher sheet carrier density at 4K. Interestingly, this finding seems to imply that the high electron mobility is correlated with the low sheet carrier density, [35, 44, 103, 264] and in contrast, Fête *et al.*'s electric field effect experiments also reveal that the carrier density is not the parameter determining the mobility. [63] Similar concepts were also applied to the bulk $SrTiO_3$ to improve the electron mobility. [129]

The third strategy is by means of δ-doping at $LaAlO_3/SrTiO_3$ interface (the dopants are confined to two-dimensional sheets like layer doping), [80] which is equivalent to the idea of inserting a few buffer layers between the $SrTiO_3$ substrate and the $LaAlO_3$ film. [44, 66, 67, 136] This approach has been experimentally and computationally proven to be able to effectively tune both the electron density and mobility. [51,181,185,186,192,209] To improve the electron mobility of the 2DEG, the ideal δ-doping (or layer doping) should be able to separate the conduction layer from the doping layer and accordingly to increase the scattering time by reducing the ionized impurity scattering. For instance, by introducing an $SrCuO_2$ layer into the $LaAlO_3/SrTiO_3$ HS in which the impurity scattering was strongly reduced, the low-temperature carrier mobility of the 2DEG was significantly improved up to 50,000 $cm^2V^{-1}s^{-1}$. [103] Transition metal dopants, such as Sc, Cr and Mn, have been found to enhance the carrier mobility while decrease carrier density. [66, 67] Rare-earth dopants have also been used to modify the transport property of $LaAlO_3/SrTiO_3$, but its main effect is the modulation of the charge carrier density instead of carrier mobility. [69, 224] Very recently, Chen *et al.* has achieved a significantly improvement of the 2DEG carrier mobility by inserting one single-unit-cell buffer layer of $La_{1-x}Sr_xMnO_3$ in the $LaAlO_3/SrTiO_3$ HS (equivalent to Mn δ-doping at Al site), in which the low-temperature electron mobility was improved up to 73,000 $cm^2V^{-1}s^{-1}$. [44] All these results imply that the choice of appropriate dopants in the δ-doping at $LaAlO_3/SrTiO_3$ interface plays an important role in influencing the carrier mobility. Inspired by these experimental findings, one may speculate that whether δ-doping with other transition-metal dopants can have similar or further improve the carrier mobility of $LaAlO_3/SrTiO_3$ with respect to Mn δ-doping, particularly for the 4*d* and 5*d* transition metals. This is because 4*d* and 5*d* orbitals are generally less localized than the 3*d* orbitals and can potentially introduce light effective mass bands. Hence, a comprehensive computational and theoretical study is of great importance to explore the electronic and energetic properties for δ-doped $LaAlO_3/SrTiO_3$ with these transition metals.

In this work, we have studied the δ-doping effects on the $LaAlO_3/SrTiO_3$ interfacial

electronic and energetic properties with 23 transition-metal dopants, from group 3 to group 10, respectively, using comprehensive first-principles electronic structure calculations. We find that there exists a trade-off between achieving light effective mass bands and obtaining energetically favorable structures for the δ-doped $LaAlO_3/SrTiO_3$ HS. This work may provide useful guidance to achieve high 2DEG mobility in the $LaAlO_3/SrTiO_3$ HS via δ-doping.

2.2 Structural modeling and computational details

A superlattice approach was used to model the $(LaAlO_3)_{7.5}/(SrTiO_3)_{5.5}$ HS, which consists of two symmetric *n*-type $(LaO)^+/(TiO_2)^0$ interfaces. The subscripts 7.5 and 5.5 represent the number of unit cells of $LaAlO_3$ and $SrTiO_3$, respectively. To resemble the experimental epitaxial material growth, all the ions and the cell parameter perpendicular to the interfacial plane were relaxed, while the in-plane lattice constant was fixed to 3.905 Å, the experimental lattice constant of $SrTiO_3$, [190] which results in a lattice mismatch of 2.97% between the $LaAlO_3$ film and the $SrTiO_3$ substrate. A total number of 23 different transition metals (TM), from group 3 to group 10, were considered as the dopants in this study. Two types of doping sites *i.e.*, TM@Al and TM@Ti, were modeled by replacing the interfacial Al and Ti atom with the TM atom, respectively. Considering two symmetric interfaces in the periodic superlattice, two symmetric doping sites (one in each interface) were created in each doped HS system.

All the density functional theory (DFT) electronic structure calculations were performed in the Vienna *Ab-initio* Simulation Package (VASP). [132, 133] The Projector Augmented Wave (PAW) potentials were used for describing ion-electron interactions. [134] The spin-polarized Generalized Gradient Approximation (GGA) was used for treating exchange-correlation functional [200]. The cutoff energy for the plane wave expansion was set to 450 eV. Γ-centered *k*-point grids for Brillouin zone sampling were set to $4 \times 4 \times 1$ for ionic relaxation and $10 \times 10 \times 1$ for static calculations, respectively. The break condition for the electronic self-consistency loop was

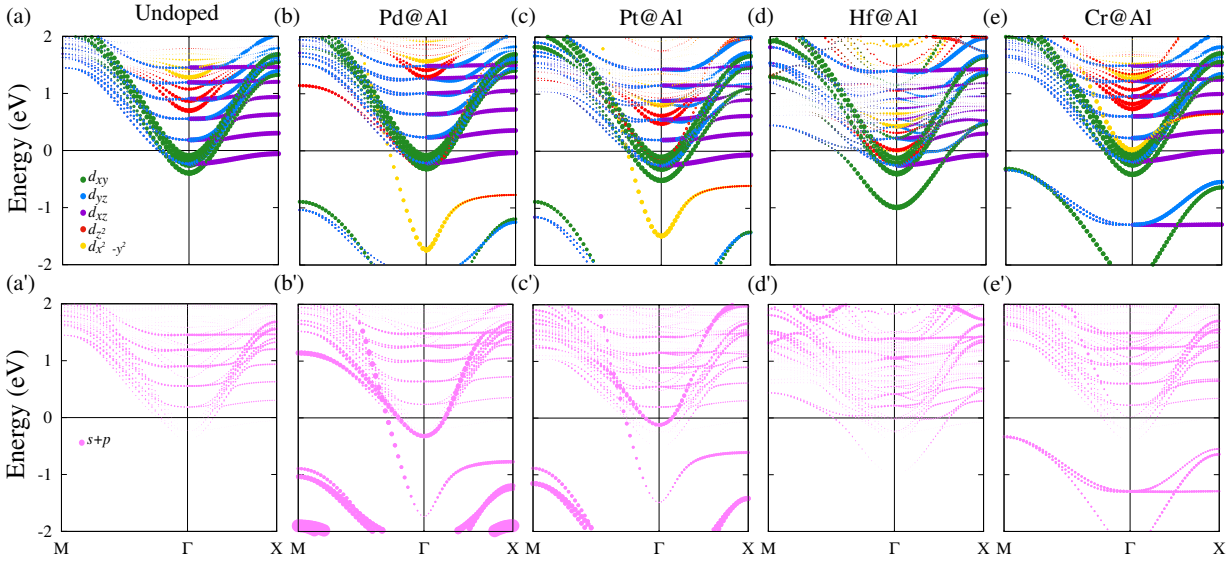

Figure 2.1: Orbital projected band structures for (a) undoped, (b) Pd-, (c) Pt-, (d) Hf- and (e) Cr-doped@Al $LaAlO_3/SrTiO_3$ HS along with their corresponding total *s*+*p* orbitals (a')-(e'). Fermi energy is set to zero. Symbol size is proportional to its population in corresponding state. Note: the symbol sizes of *s*+*p* orbitals are scaled up for illustrative purposes.

assumed for a total energy convergence of less than 10^{-6} eV. All the structures were optimized by minimizing the atomic forces up to 0.03 eV/Å.

2.3 Results and discussion

2.3.1 Band structures and effective mass

To identify appropriate TM dopants that can enhance the electron mobility of 2DEG, we calculated the electron effective mass of TM-doped $LaAlO_3/SrTiO_3$ HS using parabolic *E*-*k* line fitting. [256] This is because both electron mobility μ and electron density n determine the electron conductivity σ ($\sigma = ne\mu$), and μ is further linked to the electron effective mass m^* and average scattering time $<\tau>$: [181, 202]

$$\mu = \frac{e < \tau >}{m^*} \tag{2.1}$$

where e is the fundamental elementary charge. In this study, m^* was calculated by fitting the band structure of HS systems using the equation: [87]

$$\frac{1}{m^*} = \frac{1}{\hbar^2}\frac{\partial^2 E_{CB}}{\partial k^2} \tag{2.2}$$

where $\hbar$ is reduced Planck constant, E_{CB} is the energy of the bottom conduction band, and k is the electron wave vector. To have a comparison with the pristine $LaAlO_3/SrTiO_3$ model, we also calculated m^* for undoped system.

Herein we took undoped, Pd-, Pt-, Hf- and Cr-doped@Al $LaAlO_3/SrTiO_3$ systems as the exemplary models and showed their band structures along the k-path M-Γ-X in Fig. 2.1a-e. To explicitly identify orbital contributions to the conducting states, the electronic band structures were calculated in an orbital-resolved fashion. As expected, the bottom conduction bands of all these systems cross the Fermi level and form the n-type interfacial conducting states, and these bands are mainly contributed by d_{xy} orbitals. [59, 185, 188] For the doped systems, dopants also introduce dispersed impurity states in the band gap. For Pd- and Pt-doped systems, the impurity states crossing the Fermi level are mainly contributed by $d_{x^2-y^2}$ orbitals, and for Hf- and Cr-doped systems, the impurity states are dominated by d_{xy} orbitals. Moreover, more occupied d orbitals in these doped systems indicate that dopants introduce extra electrons into the host $LaAlO_3/SrTiO_3$ system.

Next, we calculated electronic band structures for all the considered TM@Al and TM@Ti systems. The electron effective mass m^* in each system was then evaluated and listed in Table 5.1, along with the total magnetic moment per cell and Bader charge. [246] To observe the trend of electron effective mass directly, we organized all the considered dopants by rows and columns in the periodic table in Fig. 2.2. The value of m^* for each doping system is represented by the shades of blue color, with dark blue as the high m^* and light blue as the low m^*. It clearly shows that m^* decreases significantly from group 3 to group 10 for both TM@Al and TM@Ti systems,

and the dopants causing the lowest m* are observed in the periodic table of group 9 and 10 and row 5 and 6, *i.e.*, Rh, Ir, Pd, and Pt, while in contrast, the dopants in group 3 and 4 and row 5 and 6 regions, *i.e.*, Y, Zr, and Hf, tend to lead to the highest m^*.

The reason behind this trend can be rationalized in terms of the orbital occupation of the conducting states, *i.e.*, impurity states crossing the Fermi level. For doped HS with Rh, Ir, Pd and Pt, the *d* orbitals of these TM atoms consist of a larger amount of *s* and *p* orbital populations, and due to the more dispersive and less localized nature of *s* and *p* orbitals, smaller electron effective masses are observed. [17, 76] To exemplify this observation, we plotted the $s+p$ band structures for undoped, Pd-, Pt-, Hf- and Cr-doped@Al HS models in Fig. 2.1a'-e'. In these figures, the size of each eigenstate is proportional to its population in corresponding state. Our results illustrate that the bottom conduction band near the Γ point in undoped (2.1a'), Hf- (2.1d') and Cr-doped (2.1e') HS systems are completely free of *s*+*p* components, compared to the Pd- and Pt-doped HS systems. Accordingly, a more dispersive and less localized bottom conduction band is induced by the higher population of $s+p$ orbitals in the Pd- and Pt-doped HS systems, thus resulting in a smaller effective mass.

We also listed $s+p$ orbital population for all the TM@Al- and TM@Ti-doped HS in the Table 5.1 along with the corresponding *d* orbital population. The orbital population value is calculated by averaging the orbital population of the eigenstates in the bottom conduction band. To have a clear observation of the relation between electron effective mass and $s+p$ orbital and *d* orbital population, we also plotted the dependence of effective mass, $s+p$ orbital population and *d* orbital population on different dopants in Fig. 2.3. It can be found that as the effective masses increase (Fig. 2.3a), *d* orbital populations increase (Fig. 2.3b) while the $s+p$ orbital populations decrease (Fig. 2.3c). Meanwhile, the TM-oxygen bond character is directly related to the electronegativity difference between TM atom and oxygen. As the electronegativity of TM atom increases from group 3 to group 10 in the periodic table (1.12 to 1.88), [3] the electronegativity difference between the TM atom with oxygen atom becomes smaller. As a

Table 2.1: Calculated total magnetic moment (μ_B), Bader charge, electron effective mass m^*, $s+p$ orbital and d orbital population at CBM, and the minimum interfacial formation energy change $\Delta\gamma_{min}$ (eV/Å^2) for TM@Al and TM@Ti HS. The calculated m^* for undoped HS system was also given as a comparison.

Dopants	TM@Al						TM@Ti					
	Magnetic moment	Bader charge	m^* (m_e)	s+p (%)	d (%)	$\Delta\gamma_{min}$ (eV/Å^2)	Magnetic moment	Bader charge	m^* (m_e)	$s+p$ (%)	d (%)	$\Delta\gamma_{min}$ (eV/Å^2)
Co	0.45	1.39+	0.23	12.22	87.47	-0.176	1.50	1.57+	0.10	55.90	44.01	-0.263
Fe	2.34	1.63+	0.19	18.96	80.87	-0.203	3.15	1.67+	0.11	54.14	45.74	-0.329
Ni	0.00	1.19+	0.19	16.84	82.94	-0.156	0.00	1.34+	0.14	47.88	51.93	-0.226
Ir	0.03	1.29+	0.14	25.57	73.04	-0.003	0.00	1.43+	0.10	39.86	59.24	-0.170
Ru	0.20	1.46+	0.21	9.27	88.96	-0.071	1.19	1.69+	0.15	36.06	63.52	-0.236
Pd	0.00	1.18+	0.12	19.54	80.24	-0.001	0.00	1.28+	0.10	33.77	65.83	-0.137
Pt	0.00	1.41+	0.17	15.04	84.36	0.059	0.00	1.37+	0.15	25.05	74.72	-0.120
Rh	0.00	1.35+	0.18	10.90	88.33	-0.057	0.00	1.47+	0.15	22.14	77.65	-0.196
Mn	3.32	1.52+	0.24	11.98	87.87	-0.279	3.31	1.62+	0.16	18.73	81.25	-0.425
Os	0.00	1.69+	0.18	8.39	90.01	-0.018	0.15	1.67+	0.18	15.40	83.74	-0.193
Cr	2.73	1.59+	0.45	2.44	94.64	-0.329	2.34	1.70+	0.31	9.70	90.30	-0.460
Tc	0.02	1.75+	0.25	5.58	92.40	-0.141	0.00	1.90+	0.23	6.70	92.16	-0.311
Ta	0.01	2.21+	0.31	2.90	91.45	-0.298	0.00	2.56+	0.33	3.19	92.29	-0.522
Nb	0.00	2.05+	0.32	3.03	91.52	-0.309	-0.06	2.32+	0.32	3.24	92.42	-0.515
Re	0.00	1.81+	0.24	5.08	92.55	-0.098	0.00	1.92+	0.23	5.69	92.84	-0.281
W	0.00	2.02+	0.28	3.86	92.75	-0.191	0.00	2.15+	0.27	4.08	93.25	-0.380
Mo	0.00	1.76+	0.29	3.76	93.16	-0.208	0.00	1.97+	0.28	4.25	93.78	-0.389
Ti	0.37	1.89+	0.45	2.13	92.78	-0.487	-	-	-	-	-	-
V	1.65	1.76+	0.39	3.38	94.31	-0.386	1.29	1.84+	0.36	4.43	94.56	-0.546
Y	0.00	1.96+	0.93	8.38	91.61	-0.367	0.46	2.00+	0.39	3.64	96.30	-0.503
Sc	0.03	1.61+	0.46	2.20	94.95	-0.521	0.37	1.66+	0.39	2.79	97.14	-0.616
Zr	0.14	2.13+	0.58	1.76	92.21	-0.398	0.00	2.13+	0.43	2.35	97.65	-0.619
Hf	0.00	2.42+	0.59	1.71	91.79	-0.460	0.00	2.41+	0.44	2.27	97.72	-0.683
Undoped	0.03	-	0.46	2.20	95.50	-	0.03	-	0.46	2.20	95.50	-

result, the dopants with larger electronegativity such as Rh, Ir, Pd, and Pt can have a higher degree of covalent interaction with oxygen atom. On the other hand, a covalent bonding allows a lower effective mass and higher carrier mobility for the electrons, [234, 249] while a higher degree of ionic interaction of the bond tends to trap carriers and reduces electron mobility. [122, 250] Thus TM dopants with larger electronegativity in the HS systems tends to lead to a smaller m^* value than those TM dopants with smaller electronegativity.

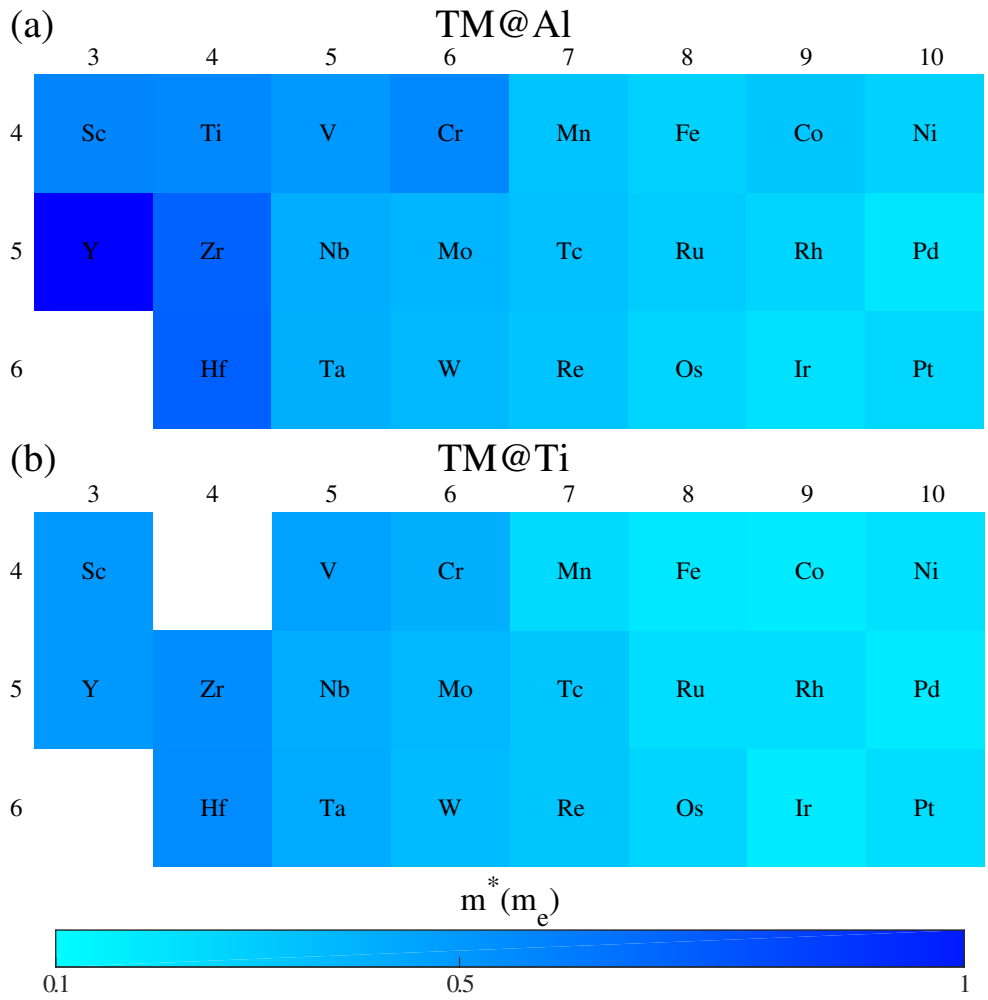

Figure 2.2: Effective mass values for (a) TM@Al and (b) TM@Ti HS plotted in row and columns of the periodic table. Dark blue is for high effective mass while light blue is for low effective mass.

2.3.2 Interfacial energetics

In this section, we studied the interfacial energetics to evaluate the thermodynamic stability of the $LaAlO_3/SrTiO_3$ HS after TM doping. Herein, we determined the energetic stability by calculating the change of interfacial energy $\Delta\gamma$ between undoped and TM-doped $LaAlO_3/SrTiO_3$ HS using the following formula: [60, 181, 186]

$$\Delta\gamma = (E_{HS}^{TM@X} - E_{HS}^{undoped} + 2\mu_X - 2\mu_{TM})/2A \tag{2.3}$$

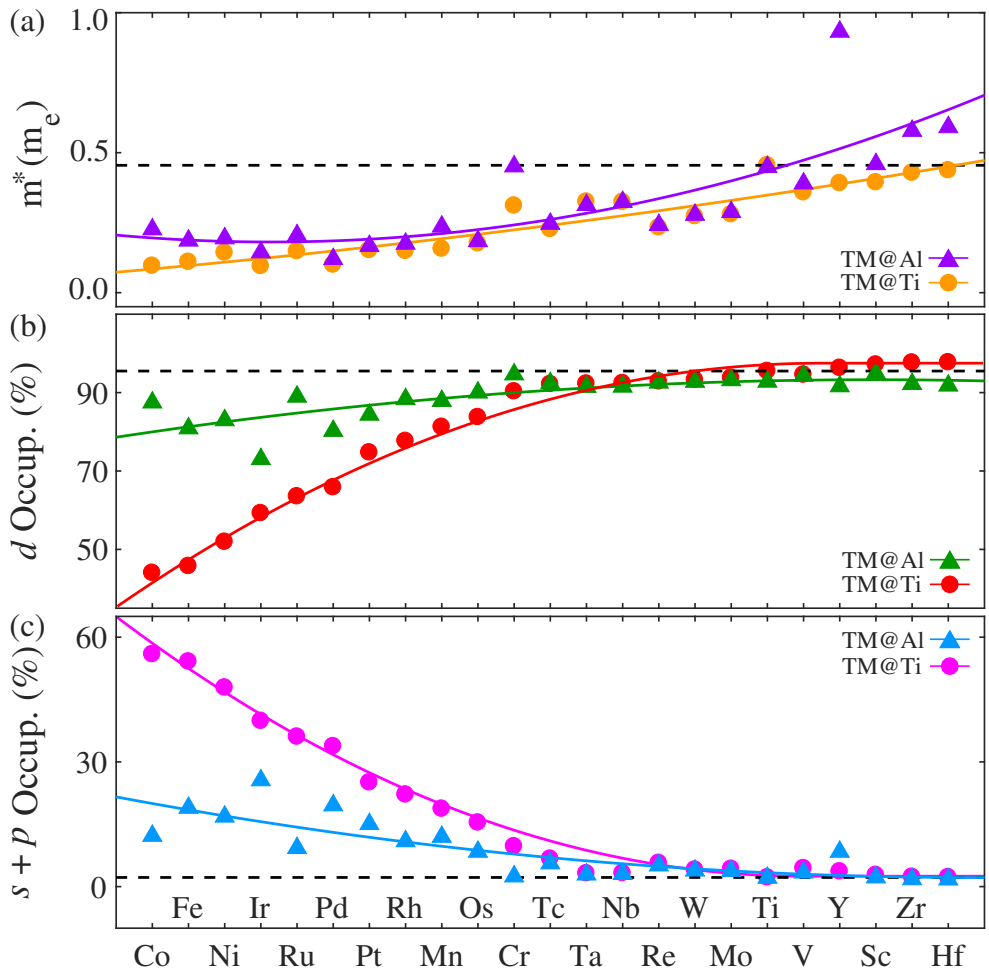

Figure 2.3: The dependence of effective mass (a), d orbital population (b) and $s+p$ orbital population (c) on different dopants for TM@Al and TM@Ti HS. The effective mass and orbital population were all calculated from the CBM. The dash line represents the calculated value for undoped $LaAlO_3/SrTiO_3$ HS and the solid lines are the guides to the eyes.

where $E_{HS}^{TM@X}$ and $E_{HS}^{undoped}$ represent the total energies for the doped and undoped $LaAlO_3/SrTiO_3$ HS systems, respectively. μ_X (X = Al or Ti) is the chemical potential of the host atom and μ_{TM} is the chemical potential of the TM dopant. A is the interfacial area and the factor of 2 accounts for two symmetric interfaces in the model. Note that $\Delta\gamma$ in eq. 2.3 can also be considered as the formation energy per unit interfacial area. A negative $\Delta\gamma$ implies that the doped $LaAlO_3/SrTiO_3$ HS is energetically more favorable than the undoped system and the doped system can be formed spontaneously at zero K.

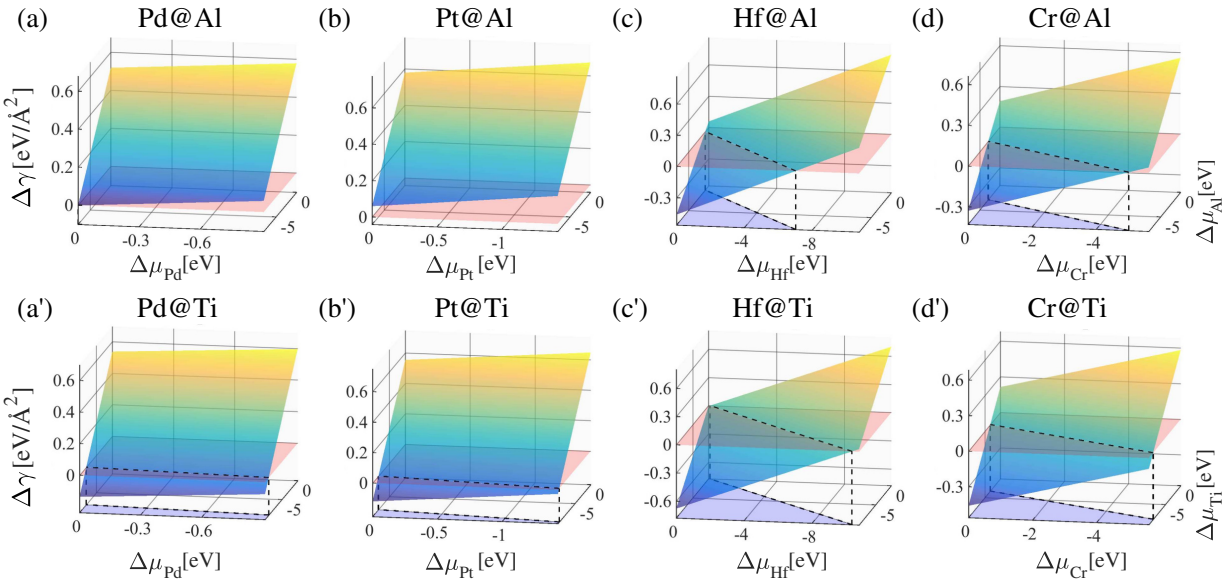

Figure 2.4: Calculated interfacial formation energy change ($\Delta\gamma$) for (a-d) TM@Al and (a'-d') TM@Ti $LaAlO_3/SrTiO_3$ HS with TM = Pd, Pt, Hf and Cr. The translucent pink plane represents $\Delta\gamma = 0$ and the blue shadow area at the bottom indicates the favorable chemical potential range in which $\Delta\gamma < 0.0$ eV and the doped $LaAlO_3/SrTiO_3$ HS can be spontaneously formed.

Let us first consider the case of TM@Al doped HS systems. Note that $\Delta\gamma$ is not fixed but dependent on the value of μ_{Al} and μ_{TM}. By introducing the variation of the chemical potentials with respect to reference bulk phases ($\mu_{Al} = \Delta\mu_{Al} + E_{Al}$ and $\mu_{TM} = \Delta\mu_{TM} + E_{TM}$), eq. 2.3 can be further written as:

$$\Delta\gamma = [E_{HS}^{TM@Al} - E_{HS}^{undoped} + 2(E_{Al} - E_{TM}) + 2(\Delta\mu_{Al} - \Delta\mu_{TM})]/2A \tag{2.4}$$

$\Delta\mu_i$ is strongly dependent on the experimental conditions, which can be divided into La_2O_3-rich and Al_2O_3-rich growth conditions, respectively. [181] In the case of TM@Al doping, La_2O_3-rich condition is expected to be energetically more favorable to form the doped structure than the Al_2O_3-rich condition as Al atom can be replaced by the TM dopant much more easily under such a condition. [181] The La_2O_3-rich condition can be further split into two sub-conditions, *i.e.*, La-rich ($\Delta\mu_{La} = 0$) and O-rich ($\Delta\mu_O = 0$) conditions. [48, 181] By using these boundary conditions, we were able to determine that: -8.69 eV $\leq \Delta\mu_{La} \leq -0.77$ eV, -7.92 eV $\leq \Delta\mu_{Al} \leq 0.0$ eV and

-5.28 eV $\leq \Delta\mu_O \leq 0$ eV.

To evaluate the energetic stability of TM@Al doped HS, we next calculated their $\Delta\gamma$ using eq. 2.4. The calculated $\Delta\gamma$ as a function of the chemical potential difference $\Delta\mu_{Al}$-$\Delta\mu_{TM}$ (and $\Delta\mu_{Ti}$-$\Delta\mu_{TM}$) for all the doping scenarios can be found in the Fig. 2.5. Herein, we took Pd@Al, Pt@Al, Hf@Al, and Cr@Al doped HS models as the exemplary systems and plotted their $\Delta\gamma$ diagrams as a function of chemical potentials of host atoms and dopants in Fig. 2.4(a-d). It shows that, for Pd@Al and Pt@Al doped HS, $\Delta\gamma$ is always positive for the entire range of $\Delta\mu_{Al}$, $\Delta\mu_{Pd}$ and $\Delta\mu_{Pt}$. In contrast, for Hf@Al and Cr@Al doped HS, there exists a wide range of chemical potentials to lead to a negative $\Delta\gamma$, i.e., with -7.92 eV $\leq \Delta\mu_{Al} \leq -0.90$ eV and -7.03 eV $\leq \Delta\mu_{Hf} \leq 0.0$ eV for Hf@Al doped HS and -7.92 eV $\leq \Delta\mu_{Al} \leq -2.91$ eV and -5.01 eV $\leq \Delta\mu_{Cr} \leq 0.0$ eV for Cr@Al doped HS, respectively. In other words, the formation of Hf- and Cr-doped HS is spontaneous by releasing enthalpy in the above chemical potential range. By following the similar procedure, we also plotted the $\Delta\gamma$ phase diagrams for Pd@Ti, Pt@Ti, Hf@Ti and Cr@Ti doped HS systems in Fig. 2.4(a'-d'). It shows that both Hf@Ti and Cr@Ti doped systems exhibit a wider range of $\Delta\mu_{TM}$ and $\Delta\mu_{Ti}$ than that in Pd@Ti and Pt@Ti doped systems to have a negative $\Delta\gamma$. Moreover, as compared to Pd (Pt)@Al doped systems, $\Delta\gamma$ of Pd (Pt)@Ti doped systems can be negative at an appropriate Ti and Pd (Pt) chemical potential range, see Fig. 2.4(a'-b') This implies that it is energetically more favorable to form TM@Ti structures than TM@Al structures in the $LaAlO_3/SrTiO_3$ HS systems.

Next, to evaluate the energetic stability for all the doped systems, we calculated the minimum interfacial energy change ($\Delta\gamma_{min}$) for each system. This is because a more negative $\Delta\gamma_{min}$ is correlated with a wider range of $\Delta\mu_{Al}$-$\Delta\mu_{TM}$ ($\Delta\mu_{Ti}$-$\Delta\mu_{TM}$) (see Fig. 2.5), so that the doped system can be epitaxially grown under a more flexible condition and more favorably to be formed. For TM@Al doped model, $\Delta\gamma_{min}$ can be obtained at Al-poor ($\Delta\mu_{Al}$ = -7.92 eV) and TM-rich condition ($\Delta\mu_{TM}$ = 0 eV). Hence, under this extreme condition, eq. 2.4 can be further

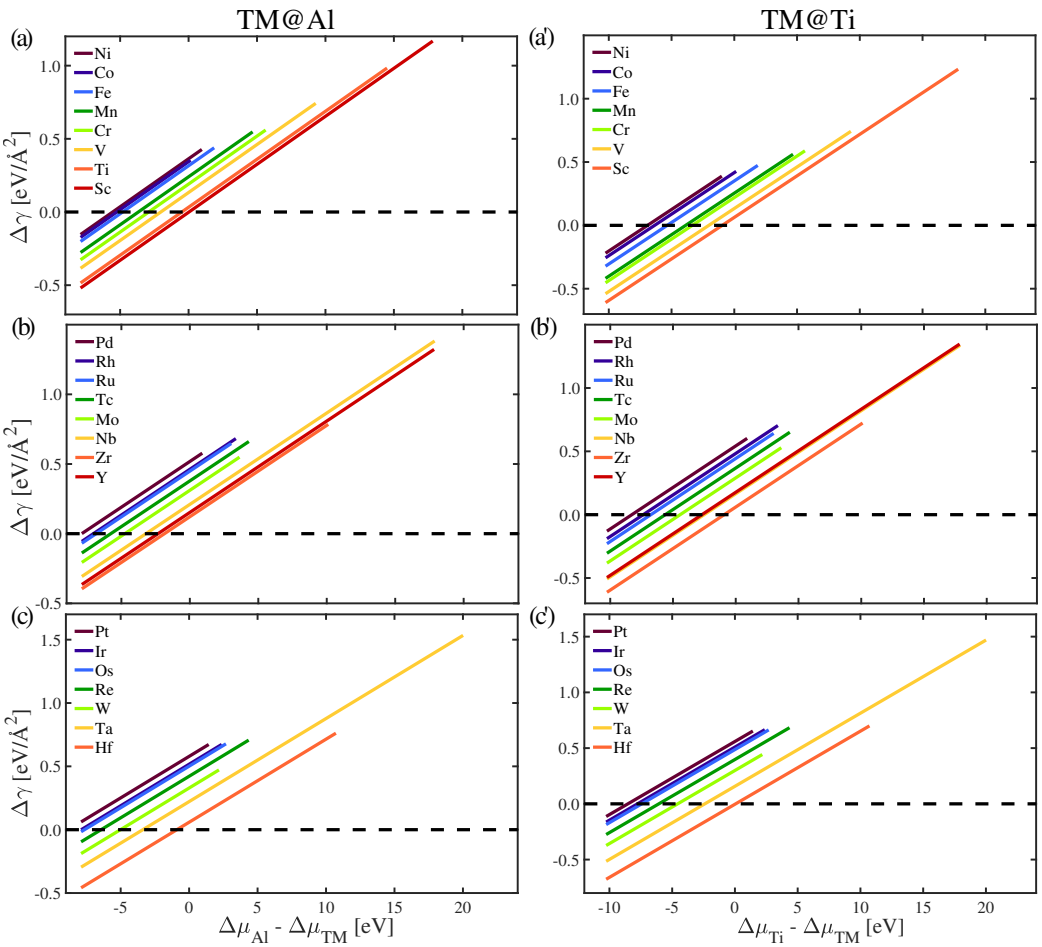

Figure 2.5: Calculated interfacial formation energy change ($\Delta\gamma_{min}$) as a function of $\Delta\mu_{Al}$-$\Delta\mu_{TM}$ for TM@Al HS (a-c) and as a function of $\Delta\mu_{Ti}$-$\Delta\mu_{TM}$ for TM@Ti HS systems (a'-c').

reduced to:

$$\Delta\gamma_{min} = [E_{HS}^{TM@Al} - E_{HS}^{undoped} + 2(E_{Al} - E_{TM} - 7.92)]/2A \tag{2.5}$$

By using eq. 7.5, we calculated the $\Delta\gamma_{min}$ for each TM@Al doped system, see Table 5.1. For a visualized trend of $\Delta\gamma_{min}$, we also organized the $\Delta\gamma_{min}$ by rows and columns of the periodic table in Fig. 2.6(a). The magnitude of $\Delta\gamma_{min}$ for each doped system is indicated by the shades of orange, with orange as the high $\Delta\gamma_{min}$ and yellow as the low $\Delta\gamma_{min}$. The case of TM@Ti doped system was also shown in Fig. 2.6(b) and Table 5.1, which was determined at Ti-poor ($\Delta\mu_{Ti}$ =

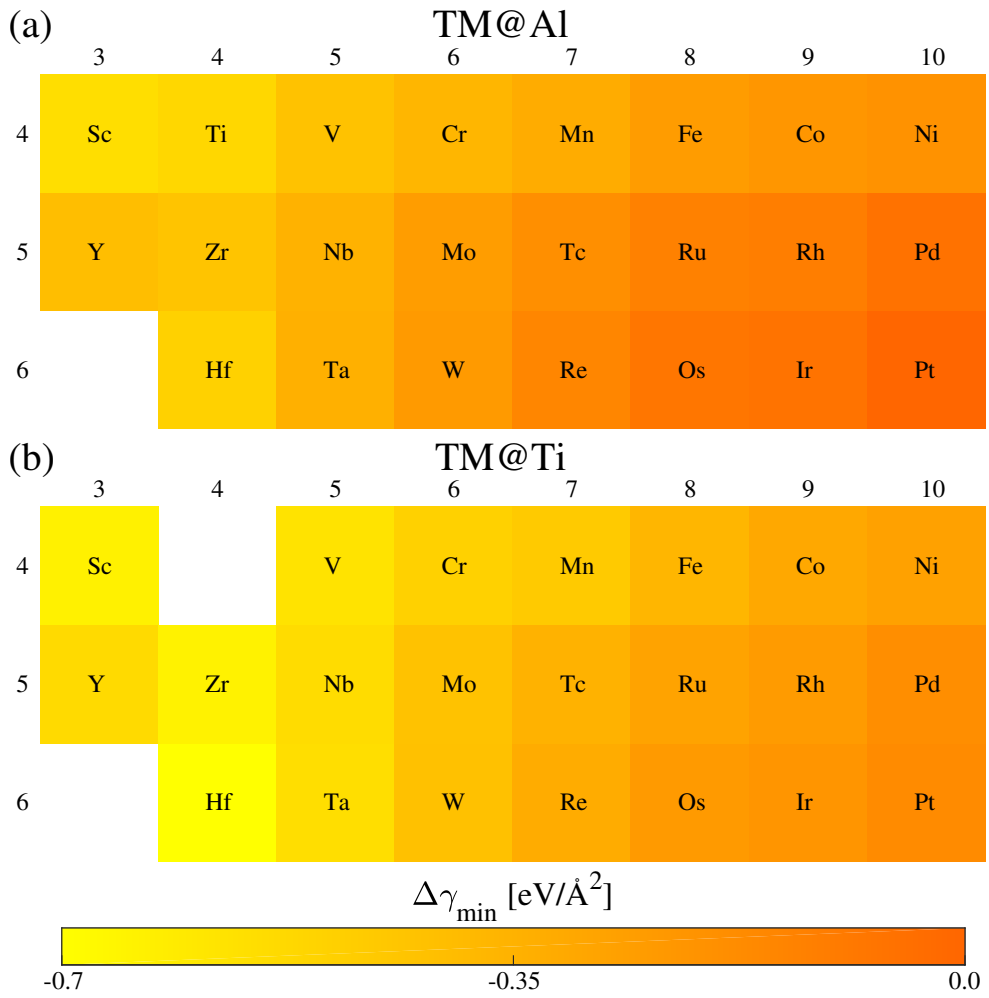

Figure 2.6: Minimum interfacial formation energy change ($\Delta\gamma_{min}$) for (a) TM@Al and (b) TM@Ti HS plotted in rows and columns of the periodic table, with orange as the high $\Delta\gamma_{min}$ and yellow as the low $\Delta\gamma_{min}$.

-10.27 eV) and TM-rich condition.

A comprehensive analysis of these results indicates three important features as below. First, the $\Delta\gamma_{min}$ of TM@Ti doped system is smaller than that of TM@Al doped one, implying that TM@Ti doping is energetic more favorable than TM@Al doping. This conclusion applies for all the TM dopants. This behavior can be rationalized by the fact that the atomic radius of TM dopant (1.49 to 2.12 Å) is much closer to that of Ti atom (1.76 Å), while much larger than that of Al atom (1.18 Å). [53] Thus, Ti site serves a more natural host space to accommodate the TM dopants than Al site. Second, in both TM@Al and TM@Ti doped systems, $\Delta\gamma_{min}$ increases

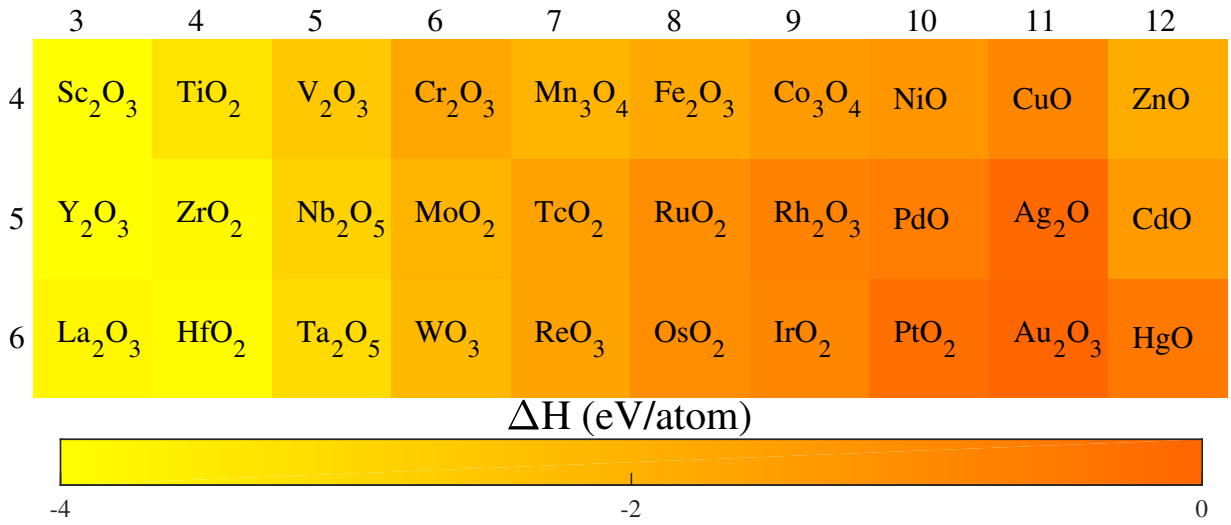

Figure 2.7: Experimental formation enthalpy (ΔH) of transition metal oxides plotted in rows and columns of the periodic table, with orange as the high ΔH and yellow as the low ΔH. The values are obtained from ref [15], ref [178] and the monograph by Kubaschewski [135].

Table 2.2: Calculated Bader charge for TM (TM = Mn and Cr) ions in the bulk $LaTMO_3$ and $SrTMO_3$ and TM δ-doped $LaAlO_3/SrTiO_3$ heterostructure system.

	$LaTMO_3$	TM@Al	$SrTMO_3$	TM@Ti
Mn	+1.78	+1.52	+1.93	+1.62
Cr	+1.85	+1.59	+2.02	+1.70

as the dopants pass from group 3 to group 10 in the periodic table. This indicates that doping is energetic more favorable for the dopants in the left side of the periodic table than those in the right side. The underlying physics can be understood from the bonding strength of the TM-O bonds. The electronegativity of TM dopants increases from group 3 to group 10 in the periodic table, and thus the ionic bond character of TM-O tends to be suppressed and the bonding strength is weakened. This finding is well consistent with the decreasing trend of the experimental enthalpies of formation for transition metal oxides from group 3 to group 10, see Fig. 2.7. This trend also agrees well with a prior computational study [101] and experimental finding, [109] respectively. For instance, the computational study shows that TM-O bond strength basically follows a decreasing order from group 3 to group 10, [101] and the experimental finding reveals that Fe-O bonding energy is much higher than that of Pd-O and Pt-O bonds. [109] Third, the

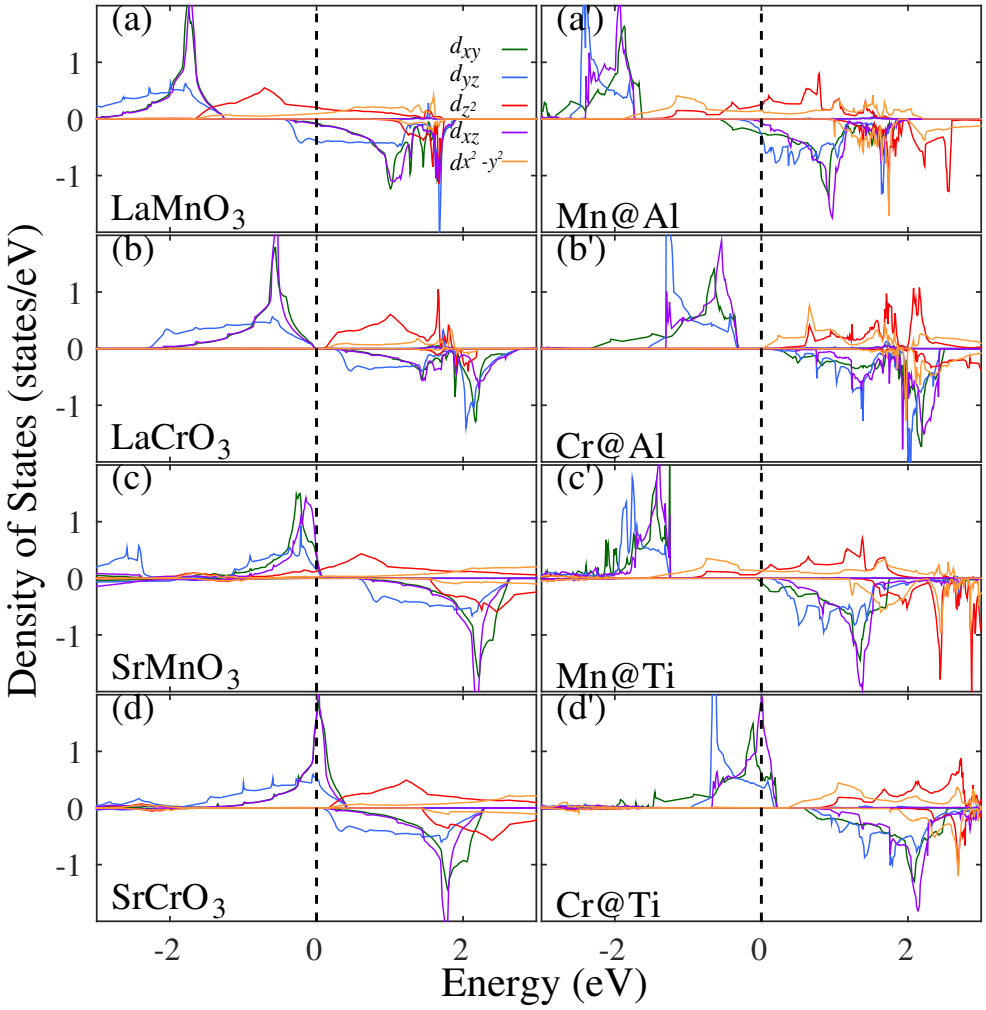

Figure 2.8: Calculated partial density of states of Mn and Cr in the bulk (a-d) $LaMnO_3$, $LaCrO_3$, $SrMnO_3$, and $SrCrO_3$ and (a'-d') δ-doped $LaAlO_3/SrTiO_3$ systems.

interfacial formation energy change ($\Delta\gamma_{min}$) is tightly correlated to the electron effective mass (m^*), that is, larger $\Delta\gamma_{min}$, smaller m^*. This is because a smaller m^* is induced by a higher degree of $s+p$ (lower degree of d) orbital population in the conduction bands, which weakens ionic bond strength of TM-O bond and thus leads to a larger $\Delta\gamma_{min}$. In other words, the TM-O bond in the systems with high m^* is more likely to be ionic, and the orbital hybridization between the TM d orbitals and O $2p$ orbitals is relatively weaker than that in the systems with smaller m^*. Interestingly, this conclusion also agrees well with a prior experimental observation in the simultaneously doped $SrTiO_3$ with both donor and acceptor species. [101] In this experimental

study, a correlation between the electrical conductivity and TM-O bonding strength was revealed. The TM dopants with weaker TM-O bonds tend to lead to higher conductivity while those with stronger TM-O bonds tend to have lower conductivity. All these results suggest that there exists an optimal balance between $\Delta\gamma_{min}$ (or TM-O bond strength) and m^*. In other words, there is a trade-off between achieving small electron effective mass and obtaining an energetically favorable TM-doped $LaAlO_3/SrTiO_3$ system. Among all the 23 considered TM dopants, we found that Mn, Fe, Co, Ni, Ru, Rh, Pd, Os and Ir can be the promising candidate dopants to form a δ-doped $LaAlO_3/SrTiO_3$ HS with small electron effective mass and thermodynamically stable structure. Actually, a recent experimental work revealed that Mn δ-doping in the $LaAlO_3/SrTiO_3$ HS system can induce an ultra-high low-temperature 2DEG mobility up to 73,000 $cm^2V^{-1}s^{-1}$, [44] which is occasionally consistent with our computational findings from the viewpoint of electron effective mass. It is noted that in this experiment the interfacial charge carrier density decreased upon Mn δ-doping, [44] and similar phenomenon also occurred in the Cr δ-doped $LaAlO_3/SrTiO_3$. [136] This is because Mn and Cr ions trap some electrons from the interfacial $(LaO)^+$ layer, which reduces the charge transfer to the $SrTiO_3$ substrate and thus the charge carrier density on the interfacial TiO_2 layer decreases. This conclusion can be drawn from a comparative analysis of the Bader charge on the Mn (Cr) ions in their bulk perovskites $LaMnO_3$ ($LaCrO_3$, $SrMnO_3$, and $SrCrO_3$) and doped $LaAlO_3/SrTiO_3$ system as well as their partial density of states, see Table 6.2 and Fig. 2.8. In addition, it is worth mentioning that the δ-doping model in our work is the substitution of one Al (Ti) atom with one dopant, and the doping concentration can be considered as 100 mol% in one layer. This model corresponds to an insertion of one $La(TM)O_3$ ($Sr(TM)O_3$) buffer layer at the $LaAlO_3/SrTiO_3$ interface or a model of a superlattice. Such an approach of inserting one buffer layer has been widely used in the $SrTiO_3$-based HS to tune interfacial charge carrier density, [94] to use local electron correlations to realize new functionalities in designed HS, [112] to improve the electron mobility by reducing impurity scattering, [103] or to modulate the spin-orbit interactions for desired materials properties. [56, 57] Despite of the

wide usage of 100 mol% δ-doping in achieving novel materials functionality of HS systems, it should be noted that tuning the doping concentration can also serve as an efficient approach to change the materials properties of HS and bulk materials. For example, Ariandos team studied the electrical and magnetic properties of Nb-doped $SrTiO_3$ and observed a reversible room-temperature ferromagnetism in the doped $SrTiO_3$ single crystal at a high doping concentration ($\geq$ 0.5 wt%). [160] At the 0.5 wt% doping concentration, they also prepared the $LaAlO_3$/Nb-$SrTiO_3$ HS and found an electric-filed-induced reversible metal-insulator transition of the insulating $LaAlO_3$ films. [159]

2.4 Conclusion

In summary, we explored δ-doping effects on the electronic and energetic properties of $LaAlO_3$/$SrTiO_3$ heterostructure with 23 transition-metal dopants from group 3 to group 10. The band structure, s(p or d) orbital populations, electron effective mass, and the interfacial energy change were discussed for each doping scenario. The following conclusions are addressed:

(i) A higher $s+p$ orbital population (lower d orbital population) of the impurity bands leads to a smaller effective mass. The dopants in the groups 9 and 10 (Co, Ni, Rh, Pd, Ir, and Pt) introduce the bands with relatively smaller electron effective mass while those in the groups 3 and 4 (Sc, Y, Ti, Zr, and Hf) introduce the bands with relatively larger electron effective mass.

(ii) The dopants in the groups 3 and 4 (Sc, Y, Ti, Zr, and Hf) lead to energetically more favorable structures compared with the dopants in other groups. The interfacial formation energy change for the δ-doped structure increases from the group 3 to group 10.

(iii) In addition to the experimentally confirmed Mn dopant, Fe, Co, Ni, Ru, Rh, Pd, Os and Ir elements are predicted to be promising candidate dopants to lead to light effective mass bands and relatively large energetic stability. This finding offers a wide avenue for the selection of candidate dopants to increase 2DEG mobility in the $LaAlO_3$/$SrTiO_3$ heterostructure via δ-doping.

2.5 Acknowledgements

Chapter 2, in full, is a reprint of the material "δ-Doping Effects on Electronic and Energetic Properties of $LaAlO_3/SrTiO_3$ Heterostructure: First-Principles Analysis of 23 Transition-Metal Dopants" as it appears in Advanced Materials Interfaces. Jianli Cheng, Yaqin Wang, Jian Luo, Kesong Yang, 4, 1700579, 2017. The dissertation author was the primary investigator and author of this paper.

Chapter 3

Electronic and Energetic Properties of $LaAlO_3/TiO_2$ and $TiO_2/LaAlO_3$ Heterostructures

In Chapter 1 and 2, we have discussed the 2DEG formed at the interface of two insulating perovskite oxides. In fact, besides the perovskite oxide HS, binary oxides involved HS have also been discovered to exhibit the interfacial 2DEGs. [172, 226] A good example is $TiO_2/LaAlO_3$ HS, the sheet carrier density and the room-temperature mobility of which are both larger than that of $LaAlO_3/SrTiO_3$ HS. [172] The enhanced electronic properties in the $TiO_2/LaAlO_3$ HS can be attributed to two possible reasons: i) TiO_2 has a fundamentally different property than that of the $SrTiO_3$; ii) growth order in the two HS models are different. In $TiO_2/LaAlO_3$ HS, TiO_2 film is grown on the $LaAlO_3$ substrate, while in $LaAlO_3/SrTiO_3$ HS, the $LaAlO_3$ film is grown on the $SrTiO_3$ substrate. The second possibility implies that the growth order between TiO_2 and $LaAlO_3$ may significantly influence the interfacial electronic properties. Accordingly, in this Chapter we show the electronic and energetic properties of the oxide HS with different epitaxial growth order between anatase TiO_2 and $LaAlO_3$. Two types of HS, *i.e.*, TiO_2 film grown on

$LaAlO_3$ substrate ($TiO_2/LaAlO_3$) and $LaAlO_3$ film grown on TiO_2 substrate ($LaAlO_3/TiO_2$), were modeled. The $TiO_2/LaAlO_3$ is intrinsically metallic and thus does not exhibit an insulator-to-metal transition as TiO_2 film thickness increases; in contrast, $LaAlO_3/TiO_2$ shows an insulator-to-metal transition as the $LaAlO_3$ film thickness increases up to 4 unit cells. The former model has a larger interfacial charge carrier density ($n \sim 10^{14}\text{cm}^{-2}$) and smaller electron effective mass ($0.47m_e$) than the later one ($n \sim 10^{13}\text{cm}^{-2}$, and $0.70m_e$). The interfacial energetics calculations indicate that $TiO_2/LaAlO_3$ is energetically more favorable than $LaAlO_3/TiO_2$, and the former HS has a stronger interface cohesion than the later one. This research provides fundamental insights into the different interfacial electronic and energetic properties of $TiO_2/LaAlO_3$ and $LaAlO_3/TiO_2$ HS.

3.1 Introduction

The revolution of sophisticated thin-film growth techniques such as molecular beam epitaxy and pulsed laser deposition has boosted creation, characterization, and engineering of the intriguing properties of artificial layered oxide heterostructures (HS) in the past decades. [38, 141, 219] One example is $LaAlO_3/SrTiO_3$ HS with n-type $(LaO)^+/(TiO_2)^0$ heterointerface, which exhibits many interesting interfacial properties such as two-dimensional electron gas (2DEG), superconductivity, and magnetism, with potential applications in the next-generation nanoelectronic devices. [149, 179, 190, 213] The discovery of 2DEG between the two wide band-gap insulators, $SrTiO_3$ and $LaAlO_3$, has triggered an avalanche of research to explore interface properties of other $SrTiO_3$- or $LaAlO_3$-based HS over the past decade. [40, 49, 172, 187, 255, 269, 277] Moreover, in addition to these perovskite-oxide-based HS, recent experimental studies show that the surfaces of $SrTiO_3$ and TiO_2 can also exhibit 2DEG because of oxygen vacancies in the near-surface region. [171, 214, 215]

In recent years, the HS consisting of anatase titanium dioxide (TiO_2) and $LaAlO_3$ has

become one of the attractive studying objects. [62, 172, 221, 254, 277] TiO_2 is a promising functional oxide with a wide range of applications in the fields such as photovoltaics, [128] photocatalysis, [73] and spintronics. [169] Anatase TiO_2 crystallizes in tetragonal phase (space group $I4_1$/amd, no. 141), with a = 3.785, and c = 9.514Å. [96] $LaAlO_3$ has a pseudo-cubic structure with a lattice constant of a = 3.789Å, [190] and thus a negligible lattice mismatch (about 0.1%) with TiO_2 in the *ab*-plane. As a result, a coherent interface between TiO_2 and $LaAlO_3$ is expected to be prepared through the epitaxial growth, improving the crystallinity of the TiO_2 ($LaAlO_3$) film. Several prior computational studies have explored electronic and magnetic properties in the TiO_2/$LaAlO_3$ (TiO_2 grown on $LaAlO_3$ substrate) HS system, including the energetics of cation intermixing and oxygen vacancies. [62, 254, 258, 259] However, it is worth mentioning that both $LaAlO_3$ and TiO_2 can be used as the substrate materials for epitaxial film growth, [130, 172, 223, 244] and consequently, $LaAlO_3$ can serve as the substrate for TiO_2 film, and vice versa. For instance, Ikuhara's group has prepared coherent TiO_2/$LaAlO_3$ heterointerfaces by depositing anatase TiO_2 film on single-crystal $LaAlO_3$. [254, 277] Hwang's team successfully grew $LaAlO_3$ film on anatase TiO_2 at 600 °C and P_{O_2} = 1×10^{-5} Torr. [244]

Very recently, Hwang's team epitaxially grew anatase TiO_2 film on $(LaO)^+$- and $(AlO_2)^-$-terminated $LaAlO_3$ (001) substrate (abbreviated as TiO_2/$LaAlO_3$), respectively, using pulsed laser deposition. [172] They found that TiO_2/$(LaO)^+$ interface is metallic while TiO_2/$(AlO_2)^-$ interface is insulating. This phenomenon is similar to the case of prototype $LaAlO_3$/$SrTiO_3$ system, though in the latter case $LaAlO_3$ is grown on $SrTiO_3$ substrate. [190] In addition, they found that the sheet carrier density ($n \sim 2\times 10^{14}$ cm^{-2}) and the room-temperature mobility ($\mu \sim 25$ cm^{2}V^{-1}s^{-1}) in the $(LaO)^+$-terminated TiO_2/$LaAlO_3$ HS are both larger than that in the prototype $LaAlO_3$/$SrTiO_3$ system ($n \sim 1-2\times 10^{13}$ cm^{-2} and $\mu \sim$ 5-10 cm^{2}V^{-1}s^{-1}). [4, 102, 116, 158, 231, 247] Compared to the prototype $LaAlO_3$/$SrTiO_3$, the higher charge carrier density and room-temperature mobility in the TiO_2/$LaAlO_3$ HS can be attributed to two possible reasons: i) TiO_2 has a fundamentally different property than that of the $SrTiO_3$ because of the distortion of Ti-O bond in the *ab*-plane;

ii) growth order in the two HS models are different. In the TiO_2/$LaAlO_3$ model, TiO_2 film is grown on the $LaAlO_3$ substrate (by forming nonpolar/polar $(TiO_2)^0$/$(LaO)^+$ heterointerface), while in the $LaAlO_3$/$SrTiO_3$ model, the $LaAlO_3$ film is grown on the $SrTiO_3$ substrate (by forming polar/nonpolar $(LaO)^+$/$(TiO_2)^0$ heterointerface). The second possibility implies that the growth order between TiO_2 and $LaAlO_3$ may significantly influence the interfacial electronic properties. Moreover, recent experimental studies show that anatase TiO_2 phase is unstable and even exhibits anatase-to-rutile phase transition when $LaAlO_3$ is grown on the TiO_2 substrate. [244, 245] In contrast, anatase TiO_2 phase can be well reserved when it is grown on the $LaAlO_3$ substrate. [52,75,172,221] These experimental facts indicate that, besides the electronic property, the growth order of the HS model may also impact its interfacial thermodynamic property and thus the growth of the film. So far, there have been few investigations into the effects of the growth order between TiO_2 and $LaAlO_3$ on their interfacial properties. Therefore, despite these interesting experimental findings, it is essential to explore the influence of the epitaxial growth order between the anatase TiO_2 and $LaAlO_3$ on their interfacial electronic and energetic properties.

In this work, we studied the electronic and energetic properties of TiO_2/$LaAlO_3$ and $LaAlO_3$/TiO_2 interface models using first-principles electronic structure calculations. A systematic comparison of the electronic structures, averaged electrostatic potential, interfacial charge carrier density, electron effective mass, and the interfacial energetics were carried out for the two models. The atomistic origin for their different interfacial materials properties were revealed and discussed. This work provides a fundamental understanding into the effects of the epitaxial growth order on the interfacial materials properties in the $LaAlO_3$-based heterostructures.

3.2 Structural modeling and computational details

In this study, we modeled two types of heterointerfaces for a comprehensive and comparison investigation: i) TiO_2 film grown on $LaAlO_3$ substrate (for convenience, this model

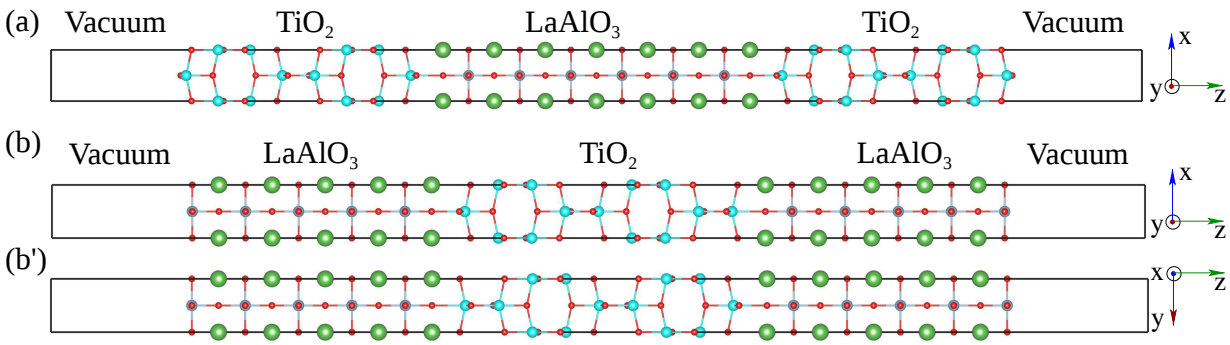

Figure 3.1: Structure models for sandwich-type (a) $TiO_2/LaAlO_3$ (TiO_2 grown on $LaAlO_3$ substrate) and (b and b′) $LaAlO_3/TiO_2$ ($LaAlO_3$ grown on TiO_2) HS models.

was abbreviated as $TiO_2/LaAlO_3$); and ii) $LaAlO_3$ film grown on TiO_2 substrate (abbreviated as $LaAlO_3/TiO_2$). Besides this, in terms of the atomic arrangement at the interface, there are two types of interface structures for each model, *i.e.*, $(TiO_2)^0/(LaO)^+$ and $(TiO_2)^0/(AlO_2)^-$. This is similar to the case of the well-known $LaAlO_3/SrTiO_3$ HS, in which $(TiO_2)^0/(LaO)^+$ interface exhibits *n*-type conductivity. The $(TiO_2)^0/(AlO_2)^-$ interface is considered to exhibit *p*-type conductivity according to the polar catastrophe mechanism, [190] though not observed in the experiment yet probably due to donor defects like oxygen vacancies. [179, 190, 279] Since the *p*-type $(TiO_2)^0/(AlO_2)^-$ interface is not the central scope of this research, we only focus on the $(TiO_2)^0/(LaO)^+$ interface model that is predicted to be energetically more stable that the other type of interface, namely, $(TiO_2)^0/(AlO_2)^-$, from *ab-initio* study by Ferrari *et al*. [62] To get rid of the surface effects of the substrate in the simulations, we employed a sandwich-type structure to model the $TiO_2/LaAlO_3$ and $LaAlO_3/TiO_2$ interfaces. In the $TiO_2/LaAlO_3$ model, a 6.5 unit-cell-thick $LaAlO_3$ was used as the substrate sandwiched by anatase TiO_2 (8 unit layers), see Fig. 3.1a. Note that such a configuration is necessary to make a symmetrical $(TiO_2)^0/(LaO)^+$ interface for a direct comparison with $LaAlO_3/TiO_2$ model, though the $LaAlO_3$ bulk substrate is not stoichiometric. One may speculate that LaO (AlO_2) termination of (001) $LaAlO_3$ could be reconstructed due to its polar nature. In contrast to this assumption, a recent first-principles computational study indicates that the LaO and AlO_2 terminations can have their corresponding

stability domains under appropriate chemical environments. [41] In fact, in the experimental side, the AlO_2 termination of (001) $LaAlO_3$ has been successfully prepared by combinatorial chemical etching and annealing process. [85] In the $LaAlO_3/TiO_2$ model, about 2 unit-cell-thick anatase TiO_2 (9 unit layers) substrate is sandwiched by $LaAlO_3$ (5 unit cells), see Fig. 3.1b. In both models a 10 Å thickness of vacuum is added on top of both sides of surfaces to avoid the interaction between the periodic images. Accordingly, a total 20 Å vacuum thickness was applied for each HS model. For the sandwich-type $LaAlO_3/TiO_2$ model, it is worth mentioning that the two interfaces of this model are not exactly identical due to the intrinsic asymmetry of bulk TiO_2. However, one side interface can be completely reproduced from the other side by rotating the HS model through 90° around the c-axis (see Fig. 3.1b and Fig. 3.1b'), and thus the identical electronic properties at both sides of the interfaces can be obtained. In addition, a systematic examination of the convergence of the surface energy of $LaAlO_3$ has indicated that a 6.5 unit-cell $LaAlO_3$ and a 2 unit-cell-thick anatase TiO_2 are thick enough to be used as the substrate.

Density functional theory (DFT) electronic structure calculations were carried out using Vienna *Ab-initio* Simulation Package (VASP). [132, 133] The Projector Augmented Wave (PAW) potentials were used for ion-electron interactions [134] and the Generalized Gradient Approximation (GGA) parameterized by the Perdew-Burke-Ernzerhof (PBE) [200] plus the on-site Coulomb interaction approach (GGA + U) was used for the exchange-correlation functional with U = 5.8 and 7.5 eV for Ti 3d and La 4f orbitals, respectively. [125, 182, 184, 186] The cutoff energy for the plane wave expansion was set to 450 eV. Γ-centered k-point grids for Brillouin zone sampling were set to $4 \times 4 \times 1$ for ionic relaxation and $10 \times 10 \times 1$ for static calculations, respectively. The break condition for the electronic self-consistency loop was assumed for a total energy convergence of less than 10^{-6} eV. To resemble the experimental epitaxial material growth, the cell parameters along *ab*-plane were fixed and all the ions were allowed to relax until the atomic forces were smaller than 0.03 eV/Å.

3.3 Results and discussion

3.3.1 Interfacial energetics

To study interfacial energetics of TiO_2/$LaAlO_3$ and $LaAlO_3$/TiO_2 HS models and compare their interfacial cohesion strength, we calculated their total formation energy per unit area (γ) and cleavage energy (E_{cleav}), respectively. The γ of the two HS models, which is referred to the equilibrium chemical potentials of the system, was calculated by the following equation:

$$\gamma = \frac{1}{2A}[E_{HS} - \sum \mu_i n_i] \tag{3.1}$$

where E_{HS} is the total energy of the HS model containing two symmetrical interfaces, n_i the number of atoms of species i, μ_i the chemical potential of species i, A the interface area, and the factor of 2 in the denominator indicates that two identical interfaces are present in the HS model. It is worth noting that, γ is the sum of the interfacial energy between TiO_2 and $LaAlO_3$, surface energy of the film (TiO_2 film in the TiO_2/$LaAlO_3$ and $LaAlO_3$ film in the $LaAlO_3$/TiO_2, and the interaction energy between the two interfaces (a nonzero value because the thickness of substrate in the HS is not large enough). In practical calculations, part of $\sum \mu_i n_i$ can be obtained from the total energy of corresponding TiO_2 and $LaAlO_3$ bulk materials. For example, for anatase TiO_2 in the HS model, its each layer consists of stoichiometric TiO_2 unit layer (one Ti atom and two O atoms), and thus the sum of $\mu_{Ti} n_{Ti}$ and $\mu_O n_O$ can be calculated from the bulk TiO_2. In contrast, $LaAlO_3$ consists of alternative $(LaO)^{+1}$ and $(AlO_2)^{-1}$ unit layers. For $LaAlO_3$/TiO_2 HS model, the $LaAlO_3$ surface is terminated with AlO_2 layer, making the HS model stoichiometric, and thus $\sum \mu_i n_i$ can be exclusively obtained from bulk TiO_2 and bulk $LaAlO_3$. For TiO_2/$LaAlO_3$ HS model, the $(LaO)^{+1}$/$(TiO_2)^0$ interface determines that there will be one extra La atom and one

extra O atom besides the stoichiometric $LaAlO_3$, and thus equation (3.1) can be rewritten as:

$$\gamma = \frac{1}{2A}[E_{HS} - E_{bulk}(TiO_2) - E_{bulk}(LaAlO_3) - \mu_{La} - \mu_O] \tag{3.2}$$

The allowed ranges of variation of μ_{La} and μ_O are linked by the thermodynamic stability of $LaAlO_3$:

$$\mu_{La} + \mu_{Al} + 3\mu_O = E_{LaAlO_3} \tag{3.3}$$

where E_{LaAlO_3} refers to the total energy of the bulk $LaAlO_3$ per formula unit. μ_i can be further expanded with respect to the total energy E_i of its elemental phase (*i.e.*, solid phase for La and Al, and O_2 molecular for O):

$$\mu_i = \Delta\mu_i + E_i \tag{3.4}$$

Accordingly, the formation enthalpy of $LaAlO_3$ ($\Delta H_f(LaAlO_3)$) can be defined as:

$$\Delta H_f(LaAlO_3) = \Delta\mu_{La} + \Delta\mu_{Al} + 3\Delta\mu_O \tag{3.5}$$

Thus $\Delta\mu_i$ are dependent on each other and by fixing values of two of the constituents one can determine the third one. To exclude the possible formation of secondary phases La_2O_3 and Al_2O_3, the following constraints must also be satisfied:

$$2\Delta\mu_{La} + 3\Delta\mu_O \leq \Delta H_f(La_2O_3) \tag{3.6}$$

$$2\Delta\mu_{Al} + 3\Delta\mu_O \leq \Delta H_f(Al_2O_3) \tag{3.7}$$

As $\Delta\mu_i$ is strongly dependent on the experimental conditions, we considered both Al_2O_3-rich, and La_2O_3-rich growth conditions. [181] The La_2O_3-rich condition can be further split into sub-conditions, *i.e.*, La-rich ($\Delta\mu_{La} = 0$) and O-rich ($\Delta\mu_O = 0$) conditions. Using the restrictions imposed by equation (3.5) and (3.6), we were able to determine that: -8.68 eV $\leq \Delta\mu_{La} \leq -0.80$

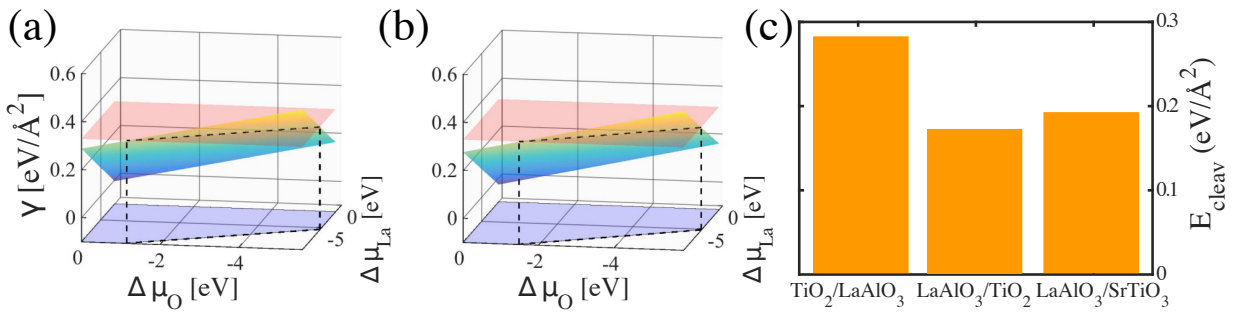

Figure 3.2: Total formation energy per unit area (γ) diagram for TiO_2/$LaAlO_3$ (color gradient plane) and $LaAlO_3$/TiO_2 (translucent pink plane) HS under Al_2O_3-rich (a) and La_2O_3-rich (b) conditions.

eV and -5.26 eV $\leq \Delta\mu_O \leq 0$ eV. Similarly, under the Al_2O_3-rich condition, by using equation (3.5) and (3.7), -9.01 eV $\leq \Delta\mu_{La} \leq -1.46$ eV and -5.04 eV $\leq \Delta\mu_O \leq 0$ eV. By employing $\Delta\mu_{La}$ and $\Delta\mu_O$, we plotted their γ diagrams under Al_2O_3-rich condition in Fig. 3.2a and under La_2O_3-rich condition in Fig. 3.2b.

It shows that γ of $LaAlO_3$/TiO_2 HS is a constant, see translucent pink plane. This is because the molar ratio of La, Al and O ions in the $LaAlO_3$/TiO_2 model is stoichiometric, and thus γ is independent of $\Delta\mu_{La}$ and $\Delta\mu_O$. For TiO_2/$LaAlO_3$ model, however, the γ value is dependent on $\Delta\mu_{La}$ and $\Delta\mu_O$, which is further determined by experimental conditions, *i.e.*, Al_2O_3-rich or La_2O_3-rich growth conditions, see color gradient plane in Fig. 3.2a and 3.2b.

Under Al_2O_3-rich condition (Fig. 3.2a), the lowest γ for the TiO_2/$LaAlO_3$ HS occurs at $\Delta\mu_{La}$ = -1.46 eV and $\Delta\mu_O$ = 0 eV, with γ = -0.056 eV/Å^2. Under La_2O_3-rich condition (Fig. 3.2b), it occurs at $\Delta\mu_{La}$ = -0.8 eV and $\Delta\mu_O$ = 0 eV, with γ = -0.029 eV/Å^2. It indicates that the formation of these two HS models could be energetically spontaneous under these extreme conditions, *i.e.*, $\Delta\mu_{La}$ = -1.46 (-0.8) eV and $\Delta\mu_O$ = 0, which rarely occurs in relativity though. Nevertheless, in a wide range of $\Delta\mu_{La}$ and $\Delta\mu_O$, the total formation energy of this system is larger than zero, indicating that extra energy is required to form the model.

The γ value of TiO_2/$LaAlO_3$ is less than that of $LaAlO_3$/TiO_2 for the most range of $\Delta\mu_{La}$ and $\Delta\mu_O$, highlighted in the blue shadow area in the bottom plane of Fig. 3.2a and 3.2b. This result

indicates that $LaAlO_3/TiO_2$ interface is energetically less stable than $TiO_2/LaAlO_3$ interface, implying that the $LaAlO_3/TiO_2$ interface will potentially undergo a structural distortion due to the weak interface cohesion. Interestingly, a series of experimental studies indicate that anatase TiO_2 tends to have an anatase-to-rutile phase transition when perovskite oxide $LaAlO_3$ is grown on TiO_2 substrate. [244,245] In contrast, when TiO_2 is grown on $LaAlO_3$ substrate, the anatase phase TiO_2 is well reserved, and there no anatase-to-rutile phase transition. [75] These experimental facts confirm that $TiO_2/LaAlO_3$ interface is energetically more stable than $LaAlO_3/TiO_2$, which is well consistent with our interfacial energetics calculations.

To compare interfacial cohesion strength of these two HS models, we calculated their cleavage energies E_{cleav} using the following formula:

$$E_{cleav} = (E_{slab}^{LaAlO_3} + E_{slab}^{TiO_2} - E_{HS})/2A \tag{3.8}$$

where E_{HS} is the total energy of the HS system, $E_{slab}^{LaAlO_3}$ and $E_{slab}^{TiO_2}$ stand for the total energy of the corresponding $LaAlO_3$ and TiO_2 slab system, respectively, and the factor of 2 in the denominator indicates two interfaces in the HS model. The $LaAlO_3$ and TiO_2 slab systems are modeled using the same supercell with the HS model to minimize the errors. The calculated E_{cleav} is 0.28 eV/Å^2 for $TiO_2/LaAlO_3$ and 0.17 eV/Å^2 for $LaAlO_3/TiO_2$, respectively, see Fig. 3.2c. To have a direct comparison with $LaAlO_3/SrTiO_3$ HS model, we also listed its E_{cleav} about 0.19 eV/Å^2. [184] Our results show that $TiO_2/LaAlO_3$ has the largest cleavage energy and thus the strongest interface cohesion, while $LaAlO_3/TiO_2$ exhibit the least cleavage energy, implying a weakest interface cohesion. The model $LaAlO_3/SrTiO_3$ system has a slightly larger cleavage energy than that of $TiO_2/LaAlO_3$ system, implying a comparable interface cohesion strength with the $TiO_2/LaAlO_3$.

3.3.2 Electronic properties

In the model $LaAlO_3/SrTiO_3$ system, one of the characteristic features is that there exists a critical film thickness of 4 unit cells of $LaAlO_3$ for an insulator-to-metal transition. [247] As a consequence, one may speculate whether there exists a similar critical film thickness to produce interfacial metallic states in the $TiO_2/LaAlO_3$ and $LaAlO_3/TiO_2$ HS models. To verify this hypothesis, we modeled the HS system by stacking TiO_2 ($LaAlO_3$) film with various unit cells on the $LaAlO_3$ (TiO_2) substrate along the (001) direction. For convenience, the two HS models are labeled as $(TiO_2)_n/LaAlO_3$ and $(LaAlO_3)_n/TiO_2$, respectively, in which n stands for the number of TiO_2 ($LaAlO_3$) unit layers. To have a clear comparison study between $TiO_2/LaAlO_3$ and $LaAlO_3/TiO_2$ HS models and to reveal the dependence of interfacial conductivity on the film thickness, we calculated their density of states (DOS), as presented in Figure 3.4. For the $(TiO_2)_n/LaAlO_3$ model, all the models exhibit metallic states even at $n = 2$ and there is no insulator-to-metal transition, which implies that there does not exist a critical film thickness to form the interfacial conductivity. In other words, the $TiO_2/LaAlO_3$ HS model is intrinsically conductive. Interestingly, the conducting states of $(TiO_2)_n/LaAlO_3$ are very different for and , in terms of shape of the DOS (Figure 3). A detailed analysis of projected DOS indicates that the metallic states are solely contributed by d_{yz} orbitals at n=2 and by d_{xy} orbitals at $n = 3$ (4) (see Fig. 3.3), which is caused by the difference of the local TiO_6 structures at the interface. For $LaAlO_3/TiO_2$ model, in contrast, an insulator-to-metal transition is observed when n increases up to 4, which indicates a critical film thickness of 4 unit cells to form the interfacial conductivity. Interestingly, this critical film thickness for insulator-to-metal transition is same with that of the $LaAlO_3/SrTiO_3$ HS. [9, 199, 247, 280]

In the prototype $LaAlO_3/SrTiO_3$ system, the surface oxygen vacancies (on the $LaAlO_3$ film) have been considered as one possible formation mechanism for the interfacial conductivity. [273, 280] *Ab-initio* studies reveal that surface oxygen vacancies can be formed spontaneously (because of negative formation energy) when the film thickness of $LaAlO_3$ is larger than 4 unit

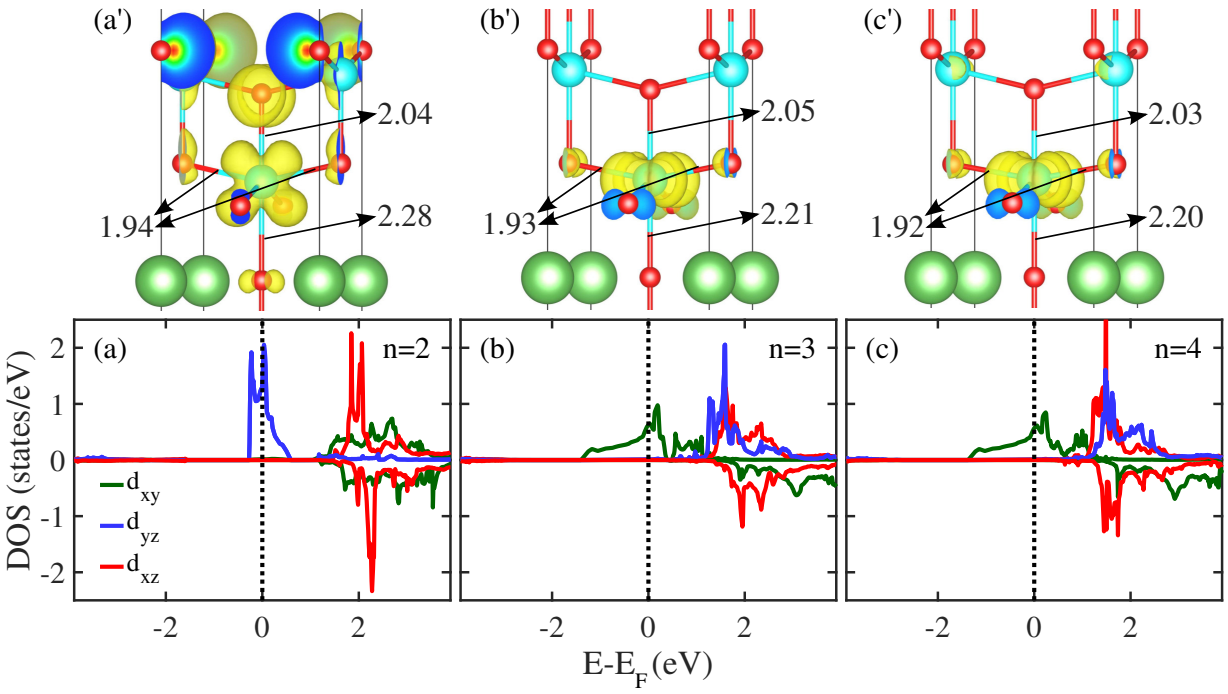

Figure 3.3: Calculated orbital-resolved Ti 3*d* DOS at the 1st interfacial TiO_2 unit layer (IF-I) for $(TiO_2)_n/LaAlO_3$ HS [n = 2 (a), 3 (b), and 4 (c)] along with their corresponding three-dimensional charge density plots (a', b', and c') projected on the bands forming the metallic states near the Fermi level.

cells. [273, 280] The emergence of surface oxygen vacancies on the surface LaO layers destroy the polar $(AlO_2)^- \cdots (LaO)^+$ structure, and thus the polar electric field in the $LaAlO_3$ disappear, which will not compensate the polar catastrophe. As a result, the electronic reconstruction driven by polar catastrophe leads to the charge transfer from $LaAlO_3$ to $SrTiO_3$, forming the interfacial conductivity. More interestingly, the calculated critical film thickness of 4 unit cells is nearly same with that (about 4-5 unit cells) derived from the standard computational model without surface oxygen vacancies. [9,199] In the latter model, the electric field becomes weak as the film thickness increases, and when the film thickness increases up to 5 unit cells, the polarization induced by the electric field is too weak to compensate the polar catastrophe, and the interfacial conductivity occurs. To investigate whether a similar phenomenon can emerge in the $LaAlO_3/TiO_2$ system, we carried out similar first-principles thermodynamic calculations by adopting same approach from prior studies [273, 280] and using experimental conditions. [172] We found that the critical

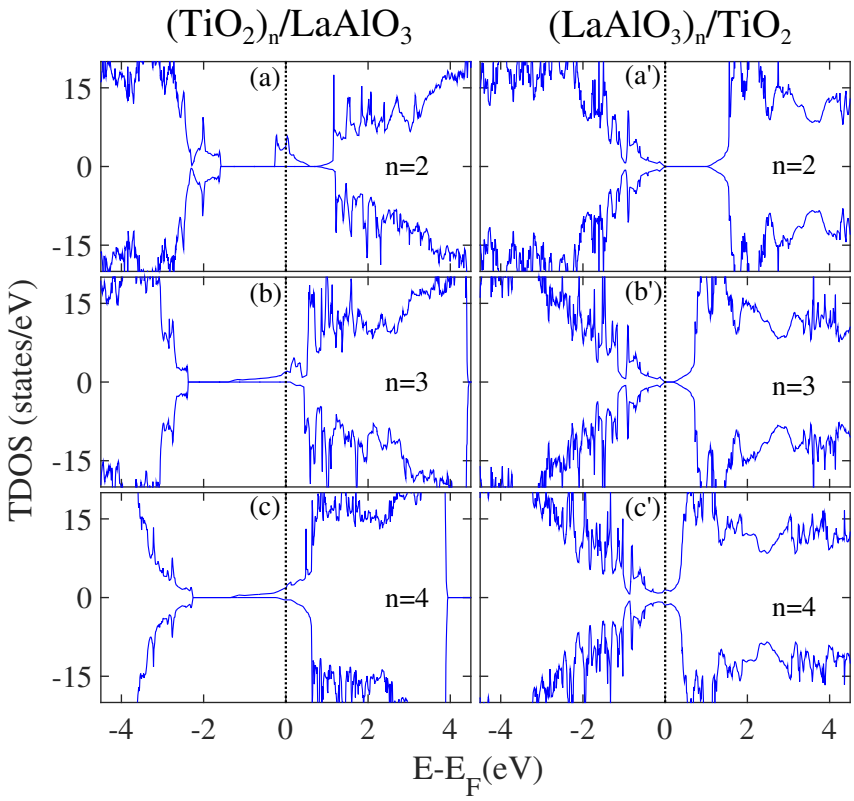

Figure 3.4: Calculated total density of states (DOS) for (a-c) $(TiO_2)_n/LaAlO_3$ (left panel) and (a'-c') $(LaAlO_3)_n/TiO_2$ (right panel). The dash lines at zero denote the Fermi level.

thickness of $LaAlO_3$ film for forming surface oxygen vacancies spontaneously is about 6 unit cells (see Fig. 3.6), which is larger than the 4 unit cells for the insulator-to-metal transition derived from above electronic structure calculations. These results imply that when $LaAlO_3$ film thickness is less than 6 unit cells, the interfacial conductivity is not caused by the surface oxygen vacancies, and when the film thickness is larger than 6 unit cells, the surface oxygen vacancies might be responsible for the interfacial conductivity. This conclusion is of great interests because it means that by fine-tuning the experimental conditions, one might distinguish different mechanisms for the interfacial conductivity, and even design the interfacial conductivity via specific mechanism. As a result, it is also quite necessary to investigate charge transfer mechanism for the standard $LaAlO_3/TiO_2$ model without surface oxygen vacancies, namely, when the $LaAlO_3$ film thickness is less than 6 unit cells.

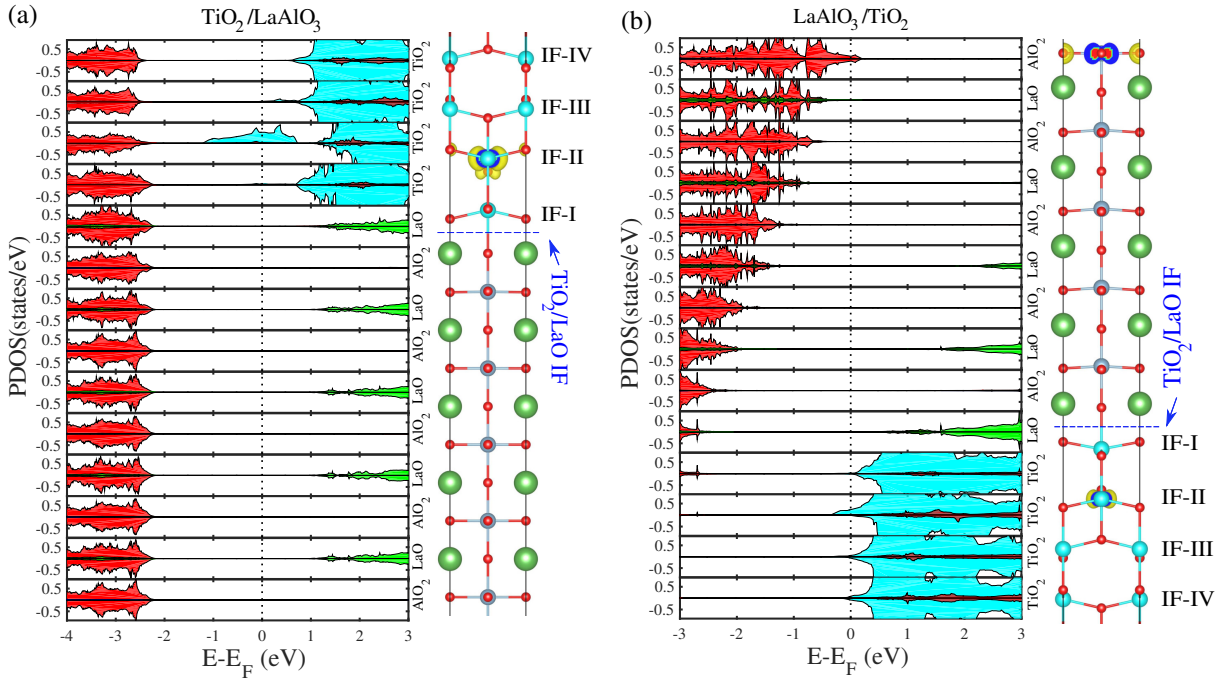

Figure 3.5: Calculated layer-resolved partial DOS along with its three-dimensional charge density projected on the bands forming the metallic states near the Fermi level for (a) $TiO_2/LaAlO_3$ and (b) $LaAlO_3/TiO_2$ HS models.

To understand the mechanism of interfacial conductivity in the two models as well as their different response to the film thickness, we next calculated their layer-resolved projected DOS along with three-dimensional charge density plot projected on the interfacial metallic states, see Fig. 3.5a for $(TiO_2)_8/LaAlO_3$ HS model and Fig. 3.5b for $(LaAlO_3)_5/TiO_2$ HS model. For convenience, we defined the 1st, 2nd and 3rd interfacial TiO_2 unit layers as IF-I, IF-II, and IF-III, respectively. [182, 184, 188] For $TiO_2/LaAlO_3$ HS model (see Fig. 3.5a), the calculated DOS shows that some Ti 3*d* states in the IF-II TiO_2 layer cross the Fermi level, forming the metallic states and solely contributing to the interfacial conductivity. This indicates that a superior confined 2DEG can be achieved in this model. A direct view of the interfacial 2DEG can also be shown from the charge density plot (right panel of Fig. 3.5a). It shows that only IF-II layer exhibits the metallic states while all the other layers away from IF-II exhibit an insulating behavior. The formation of the interfacial conductivity in the $TiO_2/LaAlO_3$ system can be explained as: one

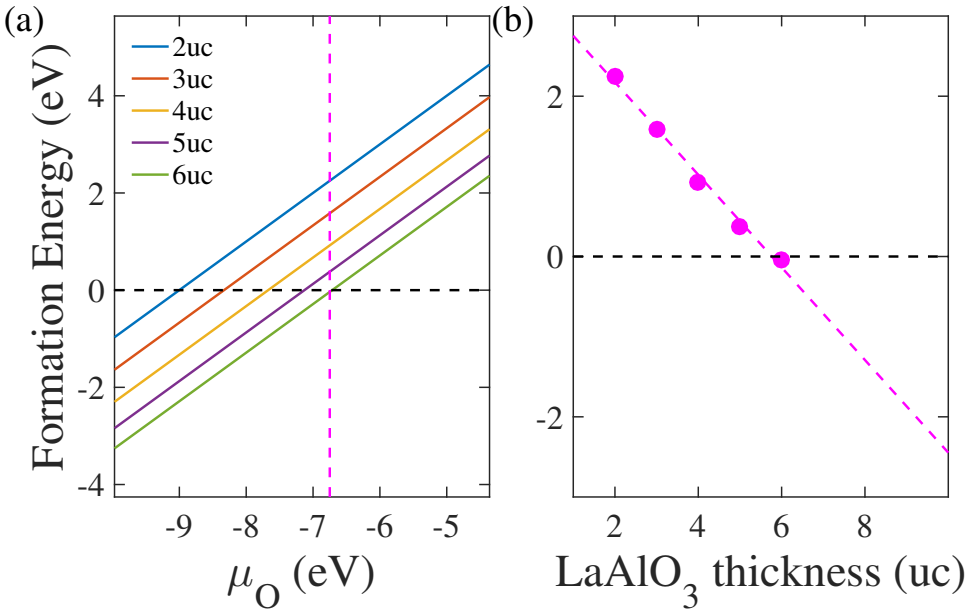

Figure 3.6: Calculated formation energy of surface oxygen vacancy as a function of (a) oxygen chemical potential (μ_O) and (b) thin film thicknesses for $LaAlO_3/TiO_2$ HS. The vertical dash line in (a) indicates the corresponding μ_O under the experimental condition, T = 998 K, P_O = 10^{-5}Torr. [172]

extra $(LaO)^+$ layer (in one side) of the nonstoichiometric $LaAlO_3$ substrate donates extra electrons to the system. These electrons are then transferred to the nonpolar TiO_2 layers, which are captured by 3*d* orbital of Ti ions of the interfacial TiO_2 layer, forming partially occupied Ti 3*d* states and the resulting 2DEG. For $LaAlO_3/TiO_2$ HS system, it shows an entirely distinct electronic structure and charge transfer scheme, see Fig. 3.5b. Unlike the $TiO_2/LaAlO_3$ HS system having an almost identical potential across the $LaAlO_3$ layers, a substantial potential drop is observed in the $LaAlO_3$ layers in $LaAlO_3/TiO_2$ HS model as O 2*p* states shift to higher energy from the interface to surface. This is caused by the electric field induced by the polar interfacial $(LaO)^+$ layer and surface $(AlO_2)^-$ layer, similar to the case of prototype $LaAlO_3/SrTiO_3$ system in which the electric field strength decreases as $LaAlO_3$ film increases. [9, 199] At $(AlO_2)^-$ surface, some O 2*p* states cross the Fermi level and become unoccupied, forming *p*-type-like metallic states at the $LaAlO_3$ film surface. At the $(TiO_2)^0/(LaO)^+$ interface, the polar catastrophe drives the charge transfer from $(LaO)^+$ layer to the $(TiO_2)^0$ layer, and the transferred electrons occupy Ti 3*d*

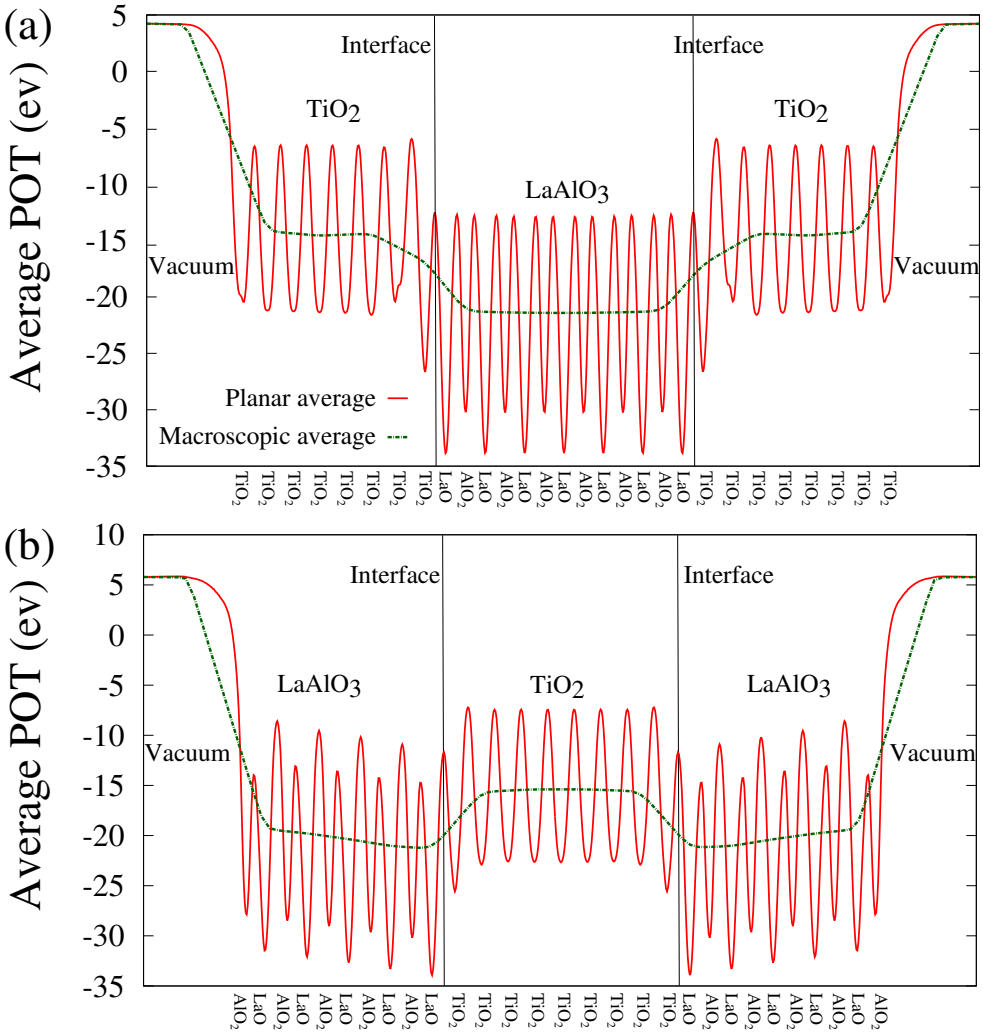

Figure 3.7: The planar and macroscopic averaged electrostatic potential across the (a) TiO_2/$LaAlO_3$ and (b) $LaAlO_3$/TiO_2 HS models.

orbitals, forming *n*-type metallic states at IF-II TiO_2 layer. Moreover, there exists an electric-field-induced "up" polarization towards the surface in the $LaAlO_3$ film for the $LaAlO_3$/TiO_2 model but no polarization in the TiO_2/$LaAlO_3$ model. A clear representation of the polarization and interfacial and surface metallic states can be well depicted in the three-dimensional projected charge density plot in the right panels of the Fig. 3.5a and Fig. 3.5b.

The difference between the two HS models can be addressed from three major perspectives, *i.e.*, the required critical film thickness to have an insulator-to-metal transition, the electrostatic

potential profile in the $LaAlO_3$ layers, and the magnitude of the interfacial charge carrier density. First, as discussed above, there is no film thickness requirement for the interfacial metallic states in the TiO_2/$LaAlO_3$ model, while a critical film thickness of 4 unit cells of $LaAlO_3$ is required to form the interfacial conducting state in the $LaAlO_3$/TiO_2 model. Second, in terms of the electrostatic potential, to clearly show their difference, we calculated the planar and macroscopic averaged electrostatic potential of the two HS systems in Fig. 3.7. It is found that TiO_2/$LaAlO_3$ HS model exhibits an almost constant electrostatic potential in the $LaAlO_3$ substrate (see Fig. 3.7a), while $LaAlO_3$/TiO_2 HS model shows a substantial slope of the electrostatic potential in the $LaAlO_3$ film (see Fig. 3.7b). The later implies that there exists an electric field in the $LaAlO_3$ layers, the magnitude of which can be further estimated by the slope of macroscopic average electrostatic potential. The calculated electric field strength of the $LaAlO_3$/TiO_2 HS model is about 0.19 eV/Å, which is comparable with previously reported values from 0.15 to 0.24 eV/Å in the $LaAlO_3$/$SrTiO_3$ HS system. [142,211,280] Third, as shown in the layer-resolved DOS plots in Fig. 3.5a and Fig. 3.5b, there are more occupied Ti 3*d* states below the Fermi level in the TiO_2/$LaAlO_3$ than that in $LaAlO_3$/TiO_2 HS model, indicating a higher interfacial charge carrier density in the TiO_2/$LaAlO_3$ than that in the $LaAlO_3$/TiO_2 HS model. To quantitatively evaluate their interfacial electron density, we calculated the orbital occupation of interfacial Ti 3*d* states at IF-II TiO_2 layer by integrating the occupied Ti 3*d* states near the Fermi level. For TiO_2/$LaAlO_3$ model, the calculated orbital occupations are 0.345. This value is well consistent with calculated total charge transfer of 0.39 *e* from Bader charge analysis. [88] For $LaAlO_3$/TiO_2 model, the calculated orbital occupation at IF-II TiO_2 layer is 0.054, which is much less than that in the TiO_2/$LaAlO_3$ model. The estimated interfacial charge carrier density is $3.64 \times 10^{13} cm^{-2}$ in the $LaAlO_3$/TiO_2 HS, which is comparable with the number in the $LaAlO_3$/$SrTiO_2$ HS. [9, 247] In contrast, about one order of magnitude enhanced interfacial charge carrier density of around $2.41 \times 10^{14} cm^{-2}$ is found for the TiO_2/$LaAlO_3$ HS model, which is well consistent with the experimental magnitude in the order of $10^{14} cm^{-2}$. [221] Nevertheless, for the perfect $LaAlO_3$/TiO_2 system, it is worth

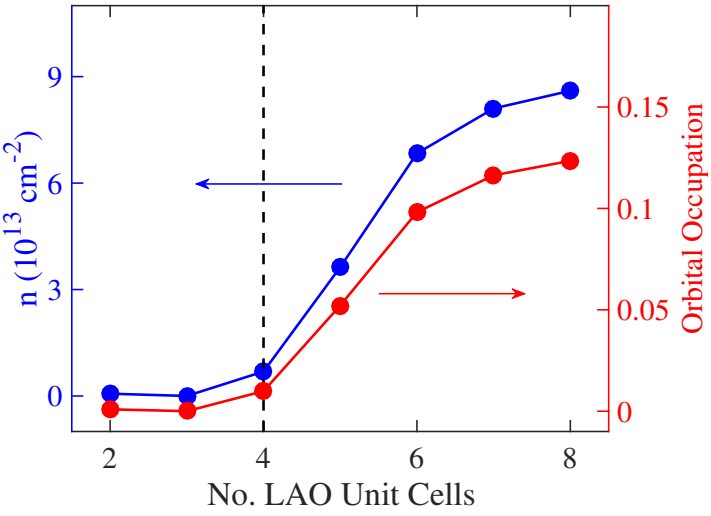

Figure 3.8: Calculated total orbital occupation and corresponding charge carrier densities as a function of the $LaAlO_3$ unit cells in $LaAlO_3/TiO_2$ HS systems.

pointing out that when the $LaAlO_3$ film thickness increases, the interfacial charge carrier density will also increase (see Fig. 3.8), similar to the case of the prototype $LaAlO_3/SrTiO_3$ HS. [235] As discussed below, this is because the electric field caused by the polar $(AlO_2)^- \cdots (LaO)^+$ structure decreases as the $LaAlO_3$ thickness increases, which leads to more charge transfer from $(LaO)^+$ to TiO_2 substrate.

The $LaAlO_3/TiO_2$ HS model shows substantially different electronic properties from the $TiO_2/LaAlO_3$ model mainly because of intrinsic electric field effects and resulting polarization in the $LaAlO_3$ film, similar to the case of $LaAlO_3/SrTiO_3$ HS system. [9, 280] When $LaAlO_3$ is deposited on the TiO_2 substrate, the surface $(AlO_2)^-$ layer and interfacial $(LaO)^+$ layer yield an electric field pointing from the interface to the surface. [8] This electric field further induces an "up" polarization pointing to the surface in the $LaAlO_3$ film, *i.e.*, the relative displacement between the cations and anions. In other words, there exist buckled O-La-O and O-Al-O chains in the $LaAlO_3$ thin film. [199, 280] For $(LaAlO_3)_n/TiO_2$ HS model, at $n < 4$, the strong enough "up" polarization neutralizes the polar catastrophe, *i.e.*, counteracts the polar-catastrophe-induced charge transfer from the $LaAlO_3$ film to the TiO_2 substrate, leading to the insulating behavior.

As the film thickness increases, the polarization strength decreases. [9] At $n \geq 4$, the relatively weak polarization in the $LaAlO_3$ film partially counteracts the polar-catastrophe-induced charge transfer, and thus the remaining electrons (less than 0.5 e) are transferred to the TiO_2 substrate, forming the interfacial metallic states. In contrast, in the $TiO_2/LaAlO_3$ model, there is no polarity in the TiO_2 film or the $LaAlO_3$ substrate, and such a compensation of polarity-induced electric field cannot occur in the $TiO_2/LaAlO_3$ HS model, which leads to significantly different materials properties from that of the $LaAlO_3/TiO_2$ HS model. In addition, it is worth mentioning that, in the $TiO_2/LaAlO_3$ HS model, more charge transfer from the $LaAlO_3$ to the TiO_2 layer also substantially enhances the magnetic moment up to around $0.48\mu_B$, with respect to a negligible magnetic moment in $LaAlO_3/TiO_2$ HS. Moreover, interestingly, we found that the ferromagnetic coupling state between the two adjacent Ti ions is energetically more favorable than its antiferromagnetic state by 180 meV, implying the existence of robust ferromagnetism in the $LaAlO_3/TiO_2$ HS system. This is different from the magnetic coupling interaction in the oxygen-deficient bulk anatase TiO_2 [268] in which the magnetic moment of the Ti ions around the oxygen vacancy is close to 1.0 μ_B, which forms a stable antiferromagnetic coupling, as in the case of $LaTiO_3$. [191]

3.3.3 Electron effective mass and conductivity

Besides the charge carrier density, another physical parameter to determine the conductivity is the electron mobility. To qualitatively compare the electron mobility and conductivity between $TiO_2/LaAlO_3$ and $LaAlO_3/TiO_2$ HS models, here we calculated their band structures and electron effective masses. The calculated band structures along the Brillouin zone path M-Γ-X for these two HS models are presented in Fig. 3.9. It shows that both the bottom conduction bands of the two HS models, which are mostly contributed by Ti $3d_{xy}$ orbital, cross the Fermi level and form the n-type interfacial metallic states. This is similar to the case of the Nb-doped anatase TiO_2 [93] and the $LaAlO_3/SrTiO_3$ HS. [59] For $LaAlO_3/TiO_2$ HS model, the O $2p$ band near the valence band edge also crosses the Fermi level, which corresponds to the AlO_2 surface

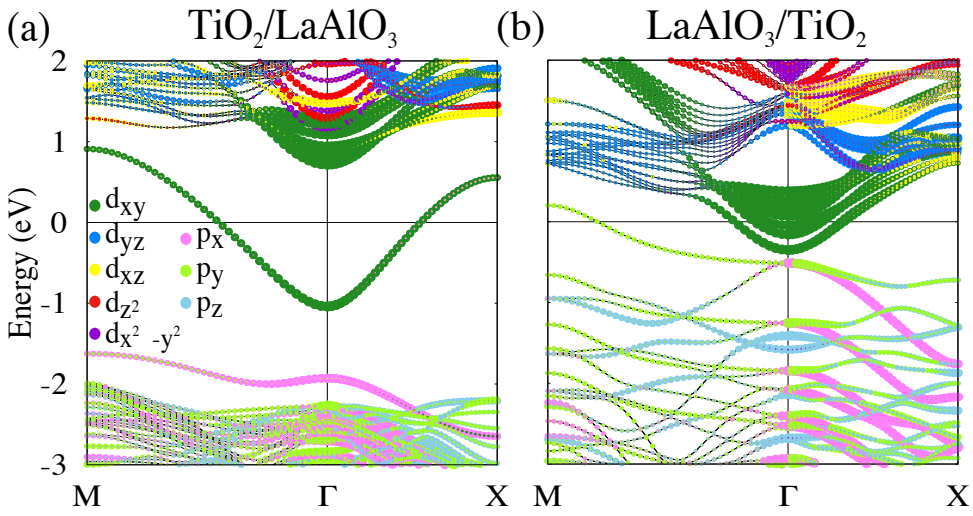

Figure 3.9: Orbital-projected band structures for (a) TiO_2/$LaAlO_3$ and (b) $LaAlO_3$/TiO_2 HS models. The horizontal solid line at zero indicate Fermi energy. The circle size of the bands is proportional to the population in the corresponding orbitals.

hole states in Fig. 3.5b. In addition, it is found that the occupied Ti 3*d* bands in TiO_2/$LaAlO_3$ have a higher electron population than that in the $LaAlO_3$/TiO_2 HS model, which is consistent with the aforementioned finding of a larger interfacial charge carrier density in the TiO_2/$LaAlO_3$ HS model.

We calculated the electron effective mass m^*/m_e of the bottom conduction bands using parabolic effective mass approximation via the following equation: [202, 256]

$$\frac{1}{m^*} = \frac{1}{\hbar^2}\frac{\partial^2 E_{cond}}{\partial k_{CBM}^2} \tag{3.9}$$

where $\hbar$ is reduced Planck constant, k_{CBM} is the electron wave vector corresponding to the bottom conduction bands, and E_{cond} is the energy of the bottom conduction band. For TiO_2/$LaAlO_3$ HS model, the calculated m^*/m_e is 0.71 along Γ-M direction and 0.47 along Γ-X direction, which are in good agreement with both theoretical and experimental values (0.4 - 0.7) for bulk anatase TiO_2. [92, 93, 105, 248] This indicates that the interfacial electronic properties of the TiO_2/$LaAlO_3$ HS system inherit the bulk materials properties of TiO_2. For $LaAlO_3$/TiO_2 HS, the calculated

m^*/m_e is 0.80 along Γ-M and 0.70 along Γ-X direction, which is comparable to that in the $LaAlO_3/SrTiO_3$ HS (0.6 - 0.7). [59, 181]

The electron mobility μ can be linked to m^* by using the following equation:

$$\mu = \frac{e < \tau >}{m^*} \tag{3.10}$$

where e is the fundamental charge, and $< \tau >$ is the average scattering time that replies on all the scattering events such as phonon scattering, ionized impurity scattering and neutral defects. [202] Consequently, the conductivity σ can be calculated from the charge carrier density n and mobility μ by the following equation: [256]

$$\sigma = ne\mu \tag{3.11}$$

By assuming that τ is a constant in the two HS models, we found that the conductivity σ in $TiO_2/LaAlO_3$ HS is approximately one order of magnitude higher than that in $LaAlO_3/TiO_2$ and $LaAlO_3/SrTiO_3$ models. Such significantly enhanced conductivity is primarily attributed to the high charge carrier density in the $TiO_2/LaAlO_3$ HS system, which is consistent with the recent experimental observation. [172, 221]

3.4 Conclusion

By using first-principles electronic structure calculations, we studied interfacial electronic and energetic properties of the $TiO_2/LaAlO_3$ (TiO_2 film grown on $LaAlO_3$ substrate) and $LaAlO_3/TiO_2$ ($LaAlO_3$ film grown on TiO_2 substrate) HS models, and found that the growth order of the epitaxial structures significantly influence the interfacial materials properties, as detailed below:

(i) The interfacial energetics calculations indicate that $TiO_2/LaAlO_3$ system is energetically more stable and also has stronger interfacial cohesion strength than $LaAlO_3/TiO_2$ system.

These results are consistent with the experimental facts of well-preserved anatase phase in the TiO_2/$LaAlO_3$ but anatase-to-rutile phase transition in the $LaAlO_3$/TiO_2 system.

(ii) For TiO_2/$LaAlO_3$ HS, it is intrinsically conducting because of the polar catastrophe at the interface, and there does not exist an insulator-to-metal transition. In contrast, for $LaAlO_3$/TiO_2 HS, there exists an insulator-to-metal transition as the film thickness increases, and the critical film thickness is about 4 unit cells of $LaAlO_3$, which is similar to the case of the prototypical $LaAlO_3$/$SrTiO_3$ HS system.

(iii) For TiO_2/$LaAlO_3$ HS, there exists a charge transfer of about 0.5 e per unit cell from $LaAlO_3$ substrate to the TiO_2 film, which leads to a high interfacial charge carrier density in the order of 10^{14} cm^{-2}. For $LaAlO_3$/TiO_2 HS, the polarity-induced polarization in the $LaAlO_3$ film partially counteracts the charge transfer from the $LaAlO_3$ film to the TiO_2 substrate, producing a much low interfacial charge carrier density in the order of 10^{13} cm^{-2}, with respect to the TiO_2/$LaAlO_3$ HS model. As a result, the estimated conductivity of TiO_2/$LaAlO_3$ is about one order of magnitude higher than that of $LaAlO_3$/TiO_2 system, which is mainly attributed to the much higher interfacial charge carrier density in the former system.

(iv) For TiO_2/$LaAlO_3$ HS, the high interfacial charge carrier density also leads to a larger magnetic moment that is mainly contributed by interfacial Ti ions, and the magnetic moments on the adjacent Ti ions form a stable ferromagnetic coupling, indicating the existence of robust ferromagnetism. In contrast, the magnetic moment in the $LaAlO_3$/TiO_2 HS is negligible.

In short, we carried out a comprehensive and comparison investigation for the TiO_2/$LaAlO_3$ and $LaAlO_3$/TiO_2 HS systems using first-principles electronic structure calculations, and revealed the influence of their epitaxial growth order on the interfacial materials properties. It is expected that the model HS system $LaAlO_3$/$SrTiO_3$ ($LaAlO_3$ grown on $SrTiO_3$ substrate) and $SrTiO_3$/$LaAlO_3$ ($SrTiO_3$ grown on $LaAlO_3$ substrate) may also exhibit significantly different interfacial properties because of different epitaxial growth order, similar to the case of HS consisting of TiO_2 and $LaAlO_3$. It is worth mentioning that, however, the two types of systems,

$TiO_2/LaAlO_3$ and $LaAlO_3/TiO_2$, are based on the ideal model that does not involve interfacial defects, and further comprehensive theoretical/computational studies of the influence of epitaxial growth order on the interfacial defect behaviors are of interests.

3.5 Acknowledgements

Chapter 3, in full, is a reprint of the material "Comparison Studies of Interfacial Electronic and Energetic Properties of $LaAlO_3/TiO_2$ and $TiO_2/LaAlO_3$ Heterostructures from First-Principles Calculations" as it appears in ACS Applied Materials and Interfaces. Jianli Cheng, Jian Luo, Kesong Yang, 9, 76827690, 2017. The dissertation author was the primary investigator and author of this paper.

Chapter 4

2DEG at Spinel/Perovskite Interface: Interplay between Polar Catastrophe and Structural Defects

In Chapter 3, we have discussed the formation of 2DEG in binary oxides involved HS, $TiO_2/LaAlO_3$. In this Chapter, we will introduce a hitherto unknown 2DEG formed at the interface between spinel $MgAl_2O_4$ and perovskite $SrTiO_3$. Our integrated approach combining experimental measurements and first-principles calculations reveals that an atomic-thin interfacial Ti-Al-O layer with a thickness of about 4 $\AA$ is key to the observed metallic transport. The critical film thickness for the insulator-to-metal transition is around 32 $\AA$, which can be explained by the co-existence of interfacial antisite defects and surface oxygen vacancies. Our magnetoresistance measurement reveals a strong Rashba spin-orbit interaction at the $MgAl_2O_4/SrTiO_3$ interface. The 2DEG observed at spinel/perovskite interface could shed light on the nature of 2DEG at oxide interfaces, and imply the existence of emergent phenomena at the interfaces between spinel group minerals and perovskite oxides.

4.1 Introduction

Taking advantages of the advanced material fabrication techniques with layer-by-layer control in heterostructures, interface engineering between oxides provides new opportunities in oxide electronics to explore novel phenomena through breaking the translation or inversion symmetry at the interface. [106, 215, 241] One prominent example is the discovery of two-dimensional electron gas (2DEG) with extremely high charge carrier density at the interface of two band-insulators $LaAlO_3$ (LAO) and $SrTiO_3$ (STO). [190, 195] The LAO/STO interface also exhibits other fantastic properties such as superconductivity, [213] magnetism, [28] and electronic phase separation. [5] Although a large amount of experimental and theoretical work has been performed, the origin of the 2DEG at the interfaces of insulating oxides is still under debate. A particularly interesting observation is the thickness-dependent insulator-to-metal transition at LAO/STO interfaces, namely the 2DEG appears at a critical thickness of four unit cells (uc, 15 $\AA$) for LAO on TiO_2-terminated STO substrate. [8, 35, 179] Takamura et al proposed that the polar catastrophe at the LAO/STO interfaces controls the critical thickness. [179] The STO substrate contains neutral $(SrO)^0$ and $(TiO_2)^0$ planes, while the LAO is composed of charged $(LaO)^{+1}$ and $(AlO_2)^{-1}$ planes. The symmetry breaking at the $(LaO)^{+1}/(TiO_2)^0$ interface results in the polar catastrophe, and the charged $(LaO)^{+1}/(AlO_2)^{-1}$ layers in the LAO film leads to a built-in electric field of $\sim$0.24 V/$\AA$. [32] The corresponding electrostatic potential increases with increasing LAO thickness, and 2DEG appears at 4 uc when the potential overcomes the energy discrepancy of 3.3 eV between the LAO valence band maximum and the STO conduction band minimum, resulting in a charge transfer from the LAO surface layer to the interface. [32] This scenario is consistent with the experiments that an electric field originated from external gating voltage can also induce the insulator-metal transition at LAO/STO interfaces. [36, 153, 247] In a later hard x-ray photoemission spectroscopy experiment, a discrepancy of the built-in fields between insulating and metallic interfaces was indeed observed. [233]

Recent advances on oxide interfaces, however, suggest that the polar catastrophe alone is not sufficient to reconcile all the experimental observations. In particular, the observation of built-in field even in the conducting LAO/STO interface is inconsistent with the model in which the built-in field should be canceled after the charge transfer. [98, 233] Actually, recent first-principles calculations showed that the polar $(AlO_2)^{-1}/(LaO)^{+1}$ configuration leads to an intrinsic polarization in the LAO film with a direction perpendicular to the interface, which neutralizes the polar catastrophe. [9] In addition to the polar catastrophe mechanism, several models involving various types of defects were developed, such as oxygen vacancies at the LAO surface [273, 280] and lattice distortions. [143, 199, 228, 280] In particular, conducting interfaces fabricated at very low oxygen pressures without post-synthesis oxygen annealing are known to contain electron-donor oxygen vacancies at the interface. [43, 231] Moreover, most $A^{3+}B^{3+}O_3$ oxides contain rare-earth elements and promote the possible existence of donor defects by cation intermixing, leading to the formation of a metallic $La_{1-x}Sr_xTiO_3$ layer at the interface. [115, 261, 265]

One intriguing discovery in the oxide interface research is that the polar catastrophe model can predict the formation of interfacial 2DEG in not only the LAO/STO case but also other systems such as $LaTiO_3$(LTO)/STO, [16] $NdAlO_3$/STO, [4] and $LaGaO_3$(LGO)/STO. [4, 201] Moreover, the threshold thickness L in these heterostructures follows the polar-catastrophe-induced charge transfer model: [211]

$$L = \Delta\Phi\varepsilon_0\varepsilon_r/eP_0 \tag{4.1}$$

where $\Delta\Phi$ is the energy difference between film valence band maximum and STO conduction band minimum, and ε_r and P_0 are the relative permittivity and formal polarization of the film, respectively. A recent work from Yangs group provided a group of combinatorial material descriptors based on the polar catastrophe with STO as the substrate and predicted 42 polar perovskite oxides that could form 2DEG at the interfaces. [269] However, far less conductive 2DEG systems have been experimentally discovered so far, indicating that other material parameters including defect characteristics must play a role.

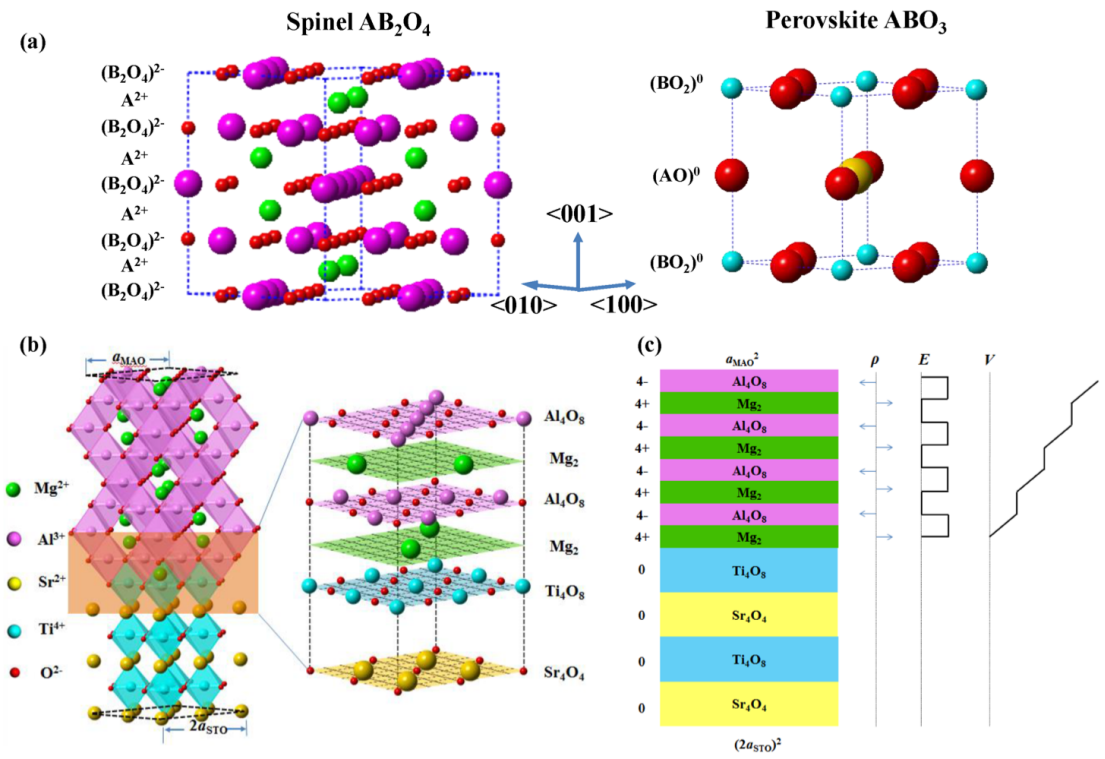

Figure 4.1: (a) Crystal structure of a general spinel AB_2O_4 and perovskite ABO_3. Spinel is always composed of charged layers A^+ and $(B_2O_4)^-$, and perovskite could be composed of charged or neutral layers. (b) Sketch of the spinel/perovskite heterojunction of $MgAl_2O_4/SrTiO_3$ (MAO/STO). The enlarged picture shows the ideal atomic distribution at the interface of MAO/STO. Because of the good matching of the oxygen sublattices between the Ti_4O_8 layer in STO and the Al_4O_8 layer in MAO, Mg_2 layer is supposed to be the first layer of MAO near the interface. (c) Schematic illustration of the polar catastrophe at the interface of MAO/STO.

We hypothesize that investigating material system besides perovskite/perovskite interfaces may provide clues on the critical parameters determining the onset of 2DEG. Spinel minerals with the general formulation of $A^{2+}B_2^{2+}O_4^{2-}$ and a cubic crystal structure possess alternatively polar planes of A^+ and $(B_2O_4)^-$ along the [001] direction, as shown in Figure 4.1a. Thus, symmetry breaking induced polar catastrophe is expected at the interface of spinel/perovskite HS. [179] In this work, the prototypical spinel mineral $MgAl_2O_4$ (MAO) was selected to form an interface with STO. MAO is a band insulator with an indirect band gap of 7.8 eV, [174] which is larger than that of the commonly investigated LAO (5.6 eV). It has a face-centered cubic (FCC) Bravais lattice with a space group *Fd3m*. The oxygen atoms are arranged in a cubic close-packed lattice,

and the cations Mg and Al occupy 1/8 tetrahedral and 1/2 octahedral sites within the oxygen sublattice, respectively. [150, 240] The lattice parameter of MAO is 8.083 $\AA$, almost twice of the lattice parameter of STO (3.905 $\AA$), [240] which leads to a lattice mismatch of 3.3% in MAO/STO, close to the case of LAO/STO (3.0%). The excellent match of oxygen sublattices and lattice constants between STO and MAO ensures the epitaxial growth of MAO on STO substrate in a layer-by-layer fashion. Moreover, there is no transition metal or rare-earth element in MAO, which eliminates the role of cation inter-diffusion. As sketched in the ideal interface structure (Figure 4.1b), the stacking sequence at the interface of MAO/STO is $(Al_2O_4)^{2-}$-Mg^{2+}/$(TiO_2)^0$-$(SrO)^0$, suggesting the existence of polar catastrophe as in the case of LAO/STO, see Figure 4.1c. Hence, the built-in polarization of MAO/STO is P_{MAO} = 4e/2S_{MAO}, [238] which predict a critical thickness of 8.08 $\AA$ (1 uc). However, we found that the threshold thickness of insulator-metal transition in MAO/STO is 32 $\AA$ (4 uc), which is much larger than the value estimated from the polar-catastrophe model. Interestingly, using high-angle annular dark field scanning transmission electron microscopy (HAADF-STEM), we discovered an atomic-thin Ti-Al-O layer with a thickness of 4 $\AA$ at the MAO/STO interface. First-principles calculations demonstrate that the Al-Ti-O atomic layers formed spontaneously at the interface, which cancels the build-in polar field in MAO and eventually induces the conductivity at the MAO/STO interface with the assistance from surface oxygen vacancies. Our results on the MAO/STO interface open a new door to the defect-based design of 2DEG at oxide interfaces.

4.2 Results and discussion

4.2.1 Layer-by-layer growth of $MgAl_2O_4$ on $SrTiO_3$

MAO films were deposited on TiO_2-terminated STO substrate by pulse layer deposition at 800 °C under 110^{-5} Torr oxygen pressure followed by 1 h annealing at 600 °C and 1 atmosphere O_2 pressure to remove oxygen vacancy. Before the deposition, the reflection high-energy electron

diffraction (RHEED) pattern shows a clear (100) symmetry of the STO substrate, see Figure 4.2a. Due to the difference of lattice symmetry between MAO film and STO substrate, the distance of RHEED patterns are doubled after the deposition of MAO layer. Oscillations of RHEED intensity during the growth suggest a layer-by-layer growth mode, as shown in Figure 4.2b. Each oscillation period corresponds to the minimum unit of the chemical composition needed to ensure charge neutrality. Thus, 4 oscillations indicate the growth of 1 u.c. MAO layer. The step- like pattern in the atomic force microscope (AFM) image of Figure 4.2c confirms the layer-by-layer growth of the MAO film. The height of the step is around 3.9 $\AA$, which represents the step of TiO_2-terminated STO substrate. In Figure 4.2d, the cross-section HADDF image of the MAO/STO heterojunction suggests a good epitaxial growth of MAO on STO and sharp interface. As the contrast in this technique is related to the atomic number Z, the MAO layer appears darker than the STO substrate because of the lower average Z numbers (Mg-12, Al-13, Ti-22, and Sr-38).

Figure 4.3a shows the HADDF blowup image at the MAO/STO interface. Based on the contrast of ions with different Z values, the ion distribution can be illustrated. However, the interface layer can neither be labeled TiO_2 nor AlO_2. In fact, the HADDF signal profile along the [001] direction in Figure 4.3c indicates Ti diffused into the adjacent MAO layer in proximity to the interface. A clear stack sequence (-Sr-O-)/(-Ti-Al-O-)/(-Ti-Al-O-)/(-Al-O-) can be observed from the layer-resolved HADDF signal profile as shown in Figure 4.3b, indicating the formation of two $TiAlO_x$ atomic layers at the interface of MAO/STO. There are two interesting properties of the interfacial Ti-Al antisite defects in the MAO/STO heterostructure. First, the abrupt drop of Ti signal at Figure 4.3c suggests the Ti-Al antisite defects is strongly confined at the interface. The thickness of interfacial $TiAlO_x$ layer estimated from Figure 4.3c is around 4 $\AA$, indicating an important role on the interfacial electron and/or orbital reconstruction at MAO/STO. In fact, Chen et al. reported 2DEG with the conducting channel of 9 $\AA$ at γ-Al_2O_3/STO interface. [43] Second, at the interfacial layers, the Ti ions do not randomly occupy the position of Al ions, but

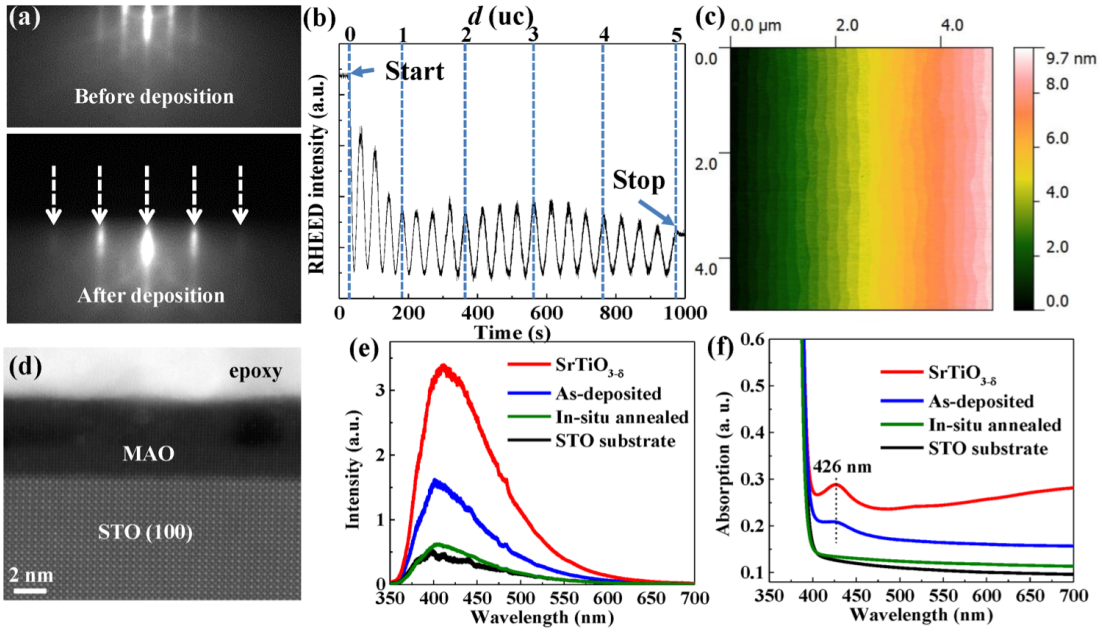

Figure 4.2: (a) RHEED patterns before and after the deposition of 5 uc MAO film, showing that the lattice parameter of MAO film is almost twice that of the substrate. (b) Oscillations of RHEED intensity during the growth suggests a layer-by-layer growth mode. (c) AFM image of the same film, confirming the layer-by-layer growth. (d) HADDF image of a 6 uc MAO on STO. (e) PL spectra and (f) absorption of 10 uc MAO/STO with and without in-situ annealing at 600 °C and 1 atm O2 pressure. As-received STO substrate and vacuum-annealed STO were also measured as references.

follow the crystal structure of STO as shown in Figure 3b. Ti ions keep the B site in perovskite ABO_3 at the $TiAlO_x$ layer of the STO side, and represent the A site of Sr ions at the $TiAlO_x$ layer of the MAO side. Interfacial Ti diffusion has also been observed in the LAO/STO interface, in which Ti is believed to keep the B site position when diffused into the LAO layer. [143, 179] Such a distribution in MAO/STO suggests the prominent role of oxygen sublattice on the interface structure. It is worthy to point out that, the absence of high Z value elements in MAO makes MAO/STO an excellent system for investigating the distribution of Ti at interface. The origin and role of the Ti-Al-O layer will be analyzed in the theoretical section.

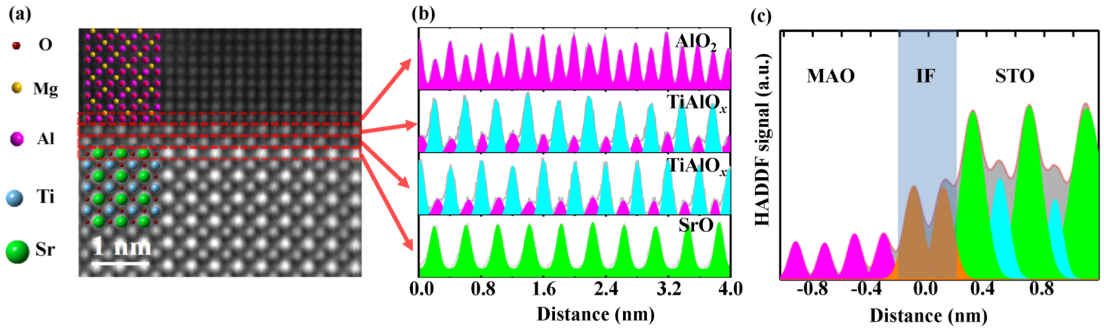

Figure 4.3: (a) HADDF image and the corresponding schematic structures of MAO and STO. Sr, Ti, and Al ions can be clearly distinguished due to their different Z values. (b) Layer-resolved HAADF signal profiles from areas outlined in (a) along the direction parallel to the interface for four atomic layers around the interface. Green, cyan, and magenta peaks denote Sr, Ti, and Al atoms, respectively. (c) HADDF signal profile from the whole HADDF image along the direction perpendicular to the interface. IF is the abbreviation of interface.

4.2.2 Oxygen vacancy defects

Photoluminescence (PL) spectrum and absorption spectrum of samples were studied to check the influence of oxygen pressure during growth on the oxygen vacancy defects, as shown in Figure 4.2e, f. STO substrate and vacuum-annealed STO were also measured for reference. The sample without annealing shows a stronger PL, which suggests the existence of a large amount of oxygen vacancies. After annealing, the PL intensity decreases to the level near that of the insulating STO substrates. The absorption edges of all the samples locate at 380 nm, which corresponds to the band gap of 3.2 eV of STO. The annealed STO and as-deposited MAO/STO heterostructure shows another absorption peak around 426 nm, suggesting an intrinsic oxygen-vacancy states of STO as donor levels below the bottom of conduction band of STO. [119] After annealing, the absorption peak from the oxygen-vacancy states disappears, and the absorption across the whole measured region also decreases to a value near that of the STO substrate. The PL and absorption spectrum suggest that the *in-situ* annealing process sufficiently reduces the oxygen vacancy defects in MAO/STO heterojunction.

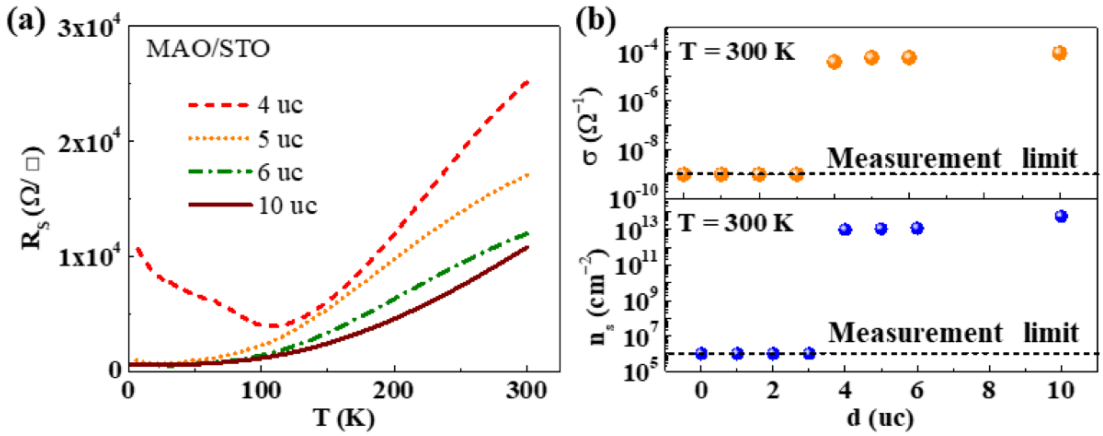

Figure 4.4: (a) Sheet resistance of the MAO/STO samples with different MAO layer thicknesses. (b) Thickness dependencies of the conductivity and charge density at room temperature for MAO/STO. The resistances of the samples with a thickness less than 4 uc are out of the measurement range. The charge density of the metallic interfaces at room temperature is at the level of 10^{-13} cm^{-2}.

4.2.3 2DEG at the $MgAl_2O_4/SrTiO_3$ interface

Charge transport properties of MAO/STO heterojunctions with in-situ annealing are studied. As shown in Figure 4.4a, although both MAO and STO are band-insulators, the temperature dependent resistances of MAO/STO samples present metallic behavior when the MAO layer exceeds 4 uc (32 $\AA$). The thickness dependencies of conductivity and charge density at room temperature show a threshold at 4 uc (Figure 4.4b), and the resistances of samples with thinner MAO layer are out of the measurement limit of 10^9 Ohm. Although the 2DEG reported in LAO/STO interfaces also has a threshold around 4 uc, [247] the lattice parameter of MAO, a = 8.083 $\AA$, is twice larger than that of LAO ($\sim$3.8 $\AA$). Hall measurement shows that the main type of charge is electron with a charge density of 5.2×10^{13} cm^{-2} and mobility of 304 cm^2/Vs for the 10 uc MAO/STO at 2 K, close to the values reported for LAO/STO interfaces. [8, 247, 274] The temperature dependencies of resistance for all the samples show low-temperature upturn, which was also reported for other 2D interfaces.

Arising from the structural inversion symmetry breaking, the Rashba spin-orbit interaction can be substantial and plays a critical role in the charge transport for 2DEG systems. [34]

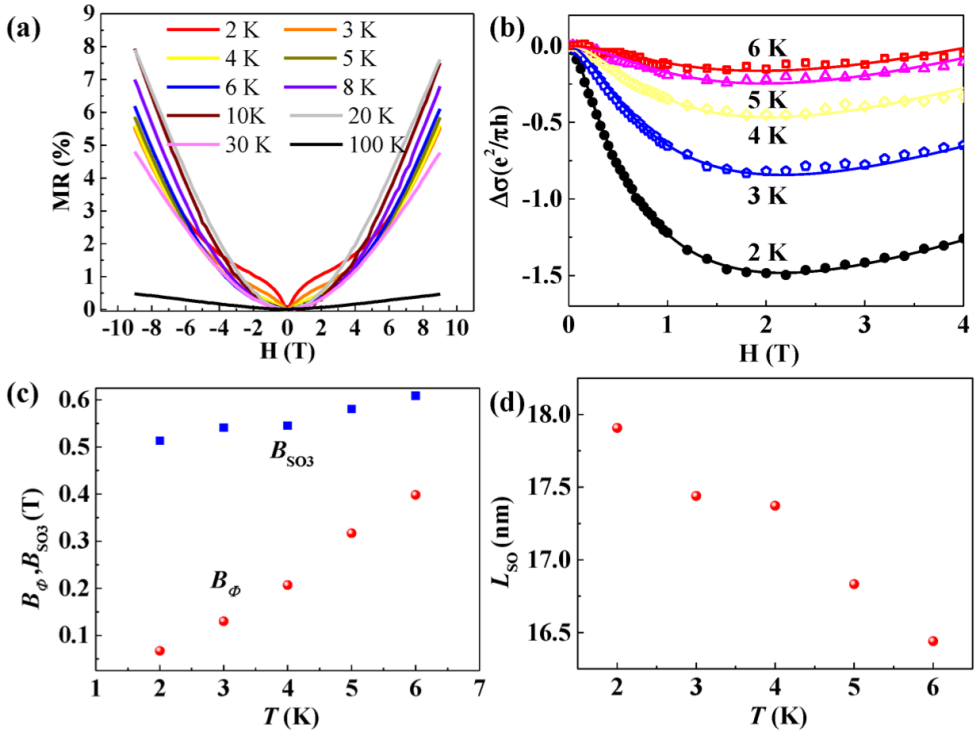

Figure 4.5: (a) Magnetoresistance of the 10 uc MAO on STO. The magnetic fields are perpendicular to the film plane. (b) Experimental $\Delta\sigma$ (symbols) and theoretical fits (lines) by the k-cubic ILP fitting. (c) Parameters used for the k-cubic ILP fitting (B_{SO1}=0). (d) Temperature dependence of the spin precession length.

According to the weak anti-localization (WAL) theory, the destructive interference effect of coherently back-scattered electrons enhances the conductivity of the system. The applied out-of-plane magnetic field suppresses the conduction enhancement and hence results in the sharp increase of the resistance at low fields. In Figure 4.5a, the magnetoresistance (MR) of MAO/STO shows a clear structure of sharp cusp around 0 T magnetic field for the temperature below 6 K, which is a typical WAL feature in a 2DEG system. [180] The conductivity difference $\Delta\sigma$, which presents a WAL correction to the conductivity by subtracting the B^2 Lorentz background, can be fitted perfectly by the k^3 spin splitting model from Iordanskii, Lyanda-Geller, and Pikus (ILP) theory in Figure 4.5b. [180] The spin precession length LSO calculated from the fitting is approximately 18 nm at 2 K (Figure 4.5d), and smaller than the value of 60 nm reported on electrically gated STO. [64, 180] The shorter LSO probably reflects the stronger atomic spin-orbit

coupling in MAO/STO than electrical gated STO.

4.2.4 Polar catastrophe in $MgAl_2O_4/SrTiO_3$

In the polar catastrophe model, the critical thickness of the interfacial 2DEG can be calculated from the equation 6.1. [211] For the prototype LAO/STO model, the critical thickness L of LAO to form interfacial 2DEG is around 13.5 $\AA$ with the parameters ε_r = 24.5, $\Delta\Phi$ ~3.3 eV, P_0= 0.529 Cm^{-2}, which is consistent with the experimental value of 4 uc. [211] For the 2DEG at MAO/STO interface, by using the physical parameters ε_r = 7.89, [7] ε_r=5.5 eV, and P_{MAO} = $4e/2S_{MAO}$, the critical thickness is estimated to be 7.3 $\AA$, which means the 2DEG should arise in 1 uc MAO (8.08 $\AA$) films. The large discrepancy of the calculated critical thickness and the experimental value (32 $\AA$) suggests that the 2DEG in MAO/STO is unlikely to be solely caused by the polar catastrophe induced charge transfer.

4.2.5 First-Principles Electronic Structure Calculations

To understand the origin of 2DEG at MAO/STO interface and the large discrepancy between the estimated and experimental critical thickness of insulator-to-metal transition, we studied the electronic structures and energetic stability of the MAO/STO system using first-principles density functional theory (DFT) calculations as follows.

Defect-free MAO/STO model

To determine the required critical thickness to form interfacial conductivity in the defect-free MAO/STO model, we built MAO/STO heterostructure-based slab models with different MAO layers and calculated their electronic structures. The conventional unit cell of MAO contains 4 alternate layers of $(Mg_2)^{+4}$ and $(Al_4O_8)^{-4}$, see Figure 4.1. To make it clear, one alternate $(Mg_2)^{+4}$ and $(Al_4O_8)^{-4}$ layer is defined as one monolayer (ML), and thus one MAO

unit cell contains 4 MLs. The layer-resolved density of states (DOS) of the MAO/STO model (with 4ML thickness for MAO) is shown in Figure 4.6. It shows a large electrostatic potential increase in the MAO film, and at the surface, i.e., $(Al_4O_8)^{-4}$, O $2p$ states cross the Fermi level, exhibiting a *p*-type conducting characteristic. At the interface, driven by the polar catastrophe at the $(Mg_2)^{+4}/(Ti_4O_8)^0$ interface, Ti 3d states near the interface cross the Fermi level and become occupied, forming *n*-type conductivity at the interface, as in the case of the prototypical LAO/STO heterostructure. The total DOS for MAO/STO heterostructure shows that there exists an insulator-to-metal transition when the MAO thickness increases up to 4ML (8.08 $\AA$), i.e., the lattice parameter of the MAO unit cell, and all the models with MAO thickness less than 4ML are insulating, see Figure 4.7. This indicates that the critical film thickness to form the interfacial conductivity is about 8.08 $\AA$, which is in a good agreement with our calculated value from equation 6.1 but not consistent with the experimental observations.

Antisite defect MAO/STO model

We next built antisite defect MAO/STO model and studied its thermodynamic stability and electronic properties based on two arguments: i) our HADDF image measurement shows the existence of the Ti-Al antisite defects; and ii) the experimentally observed critical thickness of the MAO film to form interfacial conductivity is 32 $\AA$, which is much larger than the calculated value of 8.08 $\AA$ from the defect-free model. Hence, one may speculate that the discrepancy of the critical film thickness may result from the antisite defect behavior at MAO/STO heterointerface. Herein, we modeled two types of antisite defect models: i) Antisite-I with one Ti-Al antisite set plus two substitutional Al to Ti atoms at interfacial $(Ti_4O_8)0$ layer, which forms symmetrical $(Al_3TiO_8)^{-3}$-$(Mg_2)^{+4}$-$(Al_3TiO_8)^{-3}$ structure, see Figure 4.8a; and ii) Antisite-II with two Ti-Al antisite sets at the interface, which forms symmetrical $(Al_2TiO_8)^{-2}$-$(Mg_2)^{+4}$-$(Al_2TiO_8)^{-2}$ structure, see Figure 4.8b. For Antisite-I, the built-in field is canceled by the formation of interface $(Al_3TiO_8)^{-3}$ layer, and the potential remains finite. The interfacial $(Mg_2)^{+4}$ layer donates four electrons to the two

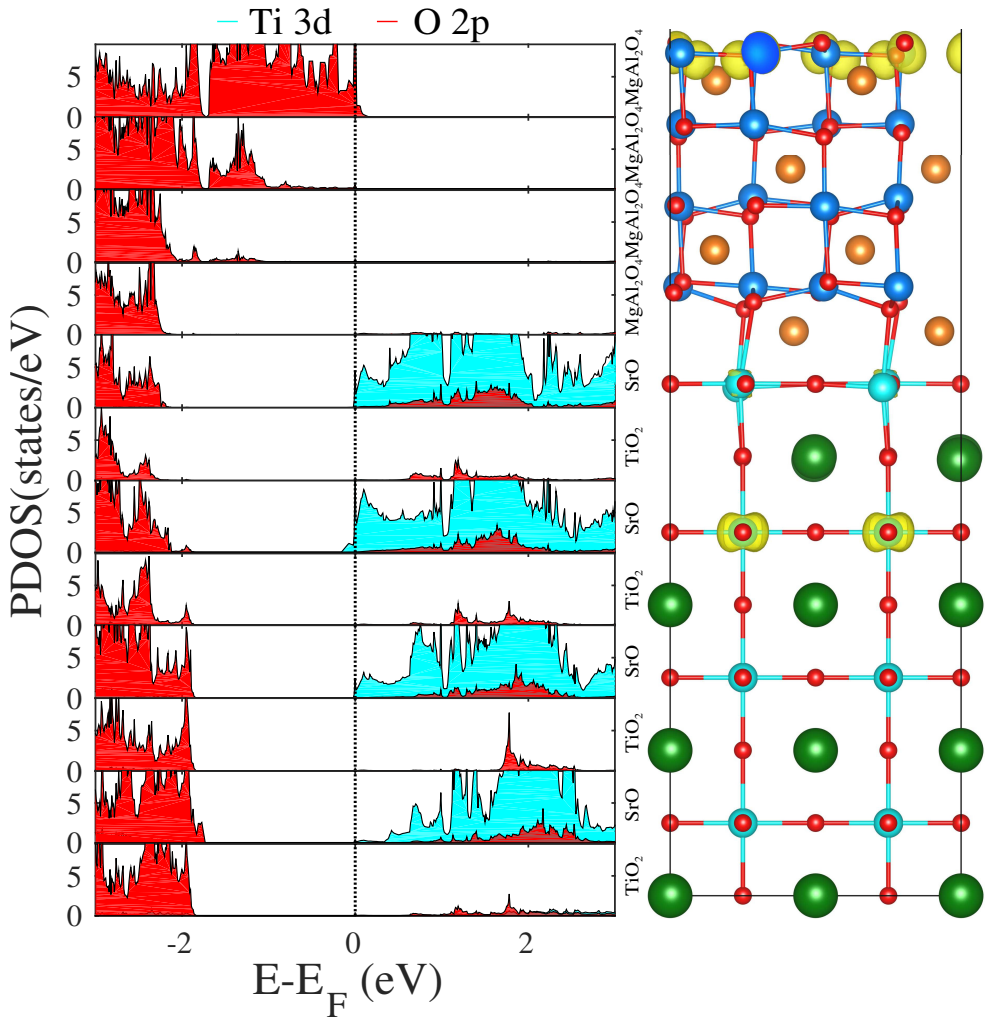

Figure 4.6: Calculated layer-resolved partial DOS for relaxed defect-free MAO/STO heterostructure-based slab, along with the partial charge density isosurfaces for the occupied bands.

adjacent $(Al_3TiO_8)^{-3}$ layers. One electron goes to upper $(Al_3TiO_8)^{-3}$ layer and the other three go to lower $(Al_3TiO_8)^{-3}$ layer, leading to a charge balance. As a result, the interface at Antisite-I is insulating, which well explains the insulating state observed experimentally. In Antisite-II, to keep the charge balance between the interfacial $(Mg_2)^{+4}$ layer and its adjacent two $(Al_2TiO_8)^{-2}$ layers, the interfacial $(Mg_2)^{+4}$ layer only needs to donate two electrons to the lower $(Al_2TiO_8)^{-2}$ layer since the upper $(Al_2TiO_8)^{-2}$ layer can accept two electrons from upper $(Mg_2)^{+4}$ layer. As a result, the interfacial $(Mg_2)^{+4}$ layer donates two remaining electrons that are captured by Ti 3*d*

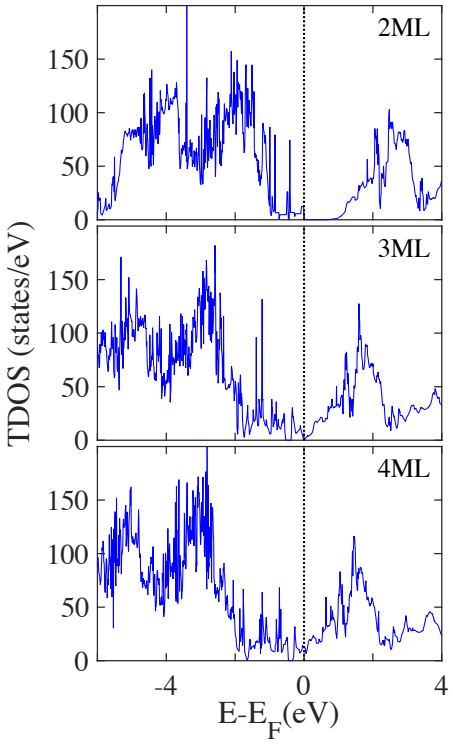

Figure 4.7: Calculated total DOS for MAO/STO HS-based slab with MAO thickness ranging from 2ML to 4ML.

orbitals in the adjacent two $(Al_2TiO_8)^{-2}$ layers, forming the interfacial conducting, see Figure 4.8b. This model can well explain the experimental observations of the coexistence of the 2DEG and antisite defects at the interface.

We next compared the thermodynamic stability between these two antisite defect models by calculating the defect formation energies (E_f^{anti}) for the two antisite models using the following formula:

$$E_f^{anti} = E_{antisite} - E_{pristine} + 2(\Delta\mu_{Ti} + E_{Ti}) - 2(\Delta\mu_{Al} + E_{Al}) \tag{4.2}$$

where $E_{antisite}$ is the total energy for Antisite-I or Antisite-II system and $E_{pristine}$ is the total energy for pristine system; E_i is the total energy of species i; $\Delta\mu_i$ is the relative chemical potential of species i. [48] It is noted that $\Delta\mu_i$ is not fixed but depends on the experimental growth conditions. The Antisite-II model has the same stoichiometry with pristine model, thus E_f^{anti} for Antisite-II

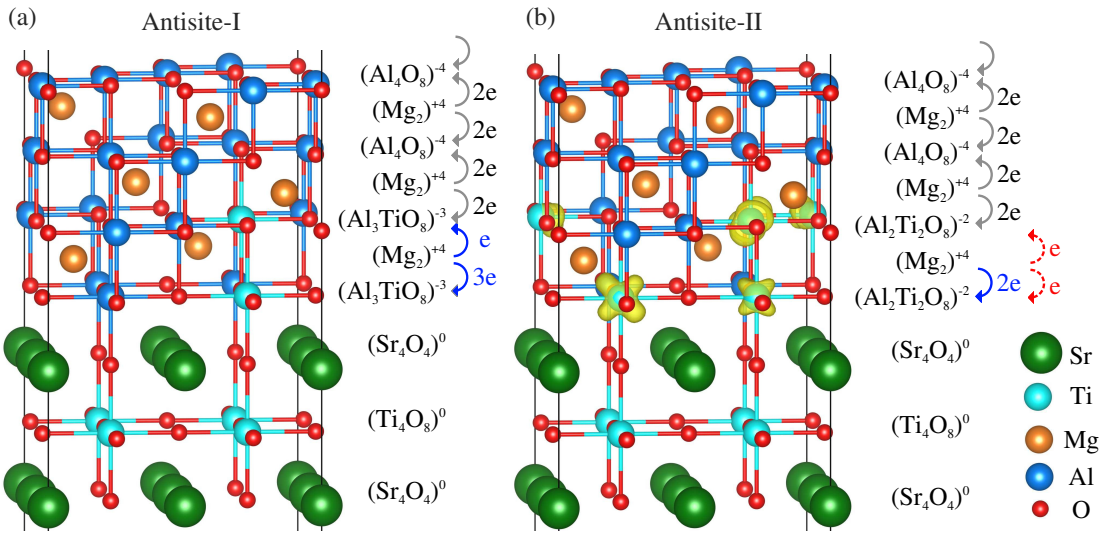

Figure 4.8: Heterostructure models of (a) Antisite-I and (b) Antisite-II along with the charge density projected on the bands forming interfacial conductivity and the charge transfer mechanism. The yellow color around Ti ion in (b) indicates the conducting 3*d* orbital.

system does not depend on $\Delta\mu_i$ and is just its total energy difference with the pristine system. By using the two boundary conditions, i.e., the exclusion of the formation of secondary phases and the experimental annealing process, we could determine the range of $\Delta\mu_{Ti}$ and $\Delta\mu_{Al}$:10.26 eV $\leq \Delta\mu_{Ti} \leq$ 7.25 eV and 7.56 $\leq \Delta\mu_{Al} \leq$ 6.12 eV . By selecting $\Delta\mu_{Ti}$ = 10.26 eV and $\Delta\mu_{Al}$ = 7.56 eV, we calculated the defect formation energies for the antisite models, as shown in Figure 4.9a. The negative formation energy of Antisite-I model indicates the spontaneous formation of Antisite-I in all the samples, and the Antisite-II is energetically unfavorable. This suggests that MAO/STO heterostructure with antisite Ti-Al defects only tends to be insulating rather than metallic, which is in accordance with the insulating MAO/STO interface below the critical thickness but cannot explain the metallicity in thicker films.

It is worth pointing out that in addition to the antisite defects at the interface, recent theoretical studies have shown that there also exist oxygen vacancies on the surface layers, such as the $(AlO_2)^-$ layer in the LAO film, due to the intrinsic charge imbalance. [37, 151, 273, 279, 280] A very recent study has also reported that even with an annealing process under 1 atm oxygen ambient, the oxygen vacancies still exist in the STO/LAO/STO heterostructure. [140]

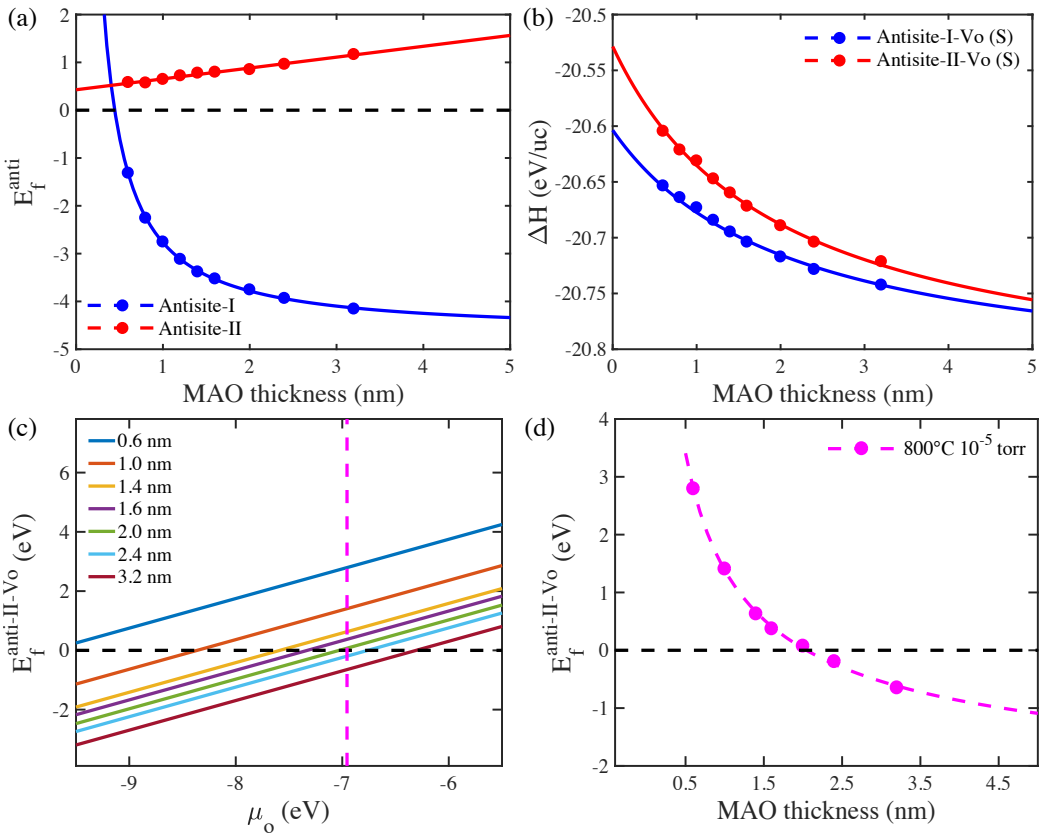

Figure 4.9: (a) Calculated defect formation energy (E_f^{anti}) for Antisite-I and Antisite-II systems as a function of the $MgAl_2O_4$ film thickness. (b) Calculated formation enthalpies (ΔH, eV per unit formula (u.f.) of $MgAl_2O_4$) for Antisite-I-Vo and Antisite-II-Vo models as a function of the $MgAl_2O_4$ film thickness. (c) Formation energy of surface oxygen vacancy in Antisite-II-Vo as a function of oxygen chemical potential at various MAO thicknesses. The magenta dash line denotes the sample deposition condition (T = 800 °C and P = 110^{-5} Torr). (d) Formation energy of surface oxygen vacancy in Antisite-II-Vo as a function of MAO thickness under the materials deposition condition.

Similarly, one may expect that the same case may occur on the surface $(Al_4O_8)^{-4}$ layer in the MAO film. Based on these considerations, we built the MAO/STO heterostructure with both interfacial Ti-Al antisites (Antisite-I and Antisite-II) and surface oxygen vacancies, and studied their energetic stability. For convenient discussion, they are named as Antisite-I-Vo and Antisite-II-Vo, respectively. First, we introduced one oxygen vacancy on the $(Al_4O_8)^{-4}$ surface layer in both antisite defect models and calculated the formation enthalpy (ΔH) of the Antisite-I-Vo and

Antisite-II-Vo models using following equation:

$$\Delta H = E^{V_o}_{antisite} - \sum_{\alpha} n_{\alpha} E_{\alpha} \tag{4.3}$$

where $E^{V_o}_{antisite}$ is the total energy of an antisite model with surface oxygen vacancy, E_{α} is the total energy of atom α in its bulk ground state, and n_{α} is the number of atom α. A low ΔH indicates an energetically more favorable state. We calculated ΔH of the Antisite-I-Vo and Antisite-II-Vo models at different film thicknesses, and fit the data as a function of MAO thickness, see Figure 4.9b. Similar to the case of antisite models without oxygen vacancies, Antisite-I-Vo model is always energetically more favorable than Antisite-II-Vo model, however, the U difference between these two models decreases as the MAO film thickness increases. As the MAO film increases up to 3.2 nm, ΔH difference is about 21 meV, smaller than the thermal excitation-energy at room temperature. This implies that there might be a co-existence of Antisite-I-Vo and Antisite-II-Vo at higher MAO thickness, and because of the existence of Antisite-II defects and surface oxygen vacancies, the system becomes metallic.

To further confirm the formation of Antisite-II-Vo at higher MAO thickness, we present the formation energy of oxygen vacancy of Antisite-II model as a function of oxygen chemical potential at various MAO thickness, in Figure 4.9c. It can be clearly noticed that formation energy decreases with the increase of MAO thickness, which indicates that the formation of oxygen vacancy becomes energetically more favorable with thicker MAO film. From Figure 4.9d under the deposition condition (T = 800 °C and P = 110^{-5} Torr), the formation energy becomes negative for 3 uc MAO film ($\sim$2.4 nm), indicating the spontaneous formation of metallic Antisite-II layer with surface oxygen vacancy. This thickness threshold is close to the experimentally observed critical thickness of 4 uc MAO ($\sim$3.2 nm) and Antisite-II-Vo model can well explain the critical thickness dependent of 2DEG at MAO/STO interface.

4.3 Conclusion

The 2DEG observed in the new type of spinel/perovskite interface can be a model system to evaluate the earlier postulated mechanism for 2DEG in LAO/STO system. Due to the lacking of rare earth elements in MAO, the existence of donor defects by La-Sr cation intermixing could be eliminated firstly. The 2DEG is also unlikely attributed to interfacial oxygen vacancy. The polar catastrophe induced direct charge transfer is also not responsible for the 2DEG in MAO/STO, as the experiment critical thickness is much larger than the calculated value.

By an integrated experimental and computational studying, we demonstrate that when MAO film thickness is less than the critical thickness, the formation of the $(Al_3TiO_8)^{-3}$-$(Mg_2)^{+4}$-$(Al_3TiO_8)^{-3}$ antisite defects (Antisite-I) at the interface leads to an insulating state, while when MAO film thickness is increased above the critical thickness, the formation of $(Al_3TiO_8)^{-2}$-$(Mg_2)^{+4}$-$(Al_3TiO_8)^{-2}$ antisite defect at the interface with surface oxygen vacancies (Antisite-II-Vo) lead to the metallic states. We also confirm that, as the MAO film thickness increases, surface oxygen vacancies promote the existence of Antisite-II-Vo model, particularly when the film thickness is larger than 3 uc (2.4 nm). The symmetry breaking induced polar catastrophe at the interface is still essential for the formation of 2DEG at MAO/STO interface, which transfers the charges from the surface oxygen vacancies to the interface.

In fact, interfacial Ti-Al antisite has been experimentally observed in LAO/STO. [143,179] The earlier reports have also proposed the thickness dependent Ti-Al antisite defects by theoretical calculations in LAO/STO system. [273] The increasing of Ti:Sr ratio with increasing MAO layer thickness calculated from X-ray photoelectron spectroscopy (XPS) measurements implies the formation of Antisite-II at thicker films.

Spinel/perovskite heterostructures in the form of a self-assembled nanocomposite system have received widely attention for the perspective of magnetoelectric coupling. [266, 276]. In a recent theoretical calculation, fully spin-polarized 2DEG was also proposed at the interface

between the two insulating spinel oxides, non-magnetic $MgAl_2O_4$ and ferromagnetic $CoFe_2O_4$. [7] Herein, the epitaxial growth of spinel/perovskite heterostructures in a layer-by-layer model and the conductive interface with high mobility reported in this paper could open a new door for design of the design of the emergent functional devices.

4.4 Acknowledgements

Chapter 4, in full, is currently being submitted for publication of the material "Two-Dimensional Electron Gas at Spinel/Perovskite Interface: Interplay between Polar Catastrophe and Structural Defects", Junfeng Ding, Jianli Cheng, Fatih Dogan, Yang Li, Weinan Lin, Yingbang Yao, Aurelien Manchon, Kesong Yang, and Tom Wu. The dissertation author was the co-author of this paper.

Chapter 5

Polarization Discontinuity Induced 2DEG in Nonpolar/Nonpolar $AHfO_3/SrTiO_3$ (A=Ca, Sr, and Ba) Heterostructures

In Chapter 2-4, we have discussed the polar discontinuity induced 2DEG in polar/nonpolar HS. As we mentioned in Chapter 1, nonpolar/nonpolar oxide HS have also been found to exhibit 2DEG via polarization discontinuity, such as $CaZrO_3/SrTiO_3$. [46, 187] Considering the structural similarity and congeneric character between $CaZrO_3$ and Hf-based perovskite oxides $AHfO_3$ (A=Ca, Sr, and Ba), one may speculate whether a 2DEG can occur in the nonpolar/nonpolar $AHfO_3/SrTiO_3$ HS. In this Chapter, by using first-principles electronic structure calculations, we explored the possibility of producing 2DEG in nonpolar/nonpolar $AHfO_3/SrTiO_3$ HS. Two types of nonpolar/nonpolar interfaces, $(AO)^0/(TiO_2)^0$ and $(HfO_2)^0/(SrO)^0$, each with AO and HfO_2 surface terminations, are modeled, respectively. The polarization domain and resulting interfacial electronic property are found to be more sensitive to the surface termination of the film rather than the interface model. As film thickness increases, an insulator-to-metal transition is found in all the heterostructures with HfO_2 surface termination: for $(AO)^0/(TiO_2)^0$ interfaces, predicted critical

film thickness for an insulator-to-metal transition is about 7, 6, and 3 unit cells for $CaHfO_3/SrTiO_3$, $SrHfO_3/SrTiO_3$, and $BaHfO_3/SrTiO_3$, respectively; for $(HfO_2)^0/(SrO)^0$ interfaces, the critical film thickness is about 7.5, 5.5, and 4.5 unit cells, respectively. In contrast, for the heterostructures with AO surface termination, $CaHfO_3/SrTiO_3$ exhibits a much larger critical film thickness about 11 - 12 unit cells for an insulator-to-metal transition; while $SrHfO_3/SrTiO_3$ and $BaHfO_3/SrTiO_3$ do not show any polarization behavior even film thickness increases up to 20 unit cells. The strain-induced polarization behavior was well elucidated from energy versus polarization profile. This work is expected to stimulate further experimental investigation to the interfacial conductivity in the nonpolar/nonpolar $AHfO_3/SrTiO_3$ HS.

5.1 Introduction

In recent years, artificially fabricated oxide heterostructures (HS) have attracted increasing interests because of their spectacular interfacial materials properties that are absent in their parent bulk oxides. [106] One prototype HS model is the polar/nonpolar $LaAlO_3/SrTiO_3$ system, which displays a high mobility two-dimensional electron gas (2DEG) at its *n*-type $(LaO)^+/(TiO_2)^0$ interface. [190] Later experimental studies have further shown that such a $LaAlO_3/SrTiO_3$ interface system exhibits an electric field tunable insulating-metallic transition, [247] superconductivity, [213] and magnetism. [28, 118]

The formation mechanism of the 2DEG in the $LaAlO_3/SrTiO_3$ HS system is primarily considered to be the polar catastrophe, [179, 182, 184, 190, 255, 257] though the oxygen vacancies, [89, 116, 158, 273] interfacial cation mixing [179, 257, 261] and surface protonation [30, 222] are also proposed to be the possible reasons. The polar catastrophe mechanism can be understood from the layer structure along [001] axis of $LaAlO_3/SrTiO_3$. $LaAlO_3$ can be considered as stacks of alternating polar $(LaO)^+$ and $(AlO_2)^-$ layers along [001] axis, whereas the $SrTiO_3$ consists of neutral $(SrO)^0$ and $(TiO_2)^0$ layers. Accordingly, when $LaAlO_3$ film is stacked on $SrTiO_3$

substrate, a polar discontinuity occurs at the interface, which leads to a charge transfer of half an electron from the charged $(LaO)^{+}$ layer to the neutral $(TiO_2)^0$ layer, and the transferred electrons are captured by Ti 3*d* orbitals, forming the interfacial metallic states. [17, 179, 237] In addition to the polar catastrophe, recent experimental studies suggest that oxygen vacancies play a major role in the interfacial conductivity via redox reactions on the surface of $SrTiO_3$ substrate particularly when the $LaAlO_3$ film is amorphous, [42, 158] which suggests new avenues to design metallic interfaces in perovskite-oxide-based HS.

Analogous to polar discontinuity, 2DEG at the interface of a HS can also be realized via polarization discontinuity between the film and substrate. [46, 107, 187, 237, 252] For instance, it has been found that the spontaneous or strain-induced polarization is responsible for the creation of interfacial metallic states in both conventional semiconductors such as AlGaN/GaN [107] and oxide HS, like ZnO/$Mg_xZn_{1-x}O$. [252] Very recently, Chen *et al.* have reported the 2DEG at the nonpolar/nonpolar $CaZrO_3/SrTiO_3$ HS, which is attributed to the strain-induced polarization in the $CaZrO_3$ film. [46] Later first-principles computational study has confirmed the formation of the 2DEG and reproduced the polarization in the $CaZrO_3$ film. [187] It shows that the in-plane compressive strain in the $CaZrO_3$ film causes a strong enough polarization toward the $SrTiO_3$ substrate, which drives the charge transfer from the $CaZrO_3$ film to the $SrTiO_3$ substrate, and leads to the formation of 2DEG. Moreover, first-principles electronic structure calculations successfully reproduced the critical film thickness for the insulator-to-metal transition, and revealed that the surface termination of the $CaZrO_3$ film could sensitively influence the film critical thickness and the formation of polarization domain. [187]

The Zr-and Hf-based alkaline earth perovskite oxides have shown promising applications in the next-generation capacitors, [121, 163] complementary metal-oxide-semiconductor, [218] and metal-oxide-semiconductor-field-effect-transistor (MOSFET) devices, [217, 229, 230] because of their exceptional physical and electrical properties such as high capacitance densities, high dielectric constants, and low gate leakage current. [97, 162, 170] For instance, a $SrTiO_3$-based

field-effect transistors with $CaHfO_3$ as gate dielectric has been fabricated in a room temperature process in spite of its inferior performance with respet to the Si-based transistors. [229, 230] In particular, among the three types of Hf-based alkaline perovskite oxides $AHfO_3$ (A=Ca, Sr, and Ba), $SrHfO_3$ has a dielectric constant of 21, [121, 162] a wide band gap of 6.1 eV, [218] and extremely low gate leakage current, [97] and is widely investigated as a suitable gate dielectric replacement in the MOSFET devices. [97, 121, 162, 170, 217, 218] As a result, it is of great interests to investigate interfacial properties of $AHfO_3/SrTiO_3$ for the possible applications in the $SrTiO_3$-based transistors. Considering the structural similarity and congeneric character between $CaZrO_3$ and Hf-based perovskite oxides $AHfO_3$ (A=Ca, Sr, and Ba), one may speculate whether a strain-induced polarization can occur in the nonpolar/nonpolar $AHfO_3/SrTiO_3$ HS systems. If it does, then the interfacial conductivity between the gate dielectric ($AHfO_3$) and the semiconductor substrate ($SrTiO_3$) can be tuned by the polarization in the $AHfO_3$ film and thus can be further controlled by the external electrical field, which makes the $AHfO_3/SrTiO_3$ interface structure readily implemented in the electronic devices.

In this work, by using first-principles electronic structure calculations, we explored the possibility of producing a 2DEG at nonpolar/nonpolar $AHfO_3/SrTiO_3$ interface via modeling HS-based slab systems. We found that there exists a critical film thickness to produce a strong enough polarization toward the interface and resulting insulator-to-metal transition. The polarization magnitude as a function of the film thickness, charge transfer mechanism, interfacial electronic states, and charge carrier density were discussed in detail.

5.2 Structural modeling and computational details

At room temperature, $SrTiO_3$ and $BaHfO_3$ bulk compounds crystallize in a cubic phase (space group no. 221, $Pm\bar{3}m$), [65, 190] while $CaHfO_3$ and $SrHfO_3$ crystals exhibit in an orthorhombic structure (space group no. 62, *Pnma*). [65] To model the epitaxially grown

Table 5.1: The experimental and DFT equilibrium lattice parameters a, lattice mismatch f, experimental and calculated band gaps E_g, and calculated VBM (E_v) and CBM (E_c) positions for the bulk $SrTiO_3$, $CaHfO_3$, $SrHfO_3$, and $BaHfO_3$ perovskites oxides.

Compound	Exp. a(Å)	Exp. f(%)	DFT a(Å)	DFT f(%)	Exp. E_g(eV)	DFT E_g(eV)	VBM E_v(eV)	CBM E_c(eV)
$SrTiO_3$	3.905 [190]	0.00	3.935	0.00	3.20 [190]	1.83	0.0	3.20
$CaHfO_3$	3.99 [210]	2.18	4.089	3.90	6.20 [210]	3.81	0.39	5.81
$SrHfO_3$	4.06 [210]	4.66	4.130	4.95	6.10 [218]	3.81	-0.35	5.75
$BaHfO_3$	4.17 [148]	6.71	4.194	6.59	6.00 [61]	3.58	-0.55	5.45

Table 5.2: The experimental and DFT equilibrium lattice parameters a, lattice mismatch f, experimental and calculated band gaps E_g, and calculated VBM (E_v) and CBM (E_c) positions for the bulk $SrTiO_3$, $CaHfO_3$, $SrHfO_3$, and $BaHfO_3$ perovskites oxides.

Compound	O-2s core level		Electrostatic potential	
	VBM (eV)	CBM (eV)	VBM (eV)	CBM (eV)
$SrTiO_3$	0.0	3.20	0.0	3.20
$CaHfO_3$	-0.39	5.81	-0.39	5.81
$SrHfO_3$	-0.35	5.75	-0.25	5.85
$BaHfO_3$	-0.55	5.45	-0.21	5.79

perovskite-based HS, one convenient approach is to treat the non-cubic perovskite compound as pseudo-cubic structure. For example, the perovskite $CaZrO_3$ exhibits in an orthorhombic phase at room temperature, [167] and it can be considered as a pseudo-cubic when it is epitaxially grown on the $SrTiO_3$ substrate with a lattice mismatch of 2.7%. [46, 187] Therefore, in this work, a pseudo-cubic phase of $CaHfO_3$ and $SrHfO_3$ was used to model the $CaHfO_3$/$SrTiO_3$ and $SrHfO_3$/$SrTiO_3$ HS. In Table 5.1, we listed their experimental and DFT equilibrium lattice constant a, lattice mismatch f with the $SrTiO_3$ substrate, experimental and calculated band gaps E_g from standard density functional theory (DFT) calculations. The lattice mismatch f between the $AHfO_3$ film and $SrTiO_3$ substrate is defined as $f = (a_f - a_s)/a_s$, where a_f is the free lattice constant of the epitaxial $AHfO_3$ film in its bulk (unstrained) state and a_s is the lattice constant of the $SrTiO_3$ substrate. The positive values of f indicate that the epitaxial films experience a compressive strain from the $SrTiO_3$ substrate.

We employed a slab model to simulate the $AHfO_3/SrTiO_3$ HS, in which a vacuum layer of 15 Å along the [001] direction was added on the HfO_2- and AO-terminated $AHfO_3$ film, respectively. Thus, two types of surface terminations exist in our model. In principle, there are also two types of interface structures, *i.e.*, AO/TiO_2 and HfO_2/SrO, in the $AHfO_3/SrTiO_3$ HS system. It is worth mentioning that in the case of polar/nonpolar $LaAlO_3/SrTiO_3$ HS system, the two types of interface structures exhibit completely different electron transport properties. [190] The $(LaO)^+/(TiO_2)^0$ interface shows *n*-type conductivity, *i.e.*, the 2DEG at the interface. In contrast, the $(AlO_2)^-/(SrO)^0$ interface was predicted to exhibit *p*-type two-dimensional hole gas according to the polar discontinuity mechanism, but experimentally shows insulating property, which is probably due to the existence of oxygen vacancies. [179, 190, 279] Hence, we modeled both two types of interfaces for the nonpolar/nonpolar $AHfO_3/SrTiO_3$ HS. In each model, the $AHfO_3$ film is stacked on the TiO_2- and SrO-terminated $SrTiO_3$ substrate along the [001] direction, respectively, in which 9 unit cells of the $SrTiO_3$ was used as the substrate. By taking account into the two types of surface terminations of the $AHfO_3$ film, four types of HS models are built and studied in this work.

The Projector Augmented Wave (PAW) [19] potentials was used for treating electron-ion interactions, and the Generalized Gradient Approximation (GGA) parameterized by Perdew-Burke-Ernzerhof (PBE) was applied for the exchange-correlation functional. [200] The cutoff energy for the plane wave expansion was set to 450 eV. Γ-centered *k*-point grids for Brillouin zone sampling were set to $4 \times 4 \times 1$ for ionic relaxation and $10 \times 10 \times 1$ for static calculations, respectively. All crystal structures were optimized by minimizing the atomic forces up to 0.03 eV/Å, and the break condition for the electronic self-consistency loop was assumed for a total energy convergence of less than 10^{-6} eV. All these parameters were found sufficient to converge the energy upon comprehensive test. To resemble the experimental epitaxial material growth, all the ions in the $AHfO_3$ film and the cell parameter perpendicular to the interfacial plane were relaxed, while that along *ab*-plane was fixed as the experimental value of $SrTiO_3$, 3.905 Å, in

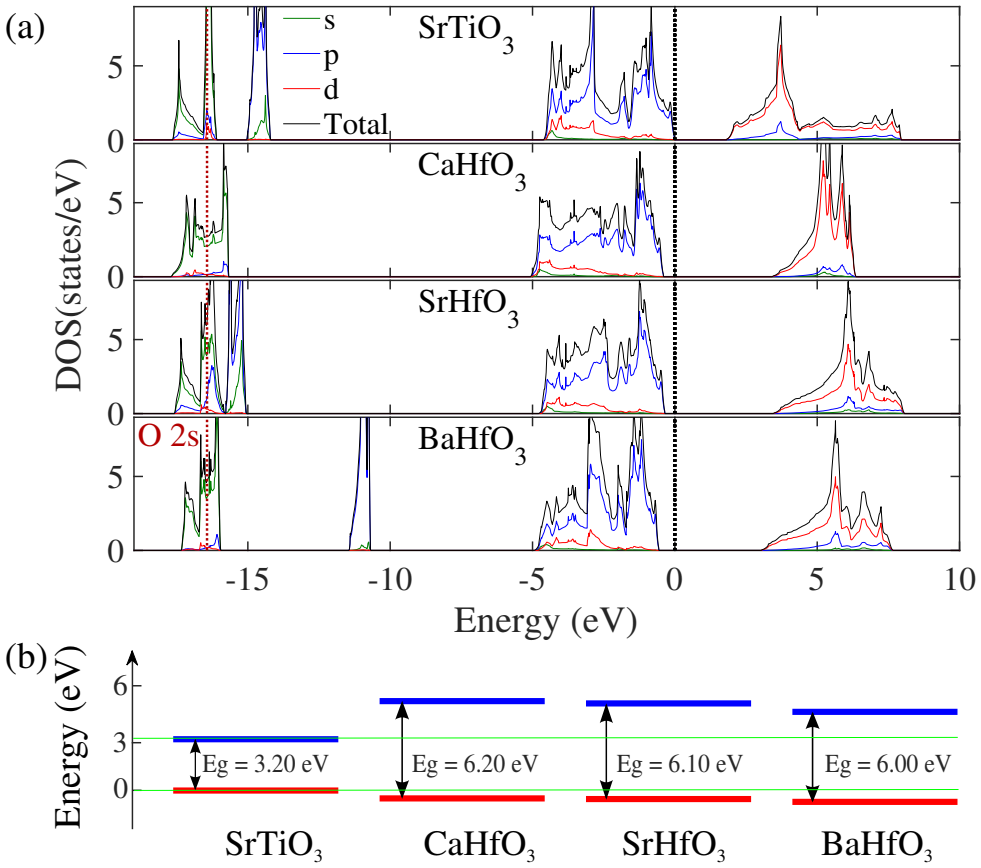

Figure 5.1: (a) Calculated total and partial DOS of $SrTiO_3$, $CaHfO_3$, $SrHfO_3$ and $BaHfO_3$. The DOS is aligned with respect to the O 2*s* state of the $SrTiO_3$. The VBM of $SrTiO_3$ was set as reference (zero) point. (b) The relative VBM (red) and CBM (blue) in each constituent after the band alignment.

the ionic relaxations. [190] The ions in the first two unit cells of $SrTiO_3$ close to the interface were allowed to relax, and the rest ions of the $SrTiO_3$ were frozen to mimic the experimental conditions of the bulk substrate. All the calculations were performed using Vienna *Ab-initio* Simulation Package (VASP). [132, 133]

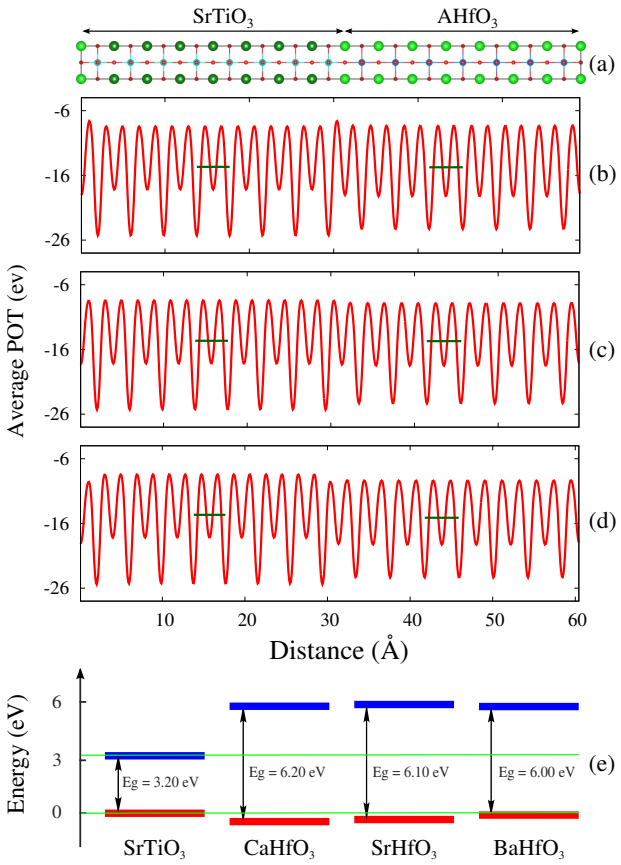

Figure 5.2: (a) Structure diagram for $(AHfO_3)_{7.5}/(SrTiO_3)_{7.5}$ superlattice model (A = Ca, Sr, and Ba). (b)-(d) Planar-averaged electrostatic potential profile as a function of distance along cdirection for $CaHfO_3/SrTiO_3$, $SrHfO_3/SrTiO_3$, and $BaHfO_3/SrTiO_3$ HS models, respectively. The red line denotes the planar-averaged electrostatic potential profile and the green line indicates macroscopic-averaged electrostatic potentials, and the latter is taken at the bulk-like region in each HS model. (e) The relative VBM (red) and CBM (blue) in each constituent after the band alignment.

5.3 Results and discussion

5.3.1 Band alignment

In order to form 2DEG in a HS, one prerequisite is that the conduction band minimum (CBM) of the electron-acceptor material, *i.e.*, $SrTiO_3$ in this work, must be lower than that of the adjacent electron-donor material, *i.e.*, $AHfO_3$, so that the transferred electrons from the donor to the acceptor can reside near the CBM, forming an *n*-type conductivity. To exam whether the

film ($AHfO_3$) and substrate ($SrTiO_3$) can form an appropriate band alignment that supports a desired charge transfer, we calculated their relative band edges by aligning core levels of O ions since both the film and substrate contain O ions, and such an approach was used in our prior study to determine the band alignment of hundreds of perovskite oxides in a high-throughput fashion. [269] In fact, a similar approach by aligning O 1*s* orbitals was also used to determine the band alignment between $LaAlO_3$ and $SrTiO_3$ in a prior study in which an all-electron full-potential augmented plan-wave method was adopted. [198] In contrast, the employed PAW potentials in this work are combined with the frozen-core approximation in the Vienna Ab-initio Simulation Package, [19, 133] and thus the core levels of O ions only consist of O 2*s* orbitals. Therefore, in our study, the O 2*s* orbitals were treated as core levels of O ions to calculate the relative band alignment between the $AHfO_3$ film and $SrTiO_3$ substrate, which is less accurate than the approach using O 1*s* orbital, though. However, as shown below, our approach still yields reasonable results because of the fact that O 2*s* orbitals are less sensitive to the chemical bonding environment than O 2*p* orbitals that mainly contributes to the valence band. In this study, we also improved our algorithm to calculate the band alignment by aligning the center of the weight of O 2*s* states (see the red dashed line in Fig. 5.1a), on the basis of our prior work in which the top of O 2*s* orbitals is used to align the band edges. [269] The valence band maximum (VBM) was then determined from the calculated total density of states (DOS) and accurate CBM was obtained by adding the experimental band gaps on the VBM. The calculated VBM and CBM of these perovskite oxides are listed in Table 5.1 and the relative band edges between the $SrTiO_3$ substrate and $AHfO_3$ film are shown in Fig. 5.1b, in which the VBM of $SrTiO_3$ was set as the reference (zero) point. In addition, to verify these results and to rationalize our approach, we also calculated their band alignments by computing the average electrostatic potentials for the $AHfO_3/SrTiO_3$ HS and the bulk $AHfO_3$ and $SrTiO_3$. [2, 17] The detailed method can be found in a prior work. [17] The calculated band alignment and electrostatic potential profile of each $AHfO_3/SrTiO_3$ HS using the electrostatic potential approach are shown in Fig. 5.2. For a clear compassion, the calculated band

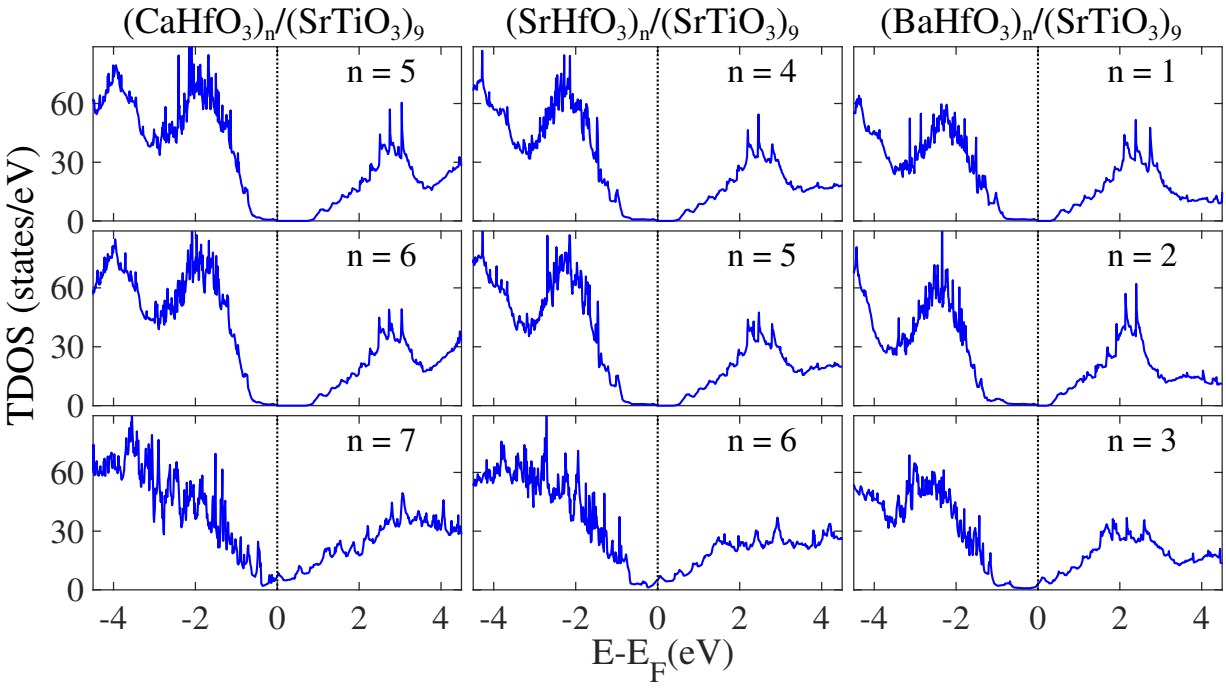

Figure 5.3: Calculated total DOS for $(AO)^0/(TiO_2)^0$ (A = Ca, Sr, and Ba) interface models $(AHfO_3)_n/SrTiO_3$ with HfO_2 surface termination. The vertical dashed line represents the Fermi level in this and each subsequent DOS figures.

edges of $AHfO_3$ and $SrTiO_3$ using the two approaches are shown in Table 6.2. These results show that both two approaches can give relatively close values and more importantly, all the CBM of $AHfO_3$ are higher than that of the $SrTiO_3$. Accordingly, if there exists a charge transfer from the $AHfO_3$ film to the $SrTiO_3$ substrate, their band alignment can guarantee a charge accumulation near the CBM of the $SrTiO_3$, forming *n*-type metallic states.

5.3.2 $(AO)^0/(TiO_2)^0$ interface

We began with analyzing the polarization and electronic property of the $(AO)^0/(TiO_2)^0$ interface model with HfO_2 surface termination. In our previous work, [187] we found that there exists a critical film thickness of about 6 $CaZrO_3$ unit cells to produce a strong enough polarization for an insulator-to-metal transition in the nonpolar/nonpolar $CaZrO_3/SrTiO_3$ HS system, which is well consistent with the experimental observation. [46] Accordingly, one may speculate whether

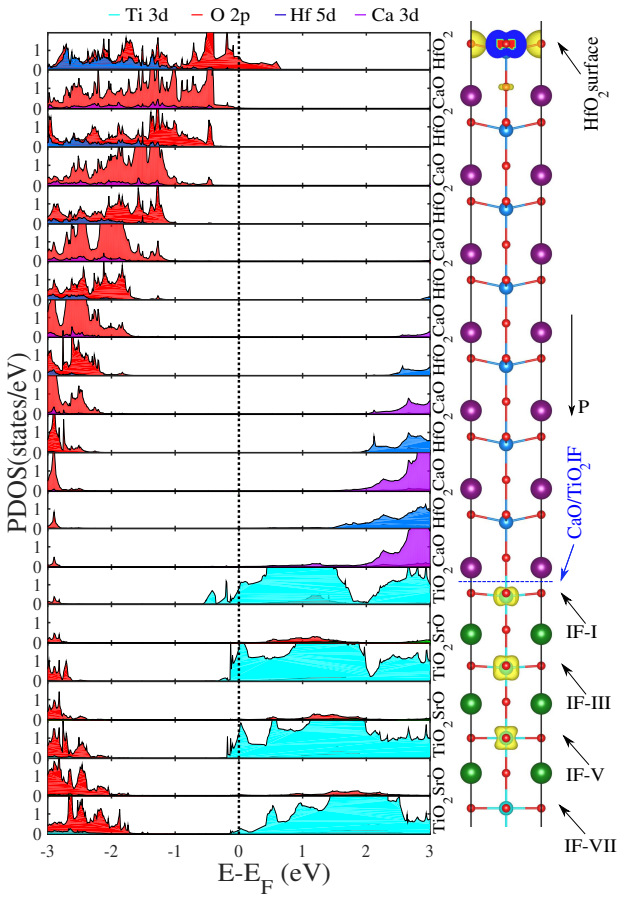

Figure 5.4: Calculated layer-resolved partial DOS for the $(CaO)^0/(TiO_2)^0$ interface model with HfO_2 surface termination in the $(CaHfO_3)_7/SrTiO_3$ HS, along with its charge density plot projected on the bands forming the metallic states.

there exists a similar critical thickness for the $AHfO_3$ film to produce the interfacial metallic states in the $AHfO_3/SrTiO_3$ HS, and if it does, what is the critical film thickness? To answer this question, we modeled the $AHfO_3/SrTiO_3$ with various unit cells of $AHfO_3$ on the TiO_2-terminated $SrTiO_3$ substrate along the [001] direction. For convenience, these HS-based slab models are denoted as $(CaHfO_3)_n/SrTiO_3$, $(SrHfO_3)_n/SrTiO_3$ and $(BaHfO_3)_n/SrTiO_3$, where n represents the number of film unit cells.

Fig. 5.3 shows the calculated total DOS for the relaxed $AHfO_3/SrTiO_3$ HS-based slab models with HfO_2 surface termination. It shows that there does exist a critical film thickness to have an insulator-to-metal transition in these three HS models, though the number of the critical

film unit cells are different. For the $(CaHfO_3)_n/SrTiO_3$ model, it is insulating at $n \leq 6$ and metallic at $n \geq 7$. For the $(SrHfO_3)_n/SrTiO_3$ model, it exhibits an insulating behavior at $n \leq 5$ and metallic behavior at $n \geq 6$. For the $(BaHfO_3)_n/SrTiO_3$ model, the system shows an insulating property at $n \leq 2$ and conducting property at $n \geq 3$. In other words, the required critical film thickness for the three HS models is 7, 6, and 3 unit cells of the $CaHfO_3$, $SrHfO_3$, and $BaHfO_3$, which decreases in the order of $CaHfO_3 > SrHfO_3 > BaHfO_3$. Interestingly, this order is opposite to that of the lattice mismatch f between these film oxides and the $SrTiO_3$ substrate, *i.e.*, $CaHfO_3 < SrHfO_3 < BaHfO_3$.

To understand the origin of metallic behavior in the $AHfO_3/SrTiO_3$ HS models, we calculated their layer-resolved DOS and three-dimensional (3D) charge density projected on the conducting bands for the $(CaHfO_3)_7/SrTiO_3$, $(SrHfO_3)_6/SrTiO_3$ and $(BaHfO_3)_3/SrTiO_3$, respectively. Herein, we took the $(CaHfO_3)_7/SrTiO_3$ HS model as an example to discuss its conducting mechanism, see Fig. 5.4. For the other two HS models, their layer-resolved DOS and 3D charge density plots are shown in Fig. S2 for $(SrHfO_3)_6/SrTiO_3$ and Fig. S3 for $(BaHfO_3)_3/SrTiO_3$ in the Supporting Information. For the $CaHfO_3/SrTiO_3$ HS model, the calculated layer-resolved DOS shows that O $2p$ states move to higher energy states from the interface layer to the surface layer of $CaHfO_3$ film, and at the surface HfO_2 layer, some O $2p$ states cross the Fermi level and become unoccupied. This indicates that there exists a net electrical field in the $CaHfO_3$ film that causes the upward shift of the electrostatic potential. As discussed below, this net electrical field also leads to the charge transfer from the $CaHfO_3$ film to the $SrTiO_3$ substrate, resulting in the formation of conducting states at the interface. The calculated partial DOS shows that these conducting states are mainly contributed by the first three TiO_2 layers (IF-I, IF-III, and IF-V) of the $SrTiO_3$ substrate, indicating the formation of 2DEG at the interface.

The charge transfer mechanism can be well elucidated from 3D charge density plot projected on the selected bands forming the interfacial and surface metallic states, see Fig. 5.4. Three features regarding the polarization-induced interfacial conductivity can be found as below.

First, the calculated charge density plot clearly shows that the interfacial conducting states mostly come from three sequential TiO_2 layers close to the interface, exhibiting the same pattern with the layer-resolved DOS plot. Second, there exists a significant downward movement of the Ca^{2+} and Hf^{4+} cations toward the interface, which is induced by the compressive strain exerted on the $CaHfO_3$ film because of the lattice mismatch between the film and substrate; and this substantial displacement between the cations and anions causes a strong polarization in the $CaHfO_3$ film. Third, the relative displacement between the Sr^{2+}/Ti^{4+} cations and O^{2-} anions in the $SrTiO_3$ substrate is much less than that in the $CaHfO_3$ film, which results in a polarization discontinuity between the film and substrate. As a consequence of these features, the strong polarization in the $CaHfO_3$ film produces an internal electrical field, which drives the charge transfer from the HfO_2 surface layer in the $CaHfO_3$ film to the interfacial TiO_2 layers in the $SrTiO_3$ substrate and thus leads to the formation of 2DEG. The same charge transfer mechanism also applies in the $SrHfO_3/SrTiO_3$ and $BaHfO_3/SrTiO_3$ HS models, see Fig. S2 and Fig. S3 of the Supporting Information, though these two systems require less film thickness than $CaHfO_3/SrTiO_3$ model to produce the interfacial conducting states.

By following the similar procedure, we investigated the electronic property of $(AO)^0/(TiO_2)^0$ interface model with AO surface termination. Our results indicate that the required critical film thickness for the formation of metallic states in $(CaHfO_3)_n/SrTiO_3$ HS is 11.5 unit cells, which is higher than that with HfO_2 surface termination (7 unit cells). By analyzing its layer-resolved DOS and 3D charge density plot projected on the bands forming the metallic states near the Fermi energy (see Fig. S4, we found that there also exists a strong enough polarization toward the interface in the $CaHfO_3$ film, leading to the charge transfer and formation of 2DEG at the interface. Surprisingly, the $(SrHfO_3)_n/SrTiO_3$ and $(BaHfO_3)_n/SrTiO_3$ HS models (with SrO and BaO surface termination, respectively) do not exhibit any polarization behavior even if n increases up to 20, which indicates that the latter two models are unlikely to form an energetically favorable polarization state.

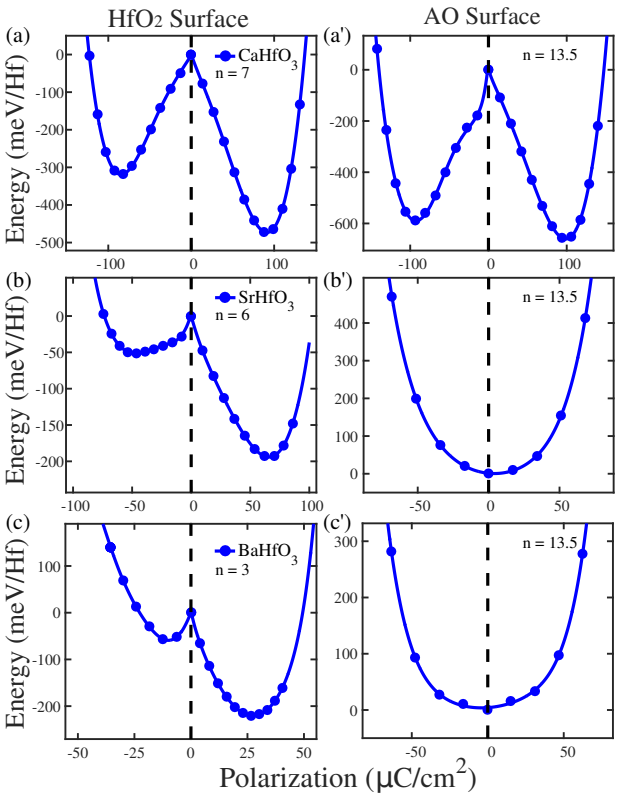

Figure 5.5: Calculated total energy as a function of averaged polarization for (a, a') $(CaHfO_3)_n/SrTiO_3$, (b, b') $(SrHfO_3)_n/SrTiO_3$, and (c, c') $(BaHfO_3)_n/SrTiO_3$ HS models with $(AO)^0/(TiO_2)^0$ interface. The left panel indicates the HS model with HfO_2 surface termination, and the right panel indicates the HS model with AO surface termination. In this and the subsequent energy versus polarization profiles, the positive and negative polarization indicate the polarization direction toward the interface and surface of the film, respectively. The total energy of the non-polarized centrosymmetric HS model was taken as reference (zero point) energy.

Next, to understand the origin of the in-plane strain induced polarization behavior in these $(AO)^0/(TiO_2)^0$ interface models, we calculated their total energies as a function of the averaged polarization over the $AHfO_3$ layers for each interface model with HfO_2 and AO surface terminations, respectively, shown in Fig. 5.5. The equation for calculating the polarization strength will be discussed later. For the interface models with HfO_2 surface termination (left panel), it shows that the energy versus polarization profile is asymmetric, see Fig. 5.5a, b and c. The minimum of positive polarization corresponds to the stable polarization state toward the interface, which reflects the charge density plot in Fig. 5.4. The minimum of negative

polarization, on the other hand, implies a meta-stable polarization toward the surface. In this case, the polarization produces an internal electrical field that drives the charge transfer from the $SrTiO_3$ substrate to the surface of the $AHfO_3$ film. As a proof concept, we took $CaHfO_3/SrTiO_3$ as an exemplary system and calculated its layer-resolved DOS along with charge density plot in Fig. S5 of the Supporting Information. It shows that the polarization leads to a two-dimensional hole gas in the interfacial region, and transferred electrons occupy Hf 5*d* orbitals on the surface, forming *n*-type surface conductivity. The interface models with AO surface termination are shown in the right panel. For the $CaHfO_3/SrTiO_3$ HS model, a double-well asymmetric energy versus polarization profile is formed, shown in Fig. 5.5a'. This can well explain the formation of the polarization domain toward the interface in the $CaHfO_3/SrTiO_3$ HS model. In contrast, for the $SrHfO_3/SrTiO_3$ and $BaHfO_3/SrTiO_3$ HS models, their energy versus polarization curve is parabolic, implying that there are no stable polarization states in these two models.

5.3.3 $(HfO_2)^0/(SrO)^0$ interface

In this section, we studied the polarization and electronic property of $(HfO_2)^0/(SrO)^0$ interface model with HfO_2 surface termination for the three $AHfO_3/SrTiO_3$ HS models. To explicitly demonstrate the required critical thickness to produce the interfacial metallic states, we calculated the total DOS for the $(AHfO_3)_n/SrTiO_3$ model with various film unit cells, see Fig. S6 in the Supporting Information. Our results show that the critical film thickness for the insulator-to-metal transition is n = 7.5, 5.5, and 4.5 for the $CaHfO_3/SrTiO_3$, $SrHfO_3/SrTiO_3$, and $BaHfO_3/SrTiO_3$, respectively. For $SrHfO_3/SrTiO_3$, with respect to $(SrO)^0/(TiO_2)^0$ interface, $(HfO_2)^0/(SrO)^0$ interface has a 0.5 less unit cell in the film, and thus it would take a 0.5 less unit cell to achieve necessary polarization (5.5 vs. 6). For $CaHfO_3/SrTiO_3$ and $BaHfO_3/SrTiO_3$, one can infer that the driving force for polarization from $(HfO_2)^0/(SrO)^0$ interfaces is weaker than that from $(CaO)^0/(TiO_2)^0$ and $(BaO)^0/(TiO_2)^0$ so that polarization occurs slower and thicker film is required for the insulator-to-metal transition (7.5 vs. 7 for $CaHfO_3/SrTiO_3$ and 4.5 vs. 3 for

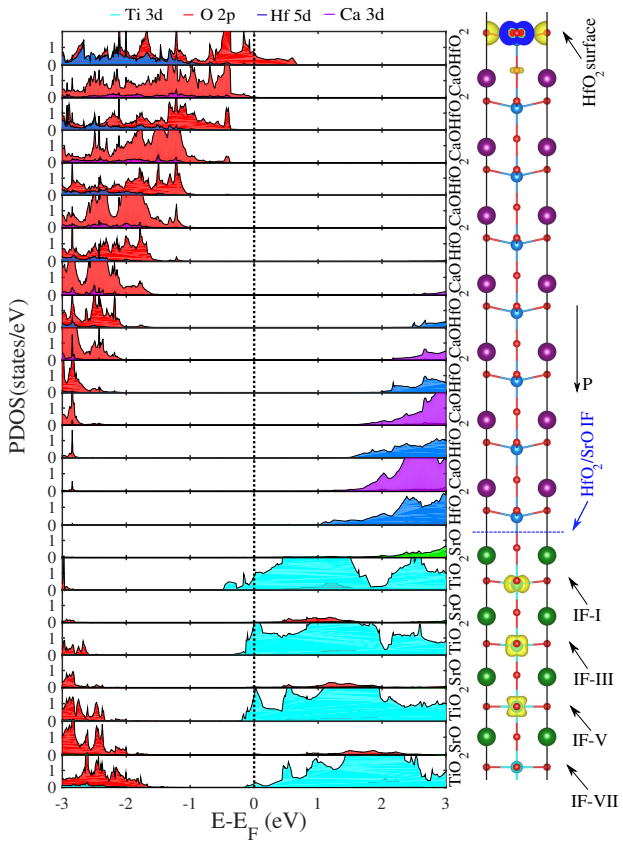

Figure 5.6: Calculated layer-resolved partial DOS for the $(HfO_2)^0/(SrO)^0$ interface model with HfO_2 surface termination in the $(CaHfO_3)_{7.5}/SrTiO_3$ HS, along with its charge density plot projected on the bands forming the metallic states near the Fermi energy.

$BaHfO_3/SrTiO_3$). This hypothesis can be explained from the surface and interface termination of these HS models. That is, in the $(HfO_2)^0/(SrO)^0$ interface model with HfO_2 surface termination, the film has a symmetrical HfO_2...HfO_2 structure, while in the $(AO)^0/(TiO_2)^0$ interface model (with HfO_2 surface termination), the film has an AO...HfO_2 structure. This fact determines that the polarization in the asymmetrical AO...HfO_2 structure occurs much quicker than the symmetrical HfO_2...HfO_2 structure under the same compressive strain.

As in the case of $(AO)^0/(TiO_2)^0$ interface model, the interfacial conductivity in the $(HfO_2)^0/(SrO)^0$ model is also caused by the polarization-driven charge transfer from the surface HfO_2 layer to the interfacial TiO_2 layers. A direct observation of this mechanism can be illustrated by the layer-resolved DOS and charge density projected on the metallic states for

the $CaHfO_3/SrTiO_3$ model, see Fig. 5.6. From its relaxed geometrical structure in the charge density plot, one can clearly see that there exists a polarization toward the $SrTiO_3$ substrate in the $CaHfO_3$ film. In contrast, the $SrTiO_3$ substrate exhibits a much weaker polarization than the $CaHfO_3$ film, and thus a polarization discontinuity occurs at the interface. As a result, the strain-induced polarization in the $CaHfO_3$ film is able to lead to a charge transfer from the surface HfO_2 layer of the film to the interfacial TiO_2 layers of the $SrTiO_3$ substrate. The transferred electrons are mainly captured by the Ti $3d$ orbitals in the first three interfacial TiO_2 layers of the $SrTiO_3$ substrate, showing n-type conducting property and 2DEG character, and meanwhile, the charge transfer produces partially unoccupied O $2p$ states at the HfO_2 surface of the film $CaHfO_3$, see Fig. 5.6. Similarly, when the film is thicker than the required critical thickness, the polarization-driven charge transfer also appears in the $SrHfO_3/SrTiO_3$ and $BaHfO_3/SrTiO_3$ HS models, whose corresponding DOS and charge density plots are shown in Fig. S7 and Fig. S8 in the Supporting Information, respectively.

For a comprehensive comparison among various types of interface models, we also studied the polarization behavior and electronic states for the $(HfO_2)^0/(SrO)^0$ interface models with AO surface termination. Similar to the case of $(AO)^0/(TiO_2)^0$ interface model (with AO surface termination), the insulator-to-metal transition only occurs in the $(CaHfO_3)_n/SrTiO_3$ HS model at $n \geq 11$ (see Fig. S9). In contrast, the $(SrHfO_3)_n/SrTiO_3$ and $(BaHfO_3)_n/SrTiO_3$ HS models remain insulating even if n increases up to 20.

To better elucidate the polarization behavior in the $(HfO_2)^0/(SrO)^0$ interface models, we plotted their energy versus polarization profiles in Fig. 5.7. Similar to the case of $(AO)^0/(TiO_2)^0$ interface models (with HfO_2 surface terminations), the $(HfO_2)^0/(SrO)^0$ interface models with HfO_2 surface termination also display an asymmetric profile, see Fig. 5.7a, b, and c. The energetically favorable polarization points toward the interface while the meta-stable polarization points toward the surface. In contrast, for the $(HfO_2)^0/(SrO)^0$ interface models with AO surface terminations (right panel), only the $CaHfO_3/SrTiO_3$ HS model exhibits an asymmetric polarization

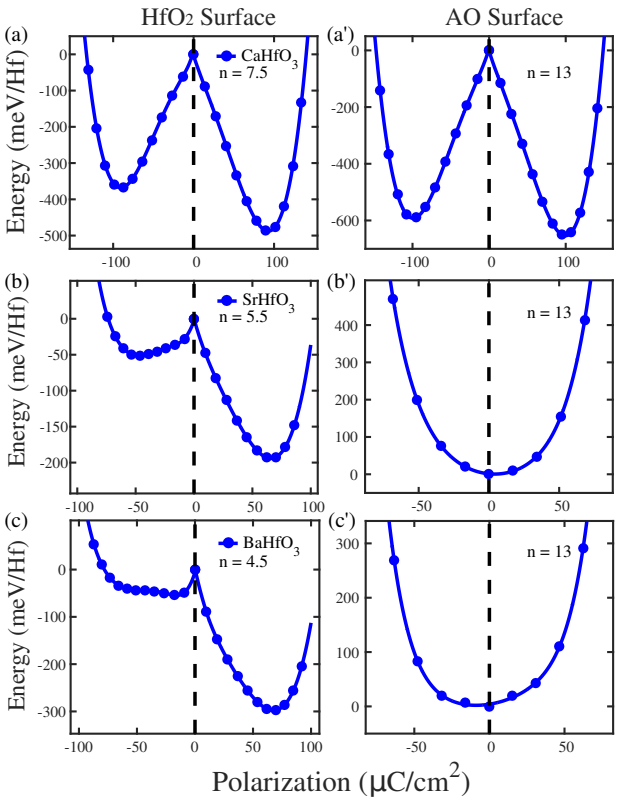

Figure 5.7: Calculated total energy as a function of averaged polarization for (a, a') $(CaHfO_3)_n/SrTiO_3$, (b, b') $(SrHfO_3)_n/SrTiO_3$, and (c, c') $(BaHfO_3)_n/SrTiO_3$ HS models with $(HfO_2)^0/(SrO)^0$ interface. The left panel indicates the HS model with HfO_2 surface termination, and the right panel indicates the HS model with AO surface termination.

profile, while the $SrHfO_3/SrTiO_3$ and $BaHfO_3/SrTiO_3$ display a parabolic curve for the energy versus polarization profile. This indicates that the $SrHfO_3/SrTiO_3$ and $BaHfO_3/SrTiO_3$ HS models with SrO (BaO) surface terminations cannot form a polarization.

As discussed above, the polarization domain is very sensitive to the surface termination of the film for both $(AO)^0/(TiO_2)^0$ and $(HfO_2)^0/(SrO)^0$ interfaces. This behavior can be explained from their surface structures. For the models with HfO_2 surface termination, the surface HfO_5 unit is half-octahedra-like structure. Under the compressive strain, the surface HfO_5 unit will reach an equilibrium state by elongating the Hf-O bond in the ab-plane and meanwhile shrinking the Hf-O bond along the c-axis, thus leading to a polarization toward the interface. In contrast, for the models with AO surface termination, there does not exist a half-octahedra-like AO_5 structure

on the surface, and the distance between the A and O ions are much longer than Hf-O bond. Hence, it is less likely to form a structural polarization in the film as compared to the model with HfO_2 surface termination. The exception is for the $CaHfO_3/SrTiO_3$, in which Ca ion is much smaller and Ca-O bond length is much shorter than Sr-O and Ba-O bond, and thus the surface CaO layer will undergo a more severe structural distortion and resulting polarization under the compressive strain.

5.3.4 Polarization and interfacial electron carrier density

To quantitatively analyze the relationship between the polarization magnitude and the thickness of $AHfO_3$ film, we took the $(HfO_2)^0/(SrO)^0$ interface as an example and calculated the polarization P in each $AHfO_3/SrTiO_3$ HS model as a function of the number of $AHfO_3$ film unit cells (n) using the following formula: [152, 278]

$$P = \frac{e}{\Omega} \sum_{i=1}^{N} Z_i^* \delta z_i \tag{5.1}$$

in which Ω is the volume of $AHfO_3$ film, N is the number of cations in the film, Z_i^* is the Born effective charge for each cation, δz_i is the relative displacement between the i-th cation (A/Hf) and the anion (O) in the corresponding AO and HfO_2 plane, that is, $\delta z_i = z_O - z_{A/Hf}$. This method works well because the polarization in the (001)-oriented perovskite film is mostly caused by the relative displacement between the cations and anions in each AO and HfO_2 layer.

The calculated average displacements between A cations and O anions (δz_{A-O}) and between Hf cations and O anions (δz_{Hf-O}) as a function of n are shown in Fig. 5.8a and 5.8b, respectively. A positive value of δz is defined as the A^{2+}/Hf^{4+} cations in the $AHfO_3$ films pointing toward the interface. The results clearly show that when n is less than the critical film unit cells (7.5 for $CaHfO_3/SrTiO_3$, 5.5 for $SrHfO_3/SrTiO_3$, and 4.5 for $BaHfO_3/SrTiO_3$), the relative displacements are nearly negligible, indicating no polarization. When the film thickness

Table 5.3: Calculated Born effective charges of the cubic $CaHfO_3$, $SrHfO_3$, and $BaHfO_3$. Z^*(A) and Z^*(Hf) refer to Born effective charge of A (Ca, Sr, and Ba) and Hf cations, respectively. Z^*_{AO} (O) and $Z^*_{HfO_2}$ (O) refer to Born effective charge of O ions in the AO and HfO_2 planes, respectively.

Compound	Z^* (A)	Z^* (Hf)	Z^*_{AO} (O)	$Z^*_{HfO_2}$ (O)
$CaHfO_3$	2.63	5.51	-4.43	-1.85
$SrHfO_3$	2.58	5.72	-4.58	-1.86
Ref. [95]	2.58	5.73	-4.55	-1.87
$BaHfO_3$	2.75	5.82	-4.55	-2.01
Ref. [271]	2.77	5.92	-4.42	-2.11

reaches the critical thickness, δz increases drastically and as n further increases, δz changes slightly. The calculated Z^*_i are listed in Table 5.3, which are in good agreement with the previous results from DFT calculations. [95, 271] The estimated polarization in each $AHfO_3/SrTiO_3$ HS model is shown in Fig. 5.8c. The polarization is negligible until the $AHfO_3$ film thickness reaches its critical thickness. The calculated polarization is about 90 $\mu C/cm^{-2}$ for $(CaHfO_3)_n/SrTiO_3$ at n = 7.5, 58 $\mu C/cm^{-2}$ for $(SrHfO_3)_n/SrTiO_3$ at n = 5.5, and 62 $\mu C/cm^{-2}$ for $(BaHfO_3)_n/SrTiO_3$ at n = 4.5. As a comparison, calculated average anion-cation displacement, polarization, and interfacial charge carrier density for the $(AO)^0/(TiO_2)^0$ interface model with HfO_2 surface termination was shown in Fig. S10 of the Supporting Information.

To further analyze the dependence of interfacial electron density on the film thickness, we calculated their interfacial electron density as a function of film unit cells, shown in Fig. 5.8d. The interfacial electron density was calculated by integrating partially occupied Ti 3d orbitals at the IF-I TiO_2 layer. [181, 185, 186] Our results show that the polarization magnitude P and interfacial electron density n share nearly the same pattern as n increases. As the film thickness increases up to the critical thickness in each model, the estimated charge density is about $7 \times 10^{13} cm^{-2}$ for both $BaHfO_3/SrTiO_3$ and $SrHfO_3/SrTiO_3$ HS model. The $CaHfO_3/SrTiO_3$ HS model exhibits the highest charge density among the three systems, about $1.1 \times 10^{14} cm^{-2}$ carrier density. This is because $CaHfO_3/SrTiO_3$ HS model has a much larger polarization than $BaHfO_3/SrTiO_3$ and

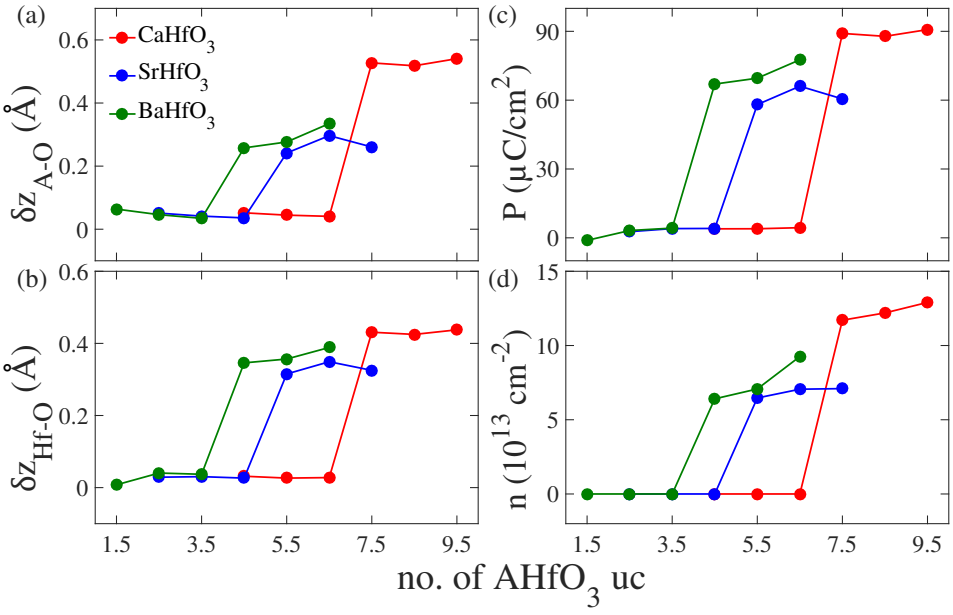

Figure 5.8: Calculated average anion-cation displacement (δz) in the corresponding AO (a) and HfO_2 (b) planes, along with the average polarization of the $AHfO_3$ film (c) and interfacial charge carrier density (d) at each $AHfO_3/SrTiO_3$ HS with $(HfO_2)^0/(SrO)^0$ interface and HfO_2 surface.

$SrHfO_3/SrTiO_3$ HS systems at their corresponding critical film thickness. This indicates that a strong polarization in the film can drive more electrons to the interface and thus increase 2DEG carrier density at the interface.

5.4 Conclusion

By using first-principles electronic structure calculations, we explored the possibility of producing interfacial conductivity via strain-induced polarization discontinuity in the $AHfO_3/SrTiO_3$ (A = Ca, Sr, and Ba) HS-based slab systems. Two types of nonpolar/nonpolar interface models, including $(AO)^0/(TiO_2)^0$ and $(HfO_2)^0/(SrO)^0$ models, each with HfO_2 and AO surface terminations were modeled. The polarization as a function of the film thickness, charge transfer mechanism, interfacial electronic states and charge carrier density were discussed. The following conclusions were derived:

(i) For the $(AO)^0/(TiO_2)^0$ interface model, when the $AHfO_3$ film is terminated with HfO_2, there exists a critical film thickness for the insulator-to-metal transition. The required critical film thickness is n = 7, 6, and 3 for $(CaHfO_3)_n/SrTiO_3$, $(SrHfO_3)_n/SrTiO_3$, and $(BaHfO_3)_n/SrTiO_3$, respectively. When the $AHfO_3$ film is terminated with AO, only the $(CaHfO_3)_n/SrTiO_3$ HS model exhibits an insulator-to-metal transition at n = 11.5, while the other two models, $SrHfO_3/SrTiO_3$ and $BaHfO_3$, do not even if n increases up to 20.

(ii) For the $(HfO_2)^0/(SrO)^0$ interface model, when the $AHfO_3$ film is terminated with HfO_2, there exists a critical film thickness for the insulator-to-metal transition at n = 7.5, 5.5, and 4.5 for $(CaHfO_3)_n/SrTiO_3$, $(SrHfO_3)_n/SrTiO_3$, and $(BaHfO_3)_n/SrTiO_3$, respectively. When the $AHfO_3$ film is terminated with AO, only the $(CaHfO_3)_n/SrTiO_3$ HS model exhibits an insulator-to-metal transition at n = 11, while the other two models do not even if n increases up to 20.

(iii) Insulator-to-metal transitions in the HS models can be explained from the polarization discontinuity between the $AHfO_3$ film and $SrTiO_3$ substrate. The polarization drives charge transfer from $AHfO_3$ film to $SrTiO_3$ substrate and results in interfacial conductivity.

In short, our computational study unraveled the relationship between the lattice mismatch, polarization, and interfacial electronic states in these nonpolar/nonpolar $AHfO_3/SrTiO_3$ HS systems. It provides another possible approach to create 2DEG via strain-induced polarization discontinuity in the nonpolar/nonpolar perovskite oxide heterostructures.

5.5 Acknowledgements

Chapter 5, in full, is a reprint of the material "First-Principles Prediction of Two-Dimensional Electron Gas Driven by Polarization Discontinuity in Nonpolar/Nonpolar $AHfO_3/SrTiO_3$ (A=Ca, Sr, and Ba) Heterostructures" as it appears in ACS Applied Materials and Interfaces. Jianli Cheng, Safdar Nazir, Kesong Yang, 8, 31959-31967, 2016. The dissertation author was the primary investigator and author of this paper.

Chapter 6

High-Throughput Design of 2DEG in Nonpolar/Nonpolar Perovskite Oxide Heterostructures

In Chapter 5, we have explored the possibility of realizing a 2DEG via strain-induced polarization discontinuity in the $AHfO_3/SrTiO_3$ (A = Ca, Sr, and Ba) HS. Similarly, the Ti-involved HS also show the discontinuous polarization across the heterointerface, such as $PbTiO_3/SrTiO_3$ and $BaTiO_3/SrTiO_3$. [58, 70] Therefore, considering the formation of a polarization discontinuity in the nonpolar/nonpolar oxide HS and its ability to create a robust interfacial 2DEG, we expect that there could be potentially more nonpolar/nonpolar perovskite oxide HS that can produce 2DEG. In this Chapter, we show that by using high-throughput first-principles calculations and a group of effective materials descriptors based on bulk perovskite materials, we are able to rapidly design more than 300 candidate 2DEG systems based on nonpolar/nonpolar perovskite heterostructures (HS). These HS are built from 34 nonpolar piezoelectric perovskite oxides that can show polarization behavior under epitaxial compressive strain and can be further divided into six groups of materials based on B-site elements: Ti-, Zr-, Hf-, Si-, Ge-, and Sn-based oxides.

By taking one compound as the substrate from each group and building all the possible HS with an appropriate lattice mismatch $0 < f < 6\%$, we have carried out comprehensive first-principles calculations to verify the formation of 2DEG in these HS. It has been found that a stable polarization and interfacial 2DEG exist in most of the selected HS. This work demonstrates an efficient way to perform high-throughput design of perovskite-oxide-based functional materials.

6.1 Introduction

Artificial interfaces between two perovskite oxides provide an ideal platform to tailor material properties by manipulating interplay between electronic and lattice degrees of freedom. [79, 212, 275] In particular, recent progress in thin film growth techniques has greatly stimulated interfacial engineering of complex oxide heterostructures (HS) into a flourishing field, giving unprecedented access to emerging materials properties for enhanced functionality and device applications. [24, 161] In principle, the novel material properties at oxide interfaces are a consequence of local symmetry breaking, charge transfer, electrostatic coupling, frustration, or epitaxial strain at the heterointerface. [282] For instance, two-dimensional electron gas (2DEG), quantum hall effect, [168, 251] superconductivity, [213] magnetism, [118] nanoscale-controlled metal-insulator transition, [47] and spin-to-charge conversion [147] have been observed at perovskite-oxide-based interfaces. Among these emerging materials properties, the 2DEG at the interface of two wide-band-gap perovskite insulators has been an active research topic in the past decade not only from the fundamental physics perspective but also because of its potential applications in the nanoelectronics. [10, 187, 190, 255, 269]

According to interfacial configurations of perovskite oxide HS, there are essentially three types of interfaces that can form the 2DEG. [255] The first one is polar/nonpolar interface, such as $(LaO)^{+}/(TiO_2)^{0}$ in the $LaAlO_3/SrTiO_3$ HS. The 2DEG formation mechanism in $LaAlO_3/SrTiO_3$ is primarily attributed to the intrinsic electronic reconstruction, *i.e.*, polar

catastrophe. [190, 257] Here and hereafter, for convenience, by following the denomination of polar/nonpolar $(LaO)^{+}/(TiO_2)^{0}$ interface in the $LaAlO_3/SrTiO_3$ HS, we define the charged layer of a perovskite oxide along [001] direction like $(LaO)^{+}$ as polar and the neutral layer like $(TiO_2)^{0}$ as nonpolar. Accordingly, the corresponding bulk oxides are considered as polar or nonpolar. Other mechanisms, such as the oxygen vacancies, [158, 273] interface cation mixing, [179] and internal structural deformation, [196, 220] have also been proposed to explain the origins of the interfacial 2DEG conductivity. Despite the controversy, the polar/nonpolar interfacial configuration plays a critical role in forming the interfacial conductivity. For example, in addition to the intensively studied $LaAlO_3/SrTiO_3$ HS, other polar/nonpolar HS have also been synthesized and found to host the 2DEG as well, such as $LaTiO_3/SrTiO_3$, [16] $GdTiO_3/SrTiO_3$ [176] and $NdGaO_3/SrTiO_3$. [83]

The second interfacial configuration to produce 2DEG in the perovskite oxide HS is polar/polar interface such as $(LaO)^{+1}/(TaO_2)^{+1}$ in the $LaAlO_3/KTaO_3$. [255, 275, 281] In the computational side, by using first-principles electronic structures calculations, we have proposed to create 2DEG in the polar/polar perovskite oxide HS based on the $LaAlO_3/A^{+}B^{5+}O_3$ (A = Na and K, B = Nb and Ta). [255] Its interfacial conductivity is attributed to two donor layers, *i.e.*, $(LaO)^{+1}$ and $(BO_2)^{+}$ (B=Nb and Ta), in this polar/polar system, which has larger interfacial charge carrier density than the polar/nonpolar $LaAlO_3/SrTiO_3$ system. In the experimental side, very recently, $LaAlO_3/KTaO_3$ interface has been successfully fabricated, and a highly mobile 2DEG has been observed at the interface; [275] Zou *et al.* has prepared a $LaTiO_3/KTaO_3$ HS and reported a 2DEG with a higher carrier mobility than that of the doped bulk $SrTiO_3$. [281]

The third interfacial configuration of the perovskite oxide HS is nonpolar/nonpolar interface. Besides the HS relying on the polar oxide layers to create the interfacial 2DEG, very recently, the nonpolar/nonpolar oxide HS have also been found to be able to produce 2DEG via the piezoelectric polarization, such as the $CaZrO_3/SrTiO_3$, both from the experiment and first-principles electronic structure calculations. [46, 187] In the $CaZrO_3/SrTiO_3$ HS, there exists

an insulator-to-metal transition when the $CaZrO_3$ film thickness goes beyond 6 unit cells, and the 2DEG is attributed to the lattice-mismatch-induced polarization in the $CaZrO_3$ film. [46] Our first-principles computational study has confirmed the formation of the interfacial metallic states and shows that the compressive strain in the $CaZrO_3$ film leads to a polarization discontinuity at the interface that drives the charges from the $CaZrO_3$ film to the $SrTiO_3$ substrate. [187] Moreover, unlike polar/nonpolar and polar/polar HS, which rely on a specific interfacial termination to form the 2DEG, the creation of 2DEG in $CaZrO_3/SrTiO_3$ systems is less sensitive to the interfacial structure and can be formed at both interfacial terminations. Soon later, we further proposed several other nonpolar/nonpolar perovskite oxide HS systems based on the $AHfO_3/SrTiO_3$ (A = Ca, Sr, and Ba). [49]

Other than the Zr- and Hf-involved perovskite oxide HS, the Ti-involved HS have also been found to exhibit the discontinuous polarization across the heterointerface, such as $PbTiO_3/SrTiO_3$ and $BaTiO_3/SrTiO_3$. [58, 70] It is known that many perovskite oxides are equipped with a ferroelectric or piezoelectric property (under an epitaxial strain). Therefore, considering the formation of a polarization discontinuity in the nonpolar/nonpolar oxide HS and its ability to create a robust interfacial 2DEG, we expect that there could be potentially more nonpolar/nonpolar perovskite oxide HS systems that can produce 2DEG. In this work, by employing high-throughput first-principles calculations and a group of combinatorial materials descriptors, we have successfully identified 34 nonpolar piezoelectric perovskite oxides, which can be divided into six groups of oxides, Ti-, Zr-, Hf-, Si-, Ge-, and Sn-based oxides. Based on these 34 nonpolar compounds, we are further able to construct 311 nonpolar/nonpolar HS systems that can potentially form a polarization discontinuity and a 2DEG at their interface. This work has demonstrated an efficient approach to perform high-throughput design of perovskite-oxide-based functional materials.

6.2 Computational details

The spin-polarized Density Functional Theory (DFT) electronic structure calculations were performed using Vienna *Ab-initio* Simulation Package (VASP), [132, 133] along with the projector augmented wave potentials [134] and Perdew-Burke-Ernzerhof generalized gradient approximation (GGA). [200] All the structures were optimized by minimizing atomic forces up to 0.03 eV/Å. The cutoff energy for the plane-wave expansion was set to 450 eV and the break condition for electronic self-consistency loop was assumed for a total energy convergence of less than 10^{-6} eV. The Γ-centered k-point grid for Brillouin zone sampling was set to $6 \times 6 \times 6$ in the ionic relaxation and $12 \times 12 \times 12$ in the static calculation. The initial magnetic moments were set to 5 μ_B on transition metals and rare-earth elements, and 1 μ_B on all other types of ions.

The strongly constrained and appropriately normed (SCAN) meta-GGA [242] and hybrid DFT calculations within Heyd-Scuseria-Ernzerhof (HSE) formalism [90] with 20% Hartree-Fock exchange were further employed to improve the lattice parameter and band gap calculations for the screened bulk perovskite oxides. A slab model with a 20 Å vacuum layer along the [001] direction was used to model the nonpolar/nonpolar HS. The thickness of substrate was set to 5 unit cells and the thickness of film was varied from 2 to 15 unit cells to investigate the critical thickness to form the interfacial 2DEG. In the ionic relaxations of HS, all the layers of film and first two unit cells of the substrates were allowed to relax and the three remaining unit cells of the substrate were freezed to mimic the experimental epitaxial film growth process. Non-spin-polarized calculations were carried out for all HS with the k-point grid set to $4 \times 4 \times 1$ in the ionic relaxation and $8 \times 8 \times 1$ in the static calculation for the HS models.

6.3 Results and discussion

A successful high-throughput materials screening lies in the development of effective materials descriptors. [55] In our prior work, we have carried out a high-throughput design of

2DEG systems based on polar/nonpolar perovskite oxide HS, in which the materials descriptors of forming interfacial 2DEG include the polar/nonpolar character, lattice mismatch, band gaps, and conduction band edges of polar perovskite oxides. [269] In that work, we built a perovskite-oxide-oriented quantum materials database that contains 3898 cubic ABO_3 compounds, and successfully identified 292 semiconductors and insulators ($E_g > 0$). Here we employ the material descriptor of $E_g > 0.25$ eV as the first condition to screen the bulk piezoelectric oxides on the basis of prior results, and are able to narrow down the list of candidate bulk perovskite oxides from 292 to 262. [6] In terms of the 2DEG formation driven by the polarization discontinuity at nonpolar/nonpolar perovskite oxide interfaces, it requires that the substrate is a non-polarized oxide such as $SrTiO_3$, and the film is a ferroelectric or piezoelectric oxide such as $PbTiO_3$, $CaZrO_3$, and $CaHfO_3$. [49, 58, 187] Note that the piezoelectric character should be caused by the lattice-mismatch-induced compressive strain in the epitaxial growth. Therefore, besides the nonpolar character, lattice mismatch, band gaps, and band edges, the polarization character of a perovskite oxide under the compressive strain, *i.e.*, the piezoelectric character, is one new critical material descriptor in searching for the 2DEG systems driven by the polarization discontinuity.

A good piezoelectric material should exhibit a morphotropic phase boundary (MPB) similar to the one in the $PbZr_xTi_{1-x}O_3$, as the region near the MPB plays a critical role in creating the high electromechanical response. [86] To identify the MPB in a perovskite oxide from first-principles calculations, Ghita *et al.* proposed an approach based on the energy difference among tetragonally, rhombohedrally and rotationally distorted perovskite oxides. [78] This is because to realize a piezoelectric effect, the energy difference between these different phase structures should be as small as possible so that the continuous phase transitions over the MPB become possible. [6] In this work, all the phase structures were constructed from the optimized 5-atom cubic perovskite structure, see Figure 6.1. The prototype structures of tetragonal and rhombohedral phases and their distorted phases were extracted from the tetragonal $PbTiO_3$ and rhombohedral $BaTiO_3$, respectively. For rotationally distorted structures, we modeled the oxygen

octahedral rotation along [111] direction in a 10-atom supercell. The ionic positions and cell shapes of all these structures were fully relaxed. The energy difference per ABO_3 unit cell among tetragonal, rhombohedral, and rotationally distorted structures is denoted as ΔE, and $\Delta E < 0.8$ eV was used as the material descriptor to identify the piezoelectric perovskite oxides. By using the energy difference among different perovskite oxide phase structures, that is, $\Delta E <$ 0.8 eV, we further narrowed down the list to from 262 to 76 candidates. In this work, we were interested in searching for the polarization-discontinuity-induced 2DEG systems based on the nonpolar/nonpolar perovskite oxide HS. This requires that both substrate and film are nonpolar oxides, *i.e.*, having a chemical formula of $A^{+2}B^{+4}O_3$, so that along [001] direction, each layer will be charge neutral. By using this condition, we ended up with 34 nonpolar piezoelectric perovskite oxides, which were used to build nonpolar/nonpolar HS systems. It is noted that the other two materials descriptors including lattice mismatch and relative band edges are determined by substrate and film together, and thus they were not used here to screen bulk perovskite oxides but used in building HS systems.

6.3.1 Bulk Piezoelectric Perovskite Oxides

By employing material descriptors including ΔE, E_g, and nonpolar character of perovskite oxides, we successfully obtained 34 candidate bulk piezoelectric perovskite oxides. These perovskites can be divided into six groups based on the B-site elements: Ti-, Zr-, Hf-, Si-, Ge-, and Sn-based oxides, which are listed in Table 7.1. For each piezoelectric perovskite oxide, we list its calculated tolerance factor (f), lattice constant a (Å), band gap E_g(eV), valence band maximum (VBM), conduction band minimum (CBM), and Born effective charge for A atom Z^*(A), B atom Z^*(B), O atom in the AO plane Z^*_{AO}(O) and O atom in the BO_2 plane $Z^*_{BO_2}$(O). The tolerance factor (t) for each selected perovskite oxide was calculated using the bond valence

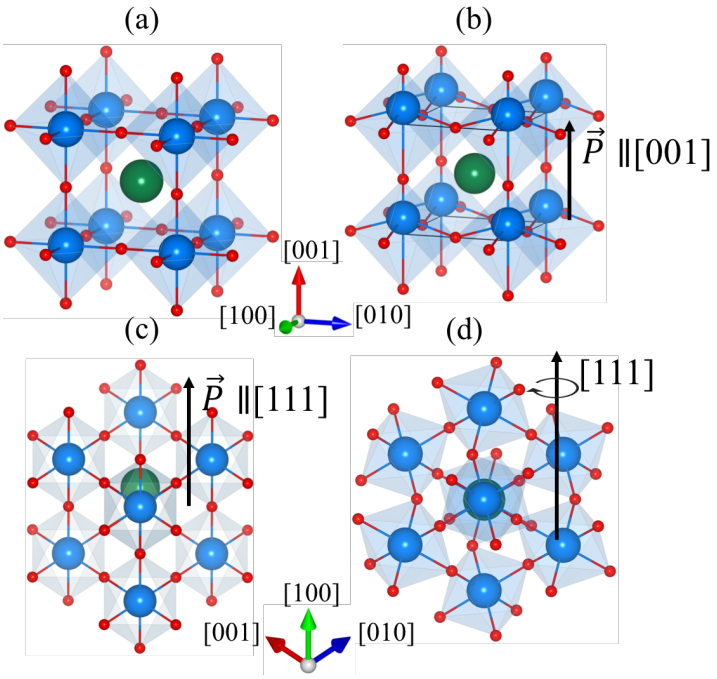

Figure 6.1: Scheme of perovskite oxide ABO_3 structures: (a) cubic, (b) tetragonal, (c) rhombohedral, and (d) structure with oxygen octahedral rotates along the [111] direction.

model: [12, 29]

$$t = \frac{R_{A-O}}{\sqrt{2}(R_{B-O})} \tag{6.1}$$

where R_{A-O} and R_{B-O} are the A-O and B-O bond lengths for an ABO_3 compound. To have a comprehensive comparison, we calculated the lattice parameters using GGA, SCAN, and HSE approaches, respectively, along with the available experimental values. The comparison of the calculated and experimental lattice constants is presented in Figure 6.2. Figure 6.2a shows that the SCAN and HSE methods yield relatively close lattice constants, while the standard GGA approach generally overestimates the lattice constants. Figure 6.2b shows the former two approaches predict lattice constants much closer to the corresponding experimental values than the standard GGA approach. Considering the well-known underestimations of band gaps of insulators and semiconductors from standard GGA calculations, [227] we also calculated the band gaps of these candidate perovskites oxides using SCAN and HSE approaches. Our calculations

Table 6.1: Calculated properties of bulk nonpolar piezoelectric perovskites oxides.

Compounds	t	a^{GGA}	a^{SCAN}	a^{HSE}	$a^{Exp.}$	E_g^{GGA}	E_g^{SCAN}	E_g^{HSE}	E_g^{EXP}	VBM	CBM	Z^*(A)	Z^*(B)	Z^*_{AO}(O)	$Z^*_{BO_2}$(O)	ΔH(eV)
$CaGeO_3$	0.98	3.777	3.730	3.729	3.724 [263]	0.70	1.66	2.83	-	0.86	1.56	2.59	4.42	-3.58	-1.71	-2.19
$BaHfO_3$	1.01	4.196	4.157	4.168	4.171 [177]	3.54	4.09	4.97	6.00 [61]	-0.50	3.04	2.74	5.81	-4.56	-2.00	-3.38
$PbHfO_3$	0.95	4.147	4.104	4.119	4.140 [31]	2.47	2.86	3.99	3.4 [206]	-0.34	2.13	3.90	5.66	-4.60	-2.48	-2.55
$SrHfO_3$	0.95	4.132	4.090	4.105	4.069 [177]	3.75	4.33	5.19	6.10 [218]	-0.38	3.37	2.58	5.71	-4.58	-1.85	-3.37
$EuHfO_3$	0.96	4.127	4.083	4.105	4.088 [1]	0.49	0.79	2.69	*2.7 [1]	2.53	3.02	2.73	5.84	-4.50	-2.04	-3.32
$SnHfO_3$	0.90	4.133	4.093	4.105	-	1.83	2.17	3.28	-	0.00	1.83	4.29	5.63	-4.57	-2.68	-2.48
$CaHfO_3$	0.90	4.096	4.053	4.070	3.990 [65]	3.68	4.28	5.18	6.20 [210]	-0.40	3.28	2.63	5.63	-4.60	-1.83	-3.26
$YbHfO_3$	0.90	4.071	4.017	4.045		3.60	4.39	5.11		-0.40	3.20	2.63	5.65	-4.57	-1.85	-3.33
$CaSiO_3$	1.05	3.602	3.563	3.567	3.485 [154]	3.60	4.89	5.83	-	1.25	4.85	2.61	4.13	-3.10	-1.82	-2.80
$BaSiO_3$	1.18	3.831	3.799	3.788	-	1.10	1.97	2.94	-	0.84	1.94	2.84	4.52	-3.57	-1.89	-2.43
$SrSiO_3$	1.11	3.689	3.651	3.650	-	2.56	3.73	4.74	-	1.45	4.01	2.61	4.28	-3.24	-1.82	-2.71
$GeSiO_3$	0.84	3.603	3.570	3.566	-	2.56	2.86	4.29	-	1.81	4.37	4.17	4.61	-2.98	-2.90	-1.71
$CdSiO_3$	1.02	3.615	3.573	3.575	-	0.75	1.40	2.54	-	1.72	2.47	2.79	4.18	-3.03	-1.97	-1.76
$SnSiO_3$	1.06	3.704	3.670	3.665	-	0.88	1.76	2.31	-	2.52	3.40	4.35	4.60	-3.08	-2.93	-1.76
$PbSiO_3$	1.11	3.741	3.701	3.699	-	1.31	2.35	2.95	-	1.97	3.28	4.06	4.38	-3.20	-2.62	-1.76
$MnSiO_3$	0.98	3.552	3.512	3.518	-	1.93	2.78	3.81		2.18	4.11	3.04	4.08	-2.99	-2.07	-1.86
$BaSnO_3$	1.01	4.180	4.134	4.130	4.116 [177]	0.57	1.45	2.45	3.1 [175]	-0.06	0.51	2.73	4.42	-3.51	-1.82	-2.22
$PbSnO_3$	0.95	4.120	4.070	4.070	4.072 [239]	1.19	2.21	3.20	-	0.30	1.49	3.91	4.33	-3.25	-2.49	-1.40
$SrSnO_3$	0.96	4.103	4.056	4.056	4.034 [177]	1.17	2.21	3.15	*4.1 [175]	0.04	1.21	2.58	4.24	-3.32	-1.75	-2.22
$CaSnO_3$	0.90	4.058	4.013	4.014	-	1.57	2.62	3.53	*4.4 [175]	0.12	1.69	2.62	4.11	-3.22	-1.75	-2.12
$GeSnO_3$	0.72	4.047	4.006	4.001	-	1.75	2.12	3.26	-	0.19	1.94	4.51	4.10	-3.11	-2.75	-1.06
$SrTiO_3$	1.00	3.938	3.905	3.900	3.905 [177]	1.78	2.15	3.17	3.20 [190]	0.00	1.78	2.55	7.44	-5.93	-2.03	-3.14
$BaTiO_3$	1.06	4.028	3.999	3.989	4.012 [216]	1.68	2.01	2.98	3.27 [260]	-0.25	1.43	2.73	7.52	-5.98	-2.13	-3.06
$PbTiO_3$	1.00	3.965	3.929	3.926	3.969 [137]	1.58	1.92	2.74	3.45 [197]	0.33	1.91	3.85	7.37	-6.08	-2.57	-2.27
$SnTiO_3$	0.95	3.943	3.914	3.906	-	1.05	1.31	2.15	-	0.80	1.85	4.26	7.26	-6.06	-2.73	-2.22
$GeTiO_3$	0.75	3.880	3.851	3.842	-	2.00	2.29	3.38	-	0.02	2.02	4.41	7.27	-6.09	-2.80	-2.00
$CaTiO_3$	0.95	3.883	3.851	3.848	3.840 [216]	1.84	2.23	3.25	*3.8 [131]	-0.02	1.82	2.57	7.38	-5.92	-2.02	-3.08
$BaZrO_3$	1.00	4.246	4.206	4.217	4.193 [177]	3.06	3.69	4.44	4.85 [33]	-0.67	2.39	2.72	6.23	-4.95	-2.00	-3.23
$PbZrO_3$	0.94	4.202	4.154	4.170	4.167 [138]	2.33	2.71	3.88	3.72 [197]	-0.69	1.64	3.89	6.06	-5.00	-2.47	-2.39
$SrZrO_3$	0.94	4.190	4.143	4.159	4.154 [124]	3.24	3.91	4.65	5.60 [144]	-0.57	2.67	2.57	6.12	-4.97	-1.87	-3.20
$SnZrO_3$	0.90	4.188	4.145	4.156	-	1.81	2.15	3.22	-	-0.31	1.50	4.26	6.02	-4.98	-2.65	-2.31
$EuZrO_3$	0.95	4.183	4.135	4.158	4.104 [1]	0.28	0.71	2.39	*2.4 [1]	2.12	2.40	2.72	6.27	-4.88	-2.06	-3.15
$CaZrO_3$	0.89	4.153	4.107	4.125	4.012 [46]	3.23	3.91	4.67	*5.5 [131]	-0.61	2.62	2.63	6.04	-4.98	-1.84	-3.07
$YbZrO_3$	0.90	4.131	4.071	4.101	-	3.34	3.95	4.78	-	-0.62	2.72	2.63	6.05	-4.95	-1.87	-3.13

show that the band gaps determined from the HSE approach are closer to experimental values. To characterize the relative band edge positions of these perovskite oxides, we calculated their VBM and CBM positions by aligning core levels of O ions and setting the VBM of $SrTiO_3$ as the reference zero-point energy. [49, 269] As discussed later, the relative positions of the CBM can be used to justify which side of the interfacial region (film or substrate) can form the 2DEG. The Born effective charge for A atom Z^*(A), B atom Z^*(B), O atom in the AO plane Z^*_{AO}(O) and O atom in the BO_2 plane $Z^*_{BO_2}$(O) were also calculated to estimate the polarization strength in the HS. We noted that Ceder's team has reported bulk piezoelectric perovskite oxides using first-principles screening approach. [6] In our work, besides all the nonpolar piezoelectric perovskite oxides reported in that study, we also identified 8 more piezoelectric compounds including $CaSnO_3$, $EuHfO_3$, $EuZrO_3$, $GeSnO_3$, $GeTiO_3$, $MnSiO_3$, $YbHfO_3$, and $YbZrO_3$. Interestingly, some of

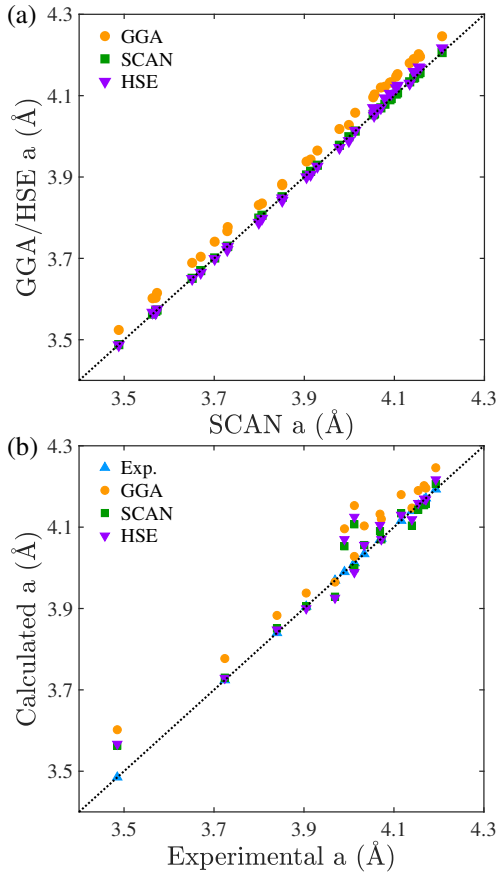

Figure 6.2: (a) A comparison for the calculated lattice constants using different functionals.(b) A comparison between experimental and theoretical lattice constants.

these compounds have been theoretically predicted to show a polarization characteristic. For instance, $CaSnO_3$ was found to form a spontaneous polarization in its bicolor superlattice of the orthorhombic phases from first-principles calculations; [232] $GeTiO_3$ has a 137 $\mu C/cm^2$ spontaneous polarization in its rhombohedral phase. [139]

6.3.2 Nonpolar/Nonpolar Heterostructures

We next built all the possible nonpolar/nonpolar HS systems using the identified 34 nonpolar piezoelectric oxides and explored their possibility to form a polarization discontinuity at their interfaces. A total number of $P(34,2) = 1122$ unique oxide HS can be generated by

Table 6.2: Calculated film critical thickness for polarization discontinuity induced 2DEG in substrate $SrTiO_3$-, $YbZrO_3$-, $CaHfO_3$-, $BaSiO_3$-, $CaGeO_3$-, and $SrSnO_3$-based HS.

$SrTiO_3$				$YbZrO_3$				$CaHfO_3$				$BaSiO_3$				$CaGeO_3$				$SrSnO_3$			
Film	$f(\%)$	t_c	t_c'	Film	$f(\%)$	t_c	t_c'	Film	$f(\%)$	t_c	t_c'	Film	$f(\%)$	t_c	t_c'	Film	$f(\%)$	t_c	t_c'	Film	$f(\%)$	t_c	t_c'
$SnTiO_3$	0.14	6	7	$SrHfO_3$	0.02	-	-	$SrSnO_3$	0.17	-	-	$GeTiO_3$	1.26	2	3	$BaSiO_3$	1.45	2	2	$PbSnO_3$	0.41	8	13
*$PbTiO_3$ [58]	0.69	9	12	$SnHfO_3$	0.05	4	7	$PbSnO_3$	0.58	10	-	$CaTiO_3$	1.34	6	11	$GeTiO_3$	2.72	3	4	$EuHfO_3$	0.58	2	2
*$BaTiO_3$ [126]	2.29	4	4	$PbHfO_3$	0.39	8	12	$EuHfO_3$	0.76	2	2	$SrTiO_3$	2.78	5	10	$CaTiO_3$	2.81	4	5	$YbZrO_3$	0.68	3	4
$GeSnO_3$	2.77	2	3	$CaZrO_3$	0.53	3	5	$YbZrO_3$	0.85	4	5	$SnTiO_3$	2.92	3	3	$SrTiO_3$	4.26	2	2	$SrHfO_3$	0.69	-	-
$CaSnO_3$	3.05	5	7	$BaSnO_3$	1.19	-	-	$SrHfO_3$	0.87	-	-	$PbTiO_3$	3.48	4	8	$SnTiO_3$	4.41	3	3	$SnHfO_3$	0.73	5	6
$YbHfO_3$	3.38	3	3	$EuZrO_3$	1.26	2	2	$SnHfO_3$	0.91	6	7	$BaTiO_3$	5.13	3	4	$PbTiO_3$	4.98	3	3	$PbHfO_3$	1.06	7	9
*$CaHfO_3$ [229]	4.03	3	4	$SnZrO_3$	1.38	3	5	$PbHfO_3$	1.24	10	13	$GeSnO_3$	5.64	2	2	-	-	-	-	$CaZrO_3$	1.20	3	5
$SrSnO_3$	4.21	-	-	$SrZrO_3$	1.43	8	13	$CaZrO_3$	1.37	5	6	$CaSnO_3$	5.92	3	4	-	-	-	-	$BaSnO_3$	1.86	-	-
$PbSnO_3$	4.63	7	7	$BaHfO_3$	1.57	-	-	$BaSnO_3$	2.04	-	-	-	-	-	-	-	-	-	-	$EuZrO_3$	1.95	2	2
$EuHfO_3$	4.80	2	2	$PbZrO_3$	1.72	5	7	$EuZrO_3$	2.12	2	-	-	-	-	-	-	-	-	-	$SnZrO_3$	2.06	3	5
$YbZrO_3$	4.90	2	2	$BaZrO_3$	2.78	-	-	$SnZrO_3$	2.24	4	5	-	-	-	-	-	-	-	-	$SrZrO_3$	2.10	6	11
$SrHfO_3$	4.93	4	6	-	-	-	-	$SrZrO_3$	2.28	12	15	-	-	-	-	-	-	-	-	$BaHfO_3$	2.26	-	-
$SnHfO_3$	4.97	3	3	-	-	-	-	$BaHfO_3$	2.44	-	-	-	-	-	-	-	-	-	-	$PbZrO_3$	2.40	5	7
$PbHfO_3$	5.32	4	4	-	-	-	-	$PbZrO_3$	2.58	7	8	-	-	-	-	-	-	-	-	$BaZrO_3$	3.48	9	12
*$CaZrO_3$ [46]	5.46	2	5	-	-	-	-	$BaZrO_3$	3.66	-	-	-	-	-	-	-	-	-	-	-	-	-	-
*$BaSnO_3$ [39]	6.15	6	-	-	-	-	-	-	-	-	-	-	-	-	-	-	-	-	-	-	-	-	-

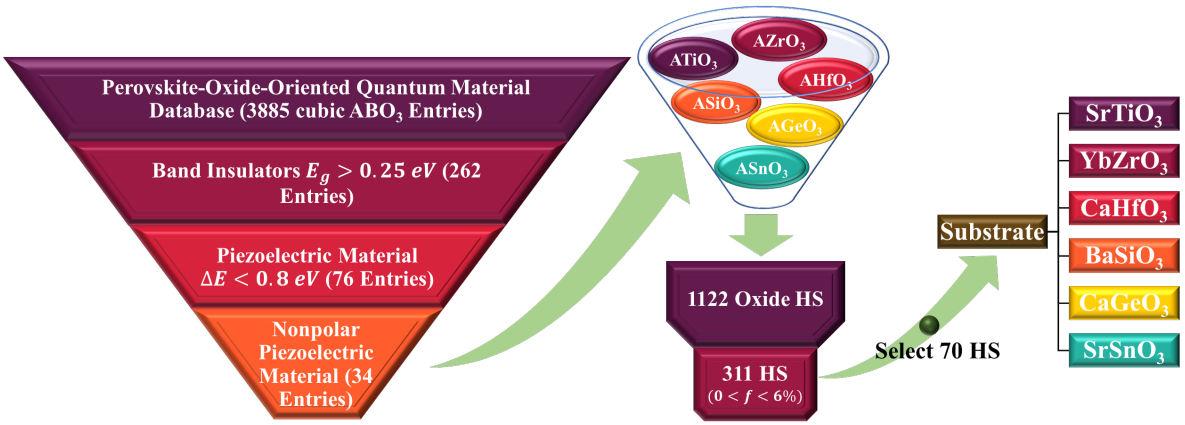

Figure 6.3: Flowchart summary of high-throughput screening and elimination procedure in this study, from first identifying all the possible nonpolar piezoelectric perovskite oxides to constructing all the candidate nonpolar/nonpolar HS and then to verifying the existence of 2DEG in 70 selected HS.

combining the 34 selected compounds. A permutation was used here because switching the epitaxial order of the substrate and film can lead to different strain on the film (compressive strain on the film will become tensile strain if switched the growth order, and vice versa), and thus drastically change its polarization and electronic properties. [48] To form a polarization discontinuity (strictly speaking to form a polarization in the perovskite film), the oxide film needs to experience a compressive strain from the substrate, and meanwhile a small lattice mismatch between the substrate and film is desired to form an ideal perovskite oxide HS. Therefore, by

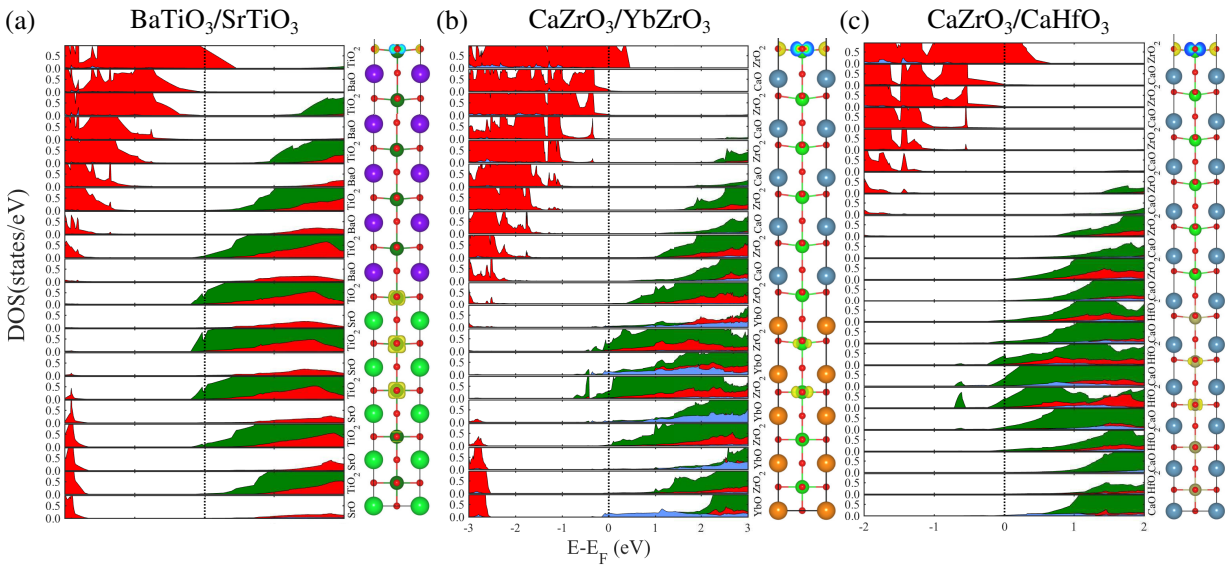

Figure 6.4: Calculated layer-resolved partial DOS along with the charge density plots projected on the bands forming the metallic states. The vertical dash line at zero point energy shows the Fermi level. The solid blue, red, and green color indicates *s*, *p* and *d* orbital, respectively.

defining $f = (a_f - a_s)/a_s$, [269] we only need to consider the HS with $0 < f < 6\%$, in which a positive f indicates that the film will experience a compressive strain from the substrate. By using this condition, we were able to generate 311 nonpolar/nonpolar HS systems.

To further examine whether these nonpolar/nonpolar HS systems can have polarization discontinuity and interfacial 2DEG, one needs to perform electronic structure calculations for all these HS models. However, as mentioned above, there are six groups of piezoelectric perovskite oxides according to the classification of B-site element. Hence, we selected one prototype perovskite oxide from each group as the substrate, chose all the possible piezoelectric oxides as the film using the condition of $0 < f < 6\%$, and built HS to verify the formation of polarization discontinuity at the interface. Thus, by using $SrTiO_3$, $YbZrO_3$, $CaHfO_3$, $BaSiO_3$, $CaGeO_3$, and $SrSnO_3$ as the substrate, we were able to generate a total number of 70 HS systems in six groups, see Table 6.2. This strategy can significantly reduce computational cost of HS models from 311 to 70, and meanwhile give reliable sample evaluation of the interfacial materials properties of all the HS models. A complete screening and elimination procedure is shown in Fig. 6.3. A series of prior

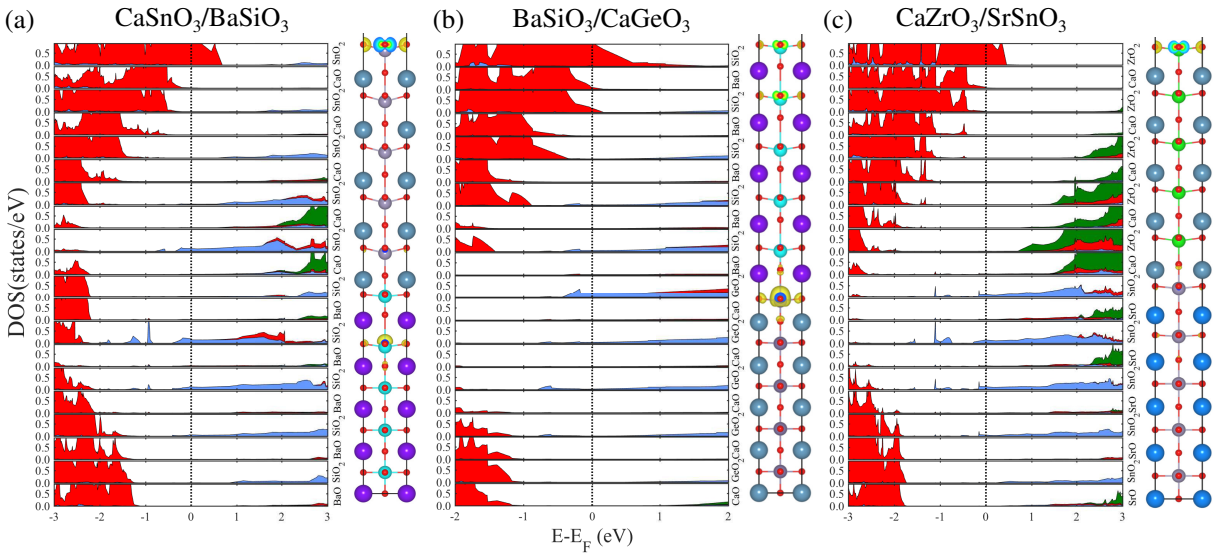

Figure 6.5: Calculated layer-resolved partial DOS along with the charge density plots projected on the bands forming the metallic states.

experimental and computational studies show that there exists a critical film thickness to form a polarization discontinuity in the nonpolar/nonpolar HS. [46, 49, 187] Here, we define t_c as the film critical thickness once polarization is formed in the film layers and $t_c^{'}$ as the film critical thickness once the polarization state is energetic more favorable than its paraelectric state. In other words, the $t_c^{'}$ is the critical film thickness to form a stable polarization state. The t_c and $t_c^{'}$ are listed in the Table 6.2. Also note that the lattice-mismatch-induced polarization can point towards either the interface or the surface of the film, *i.e.*, the vacuum, and only a strong enough polarization towards the interface can drive the charge transfer from the film to the substrate, and produce the interfacial 2DEG. In contrast, a strong polarization towards the surface will drive the charge transfer from the substrate to the film, and produce the interfacial two-dimensional hole gas (2DHG), as discussed later. In Table 6.2, we list all the possible oxide films that can form a polarization discontinuity and 2DEG at the interface for each selected substrate. 13 exceptional HS systems that cannot form interfacial metallic states, even the film thickness was increased up to 15 unit cells, include: $SrSnO_3/SrTiO_3$, $SrHfO_3/YbZrO_3$, $BaSnO_3/YbZrO_3$, $BaHfO_3/YbZrO_3$, $BaZrO_3/YbZrO_3$, $SrSnO_3/CaHfO_3$, $SrHfO_3/CaHfO_3$, $BaSnO_3/CaHfO_3$, $BaHfO_3/CaHfO_3$, $BaZrO_3/CaHfO_3$, SrHf-

$O_3/SrSnO_3$, $BaSnO_3/SrSnO_3$ and $BaHfO_3/SrSnO_3$.

In addition, we also found a correlation between critical film thickness t_c and lattice mismatch f in the $SrTiO_3$- and $BaSiO_3$-based HS. That is, a large f corresponds to a small t_c, as in the case of our prior study of $AHfO_3/SrTiO_3$ (A = Ca, Sr, and Ba) HS. [49] This is because as f increases, the film will experience a higher compression strain from the substrate so that the film tends to exhibit polarization with a smaller t_c. Also, interestingly, when the A-site element in the film of the HS is Eu, Yb, Ge, or Sn, for example, the HS systems $EuZrO_3/SrSnO_3$, $YbZrO_3/SrSnO_3$, $GeTiO_3/BaSiO_3$, and $SnTiO_3/SrTiO_3$, the HS needs a much smaller t_c to form the polarization. In particular, when $EuZrO_3$ and $EuHfO_3$ serve as the film to form a HS, the critical film thickness to form a polarization is as low as two unit cells, regardless of the f value. Accordingly, except for the lattice mismatch f, the A-site element such as Eu, Yb, Ge, or Sn also plays a significant role in determining t_c. However, it is noted that a strain-induced polarization is essentially determined by its energy preference over non-polarized state. By taking $BaTiO_3/SrTiO_3$ HS models (with different film thickness) as an example, we have calculated its total energy per unit cell (of the film) as a function of the average polarization, see Figure 6.6. It clearly shows that the ground state of $BaTiO_3/SrTiO_3$ becomes polarized as the film thickness is larger than 4 unit cells, *i.e.*, $t_c = 4$.

Next, to clearly show the polarization behavior in the oxide film and the charge transfer mechanism in these HS models, we selected one HS model from each group of the materials systems in Table 6.2 and plotted their layer-resolved density of states (DOS) and three-dimensional (3D) charge density projected on their conduction bands forming the interfacial metallic states, as shown in Figure 6.4 and 6.5. Figure 6.4 shows the results for $BaTiO_3/SrTiO_3$, $CaZrO_3/YbZrO_3$ and $CaZrO_3/CaHfO_3$, and Figure 6.5 shows the results for $CaSnO_3/BaSiO_3$, $BaSiO_3/CaGeO_3$ and $CaZrO_3/SrSnO_3$. The layer-resolved DOS show that the O $2p$ states in all these systems move to higher energy states from the interfacial layer to the surface layer, and at the surface layer, some O $2p$ states cross the Fermi level and become unoccupied. This indicates that there

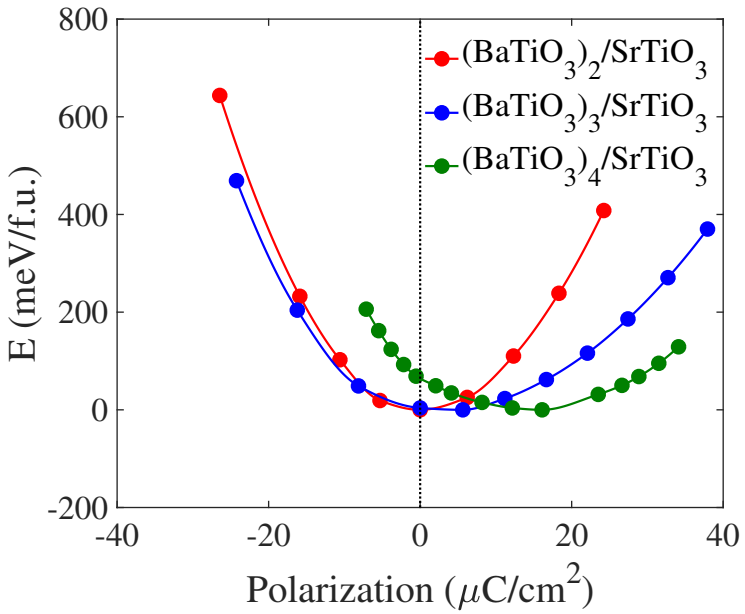

Figure 6.6: Calculated total energy per unit cell of the film as a function of the average polarization for $BaTiO_3/SrTiO_3$ HS models with different film thickness. The reference energy (zero) is taken from the lowest energy of each system.

exists an intrinsic electric field, which is caused by the relative cation-anion displacement in the oxide films, that is, the polarization towards the interface, as shown in the corresponding geometrical structures. Also note that the relative displacement between cations and anions in each substrate material is much smaller than that in its corresponding film, implying that a polarization discontinuity is formed at the interface, which is caused by the lattice-mismatch-induced compressive strain on the oxide films. Moreover, at interfacial layers, some bottom conduction bands cross the Fermi level and form the interfacial conductivity, as shown in the 3D charge density plot. This suggests that the polarization discontinuity at the interface leads to the charge transfer from the film to the substrate, and these transferred electrons generally reside near the interfacial region of the substrate, forming the interfacial conductivity. For $BaTiO_3/SrTiO_3$, $CaZrO_3/YbZrO_3$, and $CaZrO_3/CaHfO_3$ HS, their interfacial metallic states are mainly contributed from Ti 3*d*, Zr 4*d*, and Hf 5*d* orbitals, respectively, see Figure 6.4(a-c). For $CaSnO_3/BaSiO_3$, $BaSiO_3/CaGeO_3$, and $CaZrO_3/SrSnO_3$ systems, their interfacial metallic states are mainly from Si 3*s*, Ge 4*s*, and Sn 5*s* orbitals, respectively, as shown by the solid blue in Figure

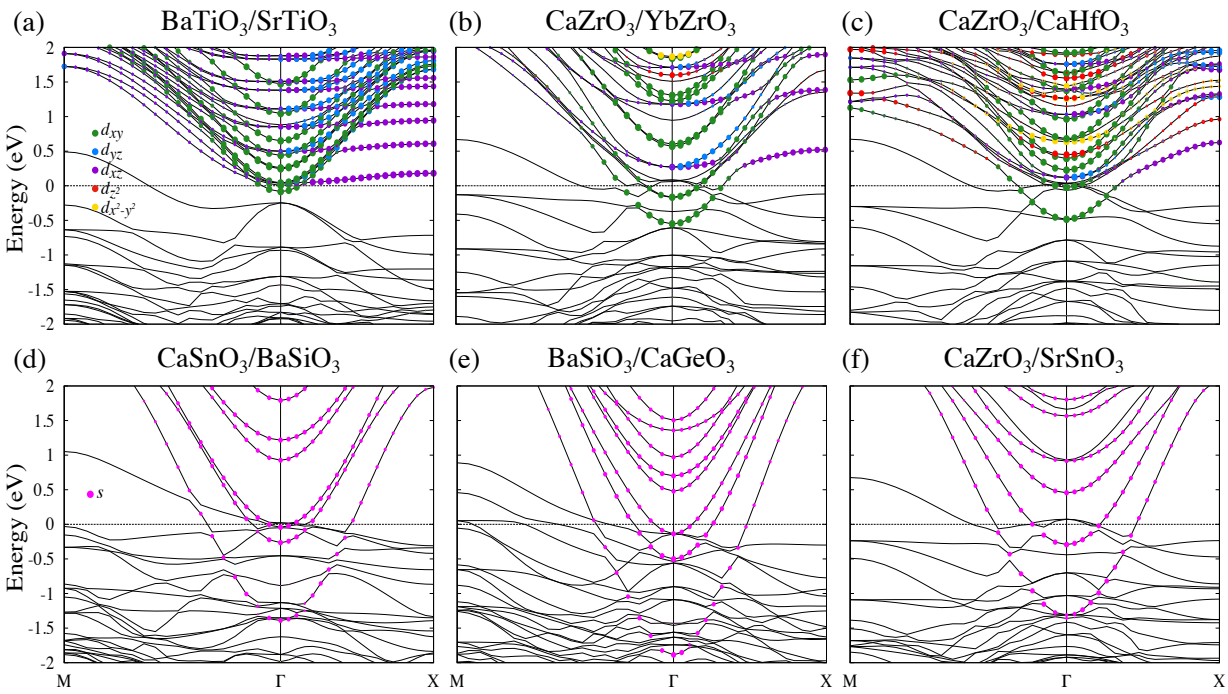

Figure 6.7: Orbital projected band structures for (a) $BaTiO_3/SrTiO_3$, (b) $CaZrO_3/YbZrO_3$, (c) $CaZrO_3/CaHfO_3$, (d) $CaSnO_3/BaSiO_3$, (e) $BaSiO_3/CaGeO_3$, and (f) $CaZrO_3/SrSnO_3$ HS. The horizontal dot line indicates the Fermi level at zero.

6.5(a-c). We then calculated the effective mass values for the 6 exemplary HS by fitting their electronic bands contributing to the 2DEG, see Figure 6.7. We found that the effective mass for $CaSnO_3/BaSiO_3$, $BaSiO_3/CaGeO_3$ and $CaZrO_3/SrSnO_3$ ($m^* \approx 0.3m_e$) are generally smaller than that in $BaTiO_3/SrTiO_3$, $CaZrO_3/YbZrO_3$ and $CaZrO_3/CaHfO_3$ HS ($m^* \approx 0.4-0.5m_e$) because of a more delocalization character of *s* orbital than that of *d* orbitals. [256] Hence, a high electron mobility is expected in Si-, Ge-, and Sn-based 2DEG HS.

Moreover, it is worth mentioning that, in the $CaSnO_3/BaSiO_3$ HS, some interfacial layers in the film also contribute to the interfacial metallic states, which indicates that the transferred electrons, from the film to the substrate driven by the polarization discontinuity, partially flow back to the film. The underlying mechanism of this intriguing phenomenon can be rationalized in terms of the band alignment between the film and substrate. In our prior work of high-throughput design of perovskite-oxide-based 2DEG systems based on the polar catastrophe, we defined one

material descriptor, *i.e.*, the band alignment between the film and substrate, to characterize the charge transfer from the film to the substrate driven by the polar catastrophe, and the resulting 2DEG at the interface. [49, 269] In the polar catastrophe mechanism, CBM of the polar film (electron donor) should be higher than that of the nonpolar substrate (acceptor), so that electrons can be confined at the side of the electron-acceptor material and form the interfacial metallic states; otherwise, the interfacial metallic states cannot be formed. However, in the nonpolar/nonpolar interface system, the donor electrons, caused by the polarization discontinuity, can form metallic states near the interfacial region in both the film and substrate since they are originally nonpolar (not charged). For the $CaSnO_3/BaSiO_3$ system, as shown in Table 7.1, the CBM of film $CaSnO_3$ is lower than that of the substrate $BaSiO_3$. After electronic reconstruction at the interface, the lower energy states at the interfacial region are both from the film and substrate, and accordingly, when the electrons are transferred from the film to the substrate via the intrinsic electric field in the film, the electrons tend to stay at a lower energy state and thus partial electrons flow back to the film. Thus, the 2DEG are contributed both from the interfacial layers in the substrate and film. For some HS, such as $SrTiO_3/SrSiO_3$ and $BaTiO_3/BaSiO_3$, the film CBM is significantly lower than that of the substrate, and even after electronic reconstruction, the film CBM is still much lower than that of the substrate, then the transferred electron will be solely accumulated in the film side near the interfacial region. Therefore, the 2DEG forms in the film side of the interfacial region, see the calculated layer-resolved DOS of these two systems in Figure 6.9. In contrast, when a film CBM is much higher than that of the substrate, there will be no electrons flowing back and the 2DEG only appear in the substrate side of the interfacial region, such as $CaZrO_3/SrSnO_3$ systems.

6.3.3 Polarization Robustness

In this section, we explored the polarization robustness in these nonpolar/nonpolar HS. Here we started by investigating the polarization stability and switching path in these systems, as

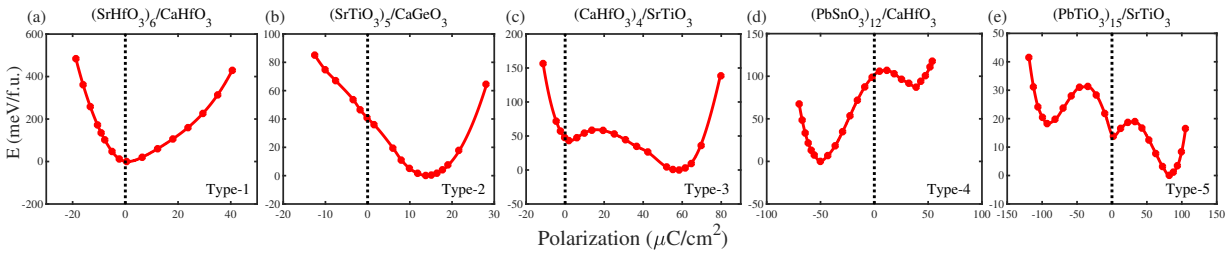

Figure 6.8: Calculated total energy per film unit cell as a function of the average polarization for (a) $(SrHfO_3)_6/CaHfO_3$, (b) $(SrTiO_3)_5/CaGeO_3$, (c) $(CaHfO_3)_4/SrTiO_3$, (d) $(PbSnO_3)_{12}/CaHfO_3$, and (e) $(PbTiO_3)_{15}/SrTiO_3$ HS. The lowest total energies of each system are taken as the reference energies.

various ferroelectric phase transitions have been found in the ferroelectric HS. [156, 157, 272] In our calculations, the first two unit cells of the substrate and all the film layers were initialized as polarized, with a small relative displacement between cations and their neighbor oxygen anions in the same plane. The initial polarization was set as either toward the interface (P_+) or toward the vacuum (P_-), and then a structural relaxation was carried out to examine the polarization stability. That is, whether the polarization can persist in the ground state optimized structure. If the polarization remains after structural relaxation, then it is stable, otherwise not stable and cannot be formed. If both the P_- and P_+ polarization cannot be formed, then the HS is intrinsically paraelectric, as discussed later in the case of $SrHfO_3/CaHfO_3$. It is worth mentioning that when polarization is switched from P_+ to P_-, the interfacial metallic states will be changed from 2DEG to 2DHG, as shown in Figure 6.10. Accordingly, further experimental studies are worth being done to verify the formation of 2DHG. In fact, recently, a 2DHG has been experimentally observed in the p-type polar/nonpolar $LaAlO_3/SrTiO_3$ interface, [45, 140] in which the 2DHG was attributed to the *p*-type $(AlO_2)^-/(SrO)^0$ interface rather than the polarization discontinuity.

Next, to determine the polarization switching behavior and potential energy barrier between different polarization states, we calculated the energy versus polarization ($E(P)$) profiles for all the HS systems in the Table 6.2 by interpolating continuously between paraelectric and ferroelectric states. [156, 270, 272] The average polarization of each unit cell in the film was

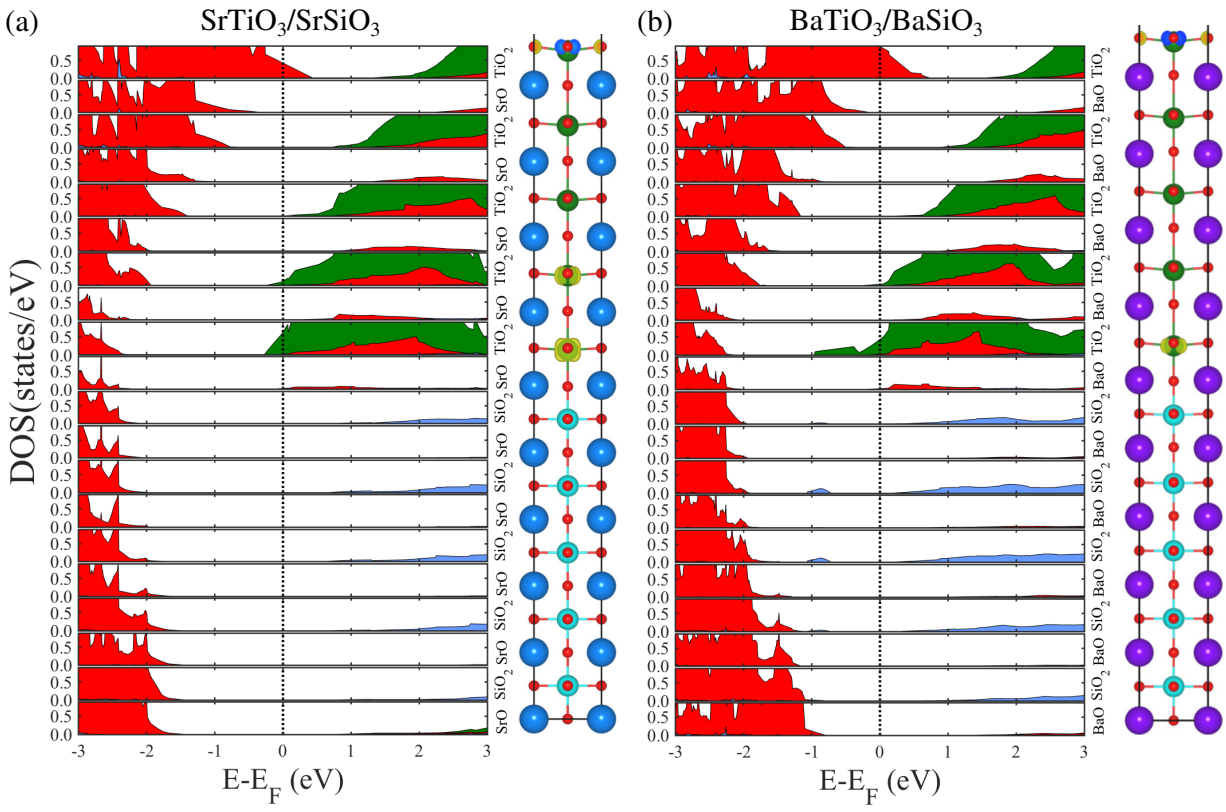

Figure 6.9: Calculated layer-resolved partial DOS along with the charge density plots projected on the bands forming the metallic states.

calculated using the following formula: [203, 278]

$$P = \frac{e}{\Omega} \sum_{i=1}^{N} Z_i^* \delta z_i \tag{6.2}$$

in which Ω and N are the average volume and number of ions in one unit cell, respectively, Z_i^* is the Born effective charge for each ion, and δz_i is the displacement of the ith atom away from its original position in paraelectric phase. Based on the obtained $E(P)$ curves, we were able to further divide the $E(P)$ profiles into five different types, according to the spontaneous polarization direction and the relative stability of paraelectric and ferroelectric states, see Talbe 6.3. Note that the $E(P)$ curve for each HS was calculated at the critical film thickness t_c of forming polarization state, and as the film thickness further increases, the $E(P)$ curve could be changed to a different

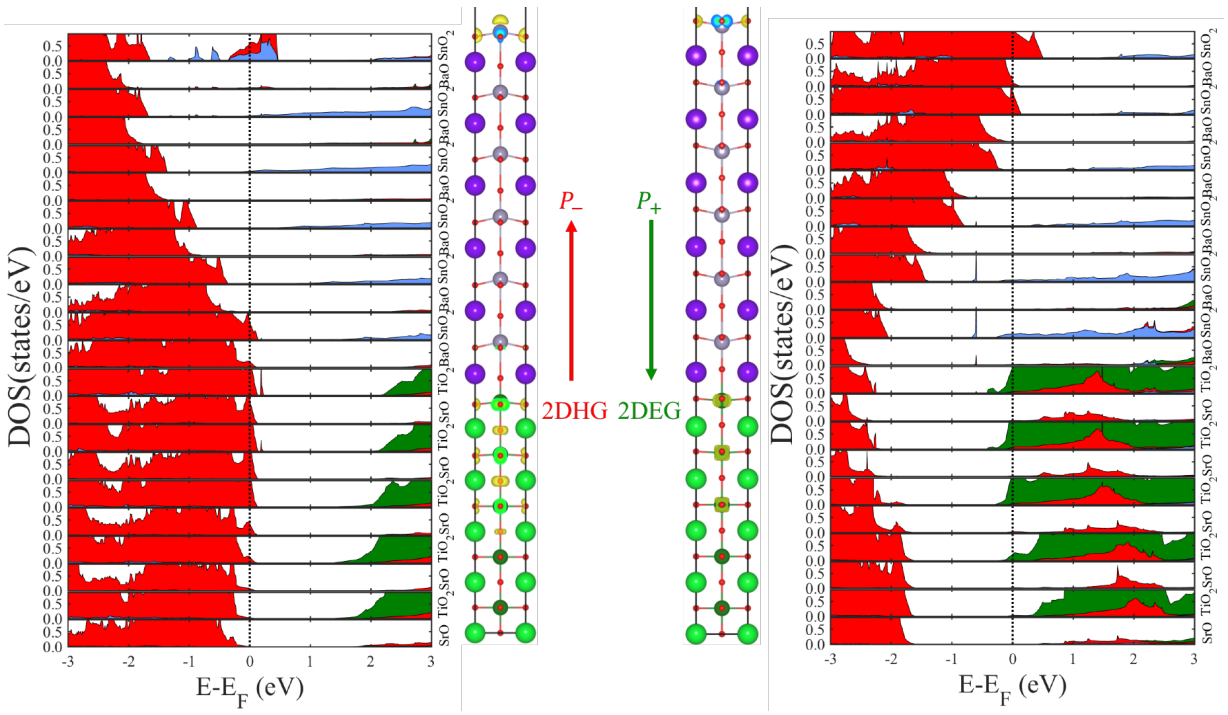

Figure 6.10: Calculated layer-resolved partial DOS for P_+ and P_- states in $BaSnO_3/SrTiO_3$ HS, along with their charge density plots projected on the bands forming the metallic states.

type. To clearly show the polarization behaviors and classification of $E(P)$ curves of these HS systems, we selected five types of HS systems based on their $E(P)$ characters, and showed their $E(P)$ profiles in Figure 6.8. Several conclusions can be derived as below:

i) For the first two types of $E(P)$ profiles, *i.e.*, Type-1 for $(SrHfO_3)_6/CaHfO_3$ and Type-2 for $(SrTiO_3)_5/CaGeO_3$, there exists only one local energy minimum, which is also the global energy minimum, see Figure 6.8(a, b). In other words, there are no metastable polarization states. For $(SrHfO_3)_6/CaHfO_3$, its ground state is non-polarized and no stable polarization state exists in the HS, while for $(SrTiO_3)_5/CaGeO_3$, its ground state has a spontaneous P_+ with a polarization direction towards the interface.

ii) For the third and fourth types of $E(P)$ profiles, *i.e.*, Type-3 for $(CaHfO_3)_4/SrTiO_3$ and Type-4 for $(PbSnO_3)_{12}/CaHfO_3$, they show an asymmetric-like double-well $E(P)$ curve, see Figure 6.8(c, d). This indicates that there exist one metastable state (local energy minimum)

Table 6.3: Polarization types for each selected HS. The polarization type for each HS system is determined at t_c film critical thickness.

Type-1	Type-2	Type-3	Type-4	Type-5
$SrSnO_3/SrTiO_3$	$BaTiO_3/SrTiO_3$	$GeSnO_3/SrTiO_3$	$EuZrO_3/YbZrO_3$	$SnTiO_3/SrTiO_3$
$SrHfO_3/YbZrO_3$	$EuHfO_3/SrTiO_3$	$YbHfO_3/SrTiO_3$	$PbSnO_3/CaHfO_3$	$PbTiO_3/SrTiO_3$
$BaSnO_3/YbZrO_3$	$SnTiO_3/BaSiO_3$	$CaHfO_3/SrTiO_3$	$EuHfO_3/CaHfO_3$	$CaSnO_3/SrTiO_3$
$BaHfO_3/YbZrO_3$	$BaSiO_3/CaGeO_3$	$YbZrO_3/SrTiO_3$	$EuZrO_3/CaHfO_3$	$PbSnO_3/SrTiO_3$
$BaZrO_3/YbZrO_3$	$SrTiO_3/CaGeO_3$	$SrHfO_3/SrTiO_3$	-	$BaSnO_3/SrTiO_3$
$SrSnO_3/CaHfO_3$	$SnTiO_3/CaGeO_3$	$SnHfO_3/SrTiO_3$	-	$PbSnO_3/SrSnO_3$
$SrHfO_3/CaHfO_3$	$PbTiO_3/CaGeO_3$	$PbHfO_3/SrTiO_3$	-	-
$BaSnO_3/CaHfO_3$	$EuHfO_3/SrSnO_3$	$CaZrO_3/SrTiO_3$	-	-
$BaHfO_3/CaHfO_3$	$EuZrO_3/SrSnO_3$	$SnHfO_3/YbZrO_3$	-	-
$BaZrO_3/CaHfO_3$	-	$PbHfO_3/YbZrO_3$	-	-
$SrHfO_3/SrSnO_3$	-	$CaZrO_3/YbZrO_3$	-	-
$BaSnO_3/SrSnO_3$	-	$SnZrO_3/YbZrO_3$	-	-
$BaHfO_3/SrSnO_3$	-	$SrZrO_3/YbZrO_3$	-	-
-	-	$PbZrO_3/YbZrO_3$	-	-
-	-	$YbZrO_3/CaHfO_3$	-	-
-	-	$SnHfO_3/CaHfO_3$	-	-
-	-	$PbHfO_3/CaHfO_3$	-	-
-	-	$CaZrO_3/CaHfO_3$	-	-
-	-	$SnZrO_3/CaHfO_3$	-	-
-	-	$SrZrO_3/CaHfO_3$	-	-
-	-	$PbZrO_3/CaHfO_3$	-	-
-	-	$GeTiO_3/BaSiO_3$	-	-
-	-	$CaTiO_3/BaSiO_3$	-	-
-	-	$SrTiO_3/BaSiO_3$	-	-
-	-	$PbTiO_3/BaSiO_3$	-	-
-	-	$BaTiO_3/BaSiO_3$	-	-
-	-	$CaSnO_3/BaSiO_3$	-	-
-	-	$GeSnO_3/BaSiO_3$	-	-
-	-	$GeTiO_3/CaGeO_3$	-	-
-	-	$CaTiO_3/CaGeO_3$	-	-
-	-	$YbZrO_3/SrSnO_3$	-	-
-	-	$SnHfO_3/SrSnO_3$	-	-
-	-	$PbHfO_3/SrSnO_3$	-	-
-	-	$CaZrO_3/SrSnO_3$	-	-
-	-	$SnZrO_3/SrSnO_3$	-	-
-	-	$SrZrO_3/SrSnO_3$	-	-
-	-	$PbZrO_3/SrSnO_3$	-	-
-	-	$BaZrO_3/SrSnO_3$	-	-

and one ground state (global energy minimum) in these systems. For $(CaHfO_3)_4/SrTiO_3$, its metastable state is non-polarized while ground state has a P_+ state towards $SrTiO_3$ substrate. This means that without an initial P_+ configuration, the HS with a Type-3 $E(P)$ character will remain non-polarized due to an energy barrier from the metastable P_0 to the ground-state P_+ (about 15 meV). Also, there is no stable P_- state in Type-3, which means even if the HS is initially with a P_- configuration, the initial polarization will eventually disappear after structural relaxation and the system becomes non-polarized. On the other hand, the HS systems with a Type-4 $E(P)$ character can exhibit a spontaneous P_- polarization and an energy barrier must be overcome to have a transition from P_- state to P_+ state in Type-4 systems.

iii) For the fifth type of $E(P)$ profile, *i.e.*, Type-5 for $(PbTiO_3)_{15}/SrTiO_3$, it has three local energy minimums at P_-, P_0, and P_+, and the global energy minimum has a P_+ towards the $SrTiO_3$ substrate. The energy barrier is about 5.15 meV from P_0 to P_+ and about 17.51 meV from P_0 to P_-. To reach the ground state (with P_+) or the metastable state (with P_-), an initial polarization must be set to overcome the energy barrier.

6.4 Conclusion

In conclusion, we have demonstrated a high-throughput computational approach to design polarization-discontinuity-induced 2DEG systems at perovskite-oxide-based nonpolar/nonpolar interfaces. Based on a large quantum materials repository of ABO_3 chemical space, and by employing a group of combinatorial materials descriptors based on the band gap and energy proximity among different perovskite phases, we were able to identify 34 nonpolar piezoelectric perovskite oxides, which can be further divided into six groups of materials based on B-site elements: Ti-, Zr-, Hf-, Si-, Ge- and Sn-based oxides. From the 34 selected piezoelectric compounds, we have constructed 311 nonpolar/nonpolar HS, based on the requirement of the lattice mismatch between the film and substrate in the range of $0 < f < 6\%$. By taking $SrTiO_3$-,

$YbZrO_3$-, $CaHfO_3$-, $BaSiO_3$-, $CaGeO_3$- and $SrSnO_3$-based HS as the exemplary models, we calculated electronic structures of 70 selected HS, and verified the formation of 2DEG at the interface. The critical thickness to form interfacial 2DEG and the energy versus polarization profiles of each HS system were also studied. This work provides a platform to accelerate the design of perovskite-oxide-based interface materials.

6.5 Acknowledgements

Chapter 6, in full, is a reprint of the material "Design of Two-Dimensional Electron Gas Systems via Polarization Discontinuity from Large-Scale First-Principles Calculations". as it appears in Journal of Materials Chemistry C. Jianli Cheng, Kesong Yang, 6, 6680-6690, 2018. The dissertation author was the primary investigator and author of this paper.

Chapter 7

Aimsgb: An Algorithm and Open-Source Python Library to Generate Periodic Grain Boundary Structures

From Chapter 2 to 6, the interfaces formed by different TMOs are called heterophase boundary, as the adjoining two TMOs differ in chemical compositions and lattice parameters. In this Chapter, we will introduce a homophase boundary, called grain boundary, which is a region in a single-phase polycrystalline material, that separates two grains with atomic mismatch. The complexity of grain boundaries is enormous, considering five macroscopic degrees of freedom, interconnectedness of grain boundary networks, etc. Due to lack of an efficient, open-source and general tool to constructure grain boundaries, here we present the aimsgb, an efficient and open-source Python library for generating atomic coordinates of periodic grain boundary models. The software framework aims to generate tilt and twist grain boundaries from cubic and non-cubic crystals for *ab-initio* and classical atomistic simulation. This framework has two useful features: i) it can calculate all the CSL matrices for generating CSL from a given Sigma (Σ) value and rotation axis, allowing the users to build the specific CSL and grain boundary models; ii) it

provides a convenient command line tool to enable easy and fast generation of tilt and twist grain boundaries by assigning an input crystal structure, the Σ value, rotation axis, and grain boundary plane. The developed algorithm in the open-source python library is expected to facilitate the studies of grain boundary in materials science. The software framework is also available on the website: `aimsgb.org`.

7.1 Introduction

Interfaces are ubiquitous in solid crystalline materials, and can exhibit material properties that are drastically different from their corresponding bulk materials, bringing potential applications in various industrial areas. One example is the discovery of two-dimensional electron gas at perovskite oxide interfaces such as $LaAlO_3/SrTiO_3$ heterointerface, [50, 190, 255, 269] in which two band insulators combines together and forms highly conducting interfacial conducting states. Compared to the heterointerface between two phase structures (or *heterophase interface*), grain boundary represents one of the simplest interfaces that consists of the same phase crystal with different orientations, and thus can be considered as a *homophase interface*. [23, 145]

As one common planar defect, grain boundaries can significantly change the mechanical, electronic, and other properties of materials. [11, 99, 120, 173, 253] Studying the influence of grain boundaries on the materials properties has been an important research subject in materials science. [22, 27, 77] For instance, grain boundaries often act as ionic blocking layers in solid electrolytes and thus degrade the ionic conductivity, severely lowering the device performance. [22, 27, 77, 164] Also structural transformations and motions of grain boundaries can also have a a significant impact on the mechanical and transport properties of polycrystalline materials, though direct experimental evidences for these phenomena are lacking due to extreme challenges of grain boundary structure characterization at high temperature from high-resolution transmission electron microscopy. [71, 72, 120] Therefore, to characterize a grain boundary structure, particularly from

a computational modeling viewpoint, is of great importance to understand the influence of grain boundaries on the materials properties, and to design high-performance engineering materials.

To describe a grain boundary from crystallography, one needs five macroscopic degrees of freedom (DOFs). [243] The five DOFs define how the two grains with required orientation are combined to form a grain boundary from a given crystal structure. Three of them describe mutual misorientations between the two adjoining grains, which are represented by a rotation axis $\boldsymbol{o}$ (two DOFs) and a rotation angle θ (one DOF). The remaining two DOFs describe the normal $\boldsymbol{n}$ to the grain boundary plane, which indicates the orientation of the grain boundary between the two disorientated grains. The geometrical alignment between $\boldsymbol{o}$ and $\boldsymbol{n}$ defines the grain boundary type: tilt ($\boldsymbol{o} \perp \boldsymbol{n}$), twist ($\boldsymbol{o} \parallel \boldsymbol{n}$), and mixed grain boundaries. [243]

Among all the types of grain boundaries, there exist one type of special grain boundaries called *coincidence-site lattice* (CSL) grain boundary. In the CSL grain boundary, some atomic sites of one grain coincide exactly with some atomic sites of the other grain, and these special atomic sites are called *coincidence sites*. The coincidence sites are spread periodically throughout the whole superimposition and create a supercell called *coincidence-site lattice* (CSL). [21, 145] The CSL grain boundaries are expected to have low grain boundary energy because of good atomic fit, [25, 26] and they have been one important research topic in the grain boundary science and engineering. Given the enormous complexity of grain boundaries (involving 5 macroscopic DOFs), a robust and efficient software that can build any CSL grain boundary structures from a minimum user input is important for the structural characterization of grain boundaries. In particular, as the emergence of high-throughput computational techniques and materials informatics, [55, 207, 267] such tool is very necessary to facilitate high-throughput computational studies of the grain boundaries.

To our best knowledge, although there are some softwares available to construct grain boundary, [189, 194] there is no universal and easy-to-use tool to generate grain boundary structures in a high-throughput fashion. For instance, Ogawa developed a so-called *GBstudio*

software to generate periodic grain boundary structures with Σ value up to 99. [189] The *GBstudio* was developed as a web-based applet by Java language, which requires users to build primitive crystal structure first and then generate one grain boundary structure for a given Σ value. The whole process of generate grain boundaries is extremely laborious and actually impossible to build a grain boundary structure for the organic-inorganic hybrid materials such as halide perovskite $CH_3NH_3SnI_3$. [13] This web-based applet also makes it extremely difficult to work with high-throughput calculations. Another graphical user interface (GUI) software to build grain boundary is *CrystalMaker*, [194] which requires users to build slab or surfaces first and then combine them as a grain boundary structure. As in the case of *GBstudio*, this GUI-based nature makes it incapable of massive production of grain boundaries. Unlike the GUI-based softwares, some species of code based on the command line interface were also developed to generate grain boundaries, which are either limited to several crystal structures only or with limited functions. [204, 262] The users are often required to modify the source code or to add new functions to obtain desired grain boundary structures.

In this article, we introduce one efficient algorithm to build periodic grain boundary models for ab-initio and classical atomistic simulation in materials science. The algorithm is implemented in an open-source python library, aimsgb, that is able to generate tilt and twist grain boundary models from a cubic or non-cubic crystal in a universal fashion by assigning a Sigma (Σ) value, rotation aixs, and grain boundary plane. The code is freely available for download at `aimsgb.org`.

7.2 Building Procedures

Here is a brief outline of the algorithm to build grain boundary.

(1) Calculate rotation angle for a given Σ value and rotation axis.

(2) Generate a rotation matrix from the rotation angle and rotation axis.

(3) Calculate coincidence-site lattice (CSL) matrix using the rotation matrix and Σ value.

(4) Generate two CSL grains from CSL matrix, and combine them based on a given grain boundary plane to build grain boundary.

7.2.1 Rotation Angle

Grain boundary represents one special interface that consists of two grains of the same phase, unlike the case of heterointerface between two phase structures. [50, 255, 269] The two grains differ in their mutual orientations and this misorientation can be described by a rotation that brings the two grains into coincidence. The rotation is characterized by a rotation axis ***o*** [*uvw*] and a rotation angle θ. In the CSL theory, the geometry of a grain boundary structure is described by an integer number (Σ), which is traditionally defined as a ratio between the volume enclosed by a CSL (*coincidence unit cell volume*) and unit cell volume of a cubic crystal with a rotation along [001] rotation axis. [205] Here, by including a rotation with any rotation axis, we redefine the Σ as a ratio between the *coincidence unit cell volume* and that of a rotated unit cell of crystal (*rotated unit cell volume*):

$$\Sigma = \frac{Coincidence\ unit\ cell\ volume}{Rotated\ unit\ cell\ volume} \tag{7.1}$$

The *rotated unit cell volume* depends on the rotation axis ***o*** [*uvw*], and equals to $(u^2+v^2+w^2)$ times of the volume of the conventional unit cell for an orthogonal lattice. In other words, the eq. 7.1 can be rewritten as:

$$\Sigma = \frac{Coincidence\ unit\ cell\ volume}{Conventional\ unit\ cell\ volume \times (u^2+v^2+w^2)} \tag{7.2}$$

For example, a rotated unit cell with a [001] rotation axis has the same volume with its conventional unit cell, while a rotated unit cell with a [111] rotation axis has a volume of three times of

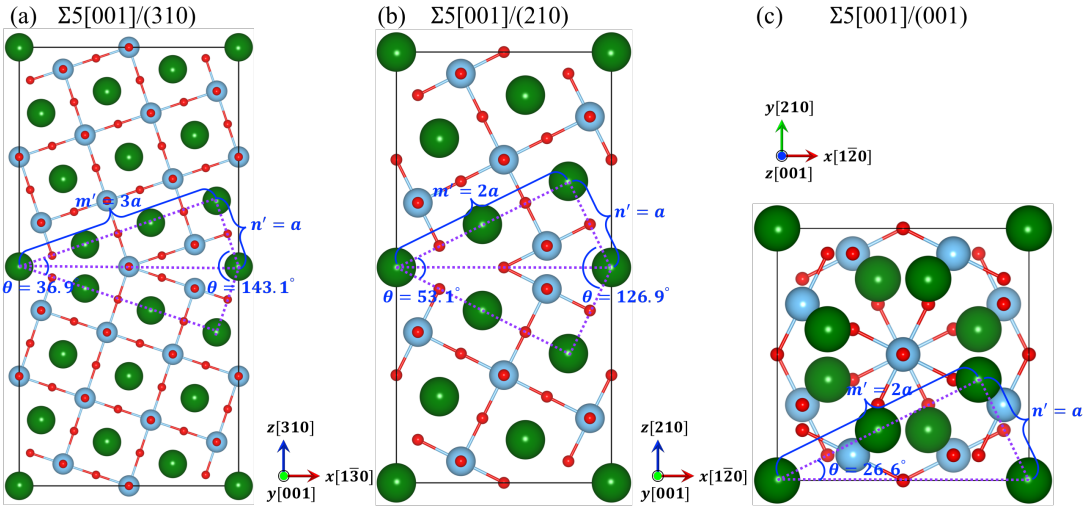

Figure 7.1: Σ5[001] grain boundary structures of cubic $SrTiO_3$. (a) Σ5[001]/(130), (b) Σ5[001]/(120), and (c) Σ5[001]/(001). The former two structures are tilted grain boundaries, and the third one is twisted grain boundary in this and subsequent two figures.

the conventional unit cell. Another equivalent definition of Σ is the ratio of the total number of sites in the coincidence unit cell to that of the rotated unit cell. Note that in some special grain boundaries, like Σ5[001]/(130), the ratio is an even number 10, and in this case, the Σ will be half of the ratio. Also, if the Σ is a multiple of $u^2+v^2+w^2$, the generated grain boundary will be same with a $\Sigma/(u^2+v^2+w^2)$ grain boundary. For example, Σ21[111] is same with Σ7[111].

To generate a CSL from a conventional unit cell of a crystal, Σ, rotation axis ***o*** [*uvw*], and rotation angle θ must satisfy the following conditions: [18, 81, 208]

$$A = \alpha\Sigma = m^2 + (u^2+v^2+w^2)n^2 \tag{7.3}$$

and

$$tan(\frac{\theta}{2}) = \frac{n}{m}(u^2+v^2+w^2)^{1/2} \tag{7.4}$$

where α = 1, 2 or 4, [18] *m* and *n* are positive integers. Thus, for a given Σ, the range of *m* and *n* can be determined as $1 \leq m \leq \left\lceil 2\sqrt{\Sigma} \right\rceil$ and $0 \leq n \leq \left\lceil 2\sqrt{\Sigma} \right\rceil$, respectively, with $\left\lceil 2\sqrt{\Sigma} \right\rceil$ mapping the least integer numbers greater than or equal to $2\sqrt{\Sigma}$. In addition, the integers *u*, *v*, *w* and the

integers m, n should be coprime, *i.e.*, with greatest common divisor (GCD) equal to 1,

$$\mathrm{GCD}(u,v,w) = 1 \qquad \text{and} \qquad \mathrm{GCD}(m,n) = 1 \tag{7.5}$$

Accordingly, by assigning $\boldsymbol{o}$ and Σ, one can determine the values of m and n from eq. 7.3 and 7.5. It is noted that for each Σ, there could be multiple sets of (m, n) values and each set corresponds to a different rotation angle θ. Here we take $SrTiO_3$ $\Sigma5$ [001] grain boundary as an example to show the process of deducing rotation angle and corresponding (m, n) values, see Fig. 7.1. For $\Sigma5$ [001] grain boundary, eq. 7.3 gives $5\alpha = m^2 + n^2$, with α = 1, 2, or 4. Note that herein $m^2 + n^2$ also represents the ratio between the area enclosed by a unit cell of CSL and the unit cell of the standard conventional crystal structure. By using eqs. 7.3 and 7.4, we are able to conclude that:

(1) At α = 1, (m, n) = (2, 1) and θ = 53.1°, or (m, n) = (1, 2) and θ = 126.9°. The area of generated CSL is five times as large as the standard conventional unit cell. Note that the two rotation angles, θ = 53.1° and 126.9°, correspond to the same grain boundary since their sum equals to 180°.

(2) At α = 2, (m, n) = (3, 1) and θ = 36.9°, or (m, n) = (1, 3) and θ = 143.1°. The area of each CSL is 10 times as large as the standard conventional unit cell. The two rotation angles here also correspond to the same grain boundary.

(3) At α = 4, (m, n) = (4, 2) or (2, 4), the CSL generated in this case is the same with that in α = 1, as shown from eq. 7.5.

As discussed later, in addition to the rotation axis $\boldsymbol{o}$ and rotation angle θ, another degree of freedom is the grain boundary plane. For example, $\Sigma5$ [001] grain boundary has three grain boundary planes, (130), (120), and (001), see Fig. 7.1. The grain planes (130) and (120) are parallel to the rotation axis [001] and belong to tilted grain boundaries, while the grain plane (001) is perpendicular to the rotation axis [001] and belongs to twisted grain boundary. In addition, to

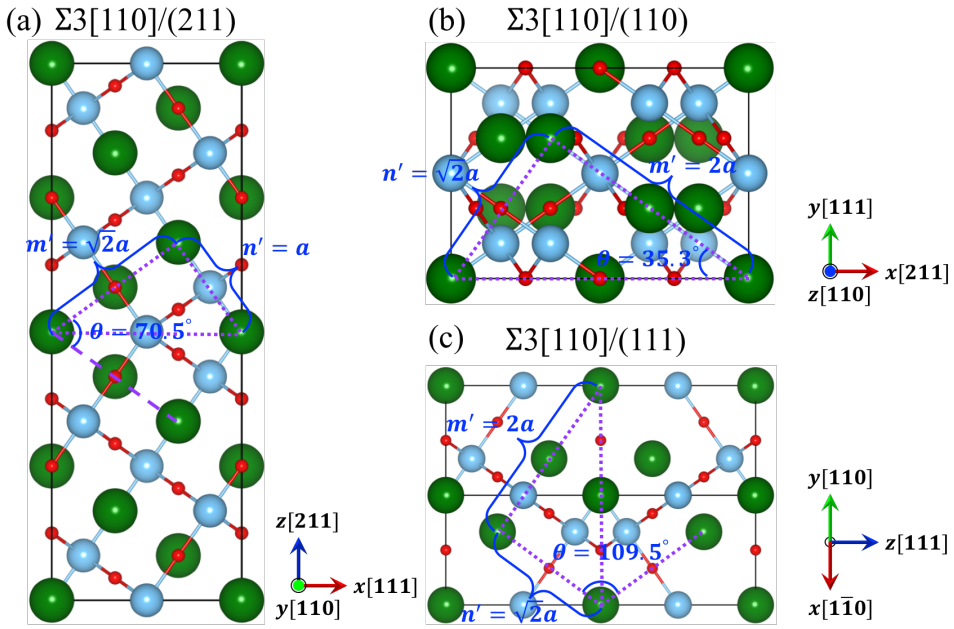

Figure 7.2: Σ3[110] grain boundary structures of cubic $SrTiO_3$. (a) Σ3[110]/(1$\bar{1}$2), (b) Σ3[110]/(111), and (c) Σ3[110]/(110). Σ3[110]/(111) is reduced primitive structure in which the angle between axis-*a* and *b* equals to 120 °.

have a clear presentation of the building procedure, we also show the Σ3 [110] and Σ3 [111] grain boundary structures of cubic $SrTiO_3$ in Fig. 7.2 and Fig. 7.3, respectively.

7.2.2 Rotation Matrix

After getting θ from a given Σ and ***o***, we are able to generate a rotation matrix (**R**) using the Rodrigues' rotation formula. [205] First, we define a unit vector $\boldsymbol{k} = [k_x, k_y, k_z]$, where $k_x^2+k_y^2+k_z^2=1$, which represents the rotation axis ***o*** [uvw], and a matrix ***K*** that denotes the cross-product matrix for the unit vector ***k***.

$$\boldsymbol{K} = \begin{bmatrix} 0 & -k_z & k_y \\ k_z & 0 & -k_x \\ -k_y & k_x & 0 \end{bmatrix} \tag{7.6}$$

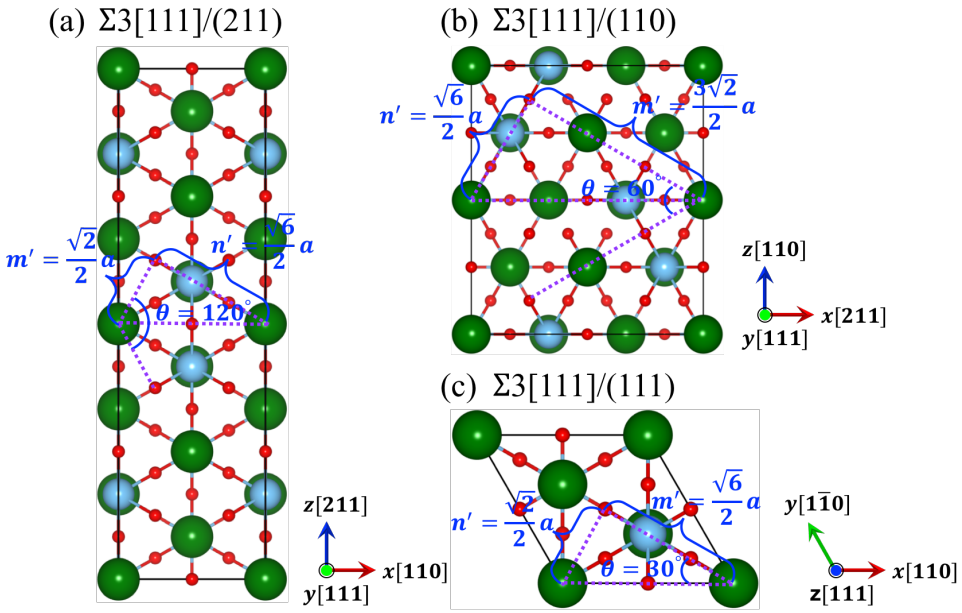

Figure 7.3: Σ3[111] grain boundary structures of cubic $SrTiO_3$. (a) Σ3[111]/(1$\bar{2}$1), (b) Σ3[111]/(10$\bar{1}$), and (c) Σ3[111]/(111). Σ3[111]/(111) is reduced primitive structure in which the angle between axis-*a* and *b* equals to 120 °.

Accordingly, a matrix $\boldsymbol{R}$ that describes a rotation with an angle θ in counterclockwise around the axis $\boldsymbol{k}$ can be given as:

$$\boldsymbol{R} = \mathbf{I} + (sin\theta)\boldsymbol{K} + (1 - cos\theta)\boldsymbol{K}^2 \tag{7.7}$$

where $\mathbf{I}$ is a 3×3 identity matrix.

7.2.3 CSL Matrix

Next step is to calculate CSL matrix from the rotation matrix $\mathbf{R}$. Here, we implement a so-called *O-lattice* theory introduced by Bollmann, [21] which is an effective tool to analyze the coincidence lattice points of two interpenetrating misoriented lattices of grains. The schematic illustration of applying *O-lattice* in deviating equivalence points in two lattices in a two-dimensional space is shown in Fig. 7.4. Assume that we have lattice $\mathbf{I}$ with basis lattice vectors $\boldsymbol{a}^{(I)}$ and $\boldsymbol{b}^{(I)}$, and lattice $\mathbf{II}$ with basis lattice vectors $\boldsymbol{a}^{(II)}$ and $\boldsymbol{b}^{(II)}$. An arbitrary point

within the elementary cell of lattice **I** can be described by a vector $\boldsymbol{x}^{(I)}$. $\boldsymbol{x}^{(I)}$ can be transformed into a vector $\boldsymbol{x}^{(II)}$ in lattice **II** by applying a transformation matrix **A**:

$$\boldsymbol{x}^{(II)} = \mathbf{A}\boldsymbol{x}^{(I)} \tag{7.8}$$

Therefore, the lattice point ($\boldsymbol{x}^{(II)}$) within the lattice **II** is an equivalent point to the one ($\boldsymbol{x}^{(I)}$) in crystal lattice **I**. Moreover, the coincidence point $\boldsymbol{x}^{(II)}$ also belong to both lattice **I**, and thus it can also be obtained from lattice **I** by adding a translation vector $\boldsymbol{t}^{(L)}$ to $\boldsymbol{x}^{(I)}$:

$$\boldsymbol{x}^{(II)} = \boldsymbol{x}^{(I)} + \boldsymbol{t}^{(L)} \tag{7.9}$$

By combining eq. 7.8 and 7.9, one can get:

$$(\mathbf{I} - \mathbf{A}^{-1})\boldsymbol{x}^{(II)} = \boldsymbol{t}^{(L)} \tag{7.10}$$

where **I** is the identity matrix, *i.e.*, unit transformation. Let us name all the coincidence points as $\boldsymbol{x}^{(0)}$, then the eq. 7.10 can be rewritten as:

$$(\mathbf{I} - \mathbf{A}^{-1})\boldsymbol{x}^{(0)} = \mathbf{T}\boldsymbol{x}^{(0)} = \boldsymbol{t}^{(L)} \tag{7.11}$$

$$\mathbf{I} - \mathbf{A}^{-1} = \mathbf{T} \tag{7.12}$$

The solution to this equation requires that $\left|\mathbf{I} - \mathbf{A}^{-1}\right| \neq 0$. It is convenient to apply transformations in the conventional crystal coordinate systems. Accordingly, the corresponding transformation matrices in the crystal coordinate system are labeled as $\mathbf{A}'$ and $\mathbf{T}'$, and the following expressions are to be calculated: [82]

$$\mathbf{I} - \mathbf{A}'^{-1} = \mathbf{T}' = \mathbf{I} - \mathbf{U}\mathbf{S}^{-1}\mathbf{R}^{-1}\mathbf{S} \tag{7.13}$$

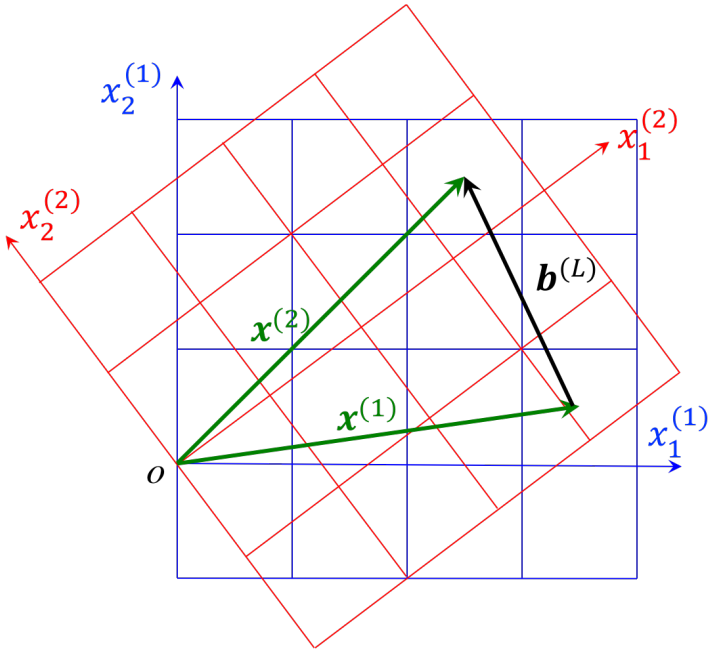

Figure 7.4: Schematic illustration of general operation on coincidence point in a two-dimensional space.

$$\det(\mathbf{T}') = \frac{n}{\Sigma} \tag{7.14}$$

$$\mathbf{X}'^{(0)} = \mathbf{T}'^{-1} \tag{7.15}$$

where **R** is rotation matrix as calculated before; n is an integer number calculated from eq. 7.14; $\mathbf{X}'^{(0)}$ is a matrix whose three column vectors are unit vectors of the O-lattice; **S** is the structure matrix which contains the unit vectors of the crystal coordinate system expressed in the orthonormal coordinates of the conventional crystal, and **S** = **I** for conventional cubic structure; **U** is a unimodular transformation matrix (det(**U**)=$\pm$1) that is used to keep $\det(\mathbf{T}') \neq 0$.

After obtaining $\mathbf{X}'^{(0)}$, next we are able to determine CSL matrix $\mathbf{C}'$ (in crystal coordinate system). Note that $\mathbf{C}'$ should always consist of integer numbers and can be determined as two steps: i) operate on two columns of $\mathbf{X}'^{(0)}$ to let them become integers and meanwhile keep their determinant unchanged; ii) multiply the third column by n so that the determinant of matrix $\mathbf{C}'$ equals to Σ. The calculated CSL matrix $\mathbf{C}'$ can be further reshaped so that each of its column vectors has the shorted length. Moreover, the CSL matrix $\mathbf{C}'$ will be orthogonalized, with the third

column vector same as the rotation axis. Note that the generated CSL matrix will be applied on a cubic lattice and therefore the CSL matrix has one important property. That is, the three numbers in each column of the CSL matrix correspond to a group of miller indices that represent a surface plane and also surface normal, since basis lattice vectors of the input crystal are orthogonal, see the table of CSL matrix in the Appendix. Also note that the CSL matrix can also be applied on a tetragonal lattice if the rotation axis is normal to the tetragonal plane, such as tetragonal TiO_2 lattice with [001] rotation.

7.2.4 Create Grain Boundary

A grain boundary consists of two grains that are symmetrical with the grain boundary plane as the mirror plane. [145] The orientation of a grain boundary plane is given by a unit vector $\boldsymbol{n}$, *i.e.*, the normal to the grain boundary plane. [146] Using the generated CSL matrix, we can build a new crystal lattice that is one grain of the grain boundary (named as grain A). The other grain of the grain boundary (named as grain B) can be obtained by applying mirror symmetry operation on grain A. After getting two grains A and B, we can build a grain boundary by combining the two grains. As discussed above, the three numbers in each column vector of a CSL matrix indicate a surface plane (also a surface normal, *i.e.*, a direction), and the third column of the CSL matrix is set the same with the rotation axis. As a result, the generated new crystal lattice from the CSL matrix has three surface planes (corresponding to three columns of a CSL matrix) and each of them can serve as a grain boundary plane. Note that the relationship between the rotation axis ($\boldsymbol{o}$) and the normal to the grain boundary plane ($\boldsymbol{n}$) determines the type of generated grain boundaries: *tilt* grain boundary for $\boldsymbol{o} \perp \boldsymbol{n}$ and *twist* grain boundary for $\boldsymbol{o} \parallel \boldsymbol{n}$. Therefore, we are able to generate two *tilt* grain boundaries by setting first two surface planes as the grain boundary plane, and one *twist* grain boundary by setting third surface plane as the grain boundary plane. In other words, one CSL matrix corresponds to three grain boundaries.

By summarizing the above building procedures, we show the complete workflow in

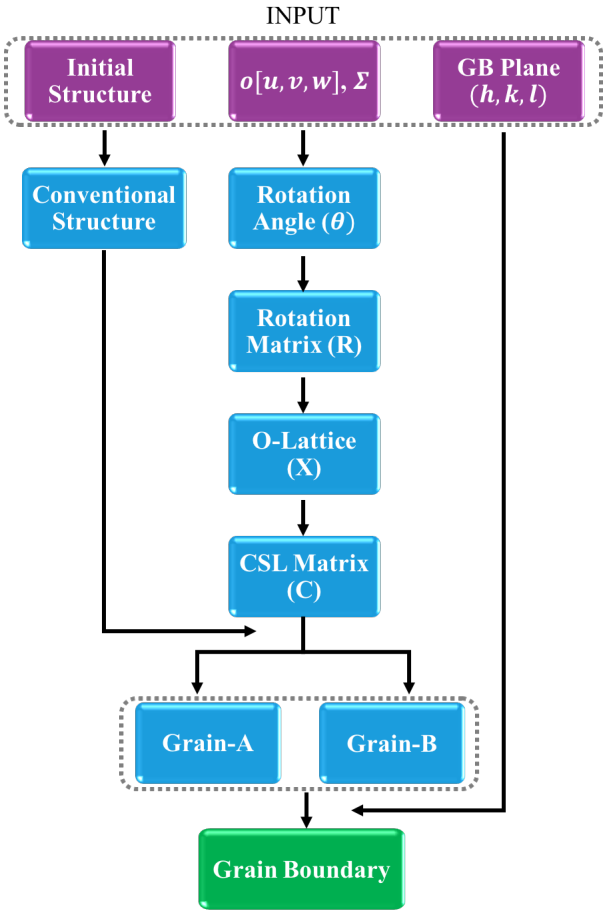

Figure 7.5: The complete building procedure for generating atomic coordinates of periodic grain boundary models from the input Σ, rotation axis, grain boundary plane and initial crystal structure

Fig. 7.5. The algorithm is implemented in an open-source python library. The representation and manipulation of structures are treated through either pymatgen [193] or structural class of AFLOW. [54] Also, to demonstrate the efficiency of our algorithm, we list the required CPU time to generate grain boundary structures for $SrTiO_3$, cubic $CH_3NH_3SnI_3$, and tetragonal anatase TiO_2, see Table 7.1. The total number of atoms in the grain boundary structure was also listed for each Σ.

Table 7.1: Required CPU time (in second) to generate grain boundary structures for $SrTiO_3$, cubic $CH_3NH_3SnI_3$, and tetragonal anatase TiO_2. Note that we excluded the time required to write to file. The total number (No.) of atoms in the grain boundary structure is listed for each Σ.

	$SrTiO_3$		$CH_3NH_3SnI_3$		TiO_2	
Σ	No. of atoms	Time (sec)	No. of atoms	Time (sec)	No. of atoms	Time (sec)
5	50	0.05	120	0.06	120	0.06
13	130	0.02	312	0.04	312	0.04
17	170	0.02	408	0.05	408	0.05
25	250	0.03	600	0.07	600	0.07
29	290	0.04	696	0.08	696	0.08
37	370	0.04	888	0.10	888	0.10
41	410	0.06	984	0.11	984	0.11
53	530	0.06	1272	0.14	1272	0.14
61	610	0.07	1464	0.16	1464	0.17
65	650	0.07	1560	0.16	1560	0.16
73	730	0.09	1752	0.20	1752	0.20
85	850	0.09	2040	0.23	2040	0.22
89	890	0.10	2136	0.23	2136	0.23
97	970	0.12	2328	0.26	2328	0.27
101	1010	0.10	2424	0.24	2424	0.25
109	1090	0.14	2616	0.30	2616	0.31
113	1130	0.12	2712	0.28	2712	0.28
125	1250	0.14	3000	0.34	3000	0.35
137	1370	0.18	3288	0.38	3288	0.37
145	1450	0.16	3480	0.36	3480	0.36
149	1490	0.17	3576	0.39	3576	0.40

7.3 Example of Building Grain Boundary

In this section, we take the Σ5[001] grain boundary as an example to illustrate the procedure of generating CSL matrix and building grain boundary. For Σ = 5 and [*uvw*]=[001] , by using eqs. 7.3 − 7.5, we can get (*m*, *n*) = (1, 2), (1, 3), (2, 1) and (3, 1). By plugging these numbers into eq. 7.4, one can get θ = 126.9°, 143.1°, 53.1° and 36.9°, respectively. As discussed before, (*m*, *n*) = (1, 2) and (*m*, *n*) = (2, 1) (or θ = 126.9° and θ = 53.1°) refer to the same grain boundary, and also do for (*m*, *n*) = (1, 3) and (*m*, *n*) = (3, 1) (or θ = 143.1° and θ = 36.9°).

For the rotation axis [001], we have the unit vector $\boldsymbol{k}$ = [0, 0, 1]. Then using θ = 53.1° and eqs. 7.6 − 7.7, we are able to get a rotation matrix **R**:

$$\mathbf{R} = \frac{1}{5}\begin{bmatrix} 3 & -4 & 0 \\ 4 & 3 & 0 \\ 0 & 0 & 5 \end{bmatrix}$$

where $S = 5$.

Choose **U**:

$$\mathbf{U} = \begin{bmatrix} 1 & 0 & 1 \\ 0 & 1 & 0 \\ 0 & 1 & 1 \end{bmatrix}$$

and plug it with **R** into eqs. 7.13 and 7.15, we can get:

$$\mathbf{T}' = \frac{1}{5}\begin{bmatrix} 2 & -4 & -5 \\ 4 & 2 & 0 \\ 4 & -3 & 0 \end{bmatrix}$$

and

$$\mathbf{X}'^{(0)} = \begin{bmatrix} 0 & 3/4 & 1/2 \\ 0 & 1 & -1 \\ -1 & -1/2 & 1 \end{bmatrix}$$

To obtain a CSL matrix, we make the matrix $\mathbf{X}'^{(0)}$ integral with each column vector having the shortest length, and meanwhile make its determinant equal to Σ, and get the following

matrix **C**:

$$\mathbf{C} = \begin{bmatrix} 0 & -1 & 2 \\ 0 & 2 & 1 \\ -1 & 0 & 0 \end{bmatrix}$$

We further reshape the matrix **C** by making its each column vector orthogonal and setting its third column vector same with the rotation axis $\boldsymbol{o}$, and get the CSL matrix:

$$\mathbf{C}' = \begin{bmatrix} 2 & 1 & 0 \\ -1 & 2 & 0 \\ 0 & 0 & 1 \end{bmatrix}$$

As mentioned above, each column vector of $\mathbf{C}'$ represents a grain boundary plane for Σ5[001] GB structure. Therefore, we have three grain boundary planes: $(2\bar{1}0)$, (120) and (001). Σ5[001]/$(2\bar{1}0)$ and Σ5[001]/(120) refer to the same tilt grain boundary, and Σ5[001]/(001) is a twist grain boundary. As a example, Fig. 7.6 shows the grain boundary structures for cubic hybrid perovskite $CH_3NH_3SnI_3$: (a) Σ5[001]/(001) and (b) Σ5[001]/(120). [13]

7.4 Conclusion

We describe an algorithm implemented in an open-source python library for generating periodic tilt and twist grain boundary models in a universal fashion for *ab-initio* and classical materials modeling. The algorithm first calculates the rotation angle from a given Sigma (Σ) value and rotation axis, and then generate a rotation matrix from the rotation angle. Next, the algorithm will build CSL matrix using the rotation matrix and Σ value. Finally, the algorithm will generate two CSL grains from CSL matrix, and combine them together to build a grain boundary based on the selected grain boundary plane. This software framework is expected to

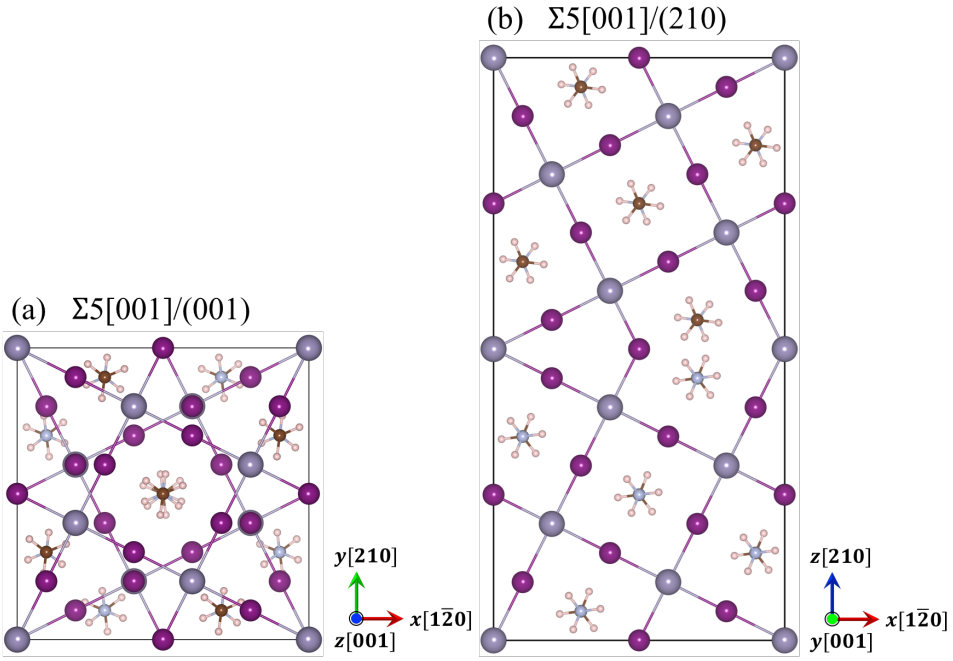

Figure 7.6: Constructed grain boundary of cubic hybrid perovskite $CH_3NH_3SnI_3$: (a) Σ5[001]/(001) and (b) Σ5[001]/(120).

enable high-throughput computational studies and materials informatics of grain boundary in materials science. The source code is free and available online: aimsgb.org.

7.5 Acknowledgements

Chapter 7, in full, is currently being submitted for publication of the material "Aimsgb: An Algorithm and Open-Source Python Library to Generate Periodic Grain Boundary Structures". Jianli Cheng, Jian Luo, Kesong Yang. The dissertation author was the primary investigator and author of this paper.

Chapter 8

Summary and Future Directions

Interfaces are ubiquitous in nanocrystalline materials and can give rise to a wide range of interesting and novel functionalities. To fully exploit this richness, it is essential to understand and control the physics emerging at interfaces with atomic precision. In this thesis, we mainly concerned ourselves with the formation of two-dimensional electron gas (2DEG) at complex oxide heterointerfaces. Our efforts centered on studying the electronic and structural properties of different 2DEG heterostructures (HS), with the goal of designing novel 2DEG HS using first-principles methods.

The prototypical complex oxide HS that exhibits 2DEG is based on interfacing epitaxial $LaAlO_3$ and $SrTiO_3$. Diverse phenomena have been observed at its interface and it is promising for designing multifunctional devices formed from this one HS. However, improving the 2DEG mobility of $LaAlO_3/SrTiO_3$ HS is still a formidable challenge. One possible way of improving the 2DEG mobility is via δ-doping at the heterointerface. In the first project, we studied the δ-doping effects on the electronic and energetic properties of $LaAlO_3/SrTiO_3$ HS with 23 transition-metal (TM) dopants. It has been found that there is a trade-off between achieving small electron effective mass and obtaining an energetically favorable TM-doped $LaAlO_3/SrTiO_3$ HS. More importantly, in addition to the experimentally confirmed Mn dopant, we proposed that Fe, Co, Ni, Ru, Rh, Pd,

Os and Ir elements can also be promising dopants to yield light effective mass bands and good energetic stability.

In addition to the intensively investigated $LaAlO_3/SrTiO_3$ HS, other polar/nonpolar HS have also been explored to create the interfacial 2DEG, such as the HS formed by $LaAlO_3$ and anatase TiO_2, which exhibits higher sheet carrier density and room-temperature mobility than $LaAlO_3/SrTiO_3$. Such enhanced electronic properties could be attributed to the different growth orders in these two HS. In the second project, we compared the electronic and energetic properties of $TiO_2/LaAlO_3$ and $LaAlO_3/TiO_2$ HS. We found that $TiO_2/LaAlO_3$ is intrinsically metallic, with a larger interfacial charge carrier density and smaller electron effective mass than $LaAlO_3/TiO_2$, which shows an insulator-to-metal transition as the $LaAlO_3$ film thickness increases up to 4 unit cells. The interfacial energetics results indicate that $TiO_2/LaAlO_3$ has a stronger interface cohesion and is energetically more favorable than $LaAlO_3/TiO_2$.

In the third project, we introduced a hitherto unknown 2DEG formed at the interface between spinel $MgAl_2O_4$ and $SrTiO_3$. Our integrated approach, combining experimental measurements and first-principles calculations, reveals that an atomic-thin interfacial Ti-Al-O layer with a thickness of about 4 $\AA$ is key to the observed metallic transport. The critical film thickness for the insulator-to-metal transition is around 32 $\AA$, which can be explained by the co-existence of interfacial antisite defects and surface oxygen vacancies. Our magnetoresistance measurement reveals a strong Rashba spin-orbit interaction at the MAO/STO interface. The 2DEG observed at spinel/perovskite interface could shed light on the nature of 2DEG at oxide interfaces, and imply the existence of emergent phenomena at the interfaces between spinel group minerals and perovskite oxides. Future work in this direction is to study the 2DEG at spinel/perovskite interface of $\gamma-Al_2O_3/SrTiO_3$. The electron mobility at this interface (140 000cm^2/V s at 2K) exceeds those hitherto observed in all-perovskite HS, thus shows promise for future applications in all-oxide devices. [43, 225] Also, similar to the $LaAlO_3/SrTiO_3$ HS, the $\gamma-Al_2O_3/SrTiO_3$ HS also shows a polar discontinuity and a critical thickness behavior of the interface conductivity.

In the first three projects, we have studied the polar discontinuity induced 2DEG in polar/nonpolar oxide HS. As we mentioned in Chapter 1, nonpolar/nonpolar oxide HS have also been found to exhibit 2DEG via polarization discontinuity. In the fourth project, we explored the possibility of producing 2DEG in nonpolar/nonpolar $AHfO_3/SrTiO_3$ HS (A=Ca, Sr, Ba). We showed that as film thickness increases, an insulator-to-metal transition is found in all HS and unlike polar/nonpolar and polar/polar HS, which rely on a specific interfacial termination to form the 2DEG, the creation of 2DEG in $AHfO_3/SrTiO_3$ is less sensitive to the interfacial structure and can be formed at both interfacial terminations. The lattice-mismatch-induced compression strain from the substrate $SrTiO_3$ leads to a large polarization in the film $AHfO_3$, which then drives the charge transfer from the film to the substrate and results in a 2DEG at the interface. Following this work, in the fifth project, we carried out a high-throughput computational screening approach to design all the possible nonpolar/nonpolar perovskite oxide HS that have the potential to produce 2DEG. Using a group of combinatorial materials descriptors, we have successfully identified 34 nonpolar piezoelectric perovskite oxides, from which we designed more than 300 novel nonpolar/nonpolar 2DEG HS. Currently, we are in progress to construct a 2DEG-HS database, which can be used for on-demand querying and retrieval of data, to store the calculated insulator-to-metal transition critical thicknesses of all the HS, as well as their accompanying meta-data (e.g., input structure, tolerance factor, band edges, etc.). Future work in this direction is high-throughput computational screening of double perovskite structures ($AA'BB'O_6$), with the aim of identifying those that can exhibit ferroelectric polarization. The presence of four different metal ions gives rise to an incredible diversity of structural combinations and physical phenomena, such as the ferroelectric $NaLaMnWO_6$. [74, 127]

In the sixth project, we introduced an efficient and open-source Python library, aimsgb, for generating atomic coordinates in periodic grain boundary models. It is designed to construct various grain boundary structures from cubic and non-cubic initial configurations. A convenient command line tool has also been provided to enable easy and fast construction of tilt and twist

boundaries by assigning the degree of fit (Σ), rotation axis, grain boundary plane and initial crystal structure. Aimsgb is expected to greatly facilitate the theoretical and experimental investigation of grain boundary properties.

In summary, our work on the formation of 2DEG at perovskite oxide heterointerfaces have lead us to understand the charge transfer mechanisms, electronic and structural properties of different 2DEG HS. This fundamental research is therefore motivated by a well-defined application, and serves as a nice illustration of the power of first-principles calculations in designing and understanding of new and unexplored materials.

Appendix A

Efficiency of aimsgb

Table A.1: Required CPU time (second) to generate grain boundary structures for $SrTiO_3$, cubic $CH_3NH_3SnI_3$, and tetragonal anatase TiO_2, including the time of writing to file. The total number (No.) of atoms in the grain boundary structure is listed for each Σ.

	$SrTiO_3$		$CH_3NH_3SnI_3$		TiO_2	
Σ	No. of atoms	Time (sec)	No. of atoms	Time (sec)	No. of atoms	Time (sec)
5	50	0.06	120	0.08	120	0.07
13	130	0.03	312	0.10	312	0.10
17	170	0.04	408	0.15	408	0.15
25	250	0.07	600	0.30	600	0.29
29	290	0.09	696	0.37	696	0.37
37	370	0.13	888	0.57	888	0.57
41	410	0.16	984	0.69	984	0.68
53	530	0.23	1272	1.10	1272	1.12
61	610	0.29	1464	1.43	1464	1.43
65	650	0.32	1560	1.61	1560	1.59
73	730	0.41	1752	2.01	1752	1.99
85	850	0.52	2040	2.69	2040	2.68
89	890	0.57	2136	2.91	2136	2.90
97	970	0.68	2328	3.49	2328	3.46
101	1010	0.71	2424	3.72	2424	3.69
109	1090	0.84	2616	4.33	2616	4.34
113	1130	0.88	2712	4.64	2712	4.60
125	1250	1.07	3000	5.64	3000	5.67
137	1370	1.29	3288	6.98	3288	6.74
145	1450	1.40	3480	7.69	3480	7.45
149	1490	1.48	3576	8.23	3576	8.01

Appendix B

Tables of Σ, rotation angle θ, GB plane and CSL matrix

Table B.1: Lists of Σ, rotation angle θ, GB plane and CSL matrix for rotation axis ***o*** along [001], [110] and [111]. *Indicates the twisted grain boundary and the others are tilted grain boundary.

[001]				[110]				[111]			
Σ	θ	GB Plane	CSL	Σ	θ	GB Plane	CSL	Σ	θ	GB Plane	CSL
5	53.13	$(2\bar{1}0)$ (120) $(001)*$	$\begin{pmatrix} 2 & 1 & 0 \\ -1 & 2 & 0 \\ 0 & 0 & 1 \end{pmatrix}$	3	70.53	$(\bar{1}11)$ $(1\bar{1}2)$ $(110)*$	$\begin{pmatrix} -1 & 1 & 1 \\ 1 & -1 & 1 \\ 1 & 2 & 0 \end{pmatrix}$	3	60.00	$(1\bar{2}1)$ $(10\bar{1})$ $(111)*$	$\begin{pmatrix} 1 & 1 & 1 \\ -2 & 0 & 1 \\ 1 & -1 & 1 \end{pmatrix}$
	36.87	$(3\bar{1}0)$ (130) $(001)*$	$\begin{pmatrix} 3 & 1 & 0 \\ -1 & 3 & 0 \\ 0 & 0 & 1 \end{pmatrix}$								
13	67.38	$(3\bar{2}0)$ (230) $(001)*$	$\begin{pmatrix} 3 & 2 & 0 \\ -2 & 3 & 0 \\ 0 & 0 & 1 \end{pmatrix}$	9	38.94	$(\bar{1}1\bar{4})$ $(\bar{2}21)$ $(110)*$	$\begin{pmatrix} -1 & -2 & 1 \\ 1 & 2 & 1 \\ -4 & 1 & 0 \end{pmatrix}$	7	38.21	$(1\bar{3}2)$ $(5\bar{1}\bar{4})$ $(111)*$	$\begin{pmatrix} 1 & 5 & 1 \\ -3 & -1 & 1 \\ 2 & -4 & 1 \end{pmatrix}$
	22.62	$(5\bar{1}0)$ (150) $(001)*$	$\begin{pmatrix} 5 & 1 & 0 \\ -1 & 5 & 0 \\ 0 & 0 & 1 \end{pmatrix}$								
17	28.07	(410) $(\bar{1}40)$ $(001)*$	$\begin{pmatrix} 4 & -1 & 0 \\ 1 & 4 & 0 \\ 0 & 0 & 1 \end{pmatrix}$	11	50.48	$(\bar{3}32)$ $(1\bar{1}3)$ $(110)*$	$\begin{pmatrix} -3 & 1 & 1 \\ 3 & -1 & 1 \\ 2 & 3 & 0 \end{pmatrix}$	13	27.80	$(1\bar{4}3)$ $(7\bar{2}\bar{5})$ $(111)*$	$\begin{pmatrix} 1 & 7 & 1 \\ -4 & -2 & 1 \\ 3 & -5 & 1 \end{pmatrix}$
	61.93	(530) $(\bar{3}50)$ $(001)*$	$\begin{pmatrix} 5 & -3 & 0 \\ 3 & 5 & 0 \\ 0 & 0 & 1 \end{pmatrix}$								
25	73.74	$(4\bar{3}0)$ (340) $(001)*$	$\begin{pmatrix} 4 & 3 & 0 \\ -3 & 4 & 0 \\ 0 & 0 & 1 \end{pmatrix}$	17	86.63	$(2\bar{2}3)$ $(3\bar{3}\bar{4})$ $(110)*$	$\begin{pmatrix} 2 & 3 & 1 \\ -2 & -3 & 1 \\ 3 & -4 & 0 \end{pmatrix}$	19	46.83	$(2\bar{5}3)$ $(8\bar{1}\bar{7})$ $(111)*$	$\begin{pmatrix} 2 & 8 & 1 \\ -5 & -1 & 1 \\ 3 & -7 & 1 \end{pmatrix}$
	16.26	$(7\bar{1}0)$ (170) $(001)*$	$\begin{pmatrix} 7 & 1 & 0 \\ -1 & 7 & 0 \\ 0 & 0 & 1 \end{pmatrix}$								
29	43.60	$(\bar{2}50)$ $(\bar{5}\bar{2}0)$ $(001)*$	$\begin{pmatrix} -2 & -5 & 0 \\ 5 & -2 & 0 \\ 0 & 0 & 1 \end{pmatrix}$	19	26.53	$(\bar{3}31)$ $(1\bar{1}6)$ $(110)*$	$\begin{pmatrix} -3 & 1 & 1 \\ 3 & -1 & 1 \\ 1 & 6 & 0 \end{pmatrix}$	21 (7)	21.79	$(1\bar{5}4)$ $(3\bar{1}\bar{2})$ $(111)*$	$\begin{pmatrix} 1 & 3 & 1 \\ -5 & -1 & 1 \\ 4 & -2 & 1 \end{pmatrix}$
	46.40	$(\bar{3}70)$ $(\bar{7}\bar{3}0)$ $(001)*$	$\begin{pmatrix} -3 & -7 & 0 \\ 7 & -3 & 0 \\ 0 & 0 & 1 \end{pmatrix}$								
37	18.92	(610) $(\bar{1}60)$ $(001)*$	$\begin{pmatrix} 6 & -1 & 0 \\ 1 & 6 & 0 \\ 0 & 0 & 1 \end{pmatrix}$	27	31.59	$(\bar{5}52)$ $(1\bar{1}5)$ $(110)*$	$\begin{pmatrix} -5 & 1 & 1 \\ 5 & -1 & 1 \\ 2 & 5 & 0 \end{pmatrix}$	31	17.90	$(1\ \bar{6}\ 5)$ $(11\ \bar{4}\ \bar{7})$ $(1\ 1\ 1)*$	$\begin{pmatrix} 1 & 11 & 1 \\ -6 & -4 & 1 \\ 5 & -7 & 1 \end{pmatrix}$
	71.08	(750) $(\bar{5}70)$ $(001)*$	$\begin{pmatrix} 7 & -5 & 0 \\ 5 & 7 & 0 \\ 0 & 0 & 1 \end{pmatrix}$								
41	77.32	$(5\bar{4}0)$ (450) $(001)*$	$\begin{pmatrix} 5 & 4 & 0 \\ -4 & 5 & 0 \\ 0 & 0 & 1 \end{pmatrix}$	33	20.05	$(\bar{4}41)$ $(1\bar{1}8)$ $(110)*$	$\begin{pmatrix} -4 & 1 & 1 \\ 4 & -1 & 1 \\ 1 & 8 & 0 \end{pmatrix}$	37	50.57	$(3\ \bar{7}\ 4)$ $(11\ \bar{1}\ 1\bar{0})$ $(1\ 1\ 1)*$	$\begin{pmatrix} 3 & 11 & 1 \\ -7 & -1 & 1 \\ 4 & -10 & 1 \end{pmatrix}$
	12.68	$(9\bar{1}0)$ (190) $(001)*$	$\begin{pmatrix} 9 & 1 & 0 \\ -1 & 9 & 0 \\ 0 & 0 & 1 \end{pmatrix}$								
53	31.89	$(\bar{2}70)$ $(\bar{7}\bar{2}0)$ $(001)*$	$\begin{pmatrix} -2 & -7 & 0 \\ 7 & -2 & 0 \\ 0 & 0 & 1 \end{pmatrix}$	41	55.88	$(\bar{3}3\bar{8})$ $(\bar{4}43)$ $(110)*$	$\begin{pmatrix} -3 & -4 & 1 \\ 3 & 4 & 1 \\ -8 & 3 & 0 \end{pmatrix}$	39 (13)	32.20	$(2\bar{7}5)$ $(4\bar{1}\bar{3})$ $(111)*$	$\begin{pmatrix} 2 & 4 & 1 \\ -7 & -1 & 1 \\ 5 & -3 & 1 \end{pmatrix}$
	58.11	$(\bar{5}90)$ $(\bar{9}\bar{5}0)$ $(001)*$	$\begin{pmatrix} -5 & -9 & 0 \\ 9 & -5 & 0 \\ 0 & 0 & 1 \end{pmatrix}$								

[001]				[110]				[111]			
Σ	θ	GB Plane	CSL	Σ	θ	GB Plane	CSL	Σ	θ	GB Plane	CSL
61	79.61	$(6\bar{5}0)$ (560) $(001)*$	$\begin{pmatrix} 6 & 5 & 0 \\ -5 & 6 & 0 \\ 0 & 0 & 1 \end{pmatrix}$	43	80.63	$(3\bar{3}5)$ $(5\bar{5}\bar{6})$ $(110)*$	$\begin{pmatrix} 3 & 5 & 1 \\ -3 & -5 & 1 \\ 5 & -6 & 0 \end{pmatrix}$	43	15.18	$(1\ \bar{7}\ 6)$ $(13\ \bar{5}\ \bar{8})$ $(1\ 1\ 1)*$	$\begin{pmatrix} 1 & 13 & 1 \\ -7 & -5 & 1 \\ 6 & -8 & 1 \end{pmatrix}$
	10.39	$(11\ \bar{1}\ 0)$ $(1\ 11\ 0)$ $(0\ 0\ 1)*$	$\begin{pmatrix} 11 & 1 & 0 \\ -1 & 11 & 0 \\ 0 & 0 & 1 \end{pmatrix}$								
65	14.25	(810) $(\bar{1}80)$ $(001)*$	$\begin{pmatrix} 8 & -1 & 0 \\ 1 & 8 & 0 \\ 0 & 0 & 1 \end{pmatrix}$	51	16.10	$(\bar{5}\ 5\ 1)$ $(1\ \bar{1}\ 10)$ $(1\ 1\ 0)*$	$\begin{pmatrix} -5 & 1 & 1 \\ 5 & -1 & 1 \\ 1 & 10 & 0 \end{pmatrix}$	49	43.57	$(3\ \bar{8}\ 5)$ $(13\ \bar{2}\ \bar{1}1)$ $(1\ 1\ 1)*$	$\begin{pmatrix} 3 & 13 & 1 \\ -8 & -2 & 1 \\ 5 & -11 & 1 \end{pmatrix}$
	75.75	$(11\ 3\ 0)$ $(\bar{3}\ 11\ 0)$ $(0\ 0\ 1)*$	$\begin{pmatrix} 11 & -3 & 0 \\ 3 & 11 & 0 \\ 0 & 0 & 1 \end{pmatrix}$								
73	41.11	$(\bar{3}80)$ $(\bar{8}\bar{3}0)$ $(001)*$	$\begin{pmatrix} -3 & -8 & 0 \\ 8 & -3 & 0 \\ 0 & 0 & 1 \end{pmatrix}$	57	44.00	$(\bar{7}74)$ $(2\bar{2}7)$ $(110)*$	$\begin{pmatrix} -7 & 2 & 1 \\ 7 & -2 & 1 \\ 4 & 7 & 0 \end{pmatrix}$	57 (19)	13.17	$(1\bar{8}7)$ $(5\bar{2}\bar{3})$ $(111)*$	$\begin{pmatrix} 1 & 5 & 1 \\ -8 & -2 & 1 \\ 7 & -3 & 1 \end{pmatrix}$
	48.89	$(\bar{5}\ 11\ 0)$ $(1\bar{1}\ \bar{5}\ 0)$ $(0\ 0\ 1)*$	$\begin{pmatrix} -5 & -11 & 0 \\ 11 & -5 & 0 \\ 0 & 0 & 1 \end{pmatrix}$								
85	81.20	$(7\bar{6}0)$ (670) $(001)*$	$\begin{pmatrix} 7 & 6 & 0 \\ -6 & 7 & 0 \\ 0 & 0 & 1 \end{pmatrix}$	59	45.98	$(\bar{3}\ 3\ 1\bar{0})$ $(\bar{5}\ 5\ 3)$ $(1\ 1\ 0)*$	$\begin{pmatrix} -3 & -5 & 1 \\ 3 & 5 & 1 \\ -10 & 3 & 0 \end{pmatrix}$	61	52.66	$(4\ \bar{9}\ 5)$ $(14\ \bar{1}\ 1\bar{3})$ $(1\ 1\ 1)*$	$\begin{pmatrix} 4 & 14 & 1 \\ -9 & -1 & 1 \\ 5 & -13 & 1 \end{pmatrix}$
	8.80	$(13\ \bar{1}\ 0)$ $(1\ 13\ 0)$ $(0\ 0\ 1)*$	$\begin{pmatrix} 13 & 1 & 0 \\ -1 & 13 & 0 \\ 0 & 0 & 1 \end{pmatrix}$								
89	64.01	$(8\bar{5}0)$ (580) $(001)*$	$\begin{pmatrix} 8 & 5 & 0 \\ -5 & 8 & 0 \\ 0 & 0 & 1 \end{pmatrix}$	67	62.44	$(\bar{7}76)$ $(3\bar{3}7)$ $(110)*$	$\begin{pmatrix} -7 & 3 & 1 \\ 7 & -3 & 1 \\ 6 & 7 & 0 \end{pmatrix}$	67	24.43	$(2\ \bar{9}\ 7)$ $(16\ \bar{5}\ \bar{1}1)$ $(1\ 1\ 1)*$	$\begin{pmatrix} 2 & 16 & 1 \\ -9 & -5 & 1 \\ 7 & -11 & 1 \end{pmatrix}$
	25.99	$(13\ \bar{3}\ 0)$ $(3\ 13\ 0)$ $(0\ 0\ 1)*$	$\begin{pmatrix} 13 & 3 & 0 \\ -3 & 13 & 0 \\ 0 & 0 & 1 \end{pmatrix}$								
97	47.92	$(9\bar{4}0)$ (490) $(001)*$	$\begin{pmatrix} 9 & 4 & 0 \\ -4 & 9 & 0 \\ 0 & 0 & 1 \end{pmatrix}$	73	13.44	$(\bar{6}\ 6\ 1)$ $(1\ \bar{1}\ 12)$ $(1\ 1\ 0)*$	$\begin{pmatrix} -6 & 1 & 1 \\ 6 & -1 & 1 \\ 1 & 12 & 0 \end{pmatrix}$	73	11.64	$(1\ \bar{9}\ 8)$ $(17\ \bar{7}\ 1\bar{0})$ $(1\ 1\ 1)*$	$\begin{pmatrix} 1 & 17 & 1 \\ -9 & -7 & 1 \\ 8 & -10 & 1 \end{pmatrix}$
	42.08	$(13\ \bar{5}\ 0)$ $(5\ 13\ 0)$ $(0\ 0\ 1)*$	$\begin{pmatrix} 13 & 5 & 0 \\ -5 & 13 & 0 \\ 0 & 0 & 1 \end{pmatrix}$								
101	11.42	$(10\ 1\ 0)$ $(\bar{1}\ 10\ 0)$ $(0\ 0\ 1)*$	$\begin{pmatrix} 10 & -1 & 0 \\ 1 & 10 & 0 \\ 0 & 0 & 1 \end{pmatrix}$	81	77.88	$(4\bar{4}7)$ $(7\bar{7}8)$ $(110)*$	$\begin{pmatrix} 4 & 7 & 1 \\ -4 & -7 & 1 \\ 7 & -8 & 0 \end{pmatrix}$	79	33.99	$(3\ 1\bar{0}\ 7)$ $(17\ \bar{4}\ 1\bar{3})$ $(1\ 1\ 1)*$	$\begin{pmatrix} 3 & 17 & 1 \\ -10 & -4 & 1 \\ 7 & -13 & 1 \end{pmatrix}$
	78.58	$(11\ 9\ 0)$ $(\bar{9}\ 11\ 0)$ $(0\ 0\ 1)*$	$\begin{pmatrix} 11 & -9 & 0 \\ 9 & 11 & 0 \\ 0 & 0 & 1 \end{pmatrix}$								
109	33.40	$(\bar{3}\ 10\ 0)$ $(1\bar{0}\ \bar{3}\ 0)$ $(0\ 0\ 1)*$	$\begin{pmatrix} -3 & -10 & 0 \\ 10 & -3 & 0 \\ 0 & 0 & 1 \end{pmatrix}$	83	17.86	$(\bar{9}92)$ $(1\bar{1}9)$ $(110)*$	$\begin{pmatrix} -9 & 1 & 1 \\ 9 & -1 & 1 \\ 2 & 9 & 0 \end{pmatrix}$	91	10.42	$(1\ 1\bar{0}\ 9)$ $(19\ \bar{8}\ 1\bar{1})$ $(1\ 1\ 1)*$	$\begin{pmatrix} 1 & 19 & 1 \\ -10 & -8 & 1 \\ 9 & -11 & 1 \end{pmatrix}$
	56.60	$(\bar{7}\ 13\ 0)$ $(1\bar{3}\ \bar{7}\ 0)$ $(0\ 0\ 1)*$	$\begin{pmatrix} -7 & -13 & 0 \\ 13 & -7 & 0 \\ 0 & 0 & 1 \end{pmatrix}$								

[001]				[110]				[111]			
Σ	θ	GB Plane	CSL	Σ	θ	GB Plane	CSL	Σ	θ	GB Plane	CSL
113	82.37	$(8\bar{7}0)$ (780) $(001)*$	$\begin{pmatrix} 8 & 7 & 0 \\ -7 & 8 & 0 \\ 0 & 0 & 1 \end{pmatrix}$	89	34.89	$(\bar{9}94)$ $(2\bar{2}9)$ $(110)*$	$\begin{pmatrix} -9 & 2 & 1 \\ 9 & -2 & 1 \\ 4 & 9 & 0 \end{pmatrix}$	93 (31)	42.10	$(4\ \ \bar{1}\bar{1}\ \ 7)$ $(6\ \ \bar{1}\ \ \bar{5})$ $(1\ \ 1\ \ 1)*$	$\begin{pmatrix} 4 & 6 & 1 \\ -11 & -1 & 1 \\ 7 & -5 & 1 \end{pmatrix}$
	7.63	$(15\ \ \bar{1}\ \ 0)$ $(1\ \ 15\ \ 0)$ $(0\ \ 0\ \ 1)*$	$\begin{pmatrix} 15 & 1 & 0 \\ -1 & 15 & 0 \\ 0 & 0 & 1 \end{pmatrix}$								
125	20.61	$(\bar{2}\ \ 11\ \ 0)$ $(\bar{1}\bar{1}\ \ \bar{2}\ \ 0)$ $(0\ \ 0\ \ 1)*$	$\begin{pmatrix} -2 & -11 & 0 \\ 11 & -2 & 0 \\ 0 & 0 & 1 \end{pmatrix}$	97	61.02	$(\bar{5}\ \ 5\ \ \bar{1}\bar{2})$ $(\bar{6}\ \ 6\ \ 5)$ $(1\ \ 1\ \ 0)*$	$\begin{pmatrix} -5 & -6 & 1 \\ 5 & 6 & 1 \\ -12 & 5 & 0 \end{pmatrix}$	97	30.59	$(3\ \ \bar{1}\bar{1}\ \ 8)$ $(19\ \ \bar{5}\ \ \bar{1}\bar{4})$ $(1\ \ 1\ \ 1)*$	$\begin{pmatrix} 3 & 19 & 1 \\ -11 & -5 & 1 \\ 8 & -14 & 1 \end{pmatrix}$
	69.39	$(\bar{9}\ \ 13\ \ 0)$ $(\bar{1}\bar{3}\ \ \bar{9}\ \ 0)$ $(0\ \ 0\ \ 1)*$	$\begin{pmatrix} -9 & -13 & 0 \\ 13 & -9 & 0 \\ 0 & 0 & 1 \end{pmatrix}$								
137	39.97	$(\bar{4}\ \ 11\ \ 0)$ $(\bar{1}\bar{1}\ \ \bar{4}\ \ 0)$ $(0\ \ 0\ \ 1)*$	$\begin{pmatrix} -4 & -11 & 0 \\ 11 & -4 & 0 \\ 0 & 0 & 1 \end{pmatrix}$	99	11.54	$(\bar{7}\ \ 7\ \ 1)$ $(1\ \ \bar{1}\ \ 14)$ $(1\ \ 1\ \ 0)*$	$\begin{pmatrix} -7 & 1 & 1 \\ 7 & -1 & 1 \\ 1 & 14 & 0 \end{pmatrix}$	103	19.65	$(2\ \ \bar{1}\bar{1}\ \ 9)$ $(20\ \ \bar{7}\ \ \bar{1}\bar{3})$ $(1\ \ 1\ \ 1)*$	$\begin{pmatrix} 2 & 20 & 1 \\ -11 & -7 & 1 \\ 9 & -13 & 1 \end{pmatrix}$
	50.03	$(\bar{7}\ \ 15\ \ 0)$ $(1\bar{5}\ \ \bar{7}\ \ 0)$ $(0\ \ 0\ \ 1)*$	$\begin{pmatrix} -7 & -15 & 0 \\ 15 & -7 & 0 \\ 0 & 0 & 1 \end{pmatrix}$								
145	83.27	$(9\bar{8}0)$ (890) $(001)*$	$\begin{pmatrix} 9 & 8 & 0 \\ -8 & 9 & 0 \\ 0 & 0 & 1 \end{pmatrix}$	107	33.72	$(\bar{3}\ \ 3\ \ \bar{1}\bar{4})$ $(\bar{7}\ \ 7\ \ 3)$ $(1\ \ 1\ \ 0)*$	$\begin{pmatrix} -3 & -7 & 1 \\ 3 & 7 & 1 \\ -14 & 3 & 0 \end{pmatrix}$	109	49.01	$(5\ \ \bar{1}\bar{2}\ \ 7)$ $(19\ \ \bar{2}\ \ \bar{1}\bar{7})$ $(1\ \ 1\ \ 1)*$	$\begin{pmatrix} 5 & 19 & 1 \\ -12 & -2 & 1 \\ 7 & -17 & 1 \end{pmatrix}$
	6.73	$(17\ \ \bar{1}\ \ 0)$ $(1\ \ 17\ \ 0)$ $(0\ \ 0\ \ 1)*$	$\begin{pmatrix} 17 & 1 & 0 \\ -1 & 17 & 0 \\ 0 & 0 & 1 \end{pmatrix}$								
149	69.98	$(\bar{1}0\ \ 7\ \ 0)$ $(\bar{7}\ \ \bar{1}0\ \ 0)$ $(0\ \ 0\ \ 1)*$	$\begin{pmatrix} -10 & -7 & 0 \\ 7 & -10 & 0 \\ 0 & 0 & 1 \end{pmatrix}$	113	64.30	$(\bar{9}98)$ $(4\bar{4}9)$ $(110)*$	$\begin{pmatrix} -9 & 4 & 1 \\ 9 & -4 & 1 \\ 8 & 9 & 0 \end{pmatrix}$	111 (37)	9.43	$(1\ \ \bar{1}\bar{1}\ \ 10)$ $(7\ \ \bar{3}\ \ \bar{4})$ $(1\ \ 1\ \ 1)*$	$\begin{pmatrix} 1 & 7 & 1 \\ -11 & -3 & 1 \\ 10 & -4 & 1 \end{pmatrix}$
	20.02	$(\bar{1}7\ \ 3\ \ 0)$ $(\bar{3}\ \ \bar{1}7\ \ 0)$ $(0\ \ 0\ \ 1)*$	$\begin{pmatrix} -17 & -3 & 0 \\ 3 & -17 & 0 \\ 0 & 0 & 1 \end{pmatrix}$								
157	57.22	$(\bar{1}\bar{1}\ \ 6\ \ 0)$ $(\bar{6}\ \ \bar{1}\bar{1}\ \ 0)$ $(0\ \ 0\ \ 1)*$	$\begin{pmatrix} -11 & -6 & 0 \\ 6 & -11 & 0 \\ 0 & 0 & 1 \end{pmatrix}$	121	79.04	$(7\ \ \bar{7}\ \ 12)$ $(6\ \ \bar{6}\ \ \bar{7})$ $(1\ \ 1\ \ 0)*$	$\begin{pmatrix} 7 & 6 & 1 \\ -7 & -6 & 1 \\ 12 & -7 & 0 \end{pmatrix}$	127	54.91	$(6\ \ \bar{1}\bar{3}\ \ 7)$ $(20\ \ \bar{1}\ \ \bar{1}9)$ $(1\ \ 1\ \ 1)*$	$\begin{pmatrix} 6 & 20 & 1 \\ -13 & -1 & 1 \\ 7 & -19 & 1 \end{pmatrix}$
	32.78	$(\bar{1}7\ \ 5\ \ 0)$ $(\bar{5}\ \ \bar{1}7\ \ 0)$ $(0\ \ 0\ \ 1)*$	$\begin{pmatrix} -17 & -5 & 0 \\ 5 & -17 & 0 \\ 0 & 0 & 1 \end{pmatrix}$								
169	45.24	$(\bar{1}2\ \ 5\ \ 0)$ $(\bar{5}\ \ \bar{1}2\ \ 0)$ $(0\ \ 0\ \ 1)*$	$\begin{pmatrix} -12 & -5 & 0 \\ 5 & -12 & 0 \\ 0 & 0 & 1 \end{pmatrix}$	123	14.65	$(\bar{1}\bar{1}\ \ 11\ \ 2)$ $(1\ \ \bar{1}\ \ 11)$ $(1\ \ 1\ \ 0)*$	$\begin{pmatrix} -11 & 1 & 1 \\ 11 & -1 & 1 \\ 2 & 11 & 0 \end{pmatrix}$	129 (43)	44.82	$(5\ \ \bar{1}\bar{3}\ \ 8)$ $(7\ \ \bar{1}\ \ \bar{6})$ $(1\ \ 1\ \ 1)*$	$\begin{pmatrix} 5 & 7 & 1 \\ -13 & -1 & 1 \\ 8 & -6 & 1 \end{pmatrix}$
	44.76	$(\bar{1}7\ \ 7\ \ 0)$ $(\bar{7}\ \ \bar{1}7\ \ 0)$ $(0\ \ 0\ \ 1)*$	$\begin{pmatrix} -17 & -7 & 0 \\ 7 & -17 & 0 \\ 0 & 0 & 1 \end{pmatrix}$								
173	17.49	$(\bar{2}\ \ 13\ \ 0)$ $(\bar{1}3\ \ \bar{2}\ \ 0)$ $(0\ \ 0\ \ 1)*$	$\begin{pmatrix} -2 & -13 & 0 \\ 13 & -2 & 0 \\ 0 & 0 & 1 \end{pmatrix}$	129	10.10	$(\bar{8}\ \ 8\ \ 1)$ $(1\ \ \bar{1}\ \ 16)$ $(1\ \ 1\ \ 0)*$	$\begin{pmatrix} -8 & 1 & 1 \\ 8 & -1 & 1 \\ 1 & 16 & 0 \end{pmatrix}$	133	8.61	$(1\ \ \bar{1}\bar{2}\ \ 11)$ $(23\ \ \bar{1}\bar{0}\ \ \bar{1}3)$ $(1\ \ 1\ \ 1)*$	$\begin{pmatrix} 1 & 23 & 1 \\ -12 & -10 & 1 \\ 11 & -13 & 1 \end{pmatrix}$
	72.51	$(\bar{1}\bar{1}\ \ 15\ \ 0)$ $(1\bar{5}\ \ \bar{1}\bar{1}\ \ 0)$ $(0\ \ 0\ \ 1)*$	$\begin{pmatrix} -11 & -15 & 0 \\ 15 & -11 & 0 \\ 0 & 0 & 1 \end{pmatrix}$								

[001]				[110]				[111]			
Σ	θ	GB Plane	CSL	Σ	θ	GB Plane	CSL	Σ	θ	GB Plane	CSL
181	83.97	$(10\ \bar{9}\ 0)$ $(9\ 10\ 0)$ $(0\ 0\ 1)*$	$\begin{pmatrix}10&9&0\\-9&10&0\\0&0&1\end{pmatrix}$	131	76.31	$(5\ \bar{5}\ 9)$ $(9\ \bar{9}\ \bar{1}0)$ $(1\ 1\ 0)*$	$\begin{pmatrix}5&9&1\\-5&-9&1\\9&-10&0\end{pmatrix}$	139	25.46	$(3\ \bar{1}\bar{3}\ 10)$ $(23\ \bar{7}\ \bar{1}6)$ $(1\ 1\ 1)*$	$\begin{pmatrix}3&23&1\\-13&-7&1\\10&-16&1\end{pmatrix}$
	6.03	$(19\ \bar{1}\ 0)$ $(1\ 19\ 0)$ $(0\ 0\ 1)*$	$\begin{pmatrix}19&1&0\\-1&19&0\\0&0&1\end{pmatrix}$								
185	72.05	$(11\ \bar{8}\ 0)$ $(8\ 11\ 0)$ $(0\ 0\ 1)*$	$\begin{pmatrix}11&8&0\\-8&11&0\\0&0&1\end{pmatrix}$	137	29.70	$(\bar{8}\ 8\ 3)$ $(3\ \bar{3}\ 16)$ $(1\ 1\ 0)*$	$\begin{pmatrix}-8&3&1\\8&-3&1\\3&16&0\end{pmatrix}$	147 (49)	16.43	$(2\ \bar{1}\bar{3}\ 11)$ $(8\ \bar{3}\ \bar{5})$ $(1\ 1\ 1)*$	$\begin{pmatrix}2&8&1\\-13&-3&1\\11&-5&1\end{pmatrix}$
	17.95	$(19\ \bar{3}\ 0)$ $(3\ 19\ 0)$ $(0\ 0\ 1)*$	$\begin{pmatrix}19&3&0\\-3&19&0\\0&0&1\end{pmatrix}$								
193	60.51	$(12\ \bar{7}\ 0)$ $(7\ 12\ 0)$ $(0\ 0\ 1)*$	$\begin{pmatrix}12&7&0\\-7&12&0\\0&0&1\end{pmatrix}$	139	42.18	$(\bar{1}\bar{1}\ 11\ 6)$ $(3\ \bar{3}\ 11)$ $(1\ 1\ 0)*$	$\begin{pmatrix}-11&3&1\\11&-3&1\\6&11&0\end{pmatrix}$	151	41.27	$(5\ \bar{1}\bar{4}\ 9)$ $(23\ \bar{4}\ \bar{1}9)$ $(1\ 1\ 1)*$	$\begin{pmatrix}5&23&1\\-14&-4&1\\9&-19&1\end{pmatrix}$
	29.49	$(19\ \bar{5}\ 0)$ $(5\ 19\ 0)$ $(0\ 0\ 1)*$	$\begin{pmatrix}19&5&0\\-5&19&0\\0&0&1\end{pmatrix}$								
197	8.17	$(14\ 1\ 0)$ $(\bar{1}\ 14\ 0)$ $(0\ 0\ 1)*$	$\begin{pmatrix}14&-1&0\\1&14&0\\0&0&1\end{pmatrix}$	153	47.69	$(\bar{5}\ 5\ \bar{1}6)$ $(\bar{8}\ 8\ 5)$ $(1\ 1\ 0)*$	$\begin{pmatrix}-5&-8&1\\5&8&1\\-16&5&0\end{pmatrix}$	157	7.93	$(1\ \bar{1}\bar{3}\ 12)$ $(25\ \bar{1}\bar{1}\ \bar{1}4)$ $(1\ 1\ 1)*$	$\begin{pmatrix}1&25&1\\-13&-11&1\\12&-14&1\end{pmatrix}$
	81.83	$(15\ 13\ 0)$ $(\bar{1}\bar{3}\ 15\ 0)$ $(0\ 0\ 1)*$	$\begin{pmatrix}15&-13&0\\13&15&0\\0&0&1\end{pmatrix}$								
205	24.19	$(\bar{3}\ 14\ 0)$ $(\bar{1}4\ \bar{3}\ 0)$ $(0\ 0\ 1)*$	$\begin{pmatrix}-3&-14&0\\14&-3&0\\0&0&1\end{pmatrix}$	163	8.98	$(\bar{9}\ 9\ 1)$ $(1\ \bar{1}\ 18)$ $(1\ 1\ 0)*$	$\begin{pmatrix}-9&1&1\\9&-1&1\\1&18&0\end{pmatrix}$	163	23.48	$(3\ \bar{1}\bar{4}\ 11)$ $(25\ \bar{8}\ \bar{1}7)$ $(1\ 1\ 1)*$	$\begin{pmatrix}3&25&1\\-14&-8&1\\11&-17&1\end{pmatrix}$
	65.81	$(\bar{7}\ 19\ 0)$ $(\bar{1}\bar{9}\ \bar{7}\ 0)$ $(0\ 0\ 1)*$	$\begin{pmatrix}-7&-19&0\\19&-7&0\\0&0&1\end{pmatrix}$								
221	84.55	$(11\ \bar{1}0\ 0)$ $(10\ 11\ 0)$ $(0\ 0\ 1)*$	$\begin{pmatrix}11&10&0\\-10&11&0\\0&0&1\end{pmatrix}$	171	12.42	$(\bar{4}45)$ $(5\bar{5}8)$ $(110)*$	$\begin{pmatrix}-4&5&1\\4&-5&1\\5&8&0\end{pmatrix}$	169	55.59	$(7\ \bar{1}\bar{5}\ 8)$ $(23\ \bar{1}\ \bar{2}2)$ $(1\ 1\ 1)*$	$\begin{pmatrix}7&23&1\\-15&-1&1\\8&-22&1\end{pmatrix}$
	5.45	$(21\ \bar{1}\ 0)$ $(1\ 21\ 0)$ $(0\ 0\ 1)*$	$\begin{pmatrix}21&1&0\\-1&21&0\\0&0&1\end{pmatrix}$								
229	15.19	$(\bar{2}\ 15\ 0)$ $(\bar{1}\bar{5}\ \bar{2}\ 0)$ $(0\ 0\ 1)*$	$\begin{pmatrix}-2&-15&0\\15&-2&0\\0&0&1\end{pmatrix}$	177	24.55	$(\bar{2}\ 2\ \bar{1}\bar{3})$ $(\bar{1}\bar{3}\ 13\ 4)$ $(1\ 1\ 0)*$	$\begin{pmatrix}-2&-13&1\\2&13&1\\-13&4&0\end{pmatrix}$	181	29.84	$(4\ \bar{1}\bar{5}\ 11)$ $(26\ \bar{7}\ \bar{1}9)$ $(1\ 1\ 1)*$	$\begin{pmatrix}4&26&1\\-15&-7&1\\11&-19&1\end{pmatrix}$
	74.81	$(\bar{1}\bar{3}\ 17\ 0)$ $(\bar{1}\bar{7}\ \bar{1}\bar{3}\ 0)$ $(0\ 0\ 1)*$	$\begin{pmatrix}-13&-17&0\\17&-13&0\\0&0&1\end{pmatrix}$								
233	63.22	$(\bar{1}\bar{3}\ 8\ 0)$ $(\bar{8}\ \bar{1}\bar{3}\ 0)$ $(0\ 0\ 1)*$	$\begin{pmatrix}-13&-8&0\\8&-13&0\\0&0&1\end{pmatrix}$	179	84.55	$(\bar{7}\ 7\ 9)$ $(9\ \bar{9}\ 14)$ $(1\ 1\ 0)*$	$\begin{pmatrix}-7&9&1\\7&-9&1\\9&14&0\end{pmatrix}$	183 (61)	7.34	$(1\ \bar{1}\bar{4}\ 13)$ $(9\ \bar{4}\ \bar{5})$ $(1\ 1\ 1)*$	$\begin{pmatrix}1&9&1\\-14&-4&1\\13&-5&1\end{pmatrix}$
	26.78	$(\bar{2}\bar{1}\ 5\ 0)$ $(\bar{5}\ \bar{2}\bar{1}\ 0)$ $(0\ 0\ 1)*$	$\begin{pmatrix}-21&-5&0\\5&-21&0\\0&0&1\end{pmatrix}$								

[001]				[110]				[111]			
Σ	θ	GB Plane	CSL	Σ	θ	GB Plane	CSL	Σ	θ	GB Plane	CSL
241	29.86	$(4\ \ 15\ \ 0)$ $(\bar{1}\bar{5}\ \ \bar{4}\ \ 0)$ $(0\ \ 0\ \ 1)*$	$\begin{pmatrix}-4 & -15 & 0\\ 15 & -4 & 0\\ 0 & 0 & 1\end{pmatrix}$	187	36.15	$(\bar{1}\bar{3}\ \ 13\ \ 6)$ $(3\ \ \bar{3}\ \ 13)$ $(1\ \ 1\ \ 0)*$	$\begin{pmatrix}-13 & 3 & 1\\ 13 & -3 & 1\\ 6 & 13 & 0\end{pmatrix}$	193	51.74	$(7\ \ \bar{1}\bar{6}\ \ 9)$ $(25\ \ \bar{2}\ \ \bar{2}\bar{3})$ $(1\ \ 1\ \ 1)*$	$\begin{pmatrix}7 & 25 & 1\\ -16 & -2 & 1\\ 9 & -23 & 1\end{pmatrix}$
	60.14	$(\bar{1}\bar{1}\ \ 19\ \ 0)$ $(\bar{1}\bar{9}\ \ \bar{1}\bar{1}\ \ 0)$ $(0\ \ 0\ \ 1)*$	$\begin{pmatrix}-11 & -19 & 0\\ 19 & -11 & 0\\ 0 & 0 & 1\end{pmatrix}$								
257	7.15	$(16\ \ 1\ \ 0)$ $(\bar{1}\ \ 16\ \ 0)$ $(0\ \ 0\ \ 1)*$	$\begin{pmatrix}16 & -1 & 0\\ 1 & 16 & 0\\ 0 & 0 & 1\end{pmatrix}$	193	75.29	$(6\ \ \bar{6}\ \ 11)$ $(11\ \ \bar{1}\bar{1}\ \ \bar{1}\bar{2})$ $(1\ \ 1\ \ 0)*$	$\begin{pmatrix}6 & 11 & 1\\ -6 & -11 & 1\\ 11 & -12 & 0\end{pmatrix}$	199	14.11	$(2\ \ \bar{1}\bar{5}\ \ 13)$ $(28\ \ \bar{1}\bar{1}\ \ \bar{1}\bar{7})$ $(1\ \ 1\ \ 1)*$	$\begin{pmatrix}2 & 28 & 1\\ -15 & -11 & 1\\ 13 & -17 & 1\end{pmatrix}$
	82.85	$(17\ \ 15\ \ 0)$ $(\bar{1}\bar{5}\ \ 17\ \ 0)$ $(0\ \ 0\ \ 1)*$	$\begin{pmatrix}17 & -15 & 0\\ 15 & 17 & 0\\ 0 & 0 & 1\end{pmatrix}$								
265	85.02	$(12\ \ \bar{1}\bar{1}\ \ 0)$ $(11\ \ 12\ \ 0)$ $(0\ \ 0\ \ 1)*$	$\begin{pmatrix}12 & 11 & 0\\ -11 & 12 & 0\\ 0 & 0 & 1\end{pmatrix}$	201	8.09	$(\bar{1}\bar{0}\ \ 10\ \ 1)$ $(1\ \ \bar{1}\ \ 20)$ $(1\ \ 1\ \ 0)*$	$\begin{pmatrix}-10 & 1 & 1\\ 10 & -1 & 1\\ 1 & 20 & 0\end{pmatrix}$	201 (67)	35.57	$(5\ \ \bar{1}\bar{6}\ \ 11)$ $(9\ \ \bar{2}\ \ \bar{7})$ $(1\ \ 1\ \ 1)*$	$\begin{pmatrix}5 & 9 & 1\\ -16 & -2 & 1\\ 11 & -7 & 1\end{pmatrix}$
	4.98	$(23\ \ \bar{1}\ \ 0)$ $(1\ \ 23\ \ 0)$ $(0\ \ 0\ \ 1)*$	$\begin{pmatrix}23 & 1 & 0\\ -1 & 23 & 0\\ 0 & 0 & 1\end{pmatrix}$								
269	75.14	$(\bar{1}\bar{3}\ \ 10\ \ 0)$ $(\bar{1}\bar{0}\ \ \bar{1}\bar{3}\ \ 0)$ $(0\ \ 0\ \ 1)*$	$\begin{pmatrix}-13 & -10 & 0\\ 10 & -13 & 0\\ 0 & 0 & 1\end{pmatrix}$	209	23.95	$(10\ \ \bar{1}\bar{0}\ \ \bar{3})$ $(\bar{3}\ \ 3\ \ \bar{2}\bar{0})$ $(1\ \ 1\ \ 0)*$	$\begin{pmatrix}10 & -3 & 1\\ -10 & 3 & 1\\ -3 & -20 & 0\end{pmatrix}$	211	6.84	$(1\ \ \bar{1}\bar{5}\ \ 14)$ $(29\ \ \bar{1}\bar{3}\ \ \bar{1}\bar{6})$ $(1\ \ 1\ \ 1)*$	$\begin{pmatrix}1 & 29 & 1\\ -15 & -13 & 1\\ 14 & -16 & 1\end{pmatrix}$
	14.86	$(\bar{2}\bar{3}\ \ 3\ \ 0)$ $(\bar{3}\ \ \bar{2}\bar{3}\ \ 0)$ $(0\ \ 0\ \ 1)*$	$\begin{pmatrix}-23 & -3 & 0\\ 3 & -23 & 0\\ 0 & 0 & 1\end{pmatrix}$								
277	65.47	$(14\ \ \bar{9}\ \ 0)$ $(9\ \ 14\ \ 0)$ $(0\ \ 0\ \ 1)*$	$\begin{pmatrix}14 & 9 & 0\\ -9 & 14 & 0\\ 0 & 0 & 1\end{pmatrix}$	211	57.62	$(\bar{7}\ \ 7\ \ \bar{1}\bar{8})$ $(\bar{9}\ \ 9\ \ 7)$ $(1\ \ 1\ \ 0)*$	$\begin{pmatrix}-7 & -9 & 1\\ 7 & 9 & 1\\ -18 & 7 & 0\end{pmatrix}$	217	20.32	$(3\ \ \bar{1}\bar{6}\ \ 13)$ $(29\ \ \bar{1}\bar{0}\ \ \bar{1}\bar{9})$ $(1\ \ 1\ \ 1)*$	$\begin{pmatrix}3 & 29 & 1\\ -16 & -10 & 1\\ 13 & -19 & 1\end{pmatrix}$
	24.53	$(23\ \ \bar{5}\ \ 0)$ $(5\ \ 23\ \ 0)$ $(0\ \ 0\ \ 1)*$	$\begin{pmatrix}23 & 5 & 0\\ -5 & 23 & 0\\ 0 & 0 & 1\end{pmatrix}$								
281	34.71	$(\bar{5}\ \ 16\ \ 0)$ $(\bar{1}\bar{6}\ \ \bar{5}\ \ 0)$ $(0\ \ 0\ \ 1)*$	$\begin{pmatrix}-5 & -16 & 0\\ 16 & -5 & 0\\ 0 & 0 & 1\end{pmatrix}$	219	57.09	$(\bar{1}\bar{3}\ \ 13\ \ 10)$ $(5\ \ \bar{5}\ \ 13)$ $(1\ \ 1\ \ 0)*$	$\begin{pmatrix}-13 & 5 & 1\\ 13 & -5 & 1\\ 10 & 13 & 0\end{pmatrix}$	219 (73)	48.36	$(7\ \ \bar{1}\bar{7}\ \ 10)$ $(9\ \ \bar{1}\ \ \bar{8})$ $(1\ \ 1\ \ 1)*$	$\begin{pmatrix}7 & 9 & 1\\ -17 & -1 & 1\\ 10 & -8 & 1\end{pmatrix}$
	55.29	$(\bar{1}\bar{1}\ \ 21\ \ 0)$ $(\bar{2}\bar{1}\ \ \bar{1}\bar{1}\ \ 0)$ $(0\ \ 0\ \ 1)*$	$\begin{pmatrix}-11 & -21 & 0\\ 21 & -11 & 0\\ 0 & 0 & 1\end{pmatrix}$								
289	56.14	$(\bar{1}\bar{5}\ \ 8\ \ 0)$ $(\bar{8}\ \ \bar{1}\bar{5}\ \ 0)$ $(0\ \ 0\ \ 1)*$	$\begin{pmatrix}-15 & -8 & 0\\ 8 & -15 & 0\\ 0 & 0 & 1\end{pmatrix}$	227	10.77	$(\bar{1}\bar{5}\ \ 15\ \ 2)$ $(1\ \ \bar{1}\ \ 15)$ $(1\ \ 1\ \ 0)*$	$\begin{pmatrix}-15 & 1 & 1\\ 15 & -1 & 1\\ 2 & 15 & 0\end{pmatrix}$	223	40.73	$(6\ \ \bar{1}\bar{7}\ \ 11)$ $(28\ \ \bar{5}\ \ \bar{2}\bar{3})$ $(1\ \ 1\ \ 1)*$	$\begin{pmatrix}6 & 28 & 1\\ -17 & -5 & 1\\ 11 & -23 & 1\end{pmatrix}$
	33.86	$(\bar{2}\bar{3}\ \ 7\ \ 0)$ $(\bar{7}\ \ \bar{2}\bar{3}\ \ 0)$ $(0\ \ 0\ \ 1)*$	$\begin{pmatrix}-23 & -7 & 0\\ 7 & -23 & 0\\ 0 & 0 & 1\end{pmatrix}$								
293	13.42	$(\bar{2}\ \ 17\ \ 0)$ $(\bar{1}\bar{7}\ \ \bar{2}\ \ 0)$ $(0\ \ 0\ \ 1)*$	$\begin{pmatrix}-2 & -17 & 0\\ 17 & -2 & 0\\ 0 & 0 & 1\end{pmatrix}$	233	21.36	$(\bar{2}\ \ 2\ \ \bar{1}\bar{5})$ $(\bar{1}\bar{5}\ \ 15\ \ 4)$ $(1\ \ 1\ \ 0)*$	$\begin{pmatrix}-2 & -15 & 1\\ 2 & 15 & 1\\ -15 & 4 & 0\end{pmatrix}$	229	33.25	$(5\ \ \bar{1}\bar{7}\ \ 12)$ $(29\ \ \bar{7}\ \ \bar{2}\bar{2})$ $(1\ \ 1\ \ 1)*$	$\begin{pmatrix}5 & 29 & 1\\ -17 & -7 & 1\\ 12 & -22 & 1\end{pmatrix}$
	76.58	$(\bar{1}\bar{5}\ \ 19\ \ 0)$ $(\bar{1}\bar{9}\ \ \bar{1}\bar{5}\ \ 0)$ $(0\ \ 0\ \ 1)*$	$\begin{pmatrix}-15 & -19 & 0\\ 19 & -15 & 0\\ 0 & 0 & 1\end{pmatrix}$								

Bibliography

[1] Hirofumi Akamatsu, Koji Fujita, Hiroyuki Hayashi, Takahiro Kawamoto, Yu Kumagai, Yanhua Zong, Koji Iwata, Fumiyasu Oba, Isao Tanaka, and Katsuhisa Tanaka. Crystal and electronic structure and magnetic properties of divalent europium perovskite oxides $EuMO_3$ (M = Ti, Zr, and Hf): Experimental and first-principles approaches. *Inorg. Chem.*, 51:4560–4567, 2012.

[2] J.-M. Albina, M. Mrovec, B. Meyer, and C. Elsässer. Structure, stability, and electronic properties of $SrTiO_3/LaAlO_3$ and $SrTiO_3/SrRuO_3$ interfaces. *Phys. Rev. B*, 76:165103, 2007.

[3] Leland C. Allen. Electronegativity is the average one-electron energy of the valence-shell electrons in ground-state free atoms. *J. Am. Chem. Soc.*, 111:9003–9014, 1989.

[4] A. Annadi, A. Putra, Z. Q. Liu, X. Wang, K. Gopinadhan, Z. Huang, S. Dhar, T. Venkatesan, and Ariando. Electronic correlation and strain effects at the interfaces between polar and nonpolar complex oxides. *Phys. Rev. B*, 86:085450, 2012.

[5] Ariando, X. Wang, G. Baskaran, Z. Q. Liu, J. Huijben, J. B. Yi, A. Annadi, A. R. Barman, A. Rusydi, S. Dhar, Y. P. Feng, J. Ding, H. Hilgenkamp, and T. Venkatesan. Electronic phase separation at the $LaAlO_3/SrTiO_3$ interface. *Nat. Commun.*, 2:188–194, 2010.

[6] Rickard Armiento, Boris Kozinsky, Marco Fornari, and Gerbrand Ceder. Screening for high-performance piezoelectrics using high-throughput density functional theory. *Phys. Rev. B*, 84:014103, 2011.

[7] R. Arras and L. Calmels. Fully spin-polarized two-dimensional electron gas at the $CoFe_2O_4/MgAl_2O_4(001)$ polar interface. *Phys. Rev. B*, 90:045411, 2014.

[8] C. W. Bark, D. A. Felker, Y. Wang, Y. Zhang, H. W. Jang, C. M. Folkman, J. W. Park, S. H. Baek, H. Zhou, D. D. Fong, X. Q. Pan, E. Y. Tsymbal, M. S. Rzchowski, and C. B. Eom. Tailoring a two-dimensional electron gas at the $LaAlO_3/SrTiO_3$ (001) interface by epitaxial strain. *Proc. Natl. Acad. Sci.*, 108:4720–4724, 2011.

[9] Maziar Behtash, Safdar Nazir, Yaqin Wang, and Kesong Yang. Polarization effects on the interfacial conductivity in $LaAlO_3/SrTiO_3$ heterostructures: a first-principles study. *Phys. Chem. Chem. Phys.*, 18:6831–6838, 2016.

[10] Maziar Behtash, Safdar Nazir, Yaqin Wang, and Kesong Yang. Polarization effects on the interfacial conductivity in the $LaAlO_3/SrTiO_3$ heterostructure: First-principles study. *Phys. Chem. Chem. Phys.*, 18:6831–6838, 2016.

[11] Maziar Behtash, Yaqin Wang, Jian Luo, and Kesong Yang. Oxygen vacancy formation in the $SrTiO_3$ $\Sigma5$ [001] twist grain boundary from firstprinciples. *J. Am. Ceram. Soc.*, 0:1–12, 2018.

[12] Nicole A. Benedek and Craig J. Fennie. Why are there so few perovskite ferroelectrics? *J. Phys. Chem. C*, 117:13339–13349, 2013.

[13] Camille Bernal and Kesong Yang. First-principles hybrid functional study of the organicinorganic perovskites $CHNH_3SnBr_3$ and $CH_3NH_3SnI_3$. *J. Phys. Chem. C*, 118:24383–24388, 2014.

[14] Feng Bi, Daniela F. Bogorin, Cheng Cen, Chung Wung Bark, Jae-Wan Park, Chang-Beom Eom, and Jeremy Levy. water-cycle mechanism for writing and erasing nanostructures at the $LaAlO_3/SrTiO_3$ interface. *Appl. Phys. Lett.*, 97:173110, 2010.

[15] M. Binnewies, R. Glaum, M. Schmidt, and P. Schmidt. *Chemical Vapor Transport Reactions*. De Gruyter, 2012.

[16] J. Biscaras, N. Bergeal, A. Kushwaha, T. Wolf, A. Rastogi, R.C. Budhani, and J. Lesueur. Two-dimensional superconductivity at a mott insulator/band insulator interface $LaTiO_3/SrTiO_3$. *Nat. Commun.*, 1:89, 2010.

[17] L. Bjaalie, B. Himmetoglu, L. Weston, A. Janotti, and C. G. Van de Walle. Oxide interfaces for novel electronic applications. *New J. Phys.*, 16:025005, 2014.

[18] G. L. Bleris and P. Delavignette. A new formulation for the generation of coincidence site lattices (CSL's) in the cubic system. *Acta Crystallogr., Sect. A: Found. Adv.*, 37:779–786, 1981.

[19] P.E. Blöchl. Projector augmented-wave method. *Phys. Rev. B*, 50:17953–17979, 1994.

[20] Daniela F. Bogorin, Chung Wung Bark, Ho Won Jang, Cheng Cen, Chad M. Folkman, Chang-Beom Eom, and Jeremy Levy. Nanoscale rectification at the $LaAlO_3/SrTiO_3$ interface. *Appl. Phys. Lett.*, 97:013102, 2010.

[21] Walter Bollmann. *Crystal Defects and Crystalline Interfaces*. Springer-Verlag Berlin Heidelberg, 1970.

[22] William J. Bowman, Madeleine N. Kelly, Gregory S. Rohrer, Cruz A. Hernandez, and Peter A. Crozier. Enhanced ionic conductivity in electroceramics by nanoscale enrichment of grain boundaries with high solute concentration. *Nanoscale*, 9:17293–17302, 2017.

[23] M. Braccini and M. Dupeux. *Mechanics of Solid Interfaces*. Wiley, 2013.

[24] Matthew Brahlek, Arnab Sen Gupta, Jason Lapano, Joseph Roth, Hai-Tian Zhang, Lei Zhang, Ryan Haislmaier, and Roman Engel-Herbert. Frontiers in the growth of complex oxide thin films: Past, present, and future of hybrid MBE. *Adv. Fun. Mater.*, 28:1702772, 2017.

[25] D.G Brandon. The structure of high-angle grain boundaries. *Acta Metallurgica*, 14:1479–1484, 1966.

[26] D.G Brandon, B Ralph, S Ranganathan, and M.S Wald. A field ion microscope study of atomic configuration at grain boundaries. *Acta Metallurgica*, 12:813–821, 1964.

[27] Stefan Breuer, Denise Prutsch, Qianli Ma, Viktor Epp, Florian Preishuber-Pflugl, Frank Tietz, and Martin Wilkening. Separating bulk from grain boundary li ion conductivity in the sol-gel prepared solid electrolyte $Li_{1.5}Al_{0.5}Ti_{1.5}(PO_4)_3$. *J. Mater. Chem. A*, 3:21343–21350, 2015.

[28] A. Brinkman, M. Huijben, M. van Zalk, J. Huijben, U. Zeitler, J.C. Maan, W.G. van der Wiel, G. Rijnders, D.H.A. Blank, and H. Hilgenkamp. Magnetic effects at the interface between nonmagnetic oxides. *Nat. Mater.*, 6:493, 2007.

[29] I. D. Brown. Bond valences-a simple structural model for inorganic chemistry. *Chem. Soc. Rev.*, 7:359–376, 1978.

[30] Keith A. Brown, Shu He, Daniel J. Eichelsdoerfer, Mengchen Huang, Ishan Levy, Hyungwoo Lee, Sangwoo Ryu, Patrick Irvin, Jose Mendez-Arroyo, Chang-Beom Eom, Chad A. Mirkin, and Jeremy Levy. Giant conductivity switching of $LaAlO_3/SrTiO_3$ heterointerfaces governed by surface protonation. *Nat. Commun.*, 7:10681, 2016.

[31] R G Burkovsky, D Andronikova, Yu Bronwald, M Krisch, K Roleder, A Majchrowski, A V Filimonov, A I Rudskoy, and S B Vakhrushev. Lattice dynamics in the paraelectric phase of $PbHfO_3$ studied by inelastic x-ray scattering. *J. Phys.: Condens. Matter*, 27:335901, 2015.

[32] C. Cancellieri, D. Fontaine, S. Gariglio, N. Reyren, A. D. Caviglia, A. Fête, S. J. Leake, S. A. Pauli, P. R. Willmott, M. Stengel, Ph. Ghosez, and J.-M. Triscone. Electrostriction at the $LaAlO_3/SrTiO_3$ interface. *Phys. Rev. Lett.*, 107:056102, 2011.

[33] L. S. Cavalcante, V. M. Longo, M. Zampieri, J. W. M. Espinosa, P. S. Pizani, J. R. Sambrano, J. A. Varela, E. Longo, M. L. Simões, and C. A. Paskocimas. Experimental and theoretical correlation of very intense visible green photoluminescence in $BaZrO_3$ powders. *J. Appl. Phys.*, 103:063527, 2008.

[34] A. D. Caviglia, M. Gabay, S. Gariglio, N. Reyren, C. Cancellieri, and J. M. Triscone. Tunable rashba spin-orbit interaction at oxide interfaces. *Phys. Rev. Lett.*, 104:126803, 2010.

[35] A. D. Caviglia, S. Gariglio, C. Cancellieri, B. Sacépé, A. Fête, N. Reyren, M. Gabay, A. F. Morpurgo, and J.-M. Triscone. Two-dimensional quantum oscillations of the conductance at $LaAlO_3/SrTiO_3$ interfaces. *Phys. Rev. Lett.*, 105:236802, 2010.

[36] A. D. Caviglia, S. Gariglio, N. Reyren, D. Jaccard, T. Schneider, M. Gabay, S. Thiel, G. Hammerl, J. Mannhart, and J.-M. Triscone. Electric field control of the $LaAlO_3/SrTiO_3$ interface ground state. *Nature*, 456:624–627, 2008.

[37] C. Cen, S. Thiel, G. Hammerl, C. W. Schneider, K. E. Andersen, C. S. Hellberg, J. Mannhart, and J. Levy. Nanoscale control of an interfacial metal-insulator transition at room temperature. *Nat. Mater.*, 7:298–302, 2008.

[38] J. Chakhalian, A. J. Millis, and J. Rondinelli. Whither the oxide interface. *Nat. Mater.*, 11:92–94, 2012.

[39] Scott A Chambers, Tiffany C Kaspar, Abhinav Prakash, Greg Haugstad, and Bharat Jalan. Band alignment at epitaxial $BaSnO_3/SrTiO_3$ (001) and $BaSnO_3/LaAlO_3$ (001) heterojunctions. *Appl. Phys. Lett.*, 108:152104, 2016.

[40] Hanghui Chen, Divine P. Kumah, Ankit S. Disa, Frederick J. Walker, Charles H. Ahn, and Sohrab Ismail-Beigi. Modifying the electronic orbitals of nickelate heterostructures via structural distortions. *Phys. Rev. Lett.*, 110:186402, 2013.

[41] Hong Chen, Yi-hong Ding, Hai-tao Yu, and Ying Xie. First-principles investigation of the electronic properties and stabilities of the $LaAlO_3$ (001) and (110) (1×1) polar terminations. *J. Phys. Chem. C*, 119:9364–9374, 2015.

[42] Y. Chen, N. Pryds, J. E. Kleibeuker, G. Koster, J. Sun, E. Stamate, B. Shen, G. Rijnders, and S. Linderoth. Metallic and insulating interfaces of amorphous $SrTiO_3$-based oxide heterostructures. *Nano Lett.*, 11:3774–3778, 2011.

[43] Y. Z. Chen, N. Bovet, F Trier, D. V. Christensen, F. M. Qu, N. H. Andersen, T. Kasama, W. Zhang, R. Giraud, J. Dufouleur, T. S. Jespersen, J. R. Sun, A. Smith, J. Nygárd, L. Lu, B. Büchner, B. G. Shen, S. Linderoth, and N. Pryds. A high-mobility two-dimensional electron gas at the spinel/perovskite interface of γ-$Al_2O_3/SrTiO_3$. *Nat. Commun.*, 4:1371, 2013.

[44] Y. Z. Chen, F. Trier, T. Wijnands, R. J. Green, N. Gauquelin, R. Egoavil, D. V. Christensen, G. Koster, M. Huijben, N. Bovet, S. Macke, F. He, R. Sutarto, N. H. Andersen, J. A. Sulpizio, M. Honig, G. E. D. K. Prawiroatmodjo, T. S. Jespersen, S. Linderoth, S. Ilani, J. Verbeeck, G. Van Tendeloo, G. Rijnders, G. A. Sawatzky, and N. Pryds. Extreme mobility enhancement of two-dimensional electron gases at oxide interfaces by charge-transfer-induced modulation doping. *Nat. Mater.*, 14:801–806, 2015.

[45] Yunzhong Chen and Nini Pryds. 2d hole gas seen. *Nat. Mater.*, 17:215, 2018.

[46] Yunzhong Chen, Felix Trier, Takeshi Kasama, Dennisi. V. Christensen, Nicolas Bovet, Zoltan. I. Balogh, Han Li, Karl. Tor. Sune Thyden, Wei Zhang, Sadegh Yazdi, Poul Norby, Nini Pryds, and Sren Linderoth. Creation of high mobility two-dimensional electron gases via strain induced polarization at an otherwise nonpolar complex oxide interface. *Nano Lett.*, 15:1849–1854, 2015.

[47] Guanglei Cheng, Pablo F. Siles, Feng Bi, Cheng Cen, Daniela F. Bogorin, Chung Wung Bark, Chad M. Folkman, Jae-Wan Park, Chang-Beom Eom, Gilberto Medeiros-Ribeiro, and Jeremy Levy. Sketched oxide single-electron transistor. *Nat. Nanotechnol.*, 6:343, 2011.

[48] Jianli Cheng, Jian Luo, and Kesong Yang. Comparison studies of interfacial electronic and energetic properties of $LaAlO_3/TiO_2$ and $TiO_2/LaAlO_3$ heterostructures from first-principles calculations. *ACS Appl. Mater. Interfaces*, 9:7682–7690, 2017.

[49] Jianli Cheng, Safdar Nazir, and Kesong Yang. First-principles prediction of two-dimensional electron gas driven by polarization discontinuity in nonpolar/nonpolar $AHfO_3/SrTiO_3$ (A = Ca, Sr, and Ba) heterostructures. *ACS Appl. Mater. Interfaces*, 8:31959–31967, 2016.

[50] Jianli Cheng and Kesong Yang. Design of two-dimensional electron gas systems via polarization discontinuity from large-scale first-principles calculations. *J. Mater. Chem. C*, 6:6680–6690, 2018.

[51] W. S. Choi, Suyoun Lee, V. R. Cooper, and H. N. Lee. Fractionally δ-doped oxide superlattices for higher carrier mobilities. *Nano Lett.*, 12:4590–4594, 2012.

[52] Regina Ciancio, Elvio Carlino, Carmela Aruta, Davide Maccariello, Fabio Miletto Granozio, and Umberto Scotti di Uccio. Nanostructure of buried interface layers in TiO_2 anatase thin films grown on $LaAlO_3$ and $SrTiO_3$ substrates. *Nanoscale*, 4:91–94, 2012.

[53] E. Clementi, D. L. Raimondi, and W. P. Reinhardt. Atomic screening constants from SCF functions. II. atoms with 37 to 86 electrons. *J. Chem. Phys.*, 47:1300–1307, 1967.

[54] S. Curtarolo, W. Setyawan, G. L. W. Hart, M. Jahnatek, R. V. Chepulskii, R. H. Taylor, S. Wang, J. Xue, K. Yang, O. Levy, M. Mehl, H. T. Stokes, D. O. Demchenko, , and D. Morgan. AFLOW: an automatic framework for high-throughput materials discovery. *Comput. Mater. Sci.*, 58:218–226, 2012.

[55] Stefano Curtarolo, Gus L. W. Hart, Marco Buongiorno Nardelli, Natalio Mingo, Stefano Sanvito, and Ohad Levy. The high-throughput highway to computational materials design. *Nat. Mater.*, 12:191–201, 2013.

[56] Shubhankar Das, Z. Hossain, and R. C. Budhani. Signature of enhanced spin-orbit interaction in the magnetoresistance of $LaTiO_3/SrTiO_3$ interfaces on δ doping. *Phys. Rev. B*, 94:115165, 2016.

[57] Shubhankar Das, A. Rastogi, Lijun Wu, Jin-Cheng Zheng, Z. Hossain, Yimei Zhu, and R. C. Budhani. Kondo scattering in δ-doped $LaTiO_3/SrTiO_3$ interfaces: Renormalization by spin-orbit interactions. *Phys. Rev. B*, 90:081107, 2014.

[58] M. Dawber, C. Lichtensteiger, M. Cantoni, M. Veithen, P. Ghosez, K. Johnston, K. M. Rabe, and J. M. Triscone. Unusual behavior of the ferroelectric polarization in $PbTiO_3/SrTiO_3$ superlattices. *Phys. Rev. Lett.*, 95:177601, 2005.

[59] P. Delugas, A. Filippetti, V. Fiorentini, D. I. Bilc, D. Fontaine, and P. Ghosez. Spontaneous 2-dimensional carrier confinement at the *n*-type $SrTiO_3/LaAlO_3$ interface. *Phys. Rev. Lett.*, 106:166807, 2011.

[60] S. V. Dudiy and B. I. Lundqvist. First-principles density-functional study of metal-carbonitride interface adhesion: Co/TiC(001) and Co/TiN(001). *Phys. Rev. B*, 64:045403, 2001.

[61] Robert A. Evarestov. Hybrid density functional theory lcao calculations on phonons in Ba(Ti, Zr, Hf)O_3. *Phys. Rev. B*, 83:014105, 2011.

[62] V. Ferrari and M. Weissmann. Tuning the insulatormetal transition in oxide interfaces: An *ab initio* study exploring the role of oxygen vacancies and cation interdiffusion. *Phys. Stat. Solidi (B)*, 251:1601–1607, 2014.

[63] A. Fête, C. Cancellieri, D. Li, D. Stornaiuolo, A. D. Caviglia, S. Gariglio, and J.-M. Triscone. Growth-induced electron mobility enhancement at the $LaAlO_3/SrTiO_3$ interface. *Appl. Phys. Lett.*, 106:051604, 2015.

[64] A. Fête, S. Gariglio, A. D. Caviglia, J.-M. Triscone, and M. Gabay. Rashba induced magnetoconductance oscillations in the $LaAlO_3$-$SrTiO_3$ heterostructure. *Phys. Rev. B*, 86:201105, 2012.

[65] Antonio Feteira, Derek C. Sinclair, Khalid Z. Rajab, and Michael T. Lanagan. Crystal structure and microwave dielectric properties of alkaline-earth hafnates, $AHfO_3$ (A=Ba, Sr, Ca). *J. Am. Ceram. Soc.*, 91:893–901, 2008.

[66] T. Fix, J. L. MacManus-Driscoll, and M. G. Blamire. Delta-Doped $LaAlO_3/SrTiO_3$ interfaces. *Appl. Phys. Lett.*, 94:172101, 2009.

[67] T. Fix, F. Schoofs, J. L. MacManus-Driscoll, and M. G. Blamire. Influence of doping at the nanoscale at $LaAlO_3/SrTiO_3$ interfaces. *Appl. Phys. Lett.*, 97:072110, 2010.

[68] B. Förg, C. Richter, and J. Mannhart. Field-effect devices utilizing $LaAlO_3$-$SrTiO_3$ interfaces. *Appl. Phys. Lett.*, 100:053506–053508, 2012.

[69] S. Frank, A. C. Michael, E. V. Mary, E. Mehmet, F. Thomas, E. K. Josee, J. L. McManus-Driscoll, and G. B. Mark. Carrier density modulation by structural distortions at modified $LaAlO_3/SrTiO_3$ interfaces. *J. Phys.: Condens. Matter*, 25:175005, 2013.

[70] Kurt D. Fredrickson and Alexander A. Demkov. Switchable conductivity at the ferroelectric interface: Nonpolar oxides. *Phys. Rev. B*, 91:115126, 2015.

[71] T. Frolov, S. V. Divinski, M. Asta, and Y. Mishin. Effect of interface phase transformations on diffusion and segregation in high-angle grain boundaries. *Phys. Rev. Lett.*, 110:255502, 2013.

[72] Timofey Frolov, David L. Olmsted, Mark Asta, and Yuri Mishin. Structural phase transformations in metallic grain boundaries. *Nat. Commun.*, 4:1899, 2013.

[73] Akira Fujishima and Kenichi Honda. Electrochemical photolysis of water at a semiconductor electrode. *Nature*, 238:37–38, 1972.

[74] T. Fukushima, A. Stroppa, S. Picozzi, and J. M. Perez-Mato. Large ferroelectric polarization in the new double perovskite $NaLaMnWO_6$ induced by non-polar instabilities. *Phys. Chem. Chem. Phys.*, 13:12186–12190, 2011.

[75] Yutaka Furubayashi, Taro Hitosugi, and Tetsuya Hasegawa. Response to comment on A transparent metal: Nb-doped anatase TiO_2 [Appl. Phys. Lett. 86, 252101 (2005)]. *Appl. Phys. Lett.*, 88:226103, 2006.

[76] S. Gariglio, A. Fête, and J-M Triscone. Electron confinement at the $LaAlO_3/SrTiO_3$ interface. *J. Phys.: Condens. Matter*, 27:283201, 2015.

[77] Michael Gellert, Katharina I. Gries, Chihiro Yada, Fabio Rosciano, Kerstin Volz, and Bernhard Roling. Grain boundaries in a lithium aluminum titanium phosphate-type fast lithium ion conducting glass ceramic: Microstructure and nonlinear ion transport properties. *J. Phys. Chem. C*, 116:22675–22678, 2012.

[78] M. Ghita, M. Fornari, D. J. Singh, and S. V. Halilov. Interplay between A-site and B-site driven instabilities in perovskites. *Phys. Rev. B*, 72:054114, 2005.

[79] Marta Gibert, Pavlo Zubko, Raoul Scherwitzl, Jorge Íñiguez, and Jean-Marc Triscone. Exchange bias in $LaNiO_3$-$LaMnO_3$ superlattices. *Nat. Mater.*, 11:195, 2012.

[80] H.-J. Gossmann and E. F. Schubert. Delta doping in silicon. *Crit. Rev. Solid State Mater. Sci.*, 18:1–67, 1993.

[81] H. Grimmer. The generating function for coincidence site lattices in the cubic system. *Acta Crystallogr., Sect. A: Found. Adv.*, 40:108–112, 1984.

[82] H. Grimmer, W. Bollmann, and D. H. Warrington. Coincidence-Site Lattices and Complete Pattern-Shift in Cubic Crystals. *Acta Crystallogr., Sect. A: Found. Adv.*, 30:197–207, 1974.

[83] F. Gunkel, K. Skaja, A. Shkabko, R. Dittmann, S. Hoffmann-Eifert, and R. Waser. Stoichiometry dependence and thermal stability of conducting $NdGaO_3/SrTiO_3$ heterointerfaces. *Appl. Phys. Lett.*, 102:071601, 2013.

[84] Felix Gunkel, Ronja A. Heinen, Susanne Hoffmann-Eifert, Lei Jin, Chun-Lin Jia, and Regina Dittmann. Mobility modulation and suppression of defect formation in two-dimensional electron systems by charge-transfer management. *ACS Appl. Mater. Interfaces*, 9:10888–10896, 2017.

[85] R. Gunnarsson, A.S. Kalabukhov, and D. Winkler. Evaluation of recipes for obtaining single terminated perovskite oxide substrates. *Surf. Sci.*, 603:151–157, 2009.

[86] R. Guo, L. E. Cross, S-E. Park, B. Noheda, D. E. Cox, and G. Shirane. Origin of the high piezoelectric response in $PbZr_{1-X}Ti_xO_3$. *Phys. Rev. Lett.*, 84:5423–5426, 2000.

[87] Geoffroy Hautier, Anna Miglio, David Waroquiers, Gian-Marco Rignanese, and Xavier Gonze. How does chemistry influence electron effective mass in oxides? a high-throughput computational analysis. *Chem. Mater.*, 26:5447–5458, 2014.

[88] Graeme Henkelman, Andri Arnaldsson, and Hannes Jónsson. A fast and robust algorithm for bader decomposition of charge density. *Comput. Mater. Sci.*, 36:354–360, 2006.

[89] G. Herranz, M. Basletić, M. Bibes, C. Carrétéro, E. Tafra, E. Jacquet, K. Bouzehouane, C. Deranlot, A. Hamzić, J.-M. Broto, A. Barthélémy, and A. Fert. High mobility in $LaAlO_3/SrTiO_3$ heterostructures: Origin, dimensionality, and perspectives. *Phys. Rev. Lett.*, 98:216803, 2007.

[90] Jochen Heyd, Gustavo E. Scuseria, and Matthias Ernzerhof. Hybrid functionals based on a screened coulomb potential. *J. Chem. Phys.*, 118:8207–8215, 2003.

[91] Nicola A. Hill. Why are there so few magnetic ferroelectrics? *J. Phys. Chem. B*, 104:6694–6709, 2000.

[92] Yasushi Hirose, Naoomi Yamada, Shoichiro Nakao, Taro Hitosugi, Toshihiro Shimada, and Tetsuya Hasegawa. Large electron mass anisotropy in a *d*-electron-based transparent conducting oxide: Nb-doped anatase TiO_2 epitaxial films. *Phys. Rev. B*, 79:165108, 2009.

[93] Taro Hitosugi, Hideyuki Kamisaka, Koichi Yamashita, Hiroyuki Nogawa, Yutaka Furubayashi, Shoichiro Nakao, Naoomi Yamada, Akira Chikamatsu, Hiroshi Kumigashira, Masaharu Oshima, Yasushi Hirose, Toshihiro Shimada, and Tetsuya Hasegawa. Electronic band structure of transparent conductor: Nb-doped anatase TiO_2. *Appl. Phys. Express*, 1:111203, 2008.

[94] Masayuki Hosoda, Christopher Bell, Yasuyuki Hikita, and H. Y Hwang. Compositional and gate tuning of the interfacial conductivity in $LaAlO_3/LaTiO_3/SrTiO_3$ heterostructures. *Appl. Phys. Lett.*, 102:091601, 2013.

[95] Z. F. Hou. Elasticity, electronic structure, and dielectric property of cubic $SrHfO_3$ from first-principles. *Phys. Stat. Solidi (B)*, 246:135–139, 2009.

[96] C. J. Howard, T. M. Sabine, and F. Dickson. Structural and thermal parameters for rutile and anatase. *Acta Cryst.*, B47:462–468, 1991.

[97] Chengqing Hu, Martin D. McDaniel, Aiting Jiang, Agham Posadas, Alexander A. Demkov, John G. Ekerdt, and Edward T. Yu. A low-leakage epitaxial high-*k* gate oxide for germanium metal-oxide-semiconductor devices. *ACS Appl. Mater. Interfaces*, 8:5416–5423, 2016.

[98] Bo-Chao Huang, Ya-Ping Chiu, Po-Cheng Huang, Wen-Ching Wang, Vu Thanh Tra, Jan-Chi Yang, Qing He, Jiunn-Yuan Lin, Chia-Seng Chang, and Ying-Hao Chu. Mapping band alignment across complex oxide heterointerfaces. *Phys. Rev. Lett.*, 109:246807, 2012.

[99] Bo-Wen Huang, Jia-Xiang Shang, Zeng-Hui Liu, and Yue Chen. Atomic simulation of bcc niobium $\Sigma 5\langle 001\rangle 310$ grain boundary under shear deformation. *Acta Mater.*, 77:258–268, 2014.

[100] Zhen Huang, Kun Han, Shengwei Zeng, Mallikarjuna Motapothula, Albina Y. Borisevich, Saurabh Ghosh, Weiming L, Changjian Li, Wenxiong Zhou, Zhiqi Liu, Michael Coey, T. Venkatesan, and Ariando. The effect of polar fluctuation and lattice mismatch on carrier mobility at oxide interfaces. *Nano Lett.*, 16:2307–2313, 2016.

[101] Shiqiang Hui and Anthony Petric. Electrical conductivity of yttrium-doped $SrTiO_3$: Influence of transition metal additives. *Mater. Res. Bull.*, 37:1215–1231, 2002.

[102] M. Huijben, G. Rijnders, D. H. A. Blank, S. Bals, S. V. Aert, J. Verbeeck, G. V. Tendeloo, A. Brinkman, and H. Hilgenkamp. Electronically coupled complementary interfaces between perovskite band insulators. *Nat. Mater.*, 5:556–560, 2006.

[103] Mark Huijben, Gertjan Koster, Michelle K. Kruize, Sander Wenderich, Jo Verbeeck, Sara Bals, Erik Slooten, Bo Shi, Hajo J. A. Molegraaf, Josee E. Kleibeuker, Sandra van Aert, Jeroen B. Goedkoop, Alexander Brinkman, Dave H. A. Blank, Mark S. Golden, Gustaaf van Tendeloo, Hans Hilgenkamp, and Guus Rijnders. Defect engineering in oxide heterostructures by enhanced oxygen surface exchange. *Adv. Fun. Mater.*, 23:5240–5248, 2013.

[104] S. Hurand, A. Jouan, C. Feuillet-Palma, G. Singh, E. Lesne, N. Reyren, A. Barthélémy, M. Bibes, J. E. Villegas, C. Ulysse, M. Pannetier-Lecoeur, M. Malnou, J. Lesueur, and N. Bergeal. Top-gated field-effect $LaAlO_3/SrTiO_3$ devices made by ion-irradiation. *Appl. Phys. Lett.*, 108:52602, 2016.

[105] Huynh Anh Huy, Bálint Aradi, Thomas Frauenheim, and Peter Deák. Calculation of carrier-concentration-dependent effective mass in nb-doped anatase crystals of TiO_2. *Phys. Rev. B*, 83:155201, 2011.

[106] H. Y. Hwang, Y. Iwasa, M. Kawasaki, B. Keimer, N. Nagaosa, and Y. Tokura. Emergent phenomena at oxide interfaces. *Nat. Mater.*, 11:103, 2012.

[107] J. P. Ibbetson, P. T. Fini, K. D. Ness, S. P. DenBaars, J. S. Speck, and U. K. Mishra. Polarization effects, surface states, and the source of electrons in algan/gan heterostructure field effect transistors. *Appl. Phys. Lett.*, 77:250–252, 2000.

[108] Masatoshi Imada, Atsushi Fujimori, and Yoshinori Tokura. Metal-insulator transitions. *Rev. Mod. Phys.*, 70:1039–1263, 1998.

[109] Takanori Inoue, Noriaki Seki, Koichi Eguchi, and Hiromichi Arai. Low-temperature operation of solid electrolyte oxygen sensors using perovskite-type oxide electrodes and cathodic reaction kinetics. *J. Electrochem. Soc.*, 137:2523–2527, 1990.

[110] P. Irvin, Y. Ma, D. F. Bogorin, C. Cen, C. W. Bark, C. M. Folkman, Chang-Beom. Eom, and J. Levy. Rewritable nanoscale oxide photodetector. *Nat. Photon.*, 4:849–852, 2010.

[111] Patrick Irvin, Joshua P. Veazey, Guanglei Cheng, Shicheng Lu, Chung-Wung Bark, Sangwoo Ryu, Chang-Beom Eom, and Jeremy Levy. Anomalous high mobility in $LaAlO_3/SrTiO_3$ nanowires. *Nano Lett.*, 13:364–368, 2013.

[112] H. W. Jang, D. A. Felker, C. W. Bark, Y. Wang, M. K. Niranjan, C. T. Nelson, Y. Zhang, D. Su, C. M. Folkman, S. H. Baek, S. Lee, K. Janicka, Y. Zhu, X. Q. Pan, D. D. Fong, E. Y. Tsymbal, M. S. Rzchowski, and C. B. Eom. Metallic and insulating oxide interfaces controlled by electronic correlations. *Science*, 331:886–889, 2011.

[113] R. Jany, M. Breitschaft, G. Hammerl, A. Horsche, C. Richter, S. Paetel, J. Mannhart, N. Stucki, N. Reyren, S. Gariglio, P. Zubko, A. D. Caviglia, and J.-M. Triscone. Diodes with breakdown voltages enhanced by the metal-insulator transition of $LaAlO_3SrTiO_3$ interfaces. *Appl. Phys. Lett.*, 96:183504, 2010.

[114] S. Jin, T. H. Tiefel, M. McCormack, R. A. Fastnacht, R. Ramesh, and L. H. Chen. Thousandfold change in resistivity in magnetoresistive La-Ca-Mn-O Films. *Science*, 264:413–415, 1994.

[115] A. S. Kalabukhov, Yu. A. Boikov, I. T. Serenkov, V. I. Sakharov, V. N. Popok, R. Gunnarsson, J. Börjesson, N. Ljustina, E. Olsson, D. Winkler, and T. Claeson. Cationic disorder and phase segregation in $LaAlO_3SrTiO_3$ heterointerfaces evidenced by medium-energy ion spectroscopy. *Phys. Rev. Lett.*, 103:146101, 2009.

[116] Alexey Kalabukhov, Robert Gunnarsson, Johan Börjesson, Eva Olsson, Tord Claeson, and Dag Winkler. Effect of oxygen vacancies in the $SrTiO_3$ substrate on the electrical properties of the $LaAlO_3SrTiO_3$ interface. *Phys. Rev. B*, 75:121404, 2007.

[117] B. Kalisky, E. M. Spanton, H. Noad, J. R. Kirtley, K. C. Nowack, C. Bell, H. K. Sato, M. Hosoda, Y. Xie, Y. Hikita, C. Woltmann, G. Pfanzelt, R. Jany, C. Richter, H. Y. Hwang, J. Mannhart, and K. A. Moler. Locally enhanced conductivity due to the tetragonal domain structure in $LaAlO_3/SrTiO_3$ heterointerfaces. *Nat. Mater.*, 12:1091–1095, 2013.

[118] Beena Kalisky, Julie A. Bert, Brannon B. Klopfer, Christopher Bell, Hiroki K. Sato, Masayuki Hosoda, Yasuyuki Hikita, Harold Y. Hwang, and Kathryn A. Moler. Critical thickness for ferromagnetism in $LaAlO_3/SrTiO_3$ heterostructures. *Nat. Commun.*, 3:922, 2012.

[119] Daisuke Kan, Takahito Terashima, Ryoko Kanda, Atsunobu Masuno, Kazunori Tanaka, Shucheng Chu, Hirofumi Kan, Atsushi Ishizumi, Yoshihiko Kanemitsu, Yuichi Shimakawa, and Mikio Takano. Blue-light emission at room temperature from Ar^+-irradiated $SrTiO_3$. *Nat. Mater.*, 4:816, 2005.

[120] Alain Karma, Zachary T. Trautt, and Yuri Mishin. Relationship between equilibrium fluctuations and shear-coupled motion of grain boundaries. *Phys. Rev. Lett.*, 109:095501, 2012.

[121] Mohamed Karmaoui, E. Venkata Ramana, David M. Tobaldi, Luc Lajaunie, Manuel P. Graca, Raul Arenal, Maria P. Seabra, Joao A. Labrincha, and Robert C. Pullar. High dielectric constant and capacitance in ultrasmall (2.5 nm) $SrHfO_3$ perovskite nanoparticles produced in a low temperature non-aqueous sol-gel route. *RSC Adv.,*, 6:51493–51502, 2016.

[122] Susan M. Kauzlarich, Shawna R. Brown, and G. Jeffrey Snyder. Zintl phases for thermoelectric devices. *Dalton T.*, 0:2099–2107, 2007.

[123] B. Keimer, S. A. Kivelson, M. R. Norman, S. Uchida, and J. Zaanen. From quantum matter to high-temperature superconductivity in copper oxides. *Nature*, 518:179, 2015.

[124] Brendan J. Kennedy, Christopher J. Howard, and Bryan C. Chakoumakos. High-temperature phase transitions in $SrZrO_3$. *Phys. Rev. B*, 59:4023–4027, 1999.

[125] Y. Kesong, D. Ying, H. Baibiao, and P. Feng Yuan. First-principles GGA+*U* study of the different conducting properties in Pentavalent-Ion-Doped anatase and rutile TiO_2. *J. Phys. D: Appl. Phys.*, 47:275101, 2014.

[126] Juho Kim, Youngnam Kim, Young Sung Kim, Jaichan Lee, Leejun Kim, and Donggeun Jung. Large nonlinear dielectric properties of artificial $BaTiO_3/SrTiO_3$ superlattices. *Appl. Phys. Lett.*, 80:3581–3583, 2002.

[127] Graham King, Andrew S. Wills, and Patrick M. Woodward. Magnetic structures of $NaLMnWO_6$ perovskites (L=Na, Nd, Tb). *Phys. Rev. B*, 79:224428, 2009.

[128] Akihiro Kojima, Kenjiro Teshima, Yasuo Shirai, and Tsutomu Miyasaka. Organometal halide perovskites as visible-light sensitizers for photovoltaic cells. *J. Am. Chem. Soc.*, 131:6050–6051, 2009.

[129] Y. Kozuka, Y. Hikita, C. Bell, and H. Y. Hwang. Dramatic mobility enhancements in doped $srtio_3$ thin films by defect management. *Appl. Phys. Lett.*, 97:012107, 2010.

[130] Theodore J. Kraus, Alexander B. Nepomnyashchii, and B. A. Parkinson. Templated homoepitaxial growth with atomic layer deposition of single-crystal anatase (101) and rutile (110) TiO_2. *ACS Appl. Mater. Interfaces*, 6:9946–9949, 2014.

[131] A Krause, W M Weber, D Pohl, B Rellinghaus, A Kersch, and T Mikolajick. Investigation of band gap and permittivity of the perovskite $CaTiO_3$ in ultrathin layers. *J. Phys. D: Appl. Phys.*, 48:415304, 2015.

[132] G. Kresse and J. Furthmüller. Efficiency of *ab-initio* total energy calculations for metals and semiconductors using a plane-wave basis set. *Comput. Mater. Sci.*, 6:15–50, 1996.

[133] G. Kresse and J. Furthmüller. Efficient iterative schemes for *ab-initio* total-energy calculations using a plane-wave basis set. *Phys. Rev. B*, 54:11169–11186, 1996.

[134] G. Kresse and D. Joubert. From ultrasoft pseudopotentials to the projector augmented-wave method. *Phys. Rev. B*, 59:1758–1775, 1999.

[135] O. Kubaschewski, C.B. Alcock, and P.J. Spencer. *Materials Thermochemistry*. Pergamon Press, 1993.

[136] Pramod Kumar, Anjana Dogra, P P S Bhadauria, Anurag Gupta, K K Maurya, and R C Budhani. Enhanced spinorbit coupling and charge carrier density suppression in $LaAl_{1-X}Cr_xO_3/SrTiO_3$ hetero-interfaces. *J. Phys.: Condens. Matter*, 27:125007, 2015.

[137] Yoshihiro Kuroiwa, Shinobu Aoyagi, Akikatsu Sawada, Jimpei Harada, Eiji Nishibori, Masaki Takata, and Makoto Sakata. Evidence for Pb-O covalency in tetragonal $PbTiO_3$. *Phys. Rev. Lett.*, 87:217601, 2001.

[138] J Kwapulinski, J Kusz, H Bhm, and J Dec. Thermal vibrations in $PbZrO_3$ single crystals. *J. Phys.: Condens. Matter*, 13:1461, 2001.

[139] A. I. Lebedev. Ab initio calculations of phonon spectra in $ATiO_3$ perovskite crystals (A = Ca, Sr, Ba, Ra, Cd, Zn, Mg, Ge, Sn, Pb). *Phys. of Solid State*, 51:362–372, 2009.

[140] H. Lee, N. Campbell, J. Lee, T. J. Asel, T. R. Paudel, H. Zhou, J. W. Lee, B. Noesges, J. Seo, B. Park, L. J. Brillson, S. H. Oh, E. Y. Tsymbal, M. S. Rzchowski, and C. B. Eom. Direct observation of a two-dimensional hole gas at oxide interfaces. *Nat. Mater.*, 17:231, 2018.

[141] J. H. Lee, G. Luo, I. C. Tung, S. H. Chang, Z. Luo, M. Malshe, M. Gadre, A. Bhattacharya, S. M. Nakhmanson, J. A. Eastman, H. Hong, J. Jellinek, D. Morgan, D. D. Fong, and J. W. Freeland. Dynamic layer rearrangement during growth of layered oxide films by molecular beam epitaxy. 13:879–883, 2014.

[142] Jaekwang Lee and A. A. Demkov. Charge origin and localization at the *n*-Type $SrTiO_3/LaAlO_3$ interface. *Phys. Rev. B*, 78:193104, 2008.

[143] P. W. Lee, V. N. Singh, G. Y. Guo, H.-J. Liu, J.-C. Lin, Y.-H. Chu, C. H. Chen, and M.-W. Chu. Hidden lattice instabilities as origin of the conductive interface between insulating $LaAlO_3$ and $SrTiO_3$. *Nat. Commun.*, 7:12773, 2016.

[144] Y. S. Lee, J. S. Lee, T. W. Noh, Douck Young Byun, Kwang Soo Yoo, K. Yamaura, and E. Takayama-Muromachi. Systematic trends in the electronic structure parameters of the 4*d* transition-metal oxides $SrMO_3$(M=Zr, Mo, Ru, and Rh). *Phys. Rev. B*, 67:113101, 2003.

[145] P. Lejček. *Grain Boundary Segregation in Metals*. Springer Berlin Heidelberg, 2010.

[146] Pavel Lejček and Siegfried Hofmann. Thermodynamics and structural aspects of grain boundary segregation. *Crit. Rev. Solid State Mater. Sci.*, 20:1–85, 1995.

[147] E. Lesne, Yu Fu, S. Oyarzun, J. C. Rojas-Sánchez, D. C. Vaz, H. Naganuma, G. Sicoli, J.-P. Attané, M. Jamet, E. Jacquet, J.-M. George, A. Barthélémy, H. Jaffrès, A. Fert, M. Bibes, and L. Vila. Highly efficient and tunable spin-to-charge conversion through rashba coupling at oxide interfaces. *Nat. Mater.*, 15:1261, 2016.

[148] Leqing Li, Brendan J. Kennedy, Yoshiki Kubota, Kenichi Kato, and Richard F. Garrett. Structures and phase transitions in $Sr_{1-X}Ba_xHfO_3$ perovskites. *J. Mater. Chem.*, 14:263–273, 2004.

[149] Lu Li, C. Richter, J. Mannhart, and R. C. Ashoori. Coexistence of magnetic order and two-dimensional superconductivity at $LaAlO_3/SrTiO_3$ interfaces. *Nat. Phys.*, 7:762, 2011.

[150] Wei-Zhen Li, Libor Kovarik, Donghai Mei, Jun Liu, Yong Wang, and Charles H. F. Peden. Stable platinum nanoparticles on specific $MgAl_2O_4$ spinel facets at high temperatures in oxidizing atmospheres. *Nat. Commun.*, 4:2481, 2013.

[151] Yun Li, Sutassana Na Phattalung, Sukit Limpijumnong, Jiyeon Kim, and Jaejun Yu. Formation of oxygen vacancies and charge carriers induced in the *n*-type interface of a $LaAlO_3$ overlayer on $LaAlO_3$(001). *Phys. Rev. B*, 84:245307, 2011.

[152] Yun Li and Jaejun Yu. Polarization screening and induced carrier density at the interface of $LaAlO_3$ overlayer on $SrTiO_3$ (001). *J. Appl. Phys.*, 108:013701, 2010.

[153] WeiNan Lin, JunFeng Ding, ShuXiang Wu, YongFeng Li, James Lourembam, Santiranjan Shannigrahi, ShiJie Wang, and Tom Wu. Electrostatic modulation of $LaAlO_3/SrTiO_3$ interface transport in an electric doublelayer transistor. *Adv. Mater. Interfaces*, 1:1300001.

[154] Lin-Gun Liu and A.E. Ringwood. Synthesis of a perovskite-type polymorph of $CaSiO_3$. *Earth Planet. Sci. Lett.*, 28:209–211, 1975.

[155] W. Liu, S. Gariglio, A. Fête, D. Li, M. Boselli, D. Stornaiuolo, and J.-M. Triscone. Magneto-transport study of top- and back-gated $LaAlO_3/SrTiO_3$ heterostructures. *APL Mater.*, 3:62805, 2015.

[156] Xiaohui Liu, Yong Wang, Pavel V. Lukashev, J. D. Burton, and E. Y. Tsymbal. Interface dipole effect on thin film ferroelectric stability: First-principles and phenomenological modeling. *Phys. Rev. B*, 85:125407, 2012.

[157] Yang Liu, Xiaojie Lou, Manuel Bibes, and Brahim Dkhil. Effect of a built-in electric field in asymmetric ferroelectric tunnel junctions. *Phys. Rev. B*, 88:024106, 2013.

[158] Z. Liu, C. Li, W. Lü, X. Huang, Z. Huang, S. Zeng, X. Qiu, L. Huang, A. Annadi, J. Chen, J. Coey, T. Venkatesan, and Ariando. Origin of the two-dimensional electron gas at $LaAlO_3/SrTiO_3$ interfaces: The role of oxygen vacancies and electronic reconstruction. *Phys. Rev. X*, 3:021010, 2013.

[159] Z. Q. Liu, D. P. Leusink, W. M. Lü, X. Wang, X. P. Yang, K. Gopinadhan, Y. T. Lin, A. Annadi, Y. L. Zhao, A. Roy Barman, S. Dhar, Y. P. Feng, H. B. Su, G. Xiong, T. Venkatesan, and Ariando. Reversible metal-insulator transition in $LaAlO_3$ thin films mediated by intragap defects: An alternative mechanism for resistive switching. *Phys. Rev. B*, 84:165106, 2011.

[160] Z. Q. Liu, W. M. Lü, S. L. Lim, X. P. Qiu, N. N. Bao, M. Motapothula, J. B. Yi, M. Yang, S. Dhar, T. Venkatesan, and Ariando. Reversible room-temperature ferromagnetism in Nb-doped $SrTiO_3$ single crystals. *Phys. Rev. B*, 87:220405, 2013.

[161] M Lorenz, M S Ramachandra Rao, T Venkatesan, E Fortunato, P Barquinha, R Branquinho, D Salgueiro, R Martins, E Carlos, A Liu, F K Shan, M Grundmann, H Boschker, J Mukherjee, M Priyadarshini, N DasGupta, D J Rogers, F H Teherani, E V Sandana, P Bove, K Rietwyk, A Zaban, A Veziridis, A Weidenkaff, M Muralidhar, M Murakami, S Abel, J Fompeyrine, J Zuniga-Perez, R Ramesh, N A Spaldin, S Ostanin, V Borisov, I Mertig, V Lazenka, G Srinivasan, W Prellier, M Uchida, M Kawasaki, R Pentcheva, P Gegenwart, F Miletto Granozio, J Fontcuberta, and N Pryds. The 2016 oxide electronic materials and oxide interfaces roadmap. *J. Phys. D: Appl. Phys.*, 49:433001, 2016.

[162] G. Lupina, G. Kozowski, J. Dabrowski, P. Dudek, G. Lippert, and H.-J. Mssig. Dielectric and structural properties of thin $SrHfO_3$ layers on tin. *Appl. Phys. Lett.*, 93:252907, 2008.

[163] Grzegorz Lupina, Piotr Dudek, Grzegorz Kozowski, Jarek Dbrowski, Gunther Lippert, Hans-Joachim Mssig, and Thomas Schroeder. Dielectric properties of thin Hf- and Zr-based alkaline earth perovskite layers. *ECS Transactions*, 25:147–151, 2009.

[164] Cheng Ma, Kai Chen, Chengdu Liang, Ce-Wen Nan, Ryo Ishikawa, Karren More, and Miaofang Chi. Atomic-scale origin of the large grain-boundary resistance in perovskite li-ion-conducting solid electrolytes. *Energy Environ. Sci.*, 7:1638–1642, 2014.

[165] S. Maekawa, T. Tohyama, S.E. Barnes, S. Ishihara, W. Koshibae, and G. Khaliullin. *Physics of Transition Metal Oxides*. Springer Berlin Heidelberg, 2004.

[166] J. Mannhart and D. G. Schlom. Oxide interfaces-An opportunity for electronics. *Science*, 327:1607–1611, 2010.

[167] M.D. Mathews, E.B. Mirza, and A.C. Momin. High-temperature x-ray diffractometric studies of $CaZrO_3$, $SrZrO_3$ and $BaZrO_3$. *J. Mater. Sci. Lett.*, 10:305–306, 1991.

[168] Y. Matsubara, K. S. Takahashi, M. S. Bahramy, Y. Kozuka, D. Maryenko, J. Falson, A. Tsukazaki, Y. Tokura, and M. Kawasaki. Observation of the quantum hall effect in δ-doped $SrTiO_3$. *Nat. Commun.*, 7:11631, 2016.

[169] Yuji Matsumoto, Makoto Murakami, Tomoji Shono, Tetsuya Hasegawa, Tomoteru Fukumura, Masashi Kawasaki, Parhat Ahmet, Toyohiro Chikyow, Shin-ya Koshihara, and Hideomi Koinuma. Room-temperature ferromagnetism in transparent transition metal-doped titanium dioxide. *Science*, 291:854–856, 2001.

[170] Martin D. McDaniel, Chengqing Hu, Sirong Lu, Thong Q. Ngo, Agham Posadas, Aiting Jiang, David J. Smith, Edward T. Yu, Alexander A. Demkov, and John G. Ekerdt. Atomic layer deposition of crystalline $SrHfO_3$ directly on Ge (001) for high-*k* dielectric applications. *J. Appl. Phys.*, 117:054101, 2015.

[171] W. Meevasana, P. D. C. King, R. H. He, S-K. Mo, M. Hashimoto, A. Tamai, P. Songsiriritthigul, F. Baumberger, and Z-X. Shen. Creation and control of a two-dimensional electron liquid at the bare $SrTiO_3$ surface. *Nat. Mater.*, 10:114–118, 2011.

[172] Makoto Minohara, Takashi Tachikawa, Yasuo Nakanishi, Yasuyuki Hikita, Lena F. Kourkoutis, Jun-Sik Lee, Chi-Chang Kao, Masahiro Yoshita, Hidefumi Akiyama, Christopher Bell, and Harold Y. Hwang. Atomically engineered metalinsulator transition at the $TiO_2/LaAlO_3$ heterointerface. *Nano Lett.*, 14:6743–6746, 2014.

[173] Y. Mishin, M. Asta, and Ju Li. Atomistic modeling of interfaces and their impact on microstructure and properties. *Acta Mater.*, 58:1117–1151, 2010.

[174] Yoshio Miura, Shingo Muramoto, Kazutaka Abe, and Masafumi Shirai. First-principles study of tunneling magnetoresistance in $Fe/MgAl_2O_4/Fe(001)$ magnetic tunnel junctions. *Phys. Rev. B*, 86:024426, 2012.

[175] Hiroshi Mizoguchi, Hank W. Eng, and Patrick M. Woodward. Probing the electronic structures of ternary perovskite and pyrochlore oxides containing Sn^{4+} or Sb^{5+}. *Inorg. Chem.*, 43:1667–1680, 2004.

[176] Pouya Moetakef, James R. Williams, Daniel G. Ouellette, Adam P. Kajdos, David Goldhaber-Gordon, S. James Allen, and Susanne Stemmer. Carrier-controlled ferromagnetism in $SrTiO_3$. *Phys. Rev. X*, 2:021014, 2012.

[177] O. Müller and R. Roy. *The major ternary structural families*. Crystal chemistry of non-metallic materials. Springer-Verlag, 1974.

[178] Yatsuhisa Nagano. Standard enthalpy of formation of platinum hydrous oxide. *J. Therm. Anal. Calorim.*, 69:831–839, 2002.

[179] N. Nakagawa, H. Y. Hwang, and D. A. Muller. Why some interfaces cannot be sharp. *Nat. Mater.*, 5:204–209, 2006.

[180] H. Nakamura, T. Koga, and T. Kimura. Experimental evidence of cubic rashba effect in an inversion-symmetric oxide. *Phys. Rev. Lett.*, 108:206601, 2012.

[181] Safdar Nazir, Maziar Behtash, Jianli Cheng, Jian Luo, and Kesong Yang. Nb and Ta layer doping effects on the interfacial energetics and electronic properties of $LaAlO_3/SrTiO_3$ heterostructure: First-principles analysis. *Phys. Chem. Chem. Phys.*, 18:2379–2388, 2016.

[182] Safdar Nazir, Maziar Behtash, and Kesong Yang. Enhancing interfacial conductivity and spatial charge confinement of $LaAlO_3/SrTiO_3$ heterostructures via strain engineering. *Appl. Phys. Lett.*, 105:141602–141605, 2014.

[183] Safdar Nazir, Maziar Behtash, and Kesong Yang. The role of uniaxial strain in tailoring the interfacial properties of $LaAlO_3/SrTiO_3$ heterostructure. *RSC Adv.*, 5:15682–15689, 2015.

[184] Safdar Nazir, Maziar Behtash, and Kesong Yang. Towards enhancing two-dimensional electron gas quantum confinement effects in perovskite oxide heterostructures. *J. Appl. Phys.*, 117:115305, 2015.

[185] Safdar Nazir, Camille Berna, and Kesong Yang. Modulated two-dimensional charge carrier density in $LaTiO_3$-layer-doped $LaAlO_3/SrTiO_3$ heterostructure. *ACS Appl. Mater. Interfaces*, 7:5305–5311, 2015.

[186] Safdar Nazir, Jianli Cheng, Maziar Behtash, Jian Luo, and Kesong Yang. Interface energetics and charge carrier density amplification by Sn-doping in $LaAlO_3/SrTiO_3$ heterostructure. *ACS Appl. Mater. Interfaces*, 7:14294–14302, 2015.

[187] Safdar Nazir, Jianli Cheng, and Kesong Yang. Creating two-dimensional electron gas in nonpolar/nonpolar oxide interface via polarization discontinuity: First-principles analysis of $CaZrO_3/SrTiO_3$ heterostructure. *ACS Appl. Mater. Interfaces*, 8:390–399, 2016.

[188] Safdar Nazir and Kesong Yang. First-principles characterization of the critical thickness for forming metallic states in strained $LaAlO_3/SrTiO_3(001)$ heterostructure. *ACS Appl. Mater. Interfaces*, 6:22351–22358, 2014.

[189] Hiroshi Ogawa. GBstudio: A builder software on periodic models of csl boundaries for molecular simulation. *Mater. Trans.*, 47:2706–2710, 2006.

[190] A. Ohtomo and H. Y. Hwang. A high-mobility electron gas at the $LaAlO_3/SrTiO_3$ heterointerface. *Nature*, 427:423–426, 2004.

[191] S. Okamoto and A. J. Millis. Electronic reconstruction at an interface between a mott insulator and a band insulator. *Nature*, 428:630–633, 2004.

[192] P. V. Ong, Jaichan Lee, and W. E. Pickett. Tunable two-dimensional or three-dimensional electron gases by submonolayer la doping of $SrTiO_3$. *Phys. Rev. B*, 83:193106, 2011.

[193] Shyue Ping Ong, William Davidson Richards, Anubhav Jain, Geoffroy Hautier, Michael Kocher, Shreyas Cholia, Dan Gunter, Vincent L. Chevrier, Kristin A. Persson, and Gerbrand Ceder. Python materials genomics (pymatgen): A robust, open-source python library for materials analysis. *Comput. Mater. Sci.*, 68:314–319, 2013.

[194] David C. Palmer. Visualization and analysis of crystal structures using crystalmaker software. *Z. Kristallogr. Cryst. Mater.*, 230:559, 2015.

[195] J.W. Park, D.F. Bogorin, C. Cen, D.A. Felker, Y. Zhang, C.T. Nelson, C.W. Bark, C.M. Folkman, X.Q. Pan, M.S. Rzchowski, J. Levy, and C.B. Eom. Creation of a two-dimensional electron gas at an oxide interface on silicon. *Nat. Commun.*, 1:94, 2010.

[196] S. A. Pauli, S. J. Leake, B. Delley, M. Björck, C. W. Schneider, C. M. Schlepütz, D. Martoccia, S. Paetel, J. Mannhart, and P. R. Willmott. Evolution of the interfacial structure of $LaAlO_3$ on $SrTiO_3$. *Phys. Rev. Lett.*, 106:036101, 2011.

[197] Chien H. Peng, Jhing-Fang Chang, and Seshu B. Desu. Optical properties of PZT, PLZT, and PNZT thin films. *MRS Proceedings*, 243:21, 1991.

[198] R. Pentcheva and W. E. Pickett. Ionic relaxation contribution to the electronic reconstruction at the *n*-type $LaAlO_3$/$SrTiO_3$ interface. *Phys. Rev. B*, 78:205106, 2008.

[199] R. Pentcheva and W. E. Pickett. Avoiding the polarization catastrophe in $LaAlO_3$ overlayers on $SrTiO_3$(001) through polar distortion. *Phys. Rev. Lett.*, 102:107602, 2009.

[200] John P. Perdew, Kieron Burke, and Matthias Ernzerhof. Generalized gradient approximation made simple. *Phys. Rev. Lett.*, 77:3865–3868, 1996.

[201] P. Perna, D. Maccariello, M. Radovic, U. Scotti di Uccio, I. Pallecchi, M. Codda, D. Marr, C. Cantoni, J. Gazquez, M. Varela, S. J. Pennycook, and F. Miletto Granozio. Conducting interfaces between band insulating oxides: The $LaGaO_3$/$SrTiO_3$ heterostructure. *Appl. Phys. Lett.*, 97:152111, 2010.

[202] YU Peter and Manuel Cardona. *Fundamentals of semiconductors: physics and materials properties*. Springer Science & Business Media, 2010.

[203] Robert M. Pick, Morrel H. Cohen, and Richard M. Martin. Microscopic theory of force constants in the adiabatic approximation. *Phys. Rev. B*, 1:910–920, 1970.

[204] Steve Plimpton. Fast parallel algorithms for short-range molecular dynamics. *J. Comput. Phys.*, 117:1–19, 1995.

[205] L. Priester. *Grain Boundaries: From Theory to Engineering*. Springer Netherlands, 2012.

[206] O. I. Prokopalo, I. P. Raevskii, M. A. Malitskaya, Yu. M. Popov, A. A. Bokov, and V. G. Smotrakov. Peculiar electric and photoelectric behavior of lead-containing perovskite-type oxides. *Ferroelectrics*, 45:89–95, 1982.

[207] Krishna Rajan. Materials informatics. *Materials Today*, 8:38–45, 2005.

[208] S. Ranganathan. On the geometry of coincidence-site lattices. *Acta Cryst.*, 21:197–199, 1966.

[209] A. Rastogi, J. J. Pulikkotil, and R. C. Budhani. Enhanced persistent photoconductivity in δ-Doped $LaAlO_3/SrTiO_3$ heterostructures. *Phys. Rev. B*, 89:125127, 2014.

[210] Erwan Rauwel, Augustinas Galeckas, Protima Rauwel, and Helmer Fjellvåg. Unusual photoluminescence of $CaHfO_3$ and $SrHfO_3$ nanoparticles. *Adv. Fun. Mater.*, 22:1174–1179, 2012.

[211] M.L. Reinle-Schmitt, C. Cancellieri, D. Li, D. Fontaine, M. Medarde, E. Pomjakushina, C.W. Schneider, S. Gariglio, Ph. Ghosez, J.-M. Triscone, and P.R. Willmott. Tunable conductivity threshold at polar oxide interfaces. 3:932, 2012.

[212] N. Reyren, M. Bibes, E. Lesne, J.-M. George, C. Deranlot, S. Collin, A. Barthélémy, and H. Jaffrès. Gate-controlled spin injection at $LaAlO_3/SrTiO_3$ interfaces. *Phys. Rev. Lett.*, 108:186802, 2012.

[213] N. Reyren, S. Thiel, A. D. Caviglia, L. F. Kourkoutis, G. Hammer, C. Richter, C. W. Schneider, T. Kopp, A. S. Rüetschi, D. Jaccard, M. Gabay, D. A. Muller, J. M. Triscone, and J. Mannhart. Superconducting interfaces between insulating oxides. *Science*, 317:1196–1199, 2007.

[214] T. C. Rödel, F. Fortuna, F. Bertran, M. Gabay, M. J. Rozenberg, A. F. Santander-Syro, and P. Le Fèvre. Engineering two-dimensional electron gases at the (001) and (101) surfaces of TiO_2 anatase using light. *Phys. Rev. B*, 92:041106, 2015.

[215] Tobias Chris Rödel, Franck Fortuna, Shamashis Sengupta, Emmanouil Frantzeskakis, Patrick Le Fèvre, Franois Bertran, Bernard Mercey, Sylvia Matzen, Guillaume Agnus, Thomas Maroutian, Philippe Lecoeur, and Andrés Felipe Santander-Syro. Universal fabrication of 2d electron systems in functional oxides. *Adv. Mater.*, 28:1976–1980, 2016.

[216] G.S. Rohrer. *Structure and Bonding in Crystalline Materials*. Cambridge University Press, 2001.

[217] C. Rossel, B. Mereu, C. Marchiori, D. Caimi, M. Sousa, A. Guiller, H. Siegwart, R. Germann, J.-P. Locquet, J. Fompeyrine, D. J. Webb, Ch. Dieker, and Jin Won Seo. Field-effect transistors with $SrHfO_3$ as gate oxide. *Appl. Phys. Lett.*, 89:053506, 2006.

[218] C. Rossel, M. Sousa, C. Marchiori, J. Fompeyrine, D. Webb, D. Caimi, B. Mereu, A. Ispas, J.P. Locquet, H. Siegwart, R. Germann, A. Tapponnier, and K. Babich. $SrHfO_3$ as gate dielectric for future cmos technology. *Microelec. Eng.*, 84:1869–1873, 2007.

[219] S. Roy, A. Solmaz, J. D. Burton, M. Huijben, G. Rijnders, E. Y. Tsymbal, and T. Banerjee. Engineering interfacial energy profile by changing the substrate terminating plane in perovskite heterointerfaces. *Phys. Rev. B*, 93:115101, 2016.

[220] S. Ryu, H. Zhou, T. R. Paudel, J. Irwin, J. P. Podkaminer, C. W. Bark, D. Lee, T. H. Kim, D. D. Fong, M. S. Rzchowski, E. Y. Tsymbal, and C. B. Eom. In-situ probing of coupled atomic restructuring and metallicity of oxide heterointerfaces induced by polar adsorbates. *Appl. Phys. Lett.*, 111:141604, 2017.

[221] Tarapada Sarkar, Kalon Gopinadhan, Jun Zhou, Surajit Saha, J. M. D. Coey, Yuan Ping Feng, Ariando, and T. Venkatesan. Electron transport at the TiO_2 surfaces of rutile, anatase, and strontium titanate: The influence of orbital corrugation. *ACS Appl. Mater. Interfaces*, 7:24616–24621, 2015.

[222] P. Scheiderer, F. Pfaff, J. Gabel, M. Kamp, M. Sing, and R. Claessen. Surface-interface coupling in an oxide heterostructure: Impact of adsorbates on $LaAlO_3/SrTiO_3$. *Phys. Rev. B*, 92:195422, 2015.

[223] Lukas Schlipf, Alexander Slepko, Agham B. Posadas, Heidi Seinige, Ajit Dhamdhere, Maxim Tsoi, David J. Smith, and Alexander A. Demkov. Epitaxial zintl aluminide $SrAl_4$ grown on a $LaAlO_3$ substrate. *Phys. Rev. B*, 88:045314, 2013.

[224] F. Schoofs, M. Egilmez, T. Fix, J. L. MacManus-Driscoll, and M. G. Blamire. Tuning the two-dimensional carrier density at $LaAlO_3/SrTiO_3$ interfaces via rare earth doping. *Solid State Commun.*, 156:35–37, 2013.

[225] P. Schütz, F. Pfaff, P. Scheiderer, Y. Z. Chen, N. Pryds, M. Gorgoi, M. Sing, and R. Claessen. Band bending and alignment at the spinel/perovskite γ-$Al_2O_3/SrTiO_3$ heterointerface. *Phys. Rev. B*, 91:165118, 2015.

[226] Hosung Seo, Agham B. Posadas, Chandrima Mitra, Alexander V. Kvit, Jamal Ramdani, and Alexander A. Demkov. Band alignment and electronic structure of the anatase $TiO_2/SrTiO_3(001)$ heterostructure integrated on Si(001). *Phys. Rev. B*, 86:075301, 2012.

[227] Wahyu Setyawan, Romain M. Gaume, Stephanie Lam, Robert S. Feigelson, and Stefano Curtarolo. High-throughput combinatorial database of electronic band structures for inorganic scintillator materials. *ACS Comb. Sci.*, 13:382–390, 2011.

[228] P. Sharma, S. Ryu, J. D. Burton, T. R. Paudel, C. W. Bark, Z. Huang, Ariando, E. Y. Tsymbal, G. Catalan, C. B. Eom, and A. Gruverman. Mechanical tuning of $LaAlO_3/SrTiO_3$ interface conductivity. *Nano Lett.*, 15:3547–3551, 2015.

[229] Keisuke Shibuya, Tsuyoshi Ohnishi, Mikk Lippmaa, Masashi Kawasaki, and Hideomi Koinuma. Single crystal $SrTiO_3$ field-effect transistor with an atomically flat amorphous $CaHfO_3$ gate insulator. *Appl. Phys. Lett.*, 85:425–427, 2004.

[230] Keisuke Shibuya, Tsuyoshi Ohnishi, Mikk Lippmaa, and Masaharu Oshima. Metallic conductivity at the $CaHfO_3SrTiO_3$ interface. *Appl. Phys. Lett.*, 91:232106, 2007.

[231] Wolter Siemons, Gertjan Koster, Hideki Yamamoto, Walter A. Harrison, Gerald Lucovsky, Theodore H. Geballe, Dave H. A. Blank, and Malcolm R. Beasley. Origin of charge density at $LaAlO_3$ on $SrTiO_3$ heterointerfaces: Possibility of intrinsic doping. *Phys. Rev. Lett.*, 98:196802, 2007.

[232] Hyunsu Sim, S. W. Cheong, and Bog G. Kim. Octahedral tilting-induced ferroelectricity in $ASnO_3$/A'SnO_3 superlattices (A, A'=Ca, Sr, and Ba). *Phys. Rev. B*, 88:014101, 2013.

[233] E. Slooten, Zhicheng Zhong, H. J. A. Molegraaf, P. D. Eerkes, S. de Jong, F. Massee, E. van Heumen, M. K. Kruize, S. Wenderich, J. E. Kleibeuker, M. Gorgoi, H. Hilgenkamp, A. Brinkman, M. Huijben, G. Rijnders, D. H. A. Blank, G. Koster, P. J. Kelly, and M. S. Golden. Hard x-ray photoemission and density functional theory study of the internal electric field in $SrTiO_3$/$LaAlO_3$ oxide heterostructures. *Phys. Rev. B*, 87:085128, 2013.

[234] G. Jeffrey Snyder and Eric S. Toberer. Complex thermoelectric materials. *Nat. Mater.*, 7:105–114, 2008.

[235] Won-Joon Son, Eunae Cho, Bora Lee, Jaichan Lee, and Seungwu Han. Density and spatial distribution of charge carriers in the intrinsic *n*-type $LaAlO_3$-$SrTiO_3$ interface. *Phys. Rev. B*, 79:245411, 2009.

[236] Kyung Song, Sangwoo Ryu, Hyungwoo Lee, Tula R. Paudel, Christoph T. Koch, Bumsu Park, Ja Kyung Lee, Si-Young Choi, Young-Min Kim, Jong Chan Kim, Hu Young Jeong, Mark S. Rzchowski, Evgeny Y. Tsymbal, Chang-Beom Eom, and Sang Ho Oh. Direct imaging of the electron liquid at oxide interfaces. *Nat. Nanotechnol.*, 13:198, 2018.

[237] Susanne Stemmer and S. James Allen. Two-dimensional electron gases at complex oxide interfaces. *Annu. Rev. Mater. Sci.*, 44:151–171, 2014.

[238] Massimiliano Stengel and David Vanderbilt. Berry-phase theory of polar discontinuities at oxide-oxide interfaces. *Phys. Rev. B*, 80:241103, 2009.

[239] F. Sugawara, Y. Syono, and S. Akimoto. High pressure synthesis of a new perovskite $PbSnO_3$. *Mater. Res. Bull.*, 3:529–532, 1968.

[240] Hiroaki Sukegawa, Yoshio Miura, Shingo Muramoto, Seiji Mitani, Tomohiko Niizeki, Tadakatsu Ohkubo, Kazutaka Abe, Masafumi Shirai, Koichiro Inomata, and Kazuhiro Hono. Enhanced tunnel magnetoresistance in a spinel oxide barrier with cation-site disorder. *Phys. Rev. B*, 86:184401, 2012.

[241] J. A. Sulpizio, Shahal Ilani, Patrick Irvin, and Jeremy Levy. Nanoscale phenomena in oxide heterostructures. *Annu. Rev. Mater. Sci.*, 44:117–149, 2014.

[242] Jianwei Sun, Adrienn Ruzsinszky, and John P. Perdew. Strongly constrained and appropriately normed semilocal density functional. *Phys. Rev. Lett.*, 115:036402, 2015.

[243] A.P. Sutton and R.W. Balluffi. *Interfaces in crystalline materials*. Clarendon Press, 1995.

[244] Takashi Tachikawa, Makoto Minohara, Yasuyuki Hikita, Christopher Bell, and Harold Y. Hwang. Tuning band alignment using interface dipoles at the Pt/anatase TiO_2 interface. *Adv. Mater.*, 27:7458, 2015.

[245] K. S. Takahashi and H. Y. Hwang. Carrier doping in anatase TiO_2 film by perovskite overlayer deposition. *Appl. Phys. Lett.*, 93:82112, 2008.

[246] W Tang, E Sanville, and G Henkelman. A grid-based bader analysis algorithm without lattice bias. *J. Phys.: Condens. Matter*, 21:084204, 2009.

[247] S. Thiel, G. Hammerl, A. Schmehl, C. W. Schneider, and J. Mannhart. Tunable quasi-two-dimensional electron gases in oxide heterostructures. *Science*, 313:1942–1945, 2006.

[248] Lukas Thulin and John Guerra. Calculations of strain-modified anatase TiO_2 band structures. *Phys. Rev. B*, 77:195112, 2008.

[249] Eric S. Toberer, Andrew F. May, Brent C. Melot, Espen Flage-Larsen, and G. Jeffrey Snyder. Electronic structure and transport in thermoelectric compounds AZn_2Sb_2 (A = Sr, Ca, Yb, Eu). *Dalton T.*, 39:1046–1054, 2010.

[250] Eric S. Toberer, Alexandra Zevalkink, Nicole Crisosto, and G. Jeffrey Snyder. The zintl compound $Ca_5Al_2Sb_6$ for low-cost thermoelectric power generation. *Adv. Fun. Mater.*, 20:4375–4380, 2010.

[251] Felix Trier, Guenevere E. D. K. Prawiroatmodjo, Zhicheng Zhong, Dennis Valbjørn Christensen, Merlin von Soosten, Arghya Bhowmik, Juan Maria García Lastra, Yunzhong Chen, Thomas Sand Jespersen, and Nini Pryds. Quantization of hall resistance at the metallic interface between an oxide insulator and $SrTiO_3$. *Phys. Rev. Lett.*, 117:096804, 2016.

[252] A. Tsukazaki, A. Ohtomo, T. Kita, Y. Ohno, H. Ohno, and M. Kawasaki. Quantum hall effect in polar oxide heterostructures. *Science*, 315:1388–1391, 2007.

[253] Arend M. van der Zande, Pinshane Y. Huang, Daniel A. Chenet, Timothy C. Berkelbach, YuMeng You, Gwan-Hyoung Lee, Tony F. Heinz, David R. Reichman, David A. Muller, and James C. Hone. Grains and grain boundaries in highly crystalline monolayer molybdenum disulphide. *Nat. Mater.*, 12:554, 2013.

[254] Liang Wang, Dean W. Matson, Evgueni Polikarpov, James S. Swensen, Charles C. Bonham, Lelia Cosimbescu, Joseph J. Berry, David S. Ginley, Daniel J. Gaspar, and Asanga B. Padmaperuma. Highly efficient blue organic light emitting device using indium-free transparent anode Ga:ZnO with scalability for large area coating. *J. Appl. Phys.*, 107:043103, 2010.

[255] Yaqin Wang, Wu Tang, Jianli Cheng, Maziar Behtash, and Kesong Yang. Creating two-dimensional electron gas in polar/polar perovskite oxide heterostructures: First-principles

characterization of $LaAlO_3/A^+B^{5+}O_3$. *ACS Appl. Mater. Interfaces*, 8:13659–13668, 2016.

[256] Yaqin Wang, Wu Tang, Jianli Cheng, Safdar Nazir, and Kesong Yang. High-mobility two-dimensional electron gas in $SrGeO_3$- and $BaSnO_3$-based perovskite oxide heterostructures: an *ab initio* study. *Phys. Chem. Chem. Phys.*, 18:31924–31929, 2016.

[257] M. P. Warusawithana, C. Richter, P. Roy, J. Ludwig, S. Paetel, T. Heeg, A. A. Pawlicki, L. F. Kourkoutis, M. Zheng, M. Lee, B. Mulcahy, W. Zander, Y. Zhu, J. Schubert, J. N. Eckstein, D. A. Muller, C. Stephen Hellberg, J. Mannhart, and D. G. Schlom. $LaAlO_3$ stoichiometry is key to electron liquid formation at $LaAlO_3/SrTiO_3$ interfaces. *Nat. Commun.*, 4:2351, 2013.

[258] M Weissmann and V Ferrari. *Ab Initio* study of a $TiO_2/LaAlO_3$ heterostructure. *J. Phys.: Conf. Ser.*, 167:012060, 2009.

[259] Mariana Weissmann, V. Ferrari, and Andrés Saúl. *Ab Initio* study of magnetism at the $TiO_2/LaAlO_3$ interface. *J. Mater. Sci.*, 45:4945–4951, 2010.

[260] S. H. Wemple. Polarization fluctuations and the optical-absorption edge in $BaTiO_3$. *Phys. Rev. B*, 2:2679–2689, 1970.

[261] P. R. Willmott, S. A. Pauli, R. Herger, C. M. Schlepütz, D. Martoccia, B. D. Patterson, B. Delley, R. Clarke, D. Kumah, C. Cionca, and Y. Yacoby. Structural basis for the conducting interface between $LaAlO_3$ and $SrTiO_3$. *Phys. Rev. Lett.*, 99:155502, 2007.

[262] Marcin Wojdyr, Sarah Khalil, Yun Liu, and Izabela Szlufarska. Energetics and structure of $< 001 >$ tilt grain boundaries in SiC. *Model. Simul. Mater. Sci. Eng.*, 18:075009, 2010.

[263] Xiang Wu, Shan Qin, Ting-Ting Gu, Jing Yang, and Geeth Manthilake. Structural and elastic properties of $CaGeO_3$ perovskite at high pressures. *Phys. Earth Planet. Inter.*, 189:151–156, 2011.

[264] Yanwu Xie, Christopher Bell, Yasuyuki Hikita, Satoshi Harashima, and Harold Y. Hwang. Enhancing electron mobility at the $LaAlO_3/SrTiO_3$ interface by surface control. *Adv. Mater.*, 25:4735–4738, 2013.

[265] Ryosuke Yamamoto, Christopher Bell, Yasuyuki Hikita, Harold Y. Hwang, Hiroyuki Nakamura, Tsuyoshi Kimura, and Yusuke Wakabayashi. Structural comparison of *n*-type and *p*-type $LaAlO_3/SrTiO_3$ interfaces. *Phys. Rev. Lett.*, 107:036104, 2011.

[266] Li Yan, Yaodong Yang, Zhiguang Wang, Zengping Xing, Jiefang Li, and D. Viehland. Review of magnetoelectric perovskite-spinel self-assembled nano-composite thin films. *J. Mater. Sci.*, 44:5080–5094, 2009.

[267] K. Yang, W. Setyawan, S. Wang, M. Buongiorno Nardelli, and S. Curtarolo. A search model for topological insulators with high-throughput robustness descriptors. *Nat. Mater.*, 11:614–619, 2012.

[268] Kesong Yang, Ying Dai, Baibiao Huang, and Yuan Ping Feng. Density functional characterization of the antiferromagnetism in Oxygen-Deficient anatase and rutile TiO_2. *Phys. Rev. B*, 81:033202, 2010.

[269] Kesong Yang, Safdar Nazir, Maziar Behtash, and Jianli Cheng. High-throughput design of two-dimensional electron gas systems based on polar/nonpolar perovskite oxide heterostructures. *Sci. Rep.*, 6:34667, 2016.

[270] Q. Yang, J. X. Cao, Y. Ma, Y. C. Zhou, X. J. Lou, and J. Yang. Interface effect on the magnitude and stability of ferroelectric polarization in ultrathin $PbTiO_3$ films from first-principles study. *J. Appl. Phys.*, 114:034109, 2013.

[271] A. Yangthaisong. Electronic and lattice vibrational properties of cubic $BaHfO_3$ from first principles calculations. *Phys. Lett. A*, 377:927–931, 2013.

[272] Binglun Yin and Shaoxing Qu. Ab initio study of the effects of interfacial structure on the ferroelectric, magnetic, and magnetoelectric coupling properties of Fe/$BaTiO_3$ multiferroic tunnel junctions. *Phys. Rev. B*, 89:014106, 2014.

[273] Liping Yu and Alex Zunger. A polarity-induced defect mechanism for conductivity and magnetism at polar−nonpolar oxide interfaces. *Nat. Commun.*, 5:5118, 2014.

[274] J. Zabaleta, V. S. Borisov, R. Wanke, H. O. Jeschke, S. C. Parks, B. Baum, A. Teker, T. Harada, K. Syassen, T. Kopp, N. Pavlenko, R. Valentí, and J. Mannhart. Hydrostatic pressure response of an oxide-based two-dimensional electron system. *Phys. Rev. B*, 93:235117, 2016.

[275] Hui Zhang, Hongrui Zhang, Xi Yan, Xuejing Zhang, Qinghua Zhang, Jing Zhang, Furong Han, Lin Gu, Banggui Liu, Yuansha Chen, Baogen Shen, and Jirong Sun. Highly mobile two-dimensional electron gases with a strong gating effect at the amorphous $LaAlO_3$/$KTaO_3$ interface. *ACS Appl. Mater. Interfaces*, 9:36456–36461, 2017.

[276] H. Zheng, J. Wang, S. E. Lofland, Z. Ma, L. Mohaddes-Ardabili, T. Zhao, L. Salamanca-Riba, S. R. Shinde, S. B. Ogale, F. Bai, D. Viehland, Y. Jia, D. G. Schlom, M. Wuttig, A. Roytburd, and R. Ramesh. Multiferroic $BaTiO_3$-$CoFe_2O_4$ nanostructures. *Science*, 303:661–663, 2004.

[277] Shijian Zheng, Craig A. J. Fisher, Takeharu Kato, Yuki Nagao, Hiromichi Ohta, and Yuichi Ikuhara. Domain formation in anatase TiO_2 thin films on $LaAlO_3$ substrates. *Appl. Phys. Lett.*, 101:191602, 2012.

[278] W. Zhong, R. D. King-Smith, and David Vanderbilt. Giant LO-TO splittings in perovskite ferroelectrics. *Phys. Rev. Lett.*, 72:3618–3621, 1994.

[279] Zhicheng Zhong, P. X. Xu, and Paul J. Kelly. Polarity-induced oxygen vacancies at $LaAlO_3$/$SrTiO_3$ interfaces. *Phys. Rev. B*, 82:165127, 2010.

[280] Jun Zhou, Teguh Citra Asmara, Ming Yang, George A. Sawatzky, Yuan Ping Feng, and Andrivo Rusydi. Interplay of electronic reconstructions, surface oxygen vacancies, and lattice distortions in insulator-metal transition of $LaAlO_3/SrTiO_3$. *Phys. Rev. B*, 92:125423, 2015.

[281] K Zou, Sohrab Ismail-Beigi, Kim Kisslinger, Xuan Shen, Dong Su, FJ Walker, and CH Ahn. $LaTiO_3/KTaO_3$ interfaces: A new two-dimensional electron gas system. *APL Mater.*, 3:036104, 2015.

[282] Pavlo Zubko, Stefano Gariglio, Marc Gabay, Philippe Ghosez, and Jean-Marc Triscone. Interface physics in complex oxide heterostructures. *Annu. Rev. Condens. Matter Phys.*, 2:141–165, 2011.